UNIVERSITÀ
DEGLI STUDI
DI BRESCIA

DOTTORATO DI RICERCA IN
INGEGNERIA CIVILE, AMBIENTALE, DELLA COOPERAZIONE
INTERNAZIONALE E DI MATEMATICA

Settore Scientifico Disciplinare: ICAR/09

Riabilitazione Strutturale di Edifici Storici e Contemporanei

XXXIII CICLO

SEISMIC BEHAVIOUR OF EXISTING RC FRAMES IN PRESENCE OF PLAIN REINFORCEMENT

DOTTORANDO:
Anthony Paderno

RELATORE:
Prof. Marco Preti

SYNOPSIS

This work refers to the analysis of the seismic behaviour of gravity load designed existing RC buildings reinforced with plain rebars. Specific attention is put on smooth bar stress-slip analysis and on the non-linear modelling of 2D frames flexural response.

A preliminary experimental study was conducted to investigate the cyclic stress-slip response of plain bar anchorages characterized by different shapes. Straight length, hook-ended and bent embedded bars were subjected to cyclic pull-out, including load reversals to apply axial compression on the rebar. The evidences showed the effectiveness of the shaped bars in ensuring an adequate anchorage, whereas significant cyclic bond degradation was observed in the performance of straight rebars. Based on the experimental results, an analytical model is defined to represent the smooth reinforcement stress-slip behaviour. Such behaviour is then implemented in a comprehensive structural model, aimed at representing the cyclic response of non-conforming RC members; a single crack opening on the joint-element interface is considered, thus a rocking behaviour is assumed to govern the overall response. Finally, this analytical concept is implemented in the numerical OpenSees environment, and it is validated throughout the simulation of more than 20 experimental tests taken from the literature, with reference to columns, beams, beam-column joints, and a 2D whole frame. The effectiveness in representing the monotonic and cyclic behaviour of substandard elements reinforced with plain rebar was proved. By the comparison with Eurocode 8 standardized approach, a significant difference is noticed in the assessed structural stiffness and deformation capacity, with respect to the proposed approach.

A further focus on the dowel longitudinal reinforcement bars behaviour is presented, in presence of coupled axial and shear load. An experimental campaign showed the effects of a constant axial load in reducing the dowel mechanism shear strength; an analytical model is then defined to predict the dowel shear-sliding behaviour in presence of the coupled loading. The investigation helps to define a verification procedure, for the sliding mechanism of RC members on a completely crossing opened crack, which can form during a cyclic excitation of large ductility demand.

SOMMARIO

Il presente lavoro analizza il comportamento sismico di edifici esistenti in CA armati con barre a superfice liscia. Particolare attenzione è posta alla definizione di una relazione tra lo sforzo assiale e lo scorrimento di barre lisce, ed alla modellazione della risposta flessionale di telai piani.

Uno studio sperimentale preliminare ha investigato la risposta ciclica di barre a superfice liscia, ancorate nel calcestruzzo secondo diverse soluzioni. Barre rettilinee, piegate e dotate di uncino terminale sono state soggette ad un'azione ciclica di pull-out, prevedendo anche l'imposizione di carichi di compressione sulle stesse. I risultati sperimentali hanno mostrato l'efficienza delle barre sagomate nel garantire un ancoraggio adeguato; le barre rettilinee hanno invece esibito un significativo degrado delle capacità di aderenza. Sulla scorta dei risultati sperimentali è stato definito un modello analitico volto a riprodurre il legame stress-slip di barre lisce. Il medesimo è poi posto a base di una tecnica di modellazione destinata alla definizione della risposta ciclica di elementi in CA non conformi alle moderne prescrizioni normative. Si assume che la stessa risposta sia governata da un meccanismo rocking, la modellazione è quindi basata sull'ipotesi che una singola fessura si formi all'interfaccia tra il nodo e gli elementi che vi convergono. La proposta analitica è successivamente implementata in un ambiente di modellazione numerica (OpenSees) ed è stata poi impiegata per la simulazione di oltre 20 prove sperimentali, effettuate su colonne, travi, giunti trave-colonna ed un intero telaio bidimensionale. L'efficacia della tecnica di modellazione nel rappresentare la risposta monotona e ciclica di strutture armate con barre a superficie liscia è stata constatata. Mediante il confronto con i risultati ottenuti da tecniche di modellazione basate sull'applicazione di indicazioni normative (Eurocodice 8), si è riscontrata una notevole differenza in termini di previsione della rigidezza elastica e di definizione delle effettive capacità deformative.

Un'ulteriore analisi è inoltre stata effettuata in relazione al comportamento a spinotto di barre d'armatura sottoposta ad azione combinata di taglio e sforzo assiale. Una campagna sperimentale ha messo in luce gli effetti di un carico assiale costante sulla resistenza a taglio del meccanismo, la quale risulta ridotta a causa dell'azione combinata. Successivamente, è stato definito un modello analitico per rappresentare il comportamento taglio-scorrimento del meccanismo. L'approfondimento ha consentito di definire una procedura di verifica nei confronti del possibile scorrimento lungo una fessura completamente aperta, la quale si può generare nel corso di una sollecitazione ciclica in presenza di domande di duttilità elevate.

CONTENTS

SEISMIC BEHAVIOUR OF EXISTING RC FRAMES IN PRESENCE OF PLAIN REINFORCEMENT

Most of the residential building stock in Italy was built after World War II, with a peak in the 70's; about 2 million of these were built with Reinforced Concrete (RC). These buildings were typically designed paying little or no attention to the seismic action or according to obsolete Codes (RD 2229, 1939). The data shown in Figure 1 (ISTAT, 2011) confirm that the seismic vulnerability of RC existing structures is a contemporary issue; in fact, about 55% of the buildings today present in Italy were built before the 70's (Figure 1).
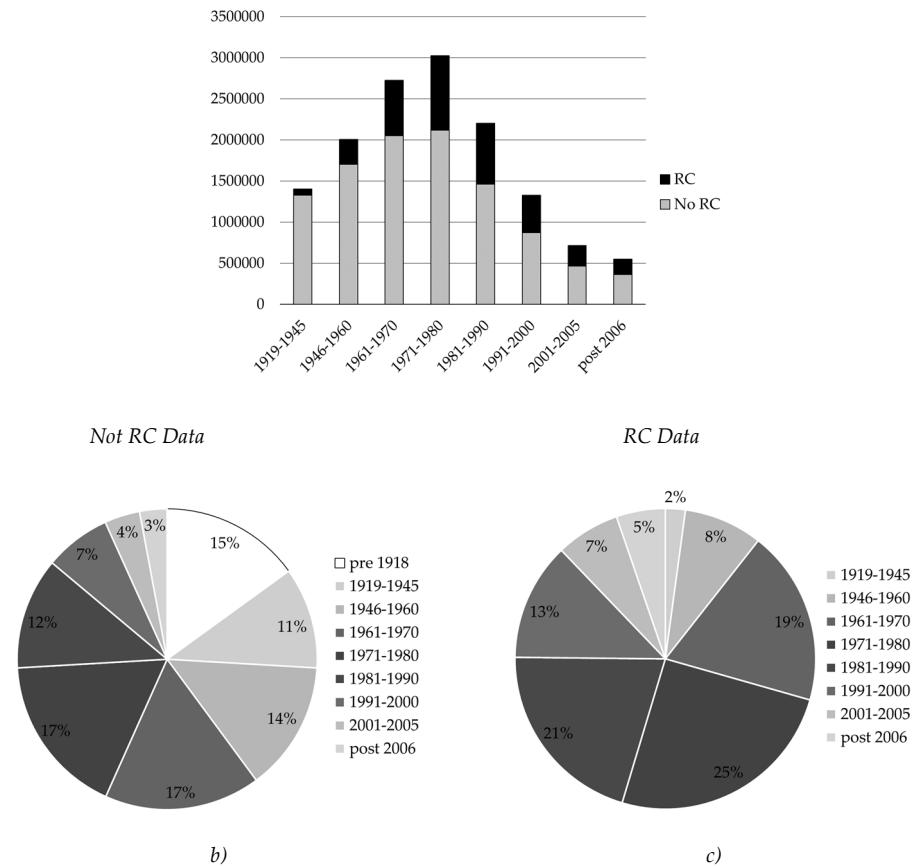
Figure 1: RC and not RC construction age distribution about the Italian residential buildings. The data are collected by Italian National Institute of Statistics (ISTAT, 2011).

The common acronym GLD (Gravity Load Designed) is herein used to identify existing RC structures characterized by:

- modern Code non-conforming design;
- lack of seismic detailing;
- use of plain reinforcement.

The typical structural issues of the GLD frames here considered were recognised in the literature (Cosenza et al., 2002). Low available ductility, strength hierarchy omission, lack of detailing, and seismic demand amplification due to structural irregularity are presented as the principle causes of brittle local and global failure mechanisms. The highest deformation demand is localized at the column ends, where low concrete confinement is available. Therefore, the rotational capacity of the elements should be reduced, due to the concrete cover spalling and to the premature longitudinal bar buckling. The additional seismic shear demand at the beam ends is the cause of reduced deformation and strength capacities, due to shear-flexure interaction (Priestley et al., 1994). Hook-end anchorage absence facilitates longitudinal rebar pull-out, especially in the exterior beam column joints. The assumption of element fix-end restraint at the joint interface can so result totally inadequate. Finally, structural and non-structural elements significantly affect the RC building seismic response. Stiff RC walls, stairs supporting systems and masonry infills are common elements in a multistorey building. Their interaction with the frame results in: i) an increase in local structural stiffness, ii) a consequent amplified structural non-regularity in plan and in elevation, iii) possible brittle failure of RC elements. Furthermore, masonry infills are susceptible to severe in-plane damage and/or Out-Of-Plane (OOP) mechanisms, which results in a threat to live safety, downtime and expensive repair.

Retrofit solutions of GLD structures have been suggested, ranging from local repairing to introduction of brand new seismic resistant elements, like shear walls, bracings, exoskeleton solution. In all cases, the existing elements are subject to load and deflection also in the retrofitted configuration, even if they are assumed as secondary elements in the rearranged seismic resistant system. Thus, their stiffness and general capacity must be assessed, to figure out their response in combination with the adjoined structural elements or local strengthening. Of outer most importance is the verification that a local collapse in an existing element may not jeopardize the efficiency of the overall retrofit intervention.

1.1 Research significance

Since a significant part of the existing building stock results as being vulnerable against the seismic action, there is an increased interest in understanding the effective structural behaviour of Code non-conforming RC buildings. Their inadequacy to guarantee a safe response under the seismic excitation was clearly demonstrated by in-site observation, after the recent earthquake disasters (Decanini et al., 2004a; Del Gaudio et al., 2017; Verderame et al., 2009c). Human and economic loss is a result of structural collapse, causing significant damage in the social asset. In addition, repair costs may result significant even after an earthquake of moderate intensity, especially due to the damage of non-structural elements (Cardone and Perrone, 2017).

Modelling techniques were developed to simulate the experimentally observed response and to extend the analysis on whole RC structures. In spite of this, the knowledge of the seismic response of RC frames reinforced with plain rebar is still incomplete. Moreover, the numerical modelling of their behaviour is often based on empirical consideration or on models that are too complex to be used in a structural analysis. The former can be typically applied in the range of parameters tested in experimental campaigns, whereas the latter are not suitable for extensive numerical analyses. Considering the poor bond performance of smooth reinforcement, the deformation capacity of the sub-standard RC members results higher with respect to the one suggested by the code formulation (CEN Eurocode 8, 2009; Di Ludovico et al., 2014; Melo et al., 2015; Verderame et al., 2010). This results in a higher deformation capacity of the entire frame, strategic in the verification of the as-built or retrofitted GLD structure safety. On the other hand, the stiffness assessment is a key aspect in the evaluation of the seismic response of RC structures; indeed it controls the internal action distribution through the frame members, due to its statically undetermined scheme. Moreover, it affects the building vibration period and the consequent determination of the seismic action intensity.

Existing RC elements in retrofitted structures

To mitigate the seismic vulnerability of existing RC buildings, strengthening interventions are often required. Frequently, to limit their invasiveness, stiff and seismic-resistant new elements are introduced, connected to the building from the outside. In this case, the design attention should not be limited to the newly-introduced reinforcing elements, but also on the intervention compatibility with the existing structure. In fact, from one hand, existing RC members and masonry non-structural elements could be considered as secondary elements; therefore, their strength is not required against the horizontal loads. On the other hand, they must accommodate the deformation imposed by the seismic resistant system. These deformations reflect in column and beam internal actions, according to the structural

stiffness; a representative model for its evaluation is thus required. Higher stiffness results in higher forces on the existing structural members, even if a strengthening intervention controls the global displacement demand; a simplified schematization is shown in Figure 2. As a result of this, brittle failure mechanisms could be activated at low deformation magnitude, resulting in an anticipated collapse. On the other hand, the energy dissipation capacity of GLD frame structures can result lower with respect to the assessed one, since both the higher deformations of the analysed elements and the pinching affecting the cyclic response reduce the hysteretic toughness. An effective instrument to adequately represent the flexural behaviour of the herein analysed structures must be defined; indeed a comprehensive analytically based model, able to represent the cyclic response of concrete structures reinforced with plain rebar, is still missing.
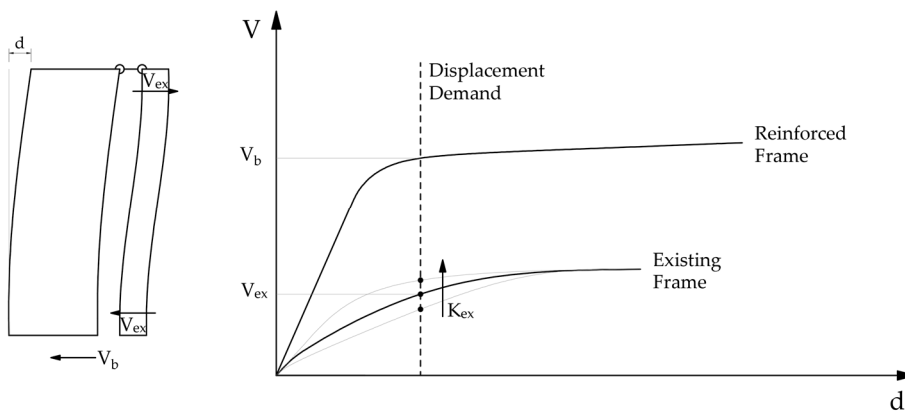
Figure 2: Force demand on reinforced and existing system in presence of a fixed control displacement.

To embrace all the above listed questions, an analytically based structural model is herein defined. It is based on the comprehensive representation of smooth bar stress-slip behaviour through their embedded length. No empirical or numerical calibration is required for its application; therefore, it can be considered as valid for a general purpose. Only two-dimensional planar bare frames are analysed in the following. In the presence of masonry infills, this approach results feasible if it follows specific interventions, directed to the infill-frame interaction mitigation (Bolis et al., 2020; Preti and Bolis, 2017), so that the structure can behave as a bare frame.

1.2 Work organisation

Approach to the bare frame study

A step-by-step approach is followed to define a model able to represent the cyclic response of the herein considered GLD frame buildings. Bar anchorage performance is firstly evaluated by means of experimental tests. An analytical model to simulate the stress-slip response of both straight and hook ended rebar is then formulated and compared with empirical results. Considering column and beam elastic behaviour, a single crack formation on their ends is assumed and the bar stress-slip modelling is implemented to assess the cyclic response of the structural members. In order to perform numerical non-linear analyses, the bar analytical model is linearized and the model is implemented in OpenSees (McKenna et al., 2000) environment. By using the numerical tool, non-linear cyclic analyses on RC frames are finally performed.
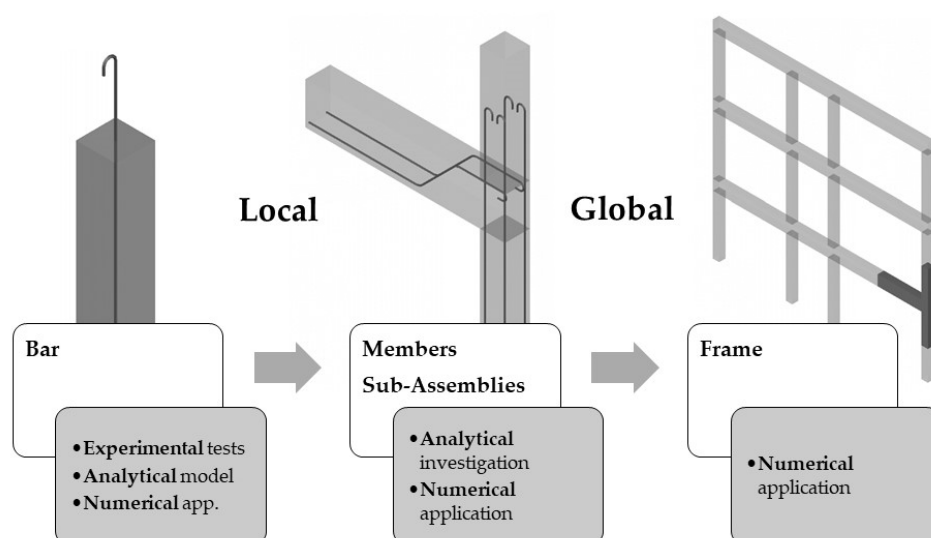
Figure 3: Approach to the research items.

Since the experimental tests on columns and beams subjected to cyclic loading (Marefat et al., 2009; Verderame et al., 2008a) showed respectively an uplift on the base crack and a sliding failure at the element ends, a focus on the shear strength of RC members in the presence of a crossing completely opened crack is pursued. Also in this case a gradual approach to the problem is followed. A preliminary experimental study on the bar dowel behaviour, considering coupled axial and shear load, is presented. Its results are then simulated by the means of an analytical model and a design strength criterion is defined.

1.3   Chapters presentation

The organization of the following chapters is herein schematized:

- **Chapter 2**

  A summary of the literature about the topics covered here is presented.

- **Chapter 3**

  Experimental tests on straight, hook-ended, and bent rebar embedded in concrete are presented. The effect of the cyclic loading on the stiffness and strength capacity of the different anchorage solutions is investigated. The role of good or bad bond condition is also analysed. Finally, analytical models to represent the stress-slip behaviour of the smooth straight embedded bar, and of the hook-end device are suggested.

- **Chapter 4**

  Experimental tests on deformed and smooth rebar under coupled axial and shear loading behaviour is investigated. The role of a constant axial load on the dowel mechanism is analysed and an analytical model to represent it is proposed.

- **Chapter 5**

  A suggestion for the GLD frame building modelling is herein presented. A lumped plasticity approach is considered, and the RC member non-linear behaviour is represented by means of rebar stress-slip relationship modelling. The proposal is then translated in a numerical code in the OpenSees environment (McKenna et al., 2000).

- **Chapter 6**

  The proposed modelling technique is applied to investigate its representativeness. Several monotonic and cyclic experimental tests on columns, beam-column joints, and a whole entire frame are simulated through their numerical representation. Local and global behaviour of the tested RC members are discussed.

- **Appendixes**

  Other details about the numerical modelling technique are finally reported in the Appendixes. Programming functions for the definition of smooth bar stress-slip relationship, sensitivity analysis about the modelling hypotheses, and further experimental validations are finally proposed.

2 LITERATURE SURVEY

The literature review here presented focuses on some topic necessary to understand the response of GLD existing RC frame building. The first covered topic is the strength and deformation capacity of RC members typical of such buildings. Particular attention is dedicated to the studies of the flexural response of slender columns and beams, and on the shear response of beam-column joints. The second topic focuses on the response of rebars under combined transverse and axial load, such as the shear dowel mechanism under the simultaneous application of an axial load to the bar. The third topic covered regards the role of masonry infills in the response of GLD RC frames, their interaction with the bare frame sway mechanism, and the possible strategic deactivation of their in-plane reaction by means of specific intervention techniques.

2.1 *Performance of smooth rebar anchorage in GLD RC frames*

Several works are available in the literature about bond mechanics. Most of these are referred to deformed bars (Cairns et al., 2012; Eligehausen et al., 1983; Filippou et al., 1983; Gambarova et al., 2000), whereas only few and not comprehensive information are available for bond and anchorage performance of smooth bars (Fabbrocino et al., 2005; Verderame et al., 2009b).

The bond capacity is mainly dependent on concrete mechanical properties, concrete confinement level (i.e. transversal axial load, transversal reinforcement layout and concrete cover), casting process, and reinforcement geometrical and mechanical properties. Generally, the bond performances are related to the concrete tensile strength, therefore by increasing concrete compression capacity the bond performance also increases. The bond condition, which are related to bleeding and other casting depending effects, significantly influence the bond strength too. Transversal compressive stress increments friction on the bar surface. On the other hand, the passive confinement plays a significant role increasing the strength of the concrete keys acting against the bar surface; hence, its role can be mainly related with the bond effectiveness of deformed rebar. Cyclic behaviour degrades the bond stress capacities. Furthermore, during the non-linear response to a seismic excitation, the plastic hinge formation is related to steel stress beyond the yielding point. Concrete damage and yield penetration are causes of bond deterioration, which affects both deformed and plain rebar.

Focusing on the smooth bar, two main source of anchorage are available for the bar reinforcement (Fabbrocino et al., 2004). The first is related to the bond across the straight length of the bar; the second is due to presence of bent end anchorage (i.e. hooks and bent rebars).

Straight bar

The typical bond-slip behaviour of a straight smooth bar is reported in Figure 4. The initial response is governed by the cohesion between steel bar surface and surrounding concrete; in this stage no slip develops, and the response is rigid. After this first branch, there is a loss of stiffness due the loss of cohesion. Successively the micro-interlocking is activated, until the bond peak bond strength $\tau_{b,max}$ is reached (Verderame et al., 2009b). Later, the strength degrades until a lower limit in the range of $0.40 \div 0.50\, \tau_{b,max}$; in this field the capacity is mainly controlled by the friction mechanism. The experimental results showed a high scatter. A dependence on the rebar surface roughness can be demonstrated, observing the reduction of results CoV (Coefficient of Variation) with sandblasting treatment of the rebar surface (Feldman and Bartlett, 2007). An influence of the shrinkage effect is also suggested, because it affects the micro-interlocking and thus the shear strength of the concrete keys around the rebar (Verderame et al., 2009b).

a)   b)
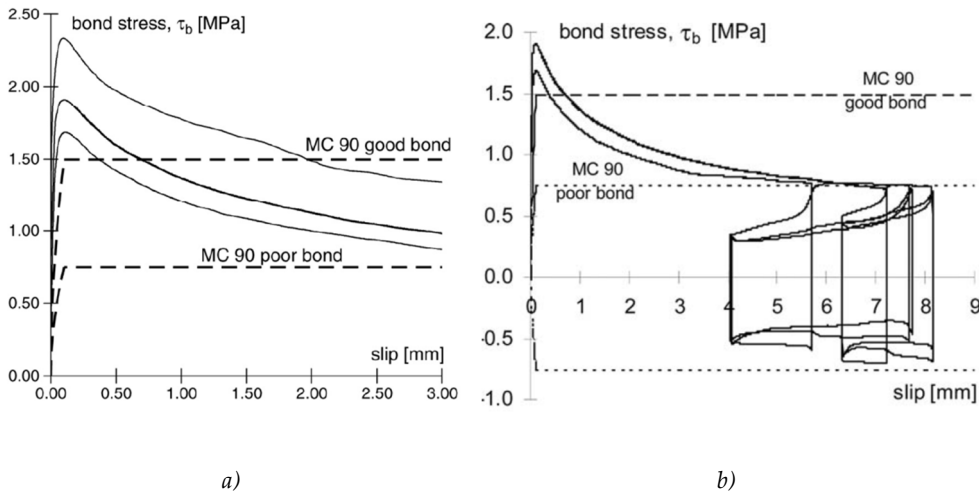
Figure 4: Bond-slip monotonic a) and cyclic b) response for a smooth rebar: pull-out test results (Fabbrocino et al., 2005, 2004).

It was observed that the experimental results are consistent with the indication of the Code (Fabbrocino et al., 2005, 2004; Model Code, 1990). In detail, the peak bond strength can be predicted by the assumption of good bond, while the residual lower limit stress can be estimated by Code indication about poor bond. The following calculations allow to define the bond stress capacity of smooth bar on their straight length before, τ_e , and after, τ_y , steel yielding (Model Code, 2010):

$$\tau_e = 0.3\sqrt{f_c}, \qquad \varepsilon < \varepsilon_{sy} \qquad\qquad (1)$$

10

$$\tau_y = \Omega_y \tau_e, \qquad \varepsilon > \varepsilon_{sy} \tag{2}$$

where the definition of the function Ω_y is related to the actual steel strain ε, to the yielding strain ε_y and to the ultimate strain ε_{su}, and the relative medium failure and yielding stresses f_{tm} and f_{ym}.

$$a = \frac{\varepsilon - \varepsilon_{sy}}{\varepsilon_{su} - \varepsilon_{sy}}, \qquad b = \left(2 - \frac{f_{tm}}{f_{ym}}\right)^2 \tag{3}$$

$$\Omega_y = 1 - 0.85\left(1 - e^{-5a^b}\right) \tag{4}$$

Hook-end device

Different rebar end hook configurations were experimentally tested (Fabbrocino et al., 2005), accounting for the role of the concrete cover and for the casting direction (respect to the rebar straight length). The aim was to investigate the response of the typical reinforcement arrangement of column and beam elements near to the foundation or the joint region. A schematic representation of the specimens is shown in Figure 5.

In the first stage of the response the slip is substantially null, until the reach of a stress level of about the 20% of the yielding one f_y. After this, the response becomes strongly non-linear and it exhibits a great variability in the slip value at the rebar yielding (Figure 5). The hook anchorage response does not show a yielding branch and in presence of high concrete cover the load capacity increases up to the rebar failure. On the other hand, a low concrete cover causes a post-yielding strength collapse, associated with a significant increase of the hook slip. This is due to concrete cover crushing. Regarding the stiffness exhibited by the different specimen typologies, it is possible to conclude that high concrete cover improve the stiffness of the hook-end anchorage, as it is visible for the different hook stress versus hook slip diagrams of Figure 5. The fact can be understood considering the concrete cover thickness role in the definition of the confinement capacity around the hook. Moreover, for the hook-end rebar orthogonal to the casting direction, it is possible to evidence a greater stiffness for the hook bent down-ward, in other words the beam top reinforcement response is stiffer than the bottom reinforcement one.

Experimental pull-out tests on smooth rebar anchorage composed both by hook-end and bonded straight length are available in the literature (Fabbrocino et al., 2004; Paolacci and Giannini, 2012). These tests showed the development of a plastic plateaux and a successive hardening phase. Therefore, the efficiency of the hook-end in anchoring a stress higher than the bar yielding one is confirmed.
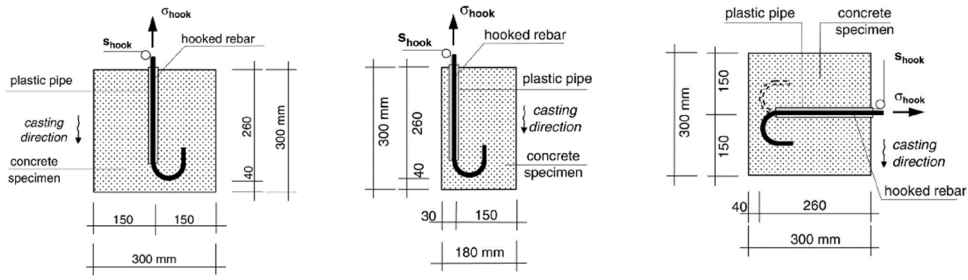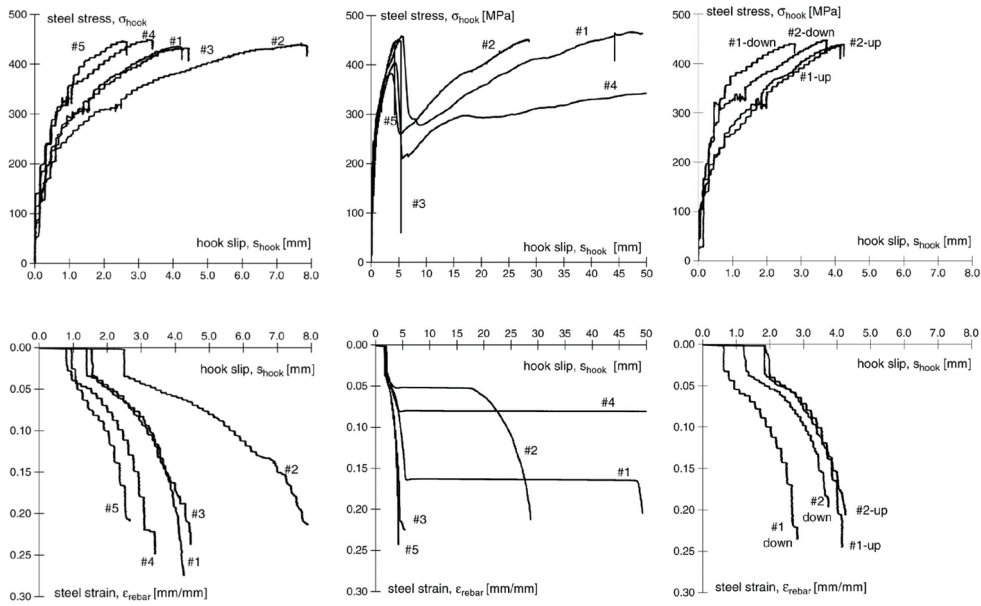
Figure 5: Pull-out experimental results about different hook-end arrangements (Fabbrocino et al., 2005). The reference yielding stress is 300MPa.

Cyclic bond behaviour of plain bars

According to the author knowledge, only some cyclic tests about the bond performance of smooth rebars are available in the literature. A short (ten diameters) embedded straight length is considered in the reference experimental pull-out set-up (Verderame et al., 2009b).

Strength deterioration affects the bond-slip behaviour during both in-cycle and cyclic response of plain rebars. The difference between the peak strength and the values governing the residual, unloading, and reloading strength is the most pronounced. This is a clear consequence of the changes in the governing physical mechanisms, which have been above presented in the discussion of the monotonic response. After the reaching of the peak, the adhesion between the bar surface and the surrounding concrete is completely lost and the micro-interlocking degrades. A strength capacity decay can thus be justified. By the observation of the experimental cyclic tests (Figure 6), it is possible to observe that increasing the number of cycles at a fixed slip value, the strength degradation effect reduces. Furthermore, it is also possible to assume that after three cycles the same reduction becomes negligible. On the other hand, no clear decreasing trend in the bond strength is visible increasing the slip magnitude. Indeed, the strength reduction is clearly visible only in the first cycle (monotonic response) and only for the low reached slip values. An asymmetry characterizes positive and negative load direction, but no significant trend was found to describe it.

Resuming, the cyclic response of plain straight rebar bond-slip behaviour is characterized by the following evidences (Figure 6):

- the bond strength exhibited during the cyclic loading at a target drift is similar to the friction residual strength exhibited in monotonic loading;
- strength degradation decrease with the number of imposed cycle and it becomes negligible after three load cycles;
- the bond strength does not significantly decrease by the increment of imposed high ($s > 2mm$) slip magnitude;
- no significant stiffness degradation is visible in the friction-based hysteresis.
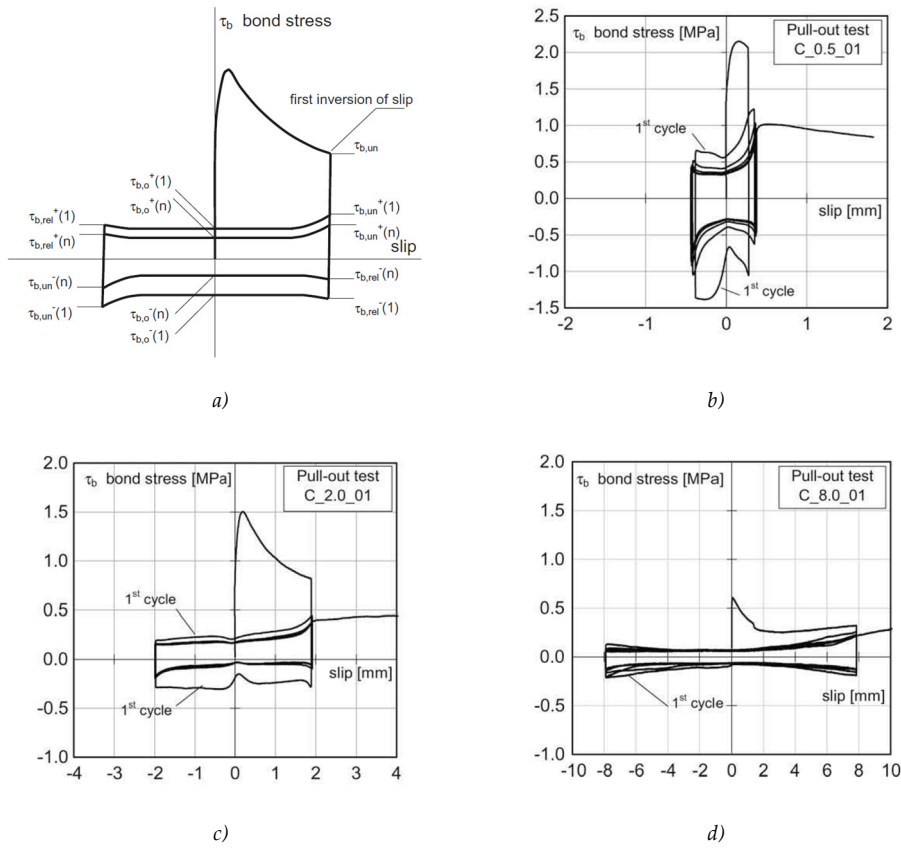
Figure 6: Schematization of the cyclic bond behaviour a) and examples of experimental response to 5 cycles up to a 0.5mm b), 2.0mm c) and 8.0mm d) imposed slip (Verderame et al., 2009b)

Steel stress-slip behaviour for a straight smooth rebar

To relate the bond stress to the bar slip, a bilinear elastic-perfectly plastic model can be considered (Figure 7.c). On the other hand, a further simplification can be introduced considering a rigid-plastic bond-slip relationships (Figure 7.b). By the assumption of a constant bond stress distribution τ_b and of a rigid-plastic bond-slip relationship, the bar equilibrium and the compatibility equations assume the following forms:

$$\pi d_b \tau_b x = \frac{\pi d_b^2}{4}(\sigma(x) - \sigma_0) \tag{5}$$

$$\sigma(x) = \sigma_0 + \frac{4\tau_b x}{d_b} \tag{6}$$

$$\varepsilon(x) = \frac{\sigma(x)}{E_s} = \frac{\sigma_0}{E_s} + \frac{4\tau_b x}{E_s d_b} = \varepsilon_0 + \frac{4\tau_b x}{E_s d_b} \tag{7}$$

$$s(x) = s_0 + \int_0^x \varepsilon(z)dz = s_0 + \frac{\sigma_0}{E}x + \frac{2\tau_b x^2}{E_s d_b} \tag{8}$$

where d_b is the bar diameter, E_s the steel young modulus, and σ_0, ε_0 and s_0 are the stress, strain and slip value in the reference point ($x = 0$).

The application of this basilar concept in the smooth bar slip calculation was proposed in the literature for the a beam-column joint deformation assessment (Metelli et al., 2015). On the other hand, more complex models consider an elastic-plastic bond-slip relationship and a simplified linear slip resulting profile (Braga et al., 2012). Other authors also suggest to consider the bond-slip degrading (post-peak) branch, to emphasize the role of the end hook anchoring effectiveness (Fabbrocino et al., 2004). Figure 8 shows an example of the latter proposal.
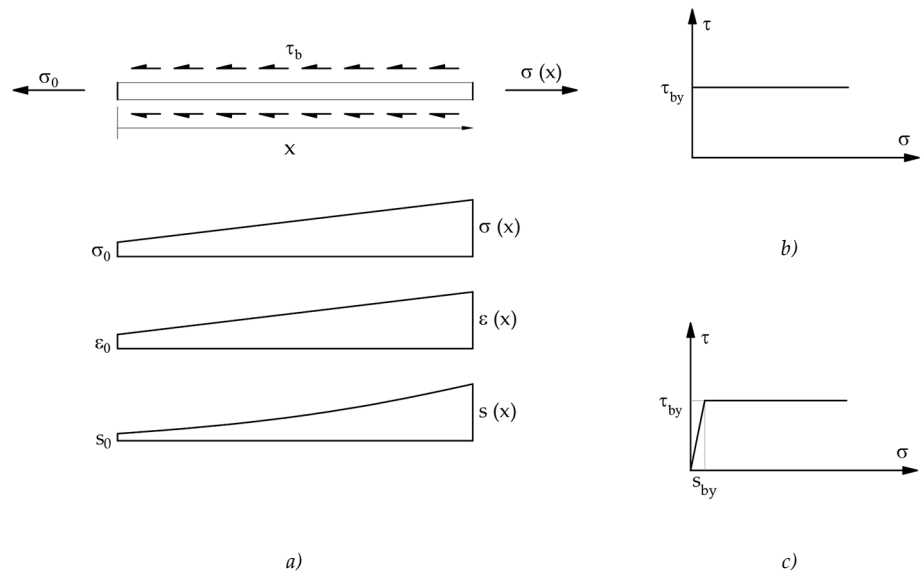
Figure 7: Equilibrium imposition on a bar straight length in hypothesis of constant bond stress on the full length a) and. rigid-plastic b) or elastic-plastic c) bond stress-bar slip relationships.
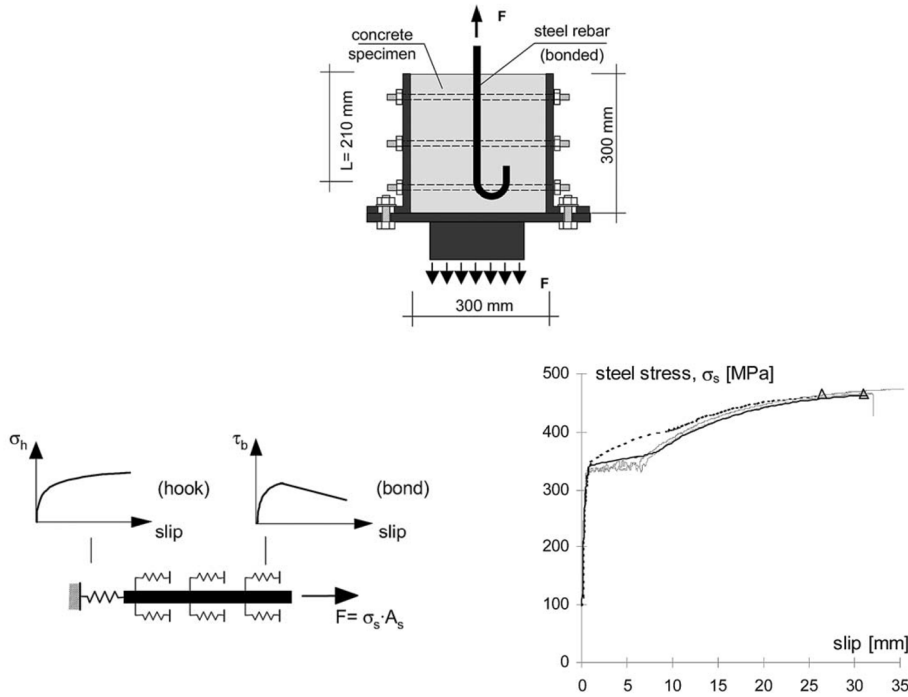
Figure 8: Simulation of a pull-out test by the mean of stress-slip models (Fabbrocino et al., 2004). Comparison between the experimental and the modelling technique results considering (continuous line) or not (dotted line) the bond degradation c).

Based on the experimental results, a simplified rule to model the average bond-slip cyclic behaviour of plain rebar is suggested (Verderame et al., 2009a). The reference skeleton curve is schematized in Figure 10, whereas the monotonic envelope in visible in Figure 9. The latter is based on the classical proposal for deformed rebar (Eligehausen et al., 1983; Filippou et al., 1983), modified by the elimination of the strength plateaux (Figure 9.b). The first branch is non-linear, whereas a linear function reproduces the strength softening. A constant residual frictional capacity is then assumed.

The mathematical formulation of the model is herein reported, with τ_b average bond stress acting on the plain rebar surface, s average slip value on the embedded length, $(\tau_{b,max}; s_{max})$ couple related to the peak point of the envelope response, and $\tau_{b,f}$ residual friction stress; the parameters α and p refine the shape of the monomial loading branch and the slope of the softening response.

$$\tau_b = \tau_{b,max} \left(\frac{s}{s_{max}} \right)^{\alpha}, \qquad s < s_{max} \qquad (9)$$

16

$$\tau_b = \tau_{b,max} - p\frac{\tau_{b,max}}{s_{max}}(s - s_{max}),$$

$$s_{max} < s < s_f$$

(10)

$$\tau_b = \tau_{b,f}, \qquad s > s_f$$

(11)
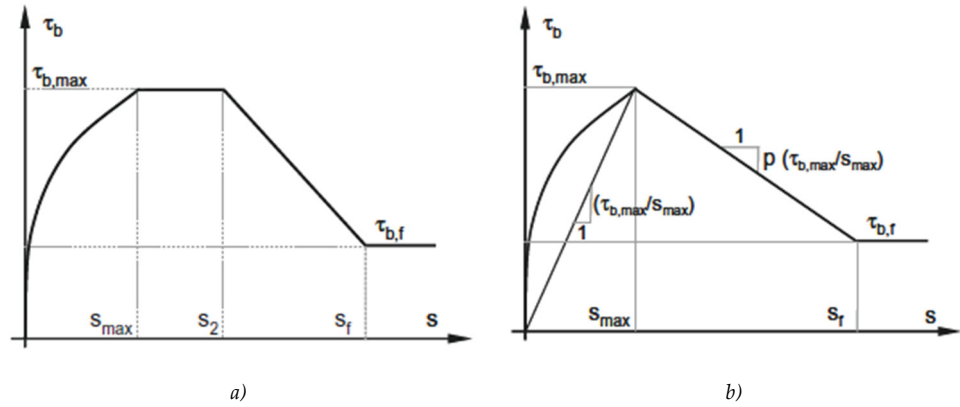
Figure 9: Original (Eligehausen et al., 1983) BPE model for deformed bar bond-slip mechanism a) and its modification for plain rebar (Verderame et al., 2009a).

The described model, also called BPE, is defined by a total number of 5 parameters. To fit its shape to the experimental observed behaviour of the plain rebar, the mean values of the reference bond stress and slip values are used; The service parameters α and p are evaluated by the imposition of an equal area underneath the experimental response and the analytical envelope (energy approach). The fitting process results are reported in Table 1. A high Coefficient of Variation characterizes the model parameters; this is an issue already noted for the experimental results; therefore, the aspect is obviously reflected into the model.

The definition of the cyclic response is related to a simplification of the experimental evidences (Verderame et al., 2009b). The unloading branch (B-H-C in Figure 29) is linear with slope k_{un}, independently from the slip value at which it starts; this is extended up to a cyclic bond resistance called $\tau_{b,c}$, which remains constant until the reach of the zero deformation level. During the first reversal loading, the bond stress in the negative direction increases by a linear function of stiffness k_{un}, reaching the value of the residual stress $\tau_{b,r}$. The successive unloading and reloading phases in the range of negative slip are controlled by the same stiffness k_{un} and by the cyclic strength $\tau_{b,c}$. Exploring slip magnitude higher than the maximum reached in the previous cycles, an increase by stiffness k_{un} allows to reach the higher frictional strength $\tau_{b,r}$, which is degraded respect to the monotonic value $\tau_{b,f}$. Note that the cyclic response is assumed to be symmetric.

17
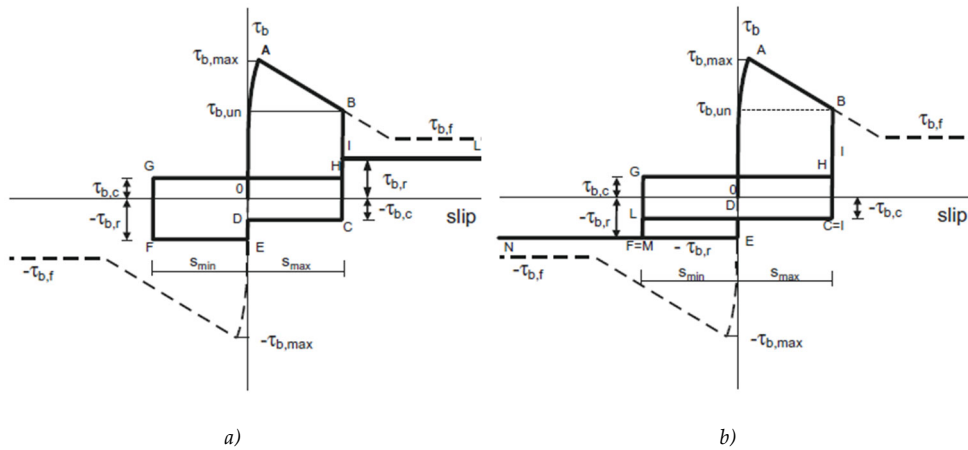
Figure 10: (Verderame et al., 2009a) proposal for bond-slip cyclic behaviour of plain rebar embedded in concrete: first cycle loading followed by reloading at incremental positive a) and negative b) slip values.

To mathematical define the cyclic model only two additional parameters are required: the cyclic strength $\tau_{b,c}$ and the residual value $\tau_{b,r}$. The latter is assumed to be independent from both the number of cycles and the slip magnitude, according to the tests results. It can be expressed as a function of the monotonic envelope friction residual strength $\tau_{b,f}$, as it is shown in Eq.(12). On the other hand, the cyclic strength is calibrated on an energy equivalence between the analytical formulation and the experimental test. A constant trend was observed in the ratio between the residual and the frictional bond strengths (Verderame et al., 2009a):

$$\frac{\tau_{b,r}}{\tau_{b,f}} = 0.68 \tag{12}$$

$$\frac{\tau_{b,c}}{\tau_{b,f}} = 0.35 \tag{13}$$

Assumed that the few experimental results on plain bar (Fabbrocino et al., 2005; Feldman and Bartlett, 2007; Verderame et al., 2009b) are consistent in affirming that: i) the peak bond stress is well estimated by the (Model Code, 2010) prediction in presence of good bond, ii) the ratio between the frictional residual strength and the peak value is constant, iv) all the required strength parameters can be expressed by a function of the square root of the cylindrical concrete compressive strength, the model can be formalized as it is visible in Figure 11.a. It is worth noting that the scatter of the parameters required for the cyclic model are lower than the ones needed for the monotonic definition of the behaviour.

Regarding the unloading stiffness, it is quantified by the overall medium value of the experimental test (Figure 11.b):

$$k_{un} = 15 \frac{MPa}{mm} \qquad (14)$$

a)   b)
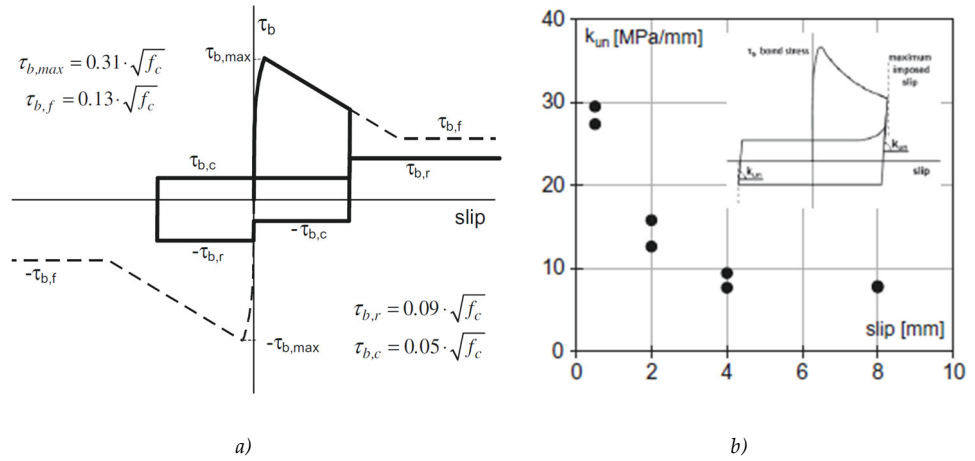
Figure 11: Final formulation of the hysteretic model proposed for the cyclic bond slip behaviour of smooth straight rebars (Verderame et al., 2009a) a) and mean values of the unloading stiffness in the reference experimental pull-out tests b) (Verderame et al., 2009b).

Model parameter	Mean value	Max value	Min value	CoV
$\tau_{b,max}$	1.24	0.61	2.15	0.38
s_{max}	0.23	0.08	0.39	0.45
α	0.26	0.10	0.57	0.63
p	0.06	0.03	0.11	0.54
$\tau_{bf}/\tau_{b,max}$	0.43	0.36	0.58	0.18
τ_{br}/τ_{bf}	0.68	0.44	0.86	0.19
τ_{bc}/τ_{bf}	0.35	0.19	0.53	0.25

Table 1: Resume of the required parameters for the modelling technique of the cyclic bond-slip behaviour of plain rebar (Verderame et al., 2009a).

Hook stress-slip behaviour

In literature different ways to represent the hook stress-slip behaviour are available. Some of these are herein summarized, listed according to the increase of accuracy in the representation. A bilinear hardening model is proposed in term of normalized hook-stress versus bar-slip (Metelli et al., 2015). It is calibrated on experimental pull-out test results on 12mm and 16mm hook diameter (Fabbrocino et al., 2004). In this way, the end anchorage is modelled with an axial spring characterized by an elastic stiffness equal to $1.13 mm^{-1}$ and a post-yielding stiffness equal to $0.048 mm^{-1}$ (Figure 12).
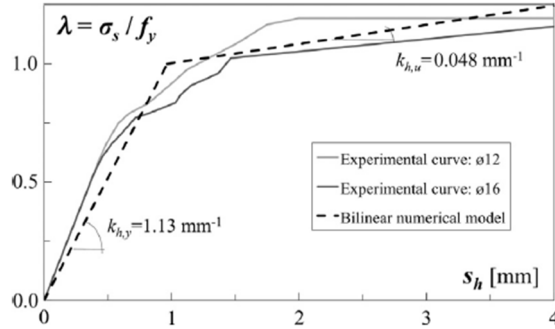
Figure 12: Bilinear modelling of the hook-end anchorage in term of normalized stress versus slip (Metelli et al., 2015).

Another suggestion (Braga et al., 2012) considers the equilibrium between the rebar axial force and a concrete stress distribution on the hook inner region, on which amplified bond stresses act (Figure 13):

$$\tau_p(s) = 2\mu \frac{F_c}{5d_b{}^2} \qquad (15)$$

The above expressed capacity is then summed to the friction contribution acting on the straight length (in absence of shaped bar), which stress-slip behaviour is assumed to be linear (Braga et al., 2012):

$$\tau_h(s) = \tau_b(s) + \tau_p(s) \qquad (16)$$

$$\tau_b(s) = \begin{matrix} (\tau_{by}/s_{by})s, & s < s_{by} \\ \tau_{by}, & s > s_{by} \end{matrix} \qquad (17)$$

The model could be adapted to the modelling of other shaped end-anchorage devices.
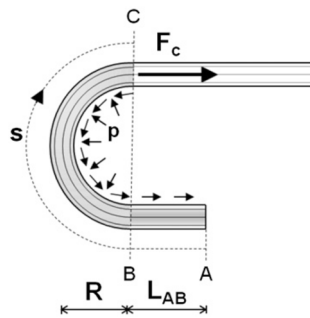
Figure 13: Friction based approach to the modelling of hook-end rebar anchorage (Braga et al., 2012).

The last approach herein reported refers to a non-linear mathematical formulation (Popov, 1984), which relates the hook stress σ_h with the hook slip s_h. The hook failure slip s_u is experimentally defined as the slip at which the rebar fails in presence of the ultimate stress f_u. A summary of the empirical calibration is reported in Figure 15 (Fabbrocino et al., 2004); different hook-end configurations are considered.

$$\sigma_h(s) = f_u \left(\frac{s_h}{s_u}\right)^{\alpha} \tag{18}$$

2.2 Columns reinforced with plain bars

GLD frame structures present significant deficiencies in the detailing of their vertical elements, designed to work mainly under compression stress and in absence of shear and bending action. In presence of seismic demand these elements result indeed totally inadequate to resist in strength; moreover, the poor material properties and the lack of confinement knock over the deformation capacity. Low column strength reflects in global soft-storey mechanism, which ductility local demand is very high. Although this mechanism can be avoided by specific structural reinforcement, the ductility of a non-retrofitted column is however a main parameter to be assessed.

In the following some experimental campaigns on RC columns with sub-standard details (i.e. low reinforcement ratio, use of plain rebar, low confinement, poor concrete quality) are presented. The reference tests were conducted on columns designed according to Italian (Di Ludovico et al., 2014; Verderame et al., 2008b, 2008a) or Portuguese (Melo et al., 2015) Code enforced until the seventies. Both monotonic and cyclic loads are considered. The main investigated parameters are:

- longitudinal reinforcement ratio;
- presence of lap-splices;
- effect of cold joint;

21

- column shear length over cross section dimension;
- axial load level;
- type of horizontal load (Monotonic or cyclic).

More experimental data are available in the database collected by (Melo et al., 2015; Ricci et al., 2013; Verderame et al., 2010).

The test set-up is similar for all the scientific test herein presented. In Figure 14 an example is reported (Di Ludovico et al., 2014). A cantilever was realized in a two-phases casting on a squat RC foundation element. The cast in two different time wants to represent the cold joint that typically characterizes the construction practice (except for the specimens in which the absence of the cold joint wants to be represented). Axial load was applied in force control on the member top by an external tie, within a hinged self-balanced system. On the other hand, the horizontal load is applied in displacement control at a distance L_V over the column base.

Referring to Figure 14.b, it is possible to define the shear length L_V as the distance between the column base (foundation-element interface) and the horizontal load application point. The chord rotation θ is defined by the ratio between the top horizontal displacement and the shear length. This is possible thanks to the simply cantilever scheme. To account for the presence of re-centring axial load (Figure 14), the following calculations must be considered:

$$M = F_{app}L_V + N\cos\theta\,\Delta_1 - N\sin\theta\left(L_V + L_{top}\right) \cong F_{app}L_V \tag{19}$$

$$V = F_{app} - N\sin\theta \cong F_{app} - N\theta \tag{20}$$

a)   b)
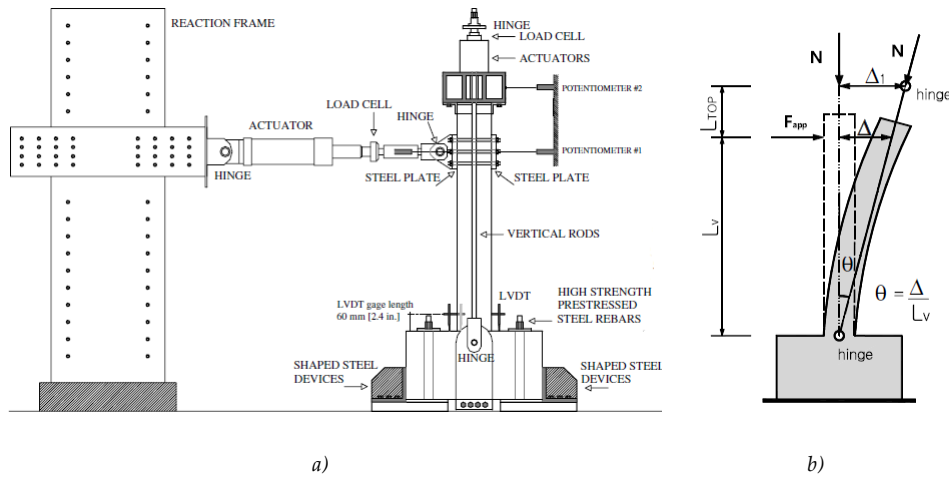
Figure 14: Example of a test set-up a) and schematization of the test control parameter b) (Di Ludovico et al., 2014).
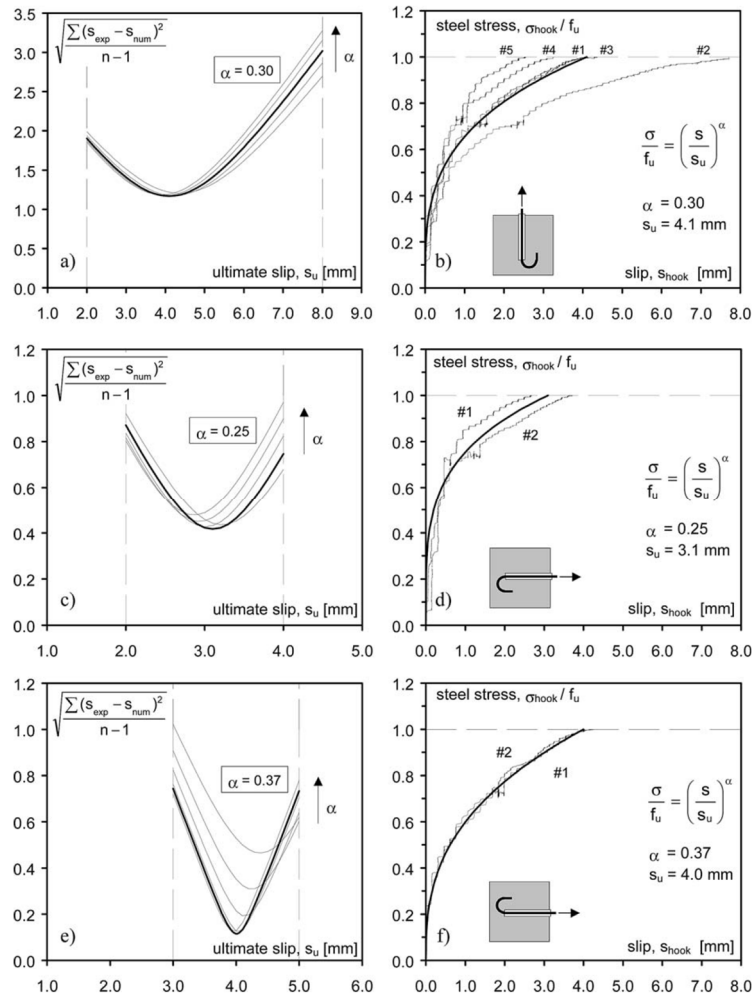
Figure 15: Calibration of the hook stress-slip non-linear model (Popov, 1984) for different anchorage configurations, (Fabbrocino et al., 2004).

Column response under monotonic loading

The monotonic tests (Verderame et al., 2008b) aim to outline the influence of the axial load level acting in the member and of the bar lap-splices at the column base. Concerning the lap-splice, the half of the specimen were characterized by an overlapping length of 40 bar diameters (commonly adopted in practice) and by a hook-end anchorage; the remaining sections present continuous reinforcement. The main results show that:

- axial load level influences the yielding and the peak strength of the column and the ultimate rotational capacity, conversely it does not affect the yielding rotation;
- overlapped longitudinal reinforcement influences the crack pattern and the yielding deformation level;
- Overstrength ratio is not affected by the investigated parameters.

The main experimental results are reported in Table 2, in which longitudinal reinforcement ratio ρ, normalized axial load ν, yielding V_y and peak V_p horizontal forces, yielding θ_y and ultimate θ_u chord rotations and the relative ratio are available for each reference specimen. The ultimate drift is quantified as the deformation level reached at a force reduction equal to 15% respect to the peak value. Note that the loss of strength registered after the peak can be strongly marked or gradual (Figure 16), due to column base damage; longitudinal reinforcement buckling and consequent concrete cover spalling cause sudden loss of strength. Despite the deficiencies in the detailing of the tested columns and the low material quality, the ultimate rotation capacities of the members seemed to be large. In fact, all the specimens could overpass the 3.50% of the normalized horizontal displacement, showing a significant ductility capacity. When comparing the capacities of column designed with sub-standard details, it is possible to observe that the ultimate rotation of the specimen with plain reinforcement was higher than the one of the specimens with deformed reinforcement (Di Ludovico et al., 2014). This high ductility capacity was allowed by a very high crack opening measured at the columns base (in the order of 20÷30mm). The presence of overlapped longitudinal reinforcement facilitated the opening of a single crack at the column base. In presence of continuous reinforcement, the number of the opened cracks was however very scarce if compared with the results of specimens with deformed rebar (Di Ludovico et al., 2014); indeed, not more than 2 cracks are active during the response. In Figure 16 the correlation between the rotation at the column base due to the crack opening and the global drift is shown, both for a specimen with overlapped rebar and one with continuous reinforcement. In presence of more than one crack, the relationship between the two rotation was strongly non-linear (Figure 16.d). On the other hand, in presence of bar-splices (Figure 16.c) the opening of a single crack caused the rigid rotation of the overall column. It is noteworthy to observe that the base rotation contributes for the most to the global drift (Di Ludovico et al., 2014). A significant part of the global deformation must be linked to the fix-end rotation, due to the bar slip into the foundation block.

ID	Overlap	ρ [%]	ν	V_y [kN]	V_p [kN]	θ_y	θ_u	V_p/V_y	μ_θ
M-270A1	Yes	0.8	0.12	39.06	40.79	0.77	5.31	1.04	7.90
M-270A2	Yes	0.8	0.12	37.44	39.24	0.72	5.46	1.05	8.50
M-270B1	No	0.8	0.12	39.30	41.66	0.95	9.54	1.06	10.04
M-270B2	No	0.8	0.12	41.44	42.38	0.96	> 6.13	1.02	> 6.39
M-540A1	Yes	0.8	0.24	58.26	62.62	0.71	> 5.05	1.07	> 7.11
M-540B1	No	0.8	0.24	60.46	63.21	0.89	3.82	1.05	4.29
C-270A1	Yes	0.8	0.12	41.50	42.96	0.79	4.85	1.03	6.14
C-270B1	No	0.8	0.12	41.15	43.00	0.76	5.30	1.04	6.97
C-270B2	No	0.8	0.12	38.97	39.89	0.95	6.30	1.02	6.63
C-540A1	Yes	0.8	0.24	63.01	64.97	0.89	3.45	1.03	3.88
C-540B1	No	0.8	0.24	60.04	61.07	1.00	3.50	1.02	3.50
C-540B2	No	0.8	0.24	63.09	64.68	0.97	2.45	1.02	2.53

Table 2: Experimental results for the column specimens subjected to monotonic (M) an cyclic loading (C) (Verderame et al., 2008b, 2008a). For the cyclic tests the data reported are referred to the positive displacement imposition.

Column cyclic behaviour

Respect to the monotonic loading, the cyclic drift imposition should showed the effect of the progressive damage during the cycles. The exhibited yielding and peak loads did not change in a significant way due to the cyclic loading effect (Table 2); therefore, the conclusions outlined for the monotonic case were confirmed also for the cyclic one (Verderame et al., 2008a).

25
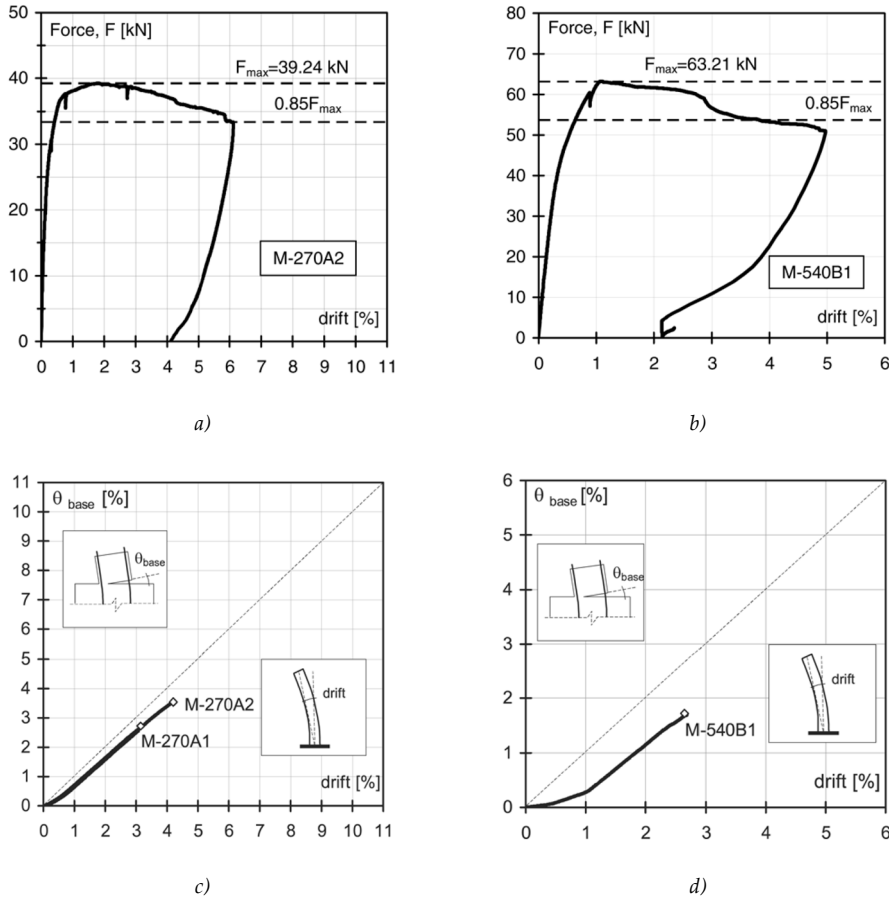
Figure 16: Column monotonic response in term of horizontal action versus drift and base rotation versus global drift (Verderame et al., 2008b). Reference to M-270A2 (low axial load and overlapped reinforcement), and of to M-540B1 (high axial load ratio and continuous reinforcement) specimens.

The columns behaviour was elastic until the first crack opening, which is located at the column-foundation interface (true in presence of a cold joint). Successive crack pattern formation depends of the observations already outlined for monotonic loading. Note that the cracks are orthogonal to the member axis cause to the poor bond performance of the plain reinforcement, which allows a rocking-controlled response. Cause to reversal displacement impositions the cracks remain opened during the response; the consequent uplift of the element increases with chord rotation increasing (Verderame et al., 2008a). Higher axial load level helps to reduce the crack opening and the consequent stronger pinching effect in the hysteretic response.

More in general. the column reinforced with plain rebar show a cyclic response characterized by a very marked pinching, which takes place soon due to smooth rebar poor bond condition. Difference in the hysteretic response of specimen with plain (CPA-3) and deformed (CD) rebar is visible in Figure 17.a. The specimen CD reached a higher peak force at a lower drift level; however, the hysteretic response of specimens with deformed reinforcement indicates an higher dissipation capacity (Melo et al., 2015). The increment of damage during the cyclic response causes a decrease in the ultimate rotation capacity of the columns, both for plain and deformed reinforcement, with an emphasized effect for the latter. The effect of the cold joint is visible in Figure 17.b. The specimen casted in two phases (CPA-1) showed cracking, cover spalling, and longitudinal rebar buckling at a lower drift demand. The higher curvature demand at the same global drift could explains this evidence (Melo et al., 2015). Increment in member stiffness (lower value of the ratio L_V/h_c with L_V shear length and h_c cross section height) resulted in maximum strength exhibited at lower drift demand and a lower ultimate capacity (Di Ludovico et al., 2014; Melo et al., 2015). Furthermore, it was observed less energy dissipation capacity and more pronounced pinching (Figure 17.d). Concrete spalling of these specimens at failure included the section core and not only the cover (as it was observed in the slender elements). Higher axial loads led to a premature failure of the member; indeed, the concrete spalling and the longitudinal reinforcement buckling caused an anticipated sudden loss of strength. At the same time, the high axial stress helped in contrasting the crack opening, thus in reducing the pinching of the hysteretic loops (Verderame et al., 2008a). Regarding the energy dissipation in presence of plain rebar, it is possible to conclude that the higher damping coefficient (Melo et al., 2015) was registered in absence of lap-splices, with higher reinforcement amount (which favourites a spread cracking) and without cold joints. Anyway, the better bond conditions guaranteed by deformed bar allowed a higher energy dissipation.
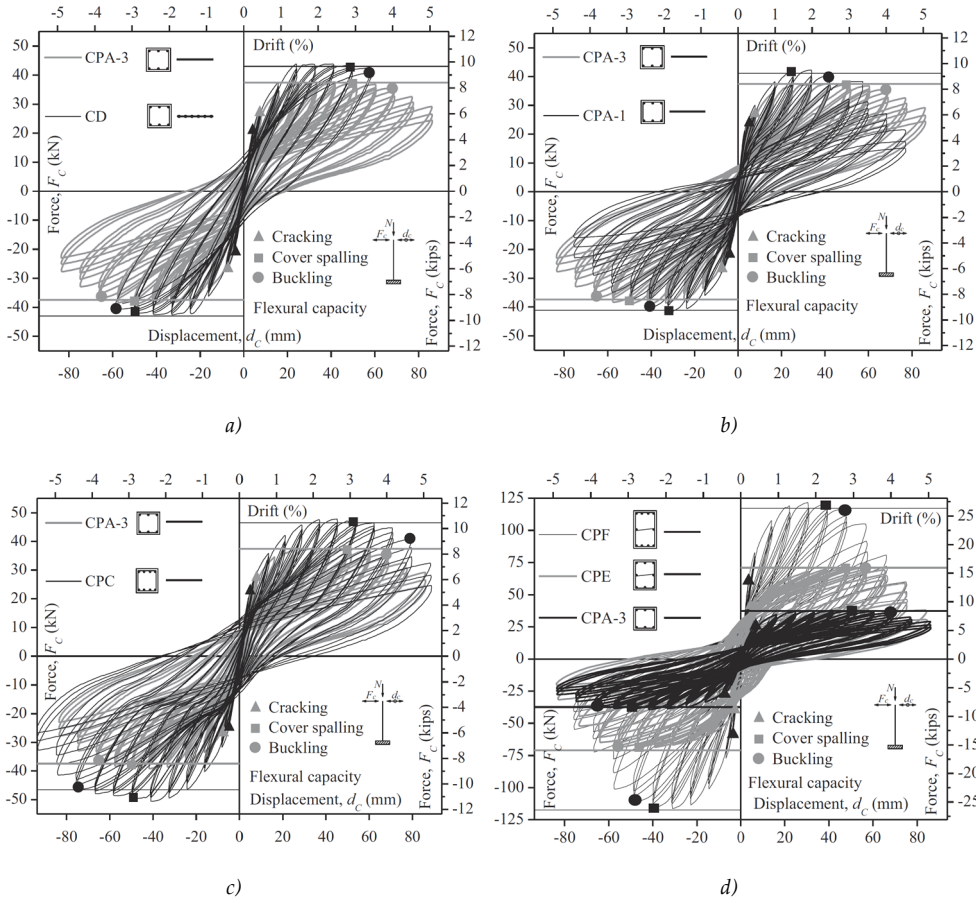
Figure 17: Experimental results on substandard columns (Melo et al., 2015). Comparison between plain (P) and deformed (D) rebar a), presence (1) or not (3) of a cold joint b), different reinforcement amount c) and different cross section dimensions d).

Columns deformation capacity in the technical Code

With reference to the collected experimental results about the seismic response of columns reinforced with smooth bar, the inadequacy of the Code predictive models in assessing their effective deformation capacities was evaluate in a quantitative way (Di Ludovico et al., 2014; Melo et al., 2015; Ricci et al., 2013; Verderame et al., 2010). (CEN Eurocode 8, 2009) suggests the formulation of Eq.(21) to define the ultimate rotation capacity of a column at the incipient collapse. The required parameters are the depth of the cross section h, the shear span L_V, the normalized axial load ν, the mechanical longitudinal reinforcement ratio in tension ω and compression ω', concrete compressive strength f_c and the confining steel yielding stress f_{yw}, the ratio

of the shear reinforcement ρ_{sx} and the diagonal one ρ_d; moreover the confinement efficiency factor α has to be taken equal to zero if stirrups with 90° hook end are employed. Also member hierarchy in the global structure is considered ($\gamma_{el} = 1.5$ for primary elements and $\gamma_{el} = 1.0$ for secondary elements).

$$\theta_u = \frac{1}{\gamma_{el}} 0.016(0.3)^\nu \cdot$$

$$\left[\frac{max(0.01; \omega')}{max(0.01; \omega)} f_c\right]^{0.225} \left(min\left(9; \frac{L_V}{h}\right)\right)^{0.35} 25^{\left(\alpha\rho_{sx}\frac{f_{yw}}{f_c}\right)}(1.25^{100\rho_d}) \qquad (21)$$

For member without seismic detailing the result of Eq.(21) has to be divided by a factor equal to 1.2. Furthermore, another coefficient reduction coefficient must be used to adapt the above formulation in presence of not adequate overlapping length. In presence of smooth rebar a coefficient equal to 0.8 is suggested to account for the poor bond condition, and it includes the lack of seismic detailing. Also in this case a further correction is adopted in presence of inadequate overlapping length l_0. The highest reduction are applied with lap splices length lower than 40 times the longitudinal reinforcement diameter d_{bl}, value in which the correction defined by Eq.(22) reach its maximum value in 0.95.

$$0.019[10 + min(40; l_0/d_{bl})] \qquad (22)$$

The shear span in Eq.(21) has to be calculated at the end of the overlapping length, assuming that the ultimate condition is controlled in the region right after the end of the lap. It is worth noting that the correction to apply in case of lap-slices is true only in presence of hook-end anchorage. Indeed the member fail in a brittle way if the hook is not provided (Ilki et al., 2009; Yalcin et al., 2008).

Empirical formulation for the deformation capacity assessment

As already mentioned, the Code provisions are aimed to reduce the ultimate capacity of member with lack in seismic detailing and in presence of smooth rebar. On the other hand, the experimental studies showed a not negligible deformation capacity of these members, due to developing of a rocking mechanism. An upgrade of the European Code (CEN Eurocode 8, 2009, 2005) allows to account for these observations (Figure 18); despite this, the experimental results show the adjustment is not sufficient to well predict the capacity. Therefore, it is useful to highlight a series of correction coefficient, that applied at the purely empirical code formulation can better represent the effective column ultimate capacity. The approach to this aim is based on the calibration of corrective coefficients, using statistical instruments such as regression methods.

29

Working on 22 available experimental results on column with sub-standard detailing, a first suggestion (Verderame et al., 2010) is presented in Eq.(23) and Eq.(24). Continuous reinforcement is considered, and the coefficient γ_{el} is assumed equal to 1.0.

$$\theta_u = \theta_y + \theta_u{}^{pl} \tag{23}$$

$$\theta_u{}^{pl} = \frac{1}{\gamma_{el}} 0.0145(0.25)^\nu \cdot$$

$$\left[\frac{max(0.01;\ \omega')}{max(0.01;\ \omega)}\right]^{0.3} f_c{}^{0.2} \left(min\left(9;\frac{L_V}{h}\right)\right)^{0.35} 25^{\left(\alpha\rho_{sx}\frac{f_{yw}}{f_c}\right)}(1.275^{100\rho_d}) \tag{24}$$

In presence of lap-splices the correction of Eq.(25) is proposed, but no modification on the shear span L_V is required. It is worth noting that the latter choice is consistent with the experimental observations on RC elements with plain rebar overlapped at the member base, which show the opening of only a crack and the development of a rocking mechanism (Arani et al., 2013, 2010). The proposed value sets the effective overlapping length limit (in presence of hook-end device) to $50d_{bl}$. The suggested value is higher than the Code proposal (CEN Eurocode 8, 2009), but the latter imposes the reduction of the shear length due to the presence of lap splices.

$$0.02 min(50; l_0/d_{bl}) \tag{25}$$

Thanks to further available tests, a new statistical fit was followed by other authors (Melo et al., 2015). In this case the proposed formulation is referred to members with continuous reinforcement or with overlapping length equal or higher than $30d_{bl}$; on the other hand the shear span to has to be evaluated from the lap end, according to the Code approach (CEN Eurocode 8, 2009). The proposal provides for the correction of the Eq.(21) (considering $\gamma_{el} = 1.0$) by the application of the following coefficient:

$$\alpha_{slip} = -0.055 \left(\nu^{1/2} f_c L_V{}^{1/3}\right) + 1.72 \tag{26}$$

The correction account for axial load ratio ν, concrete compressive strength f_c and shear span L_V. It can result higher than 1.00, indicating thus a higher deformation capacity of members reinforced with plain bar, with respect to others reinforced with deformed one. This is confirmed by the experimental evidence above discussed. Statistical analysis shows that the proposed formulation is characterized by an average value of predicted rotation θ_{um} over experimental rotation $\theta_{u,exp}$ equal to 1.00. The results dispersion is also reduced (see Figure 18).

Comparison with other Code (ASCE, 2007a, 2007b) predictive models are available in (Ricci et al., 2013) and (Di Ludovico et al., 2014). The latter also shows the influence of stirrups closure with right-angle. Code predictions about the absence of 135° stirrups closure was found to be too unfavourable in the assessment of the column ultimate rotation capacity.
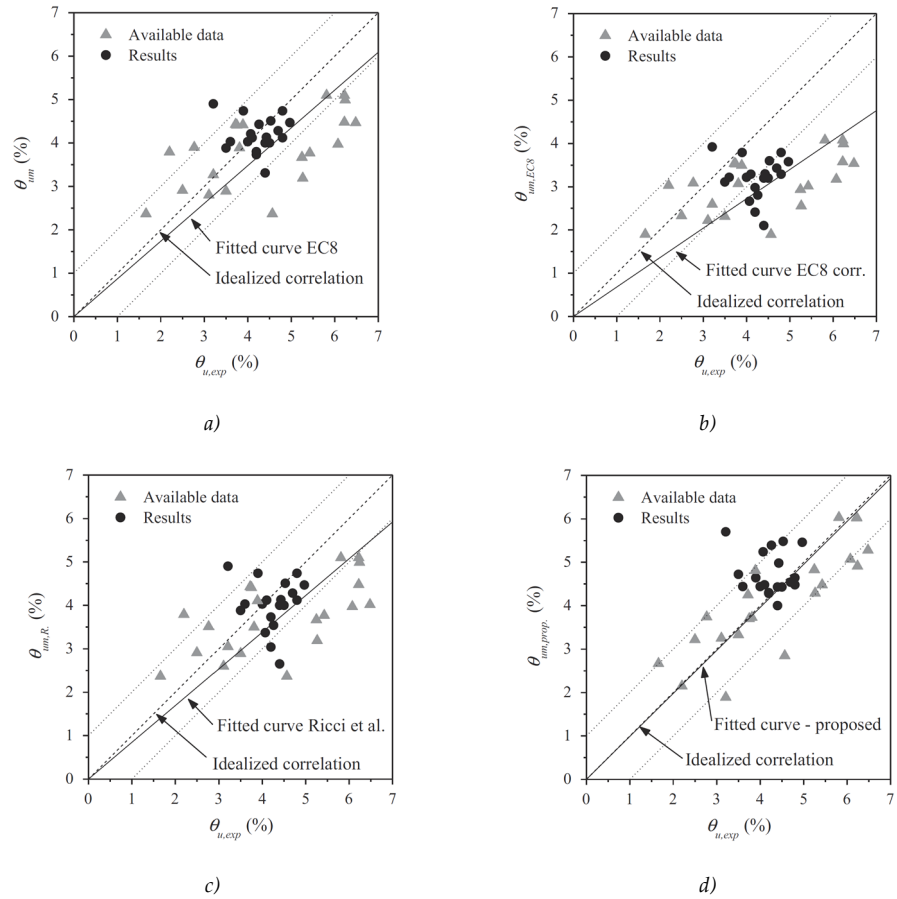
Figure 18: Predicted chord rotation values over experimental ones (CEN Eurocode 8, 2005) a), (CEN Eurocode 8, 2009) b), (Verderame et al., 2010) c) and (Melo et al., 2015) d).

2.3 Non-linear behaviour of beam reinforced with plain rebar

The previous highlighted experimental response refers to columns, which non-linear behaviour can be considered more influencing than the beam one in the seismic response assessment. Indeed, the herein considered GLD buildings are characterized by a tendency to develop a soft storey mechanism, due to their design without hierarchy strength principles application. Because of this, only few experimental tests about substandard beam members reinforced with plain rebar are available (Fernandes et al., 2011; Marefat et al., 2009).

Influence of the detailing in the non-linear response

Different beam arrangements were tested with a test set-up similar to the one presented for the column specimens (Figure 14), expect for the absence of axial load (Marefat et al., 2009). The reference specimens include members with plain or deformed rebar. They were designed for seismic load or not (Substandard specimens). Hoops spacing of $d/4$ (with d cross section depth) was the conforming value adopted according to (ACI Committee 318, 1999), whereas the substandard ones present lack in detailing, and their geometry is representative of the GLD members (deep section and low amount of reinforcement). The crack pattern exhibited by the different members helps to outline some interesting results:

- plain reinforcement causes the opening of few cracks with a spacing similar to the cross section depth;
- lower stirrups spacing helps in spreading the cracks on a higher length and in reducing their width, despite the use of plain reinforcement;
- cracks developed in presence of plain reinforcement are almost perpendicular to the beam axis, showing a pure flexural mechanism.

By the observation of the hysteretic response of specimens with standard detailing (slender section with significant reinforcement amount) and plain (Figure 19.b) or deformed (Figure 19.c) rebar, it is clearly visible that the beam deformation capacities are significantly higher respect to the one observed for the columns. The initial stiffness is very similar in the two different arrangements, which configuration is the same except for the reinforcement type. The response at high deformation level is stable both for specimens with plain and deformed reinforcement. The former showed a loss of strength after the reach of the peak and a strong pinching due to the bar slippage; on the other hand, the latter was characterized by an hardening post-yielding response and by a low pinching effect, which increased by increasing the imposed displacement. The different contributions to the overall deformation were calculated (Marefat et al., 2009). The measured bar slip influence was up to the 50% in the substandard specimens and up to 40% in the standard ones reinforced with plain rebar.

Interesting results were shown by a unidirectional cyclic test on a two-span beam collected from a real structure (Fernandes et al., 2011). The reference element was reinforced with plain longitudinal bar, and U-shape smooth hoops. The concrete was a low-strength class and it presented high-size aggregates. The test set-up (Figure 20.a) was consistent with the gravity load applied on the sub-structure in-situ conditions. This is far to represent a typical seismic loading on a frame beam element. Despite this, the experimental results are useful to highline the poor plain rebar bond capacities in the development of the beam non-linear behaviour.
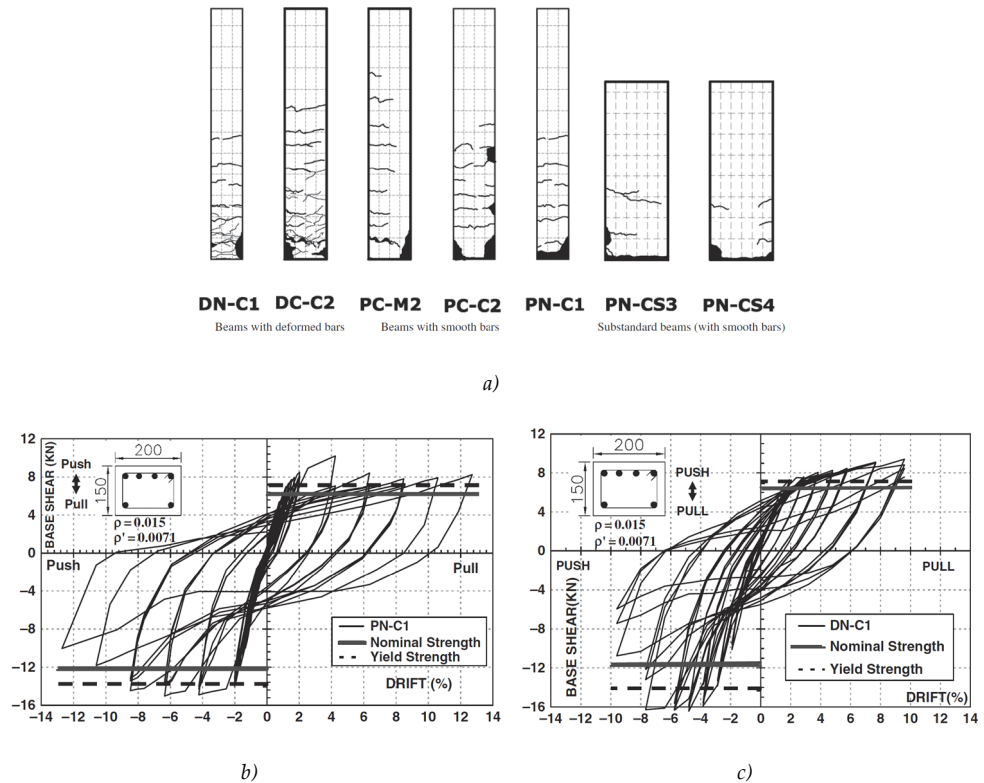
Figure 19: Crack pattern of two beam specimens tested by (Marefat et al., 2009), a); hysteretic response in presence of non-conforming stirrups spacing for elements with plain b) and deformed c) reinforcement.

The main conclusions of the experimental tests were relative to the plastic hinge aspect and to the great deformation capacity of the member. On the central support, only a crack opened, and it reached significant width. In the mid-span more than one crack opened, but their width was however high. Also the extension of this plastic hinge is worth to note: the top one is 5cm length, whereas the bottom ones has a length lower than 15cm. Both of these conclusions are very strong related to the poor bond performance of smooth reinforcement and to the consequent slip of the longitudinal rebar. The different plastic hinges length observed can be related to a different bending moment demand. Indeed, a high bending gradient is requested near the central support, due to the specific loading scheme (Figure 20.a). It is worth noting that this condition characterizes also the seismic demand on the beam top-side near the beam-column joints; thus a similar crack pattern can be observed in this region due to seismic actions. Another significant data is related to the max span deflection registered during the test. Its value reaches an amplitude of 12cm, in other word the beam is capable to reach (at failure) a normalized deflection equal to $L/33$.
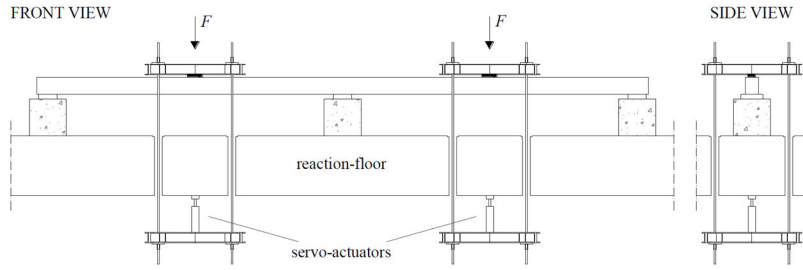
a)
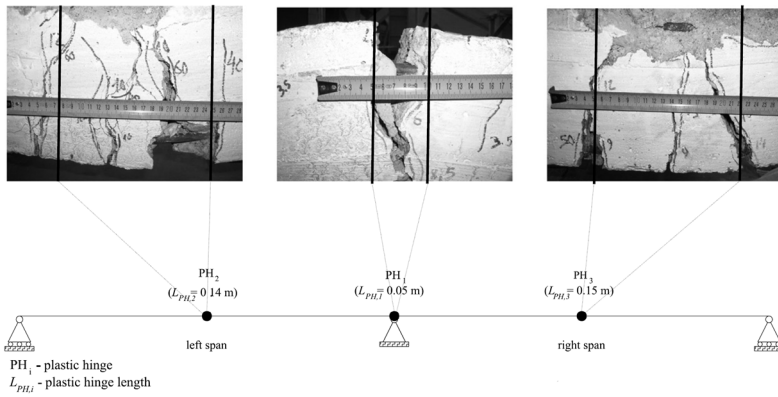
b)

Figure 20: Test set-up a) and plastic damages b) of a substandard beam elements collected from a real structure and subjected to cyclic unidirectional loading (Fernandes et al., 2011).

Sliding failure of squat beams

The absence of significant axial load is well reflected in the non-linear response of substandard squat members (PN-CS3 and PN-CS4 in Figure 19.a). In these specimens a cross crack opened at the beam end, allowing a sliding failure of the section (Marefat et al., 2009) This mechanism was controlled only by the dowel action of the longitudinal reinforcement. This type of failure (Figure 21.b) is not shown by the specimens characterized by seismic detailing; however, it is worth noting that the same are also slender with respect to the substandard ones.
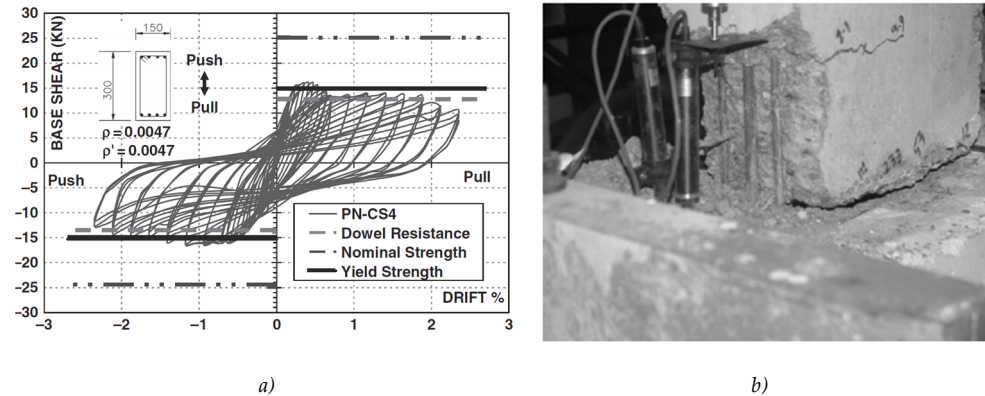
Figure 21: Hysteretic response a) and sliding failure b) of sub-standard squat beam reinforced with plain rebar (Marefat et al., 2009).

The geometry of the herein analysed specimens wanted to represent the typical beam configuration in the existing GLD buildings. Indeed, these beam members are typically realized by a high cross section depth and by a low reinforcement amount. Referring to the specific test, the slenderness representative ratio is $L_V/d = 2.83$; therefore it can be concluded that the sliding failure can be mainly due to the squat geometry of the specimens. Despite this, it is interesting to observe the hysteretic response of the specimen PN-CS4, visible in Figure 21.a. It is clearly visible that after the reach of the peak strength a significant lower resistance is exhibited, and a strong slip of the rebar governs the response. This is shown by the local strength drop and by a significant pinching effect. At the large deformation imposition, the strength was governed by a stable dowel mechanism; on the other hand, the slippage of the bar increased, and it favoured the rebar buckling at the beam failure.

2.4   RC beam-column joints without seismic detailing

In the GLD frames, the joints between beam and column members are typically characterized by the following peculiarities:

- no vertical or horizontal hoops are placed in the joint panel region;
- beam reinforcement bars are anchored in the joint panel region;
- column reinforcement bars are overlapped above the joint region.

Experimental tests on non-detailed beam-column sub-assembly confirm their bad performance against the seismic action; especially for the most vulnerable external T-joints. Low reinforcement ratio at the beam end is often unable to resist the bending moment demand; however, the bar yielding can be sufficient to cause a shear failure of the joint. Only in presence of very low reinforcement amount, the force introduced in the panel by the beam longitudinal rebars cannot be sufficient to cause the panel

35

diagonal cracking. On the other hand, if the same reinforcement rebars are not well anchored in the joint region (by an effective end-hook) their pull-out limits the force introduced in the joint; also in this case its shear failure can thus be avoided. In any case, the shear and the pull-out joint failures are related to non-ductile collapse. In the following, the definition of the joint panel shear strength is presented, and the cyclic response of different beam-column joint sub-assembly configuration is described.

Shear capacity of an RC joint

The forces acting on a joint panel during an earthquake are schematized in Figure 22 with specific reference to an external T-type configuration, which more suffers the shear failure. In this section different methods to define the force related to the joint collapse are discussed. They can be summarized in two families: the first is based on the calculation of the elastic stress acting in the shear panel (Principle Stress Limitation Model), the latter uses a more complex approach based on the concrete non-linear behaviour (Strut & Tie Models and their particularization).
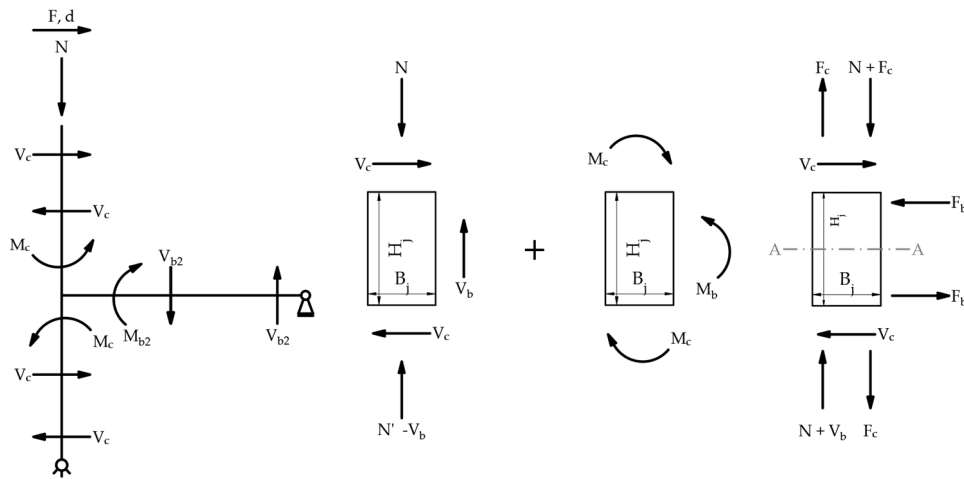
Figure 22: External seismic force acting on a T-joint with frame storey displacement from left to right.

Since the shear action on the joint panel is defined by the beam reinforcement tensile force F_b, an upper limit to this action can be identified with the yielding of the beam rebars:

$$V_{Ej} = A_s f_y - V_c \qquad (27)$$

where A_s is the top or bottom beam total reinforcement, f_y the reinforcement yield stress and V_c the column shear force. As a consequence of this, the beam with low longitudinal reinforcement will not experience the joint shear failure, because the maximum force introduced by them is not sufficient to reach the joint shear strength defined in the following (Beschi et al., 2015; Masi et al., 2013; Russo and Pauletta, 2012). On the other hand, the knowledge of the reinforcement amount is not sufficient to define a limit point between a shear and a flexural mechanism; indeed, the bond efficiency has a principal role in the transfer of the reinforcement stress to the shear panel.
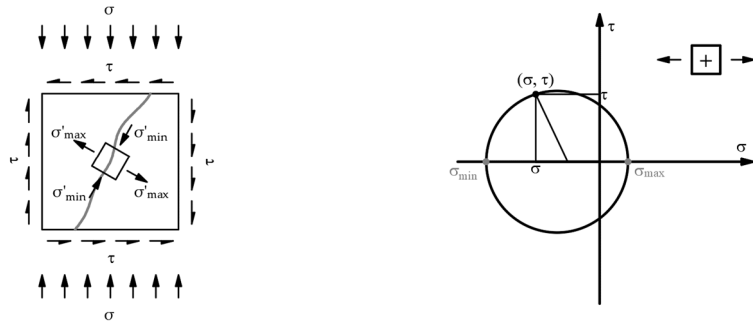
Figure 23: Shear panel stress state and its representation in the Mohr's circle.

The stress acting in a generic shear panel is represented in Figure 23. The column axial load defines the normal stress σ and the beam rebars tension force controls the shear stress τ. The role of the column shear V_c is less significant, and it is always opposite to the first contribution. Defined the joint surface A_j, mathematical calculations to find the principle stresses are below presented; the nomenclature is available in Figure 24, the b and c subscripts are relative to beam and column elements.
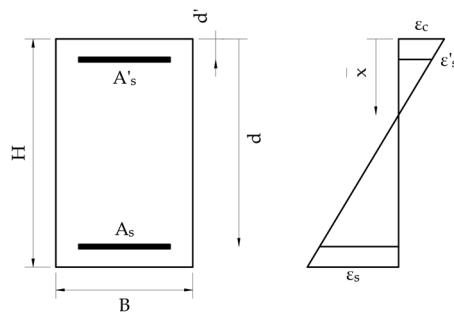
Figure 24: Beam and Column cross section nomenclature.

$$H_j = min(H_b, H_c), \qquad B_j = min(B_b, B_c),$$
$$A_j = B_j H_j \qquad\qquad (28)$$

$$z \simeq 0.9d, \qquad F_b = \frac{M_b}{z} \qquad\qquad (29)$$

$$\sigma = \frac{N}{A_j} \qquad\qquad (30)$$

$$\tau = \frac{(F_b - V_c)}{A_j} \qquad\qquad (31)$$

$$\sigma_{max} = \frac{\sigma}{2}\left(1 + \sqrt{1 + \frac{4\tau}{\sigma}}\right) \qquad\qquad (32)$$

$$\sigma_{min} = \frac{\sigma}{2}\left(1 - \sqrt{1 + \frac{4\tau}{\sigma}}\right) \qquad\qquad (33)$$

Regarding the Eq.(30), some authors suggest to consider also the beam shear action V_b in the definition of the normal stress acting on the exterior joint panel (O'Reilly and Sullivan, 2017; Sharma et al., 2011), because of the absence of equal and opposite action on the other joint side. In this way:

$$\sigma = \frac{N + V_b}{A_j} \qquad\qquad (34)$$

The Principle Stress Limitation Model (herein called PSLM) introduces a lower σ_{min} and an upper σ_{max} limit to the joint panel elastic tension, relating these with the concrete compressive p_c and tensile p_t strengths. This choice wants to represent the failure of the compressive strut or the reach of the panel first diagonal cracking. The former is typical of high compression stress in the joint (interior connections), the latter of low axial stress value (interior or exterior connections). The resulting joint strength capacity is expressed in the form of Eq.(36), which relates the cracking stress to the concrete compressive and tensile strength. An overview of the k-values is reported in Table 3, with reference to different element detailing in term of reinforcement type and beam rebar anchorage.

$$p_c = -k_c f_c, \qquad p_t = k_t \sqrt{f_c} \qquad\qquad (35)$$

Different researchers well analysed this approach. The first k-values was proposed for the RC interior and exterior joints reinforced with deformed rebar and 90° bent anchorage (Priestley, 1997); both in-side and out-side bending were considered. More recently, experimentally observed joint shear cracking were justified by the principle

stress calculation method, considering detailed and not detailed specimens reinforced with deformed rebars (Masi et al., 2013). Some provision is also available for structures reinforced with smooth bars anchored in the joint region with hook-end (Pampanin et al., 2003) . They were later discussed by other authors on external sub-assembly (Metelli et al., 2015; O'Reilly and Sullivan, 2017). The approach is also followed also in the New Zealand Standards (NZS 3101, 1995). It is noteworthy to evidence the difference between the limit suggested by the Italian Code (Circolare applicativa NTC, 2019; Norme Tecniche per le Costruzioni, 2018) for the joint shear verification, and the experimental evidence. The latter showed a panel cracking at a load level consistent with the assumption of the coefficient $k_t = 0.2$, the former suggest the panel cracking to arise at a load level consistent with the assumption $k_t = 0.3$.

Reference	Joint tipology	Detailing	Limit formulation
(Priestley, 1997)	Interior	Deformed bars	$p_t > 0.50 f_c$ $p_t < 0.29\sqrt{f_c}$
	Exterior	Deformed bars bent away from the joint	$p_t < 0.29\sqrt{f_c}$
	Exterior	Deformed bars bent into the joint panel	$p_t < 0.42\sqrt{f_c}$
(Pampanin et al., 2003)	Interior	Smooth bars	$p_t < 0.29\sqrt{f_c}$
	Exterior	Smooth bars with hook-end	$p_t < 0.20\sqrt{f_c}$
(O'Reilly and Sullivan, 2017)	Exterior	Smooth bars with hook-end	$p_t < 0.135\sqrt{f_c}$

Table 3: Application of the PSLM method to different RC elements; different authors proposals.

Nowadays, the modern Codes refer to an analogue method, which takes into account more detailing parameters (ACI Committee 318, 1999; CEN Eurocode 8, 2009; Norme Tecniche per le Costruzioni, 2018).

Once the limit described in the Eq.(35) is defined, it is possible to calculated the joint strength by the integration of the related shear stress v_j. These are calculated on the Mohr's circle. According to the diagram of Figure 23, the normal stress σ is positive for tension, therefore the axial stress due to column vertical load has to be input as negative.

$$p_c \sqrt{1 - \frac{\sigma}{p_t}} \le v_j \le p_t \sqrt{1 - \frac{\sigma}{p_t}} \qquad (36)$$

$$V_{Rj} = v_j A_j \qquad (37)$$

The PSLM approach is very powerful and useful. On the other hand, it can be discussed because a significant part of the joint shear action is carried by the diagonal compressive strut. For these reasons, different other authors proposed alternative methods based on the Strut & Tie model concept. Considering the combined shear and axial stress acting in the joint region, it is possible to notice that the concrete performance could be disturbed by transversal tensile stress. This results in a concrete lower strength and stiffness capacities. The reference concept is well outlined by Vecchio and Collins for different structural applications (Vecchio and Collins, 1986). On the same basis, a Softened Strut and Tie Model was proposed (Hwang and Lee, 2000, 1999). Diagonal, horizontal, and vertical mechanisms can develop in the joint panel, depending on the reinforcement detailing. The concrete struts can be equilibrated by horizontal hoops, column vertical rebars, and beam horizontal reinforcement. To apply this method, an iterative procedure involving equilibrium, compatibility, and constitutive laws is required to define the softening coefficient. A simplified version can be however found in (Hwang and Lee, 2002).

Where no horizontal hoops are placed into the joint region, the only possible mechanism include a single diagonal strut. A particularization for non-confined exterior joints was proposed to account for smooth hooked end rebars (Metelli et al., 2015). It is possible to refer at it with the name MSSTM (Modified Softened Strut and Tie Model). This proposal is based on SSTM, which allow to define a softened compressive stress ξf_c acting in the diagonal strut, which balances the joint shear action by its horizontal component. Therefore, the inclination of the strut is fundamental to define the joint shear strength. On the bases of specific experimental evidence outlined in the following (Beschi et al., 2015; Braga et al., 2009; Pampanin et al., 2002), MSSTM method assumes a higher inclination of the strut, with respect to the panel geometrical diagonal. The analytical definition of it, on a new joint panel reference geometry $(H_j; B_j)$ is then suggested. Called h_s the distance of the first column stirrup outside the joint panel region (with $h_s \le H_c/4$), and c the concrete cover of the longitudinal reinforcement, the modified joint dimensions are expressed with Eq.(39) and Eq.(40).
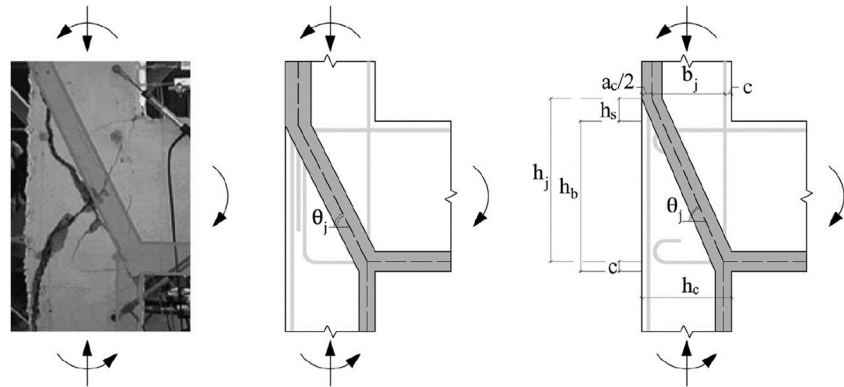
Figure 25: Identification of the concrete strut in a T-joint specimen specimen (Pampanin et al., 2002) and schematization of its inclination and geometry (Metelli et al., 2015).

$$a_c = \left(0.25 + 0.85\frac{N}{A_j f_c}\right)H_c \qquad (38)$$

$$H_j = H_b + h_s - c \qquad (39)$$

$$B_j = H_c - \frac{a_c}{2} - c \qquad (40)$$

$$\theta_j = \frac{H_j}{B_j} \qquad (41)$$

The depth a_c of this strut into the panel was originally defined by the means of Eq.(38) (Paulay and Priestley, 1992). MSSTM method updates the proposal with the reduction of the reference depth, in order to account for the specific application herein considered:

$$a_c' = a_c \sin\theta_j \qquad (42)$$

Finally, the joint shear strength is defined by the following:

$$V_{Rj} = \xi f_c a_c' min(B_b; B_c)cos\theta_j \qquad (43)$$

The suggestion shows a very good accuracy in predicting the joint shear strength (Metelli et al., 2015; O'Reilly and Sullivan, 2017). Despite this, the shortcoming of the method is its requirement to solve an iterative procedure. Therefore, the simpler PSLM method seems to be more adequate in the common assessment analysis. Other methods to evaluate the joint shear strength were proposed by several authors. For a detailed analysis a critical review is available in the literature (Sharma et al., 2011).

Experimental response of beam-column joints

The most of the experimental campaign on beam-column sub-assembly concerns external T-joints, because of their higher vulnerability to the joint shear panel failure (Beschi et al., 2015; Braga et al., 2009; Pampanin et al., 2002). The main experimental results are herein discussed, focusing on the joint deformation capacity and on the mechanisms that govern its failure. All the campaigns treat displacement-control tests (in presence of axial load on the column), and the output curves are column shear versus top displacement (or global drift) $V - d$ (or $V - \theta$). The test set-up is shown in Figure 26, both for exterior and interior joints; it can be considered representative of all the herein presented works. The column and the beam members are detailed in a consistent way with what have been previously discussed. The joint panel reflects the typical features above presented regarding non-conforming (or non-detailed) elements.

It is noteworthy to divide the situation in which a joint is subjected to shear failure from another in which it is not. Referring to Figure 22, it is clearly visible that the maximum shear action acting in the node panel V_j is governed by two forces: the column shear V_c and the reinforcement push or pull action F_b. By the equilibrium imposition on the substructure, it can be demonstrated that the higher contribution is the one related to the beam-side; therefore, an upper limit to this force can be identified by the beam rebar yielding. If this force is not able to cause the panel cracking, no joint shear failure occurs and so the mechanism can only be flexural (Russo and Pauletta, 2012). This concept has to be applied both to the top and the bottom side of the beam; if asymmetric reinforcement is placed the shear failure can occur in a single direction of excitation (Beschi et al., 2015). This simple consideration allows to predict the failure mechanism of a specific joint with the knowledge of the global and local geometry, of the longitudinal beam reinforcement amount A_s, and of the material mechanics $(f_c; f_y)$.

$$V_j = F_b - V_c \tag{44}$$

$$F_{b,max} = A_s f_y \tag{45}$$

A symmetric configuration of beam reinforcement should cause the same failure mechanism in both positive and negative directions of loading. However, this is not clear by the observation of a specific T-joint experimental response (Pampanin et al., 2002), which is shown by the capacity curve in Figure 27.a. The authors (Pampanin et al., 2002) speak about a hybrid failure, interested both by shear cracking and by beam bar slippage into the joint region. Until the reach of 1.00% drift, no significant damage occurred in the specimen and only the pinching effect related to bar-slip was visible in the curve. After this deformation level, in positive action (rightward) the first diagonal cracking of the joint took place and a sudden loss of strength was

registered. Moving toward left-side, beam yielding anticipated the shear failure; however, during the reloading cycle at the same drift level, the opposite panel crack was formed, and symmetric response was exhibited. The illustrated hybrid mechanism can be related to a lower capacity of the upper beam reinforcement anchorage in introducing force in the joint. Although this considerations, it is worth noting that the second cracking appeared at a lower load level, probably due to a general increased damage and to ductility demand on the adjacent beam (Priestley, 1997). At higher deformation imposition, a concrete wedge mechanism characterized the joint response, with an increasing loss of strength. The authors (Pampanin et al., 2002) relate this mechanism to a push-out effect of hook-end bar in compression (Figure 27.c).
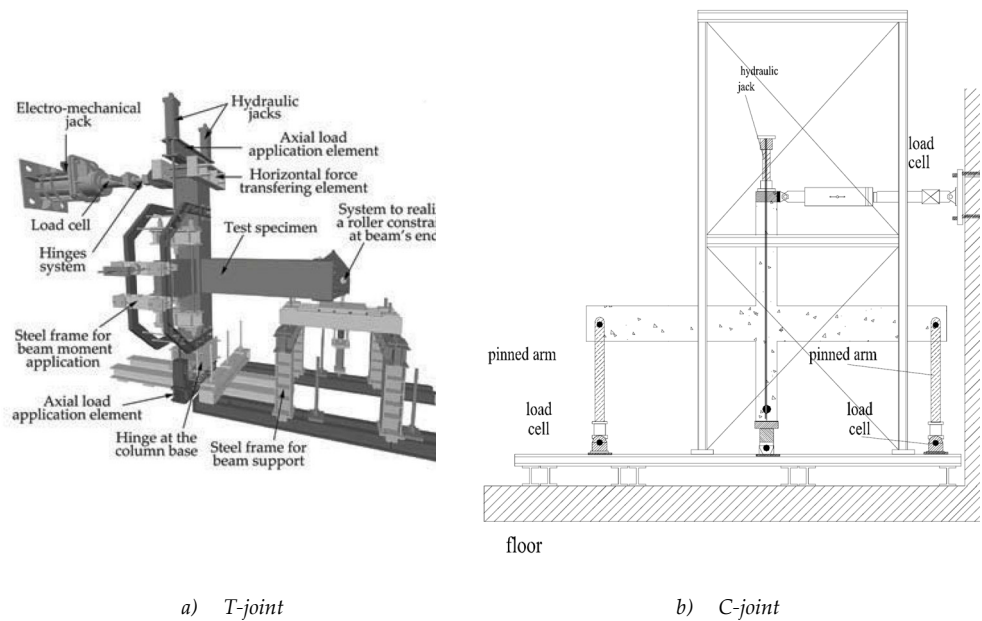
a) T-joint   b) C-joint

Figure 26: 3D representation of the test set-up for an external T-joint specimen a) (Beschi et al., 2015) and schematization of a similar arrangement for an interior C-joint b) (Pampanin et al., 2002).

43

a)   b)

c)
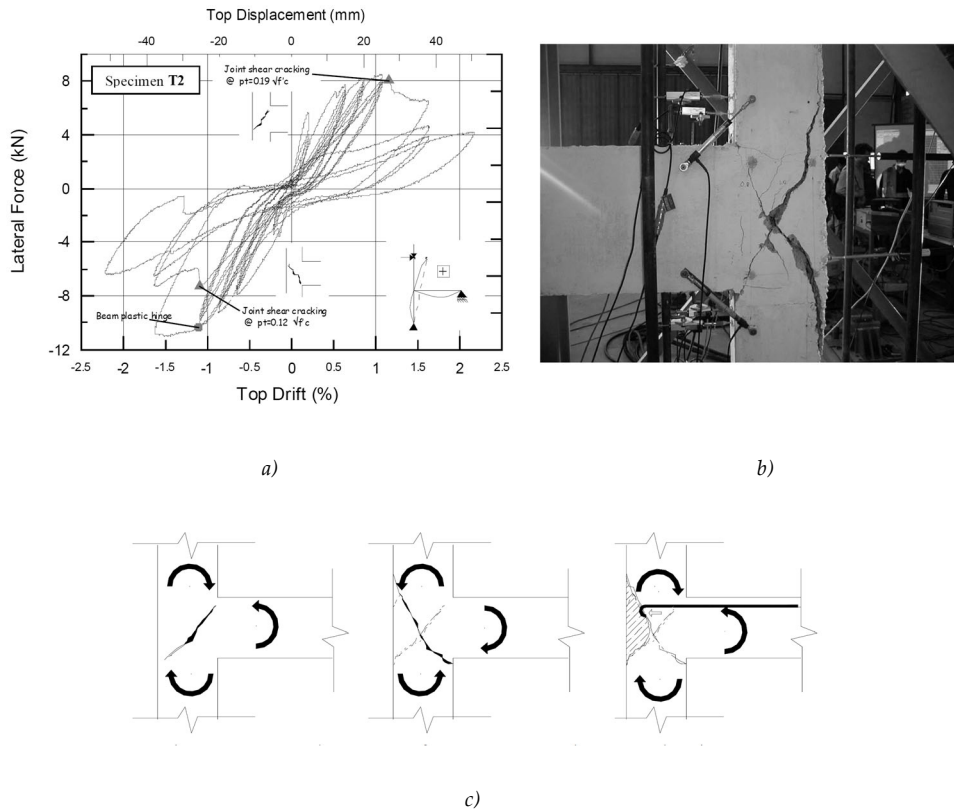
Figure 27: Experimental response of a T-joint with symmetric reinforcement in its members a), b), and schematization of the concrete wedge expulsion c) (Pampanin et al., 2002).

The influence of the member anchorage performance was shown testing an exterior T-joint with plain bar and no hook at their end (Russo and Pauletta, 2012). These specimen (Figure 29) were characterized by a peak of strength related to the beam cracking force, and a sudden loss of strength due to longitudinal rebar anchorage fail. This dangerous lack of detailing did not allow the beam to reach its yielding moment, therefore the sub-assembly seismic capacity is strongly reduced. No panel shear cracking was possible. In the same campaign (Russo and Pauletta, 2012), a design deficiencies related to the use of bent rebar was also shown. Indeed, their prematurely bent down did not allow the development of the bending capacity of the cross section adjacent to the joint. Specimen detailing and its V-d capacity curve are reported in Figure 30. It is worth noting that the bent position also influences the crack pattern of the beam (Braga et al., 2009; Russo and Pauletta, 2012).

a)   *b)*
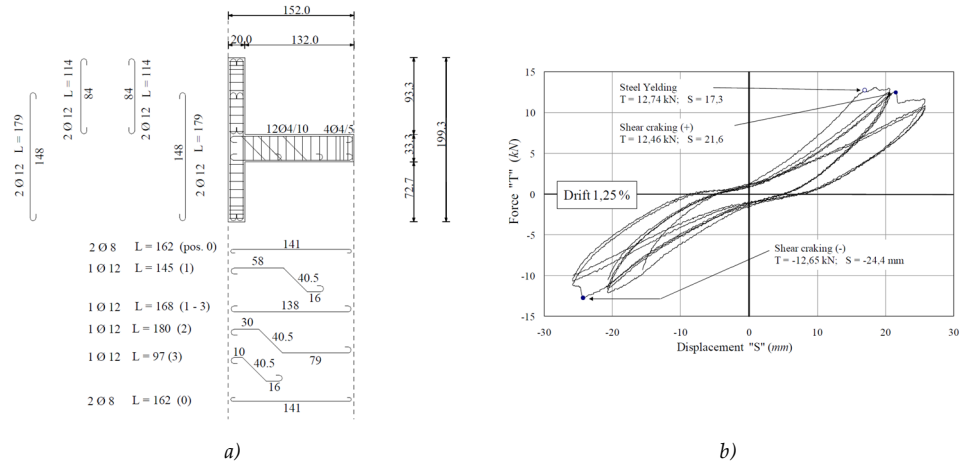
Figure 28: External T-joint arrangement a) and details about its response at the panel crack b) (Braga et al., 2009).

a)   *b)*
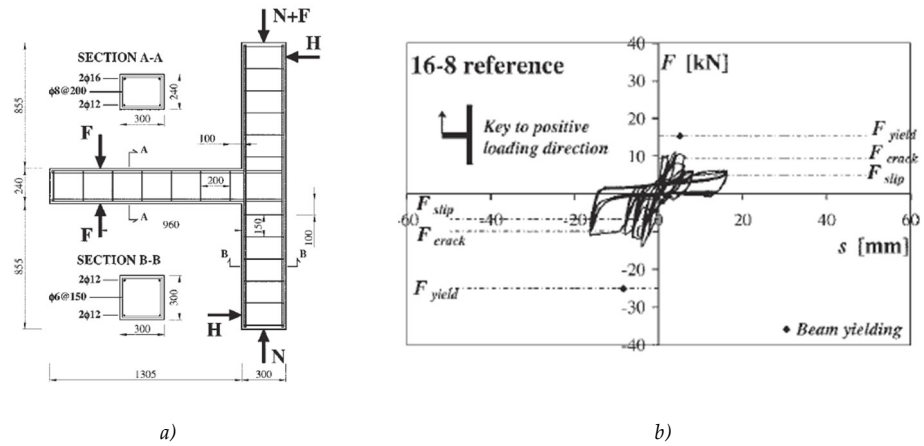
Figure 29: Reduced 2:3 scale exterior T-joint with plain rebar and absence of hook-end detail: schematization a) and capacity curve b) (Russo and Pauletta, 2012).

45
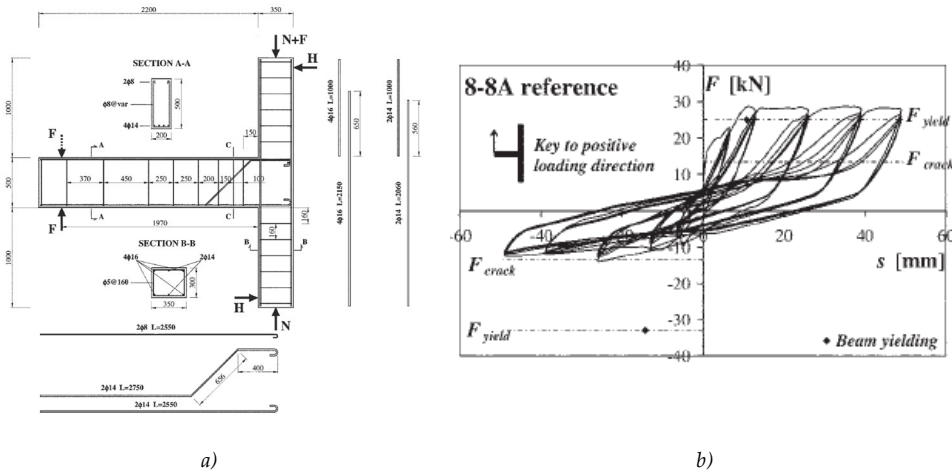
Figure 30: Full scale exterior T-joint with beam reinforcement amount deficiencies: reinforcement detailing a) and capacity curve b) (Russo and Pauletta, 2012).

A sub-assemblage with asymmetric reinforcement in the beam was observed to exhibit different failure mechanism in the different loading direction (Beschi et al., 2015). A flexural mechanism is well defined with positive displacement imposition (tension in the lower reinforcement of the beam), and a shear failure characterizes the opposite displacement action. In both the cases no significant damage arises before the reach of a drift equal to 1.00%. The tests confirm that the flexural mechanism was not characterized by a significant strength deterioration, but the shear one is. With an imposition of a deformation equal to 3.00% leftward drift, the strength reduction was quantified in the 60÷70% of the force that causes the panel cracking. The authors (Beschi et al., 2015) suggest the reach of an incipient collapse limit state around a normalized deformation (drift) of 1.50%. The diagonal crack opening at this stage was 2*mm*.
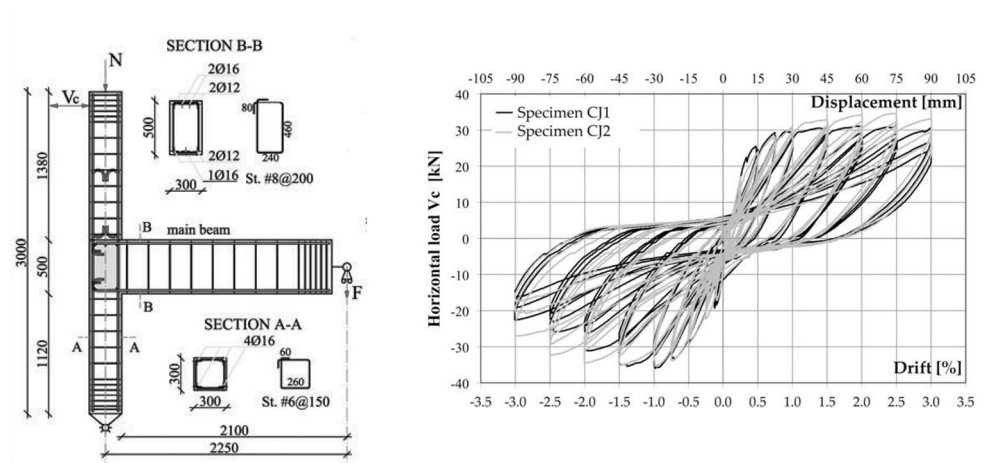
Figure 31: Response of 2 T-Joint specimens characterized by beam asymmetric reinforcement (Beschi et al., 2015).

Corner L-joints were characterized by a flexural mechanism in the column (Pampanin et al., 2002), which has low reinforcement amount respect to the beam. The ductility of this arrangement is significant thanks to the low applied axial level, which is a peculiar feature of the corner joint. Like shown in Figure 32, drift level higher than 3.00% were reached without significant loss of strength. Above this level, damage occurred in the top beam side, probably due to the column rebar slippage and to high stress concentration in the hook-end anchorage.

a)   b)
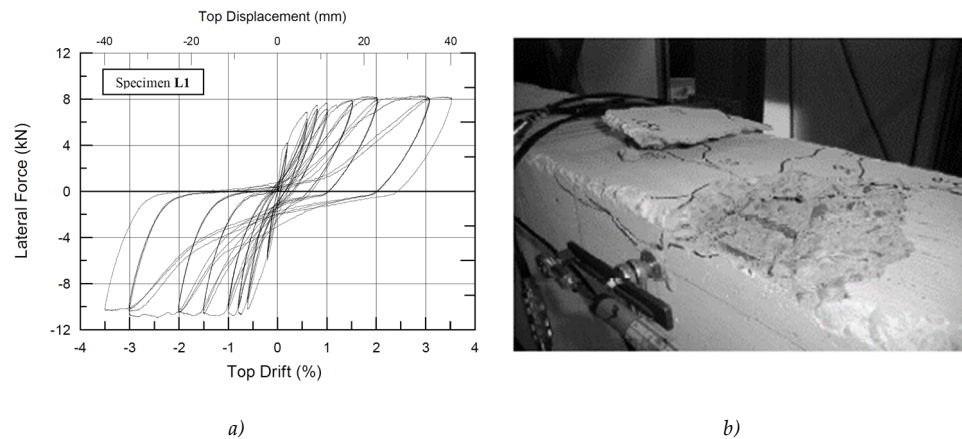
Figure 32: L-joint specimen: capacity curve a) and top beam side concrete damage b) (Pampanin et al., 2002).

Interior joints showed a clear weak-column mechanism. Experimental results are available both for 2:3 scaled and full scale specimens (Braga et al., 2009). Prior to the reach of 1.00% drift level, the tests results showed a crack pattern characterized by the following:

- joint panel micro-cracking;
- flexural cracks near the interfaces in the upper and lower columns;
- beam cracking near the joint region;
- beam cracking in the location of reinforcement bending for bent rebars.

Increasing the deformation level, the damage localized itself in the joint-column interfaces, where concrete crushing and cover spalling are observed. These phenomena cause a progressive reduction of strength in the incremental cycles' imposition at the same displacement magnitude (Figure 33). The subassembly was however able to reach a maximum drift equal to the 7.00%. At this deformation level, the strength was equal to one fourth of the original one. The authors (Braga et al., 2009) outline that this strength loss effect is stronger in specimens reinforced with deformed reinforcement, because of their tendency to damage the concrete around the bars. These results are confirmed by the test carried on by (Pampanin et al., 2002) on two similar specimens without bent rebar.
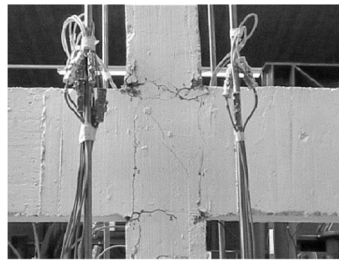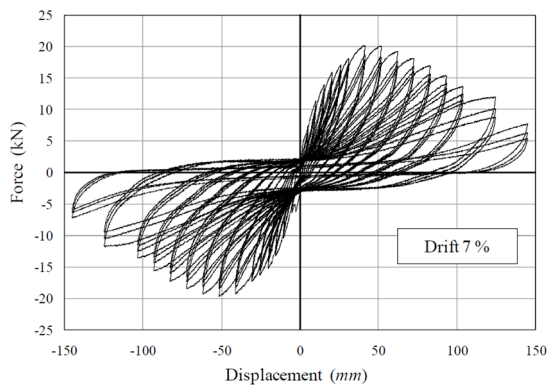
Figure 33: Experimental response of an internal 2:3 scaled joint: shear vs. top displacement curve a), sub-assemblage crack pattern b) and focus on a beam-column interface. c) (Braga et al., 2009).

Summary about the joint seismic capacity

Generally, it is possible to conclude that the slippage of plain bars causes significant pinching of the overall response, with a consequent lower energy dissipation capacity of the substructure. At the same time the phenomenon allows a global higher flexibility of the system, therefore a higher deformation capacity of it. External T-joints are subjected to hybrid mechanism, which can assume strong brittle behaviour in the case of large shear damage. The internal ones are instead characterized by a flexural mechanism of the columns; furthermore, a great ductility capacity is also observed for the corner L-Joint. It can be argued that all the joint typologies are able to show deformation capacity without any evident sign of strong damage until 1.00% of normalized displacement imposition (drift), regardless of their different failure mechanisms. Over this deformation level, significant concrete damage can be observed, but it does not frustrate the stability of the sub-assemblage at higher deformation. Anyway, it can be suggested not to overpass the deformation limit over which the response becomes very difficult to predict (e.g. 1.50%).

Loss of anchorage effect

The poor bond performance of plain reinforcement can affect the RC member behaviour near to a beam-column joint (Figure 34). The reinforcement bars considered in compression under the hypothesis of plane section and perfect bond can result stressed in tension, because of the bar slippage into the joint region. This phenomenon (loss of anchorage) significantly influences the definition of the structural behaviour (Braga et al., 2012; Laterza et al., 2017), since it reflects into a loss of strength of the member in the joint-member adjacency and to a ductility capacity reduction (Figure 35). All the presented effects are depending on the axial load (Calvi et al., 2002a; Fabbrocino et al., 2004). It can be demonstrated that the loss of anchorage can also reflect in a modification of the strength hierarchy, and that the non-ductile weak-column-strong-beam mechanism can be amplified (Calvi et al., 2002a).
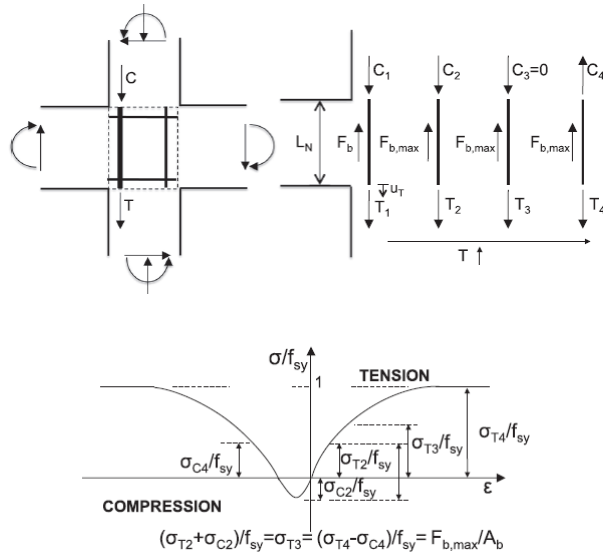
Figure 34: Column longitudinal rebar loss of anchorage in an interior beam-column joint;
(Laterza et al., 2017).
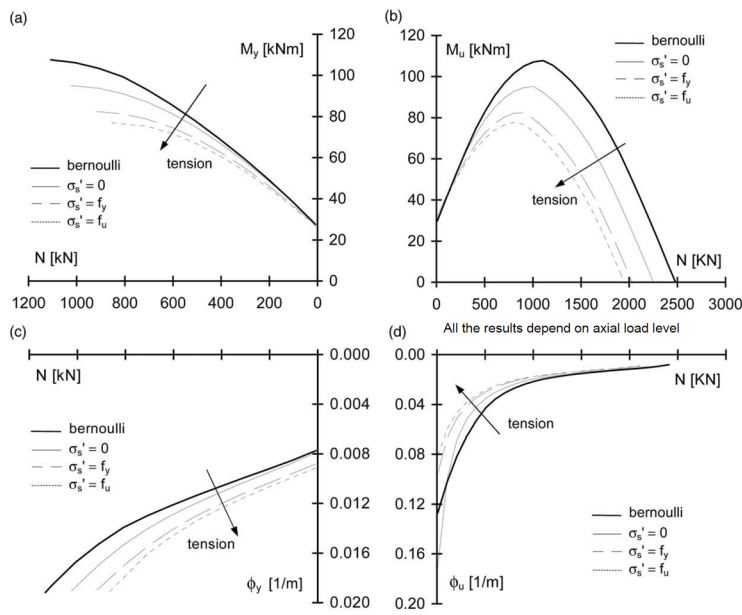
Figure 35: Loss of anchorage effects on: bending capacity at yielding a), M-N interaction
diagram b), and yielding c) and ultimate d) curvature; (Fabbrocino et al., 2004).

2.5   Modelling of the frame structures

The available ways to approach the assessment of reinforced concrete structures are several. They are different for the number of the phenomena they can consider, for the accuracy they can offer, and for the results quality. Each method requires specific implementation instrument. Typically, a more detailed approach needs computer-based solver time requiring, and the increase of output information is often related to a non-negligible effort in their interpretation. Therefore, the choice of the assessment method must be strongly related to the aim of the analysis. Seismic behaviour of RC structure needs the modelling of the post-elastic phase, indeed the vulnerability of a structure is strongly related to it. Ductile mechanisms have to be divided from brittle ones, strength and stiffness degradation can significantly influence the non-linear member behaviour, the cyclic response has to be defined in order to quantify the structural capacity to dissipate the input earthquake energy and so on.

The model of the non-linear structural analysis can be divided depending on their discretization level (Cosenza et al., 2002):

- "point by point" modelling, which works on points and finite elements characterized by specific constitutive laws;
- "member by member" modelling, based on the representation of jointed members whose non-linear behaviour is related to lumped plastic hinges or spread plasticity on a finite length;
- "global" models, which refer to the entire structure reducing its behaviour to a system with few degrees of freedom, or reproducing it with macro-models able to schematize the behaviour of few sub-structure parts.

More in general it is possible to divide micro-models from macro-models, reducing the complexity and the precision of the representation by the passage from the former to the latter (Marino et al., 2019). Although of this, it is value to remember that one of the main goals of a structural seismic analysis is to identify the expected damage mechanism, and to evaluate its implication on the overall structure seismic response. Therefore, global methods are not satisfactory in the case of damage assessment (e.g. Expected Annual Loss EAL analysis). Where the non-linear behaviour of a member or a structural sub-assembly is well known (i.e. for elements designed under the suggestions of the modern Codes), their behaviour can be well represented by simplified methods, implementable also in commercial calculation tools. In the case of existing structures, the problem is more complex. The non-linear behaviour of RC elements is indeed strongly influenced by the lack of seismic detailing. Significant strength and stiffness degradation can be related to brittle mechanisms, and poor bond performance of smooth rebar can change the common hypotheses on which the modern calculation and the numerical tools are based.

51

The approaches used to define the modelling tools can be also divided considering the hypothesis on which they are based. A mechanical approach is mainly related to theoretical concepts; on the other hand, the empirical models are fitted on experimental tests. Hybrid methods can also be defined. The adoption of complex non-linear analysis method requires the knowledge of the capacity of the structural elements. In the previous sections a detailed insight into the non-linear monotonic and cyclic response of column, beam and beam-column joints has been presented. In this one, a brief overview on the tools available to represent the same behaviour is reported.

Frame members modelling

In the literature two main families of member modelling are available: the lumped plasticity approach and the fibre-based model. The former is the simplest; indeed it provides the non-linear element modelling only in the member ends (Figure 37), where are greater both the bending action (due to gravity and seismic loads) and the shear one (in particular in presence of infill-frame interaction). These models can results very useful to describe the member behaviour with few parameters; on the other hand, they need the calibration of the numerical hinge, especially if they are experimental based (Haselton et al., 2008; O'Reilly and Sullivan, 2017). Both flexural and shear mechanisms can be represented by the adoption of specific Moment-Curvature $M - \varphi$ (or Moment-Rotation $M - \theta$) and Shear action-Transverse deformation $V - \gamma$ relationships. Furthermore, the two behaviours can be considered coupled or uncoupled, according to the expected structural behaviour.

Fibre models are more refined. They represent an RC element by the discretization of it in some reference sections (Figure 36.a) (Monti and Spacone, 2000; Petrangeli et al., 1999; Spacone et al., 1996). Each section is discretized with a division it in several fibres. These method can be so classified between the "member by member" family and the "point by point" one (Cosenza et al., 2002; Manfredi and Pecce, 1998). Theoretically, fibre-based models do not need any calibration process. The non-linear behaviour is indeed located in the fibres, which must be characterized by specific stress-deformation law (both for concrete and steel). The section strains are defined by the use of a defined shape functions (Figure 36.c), and the member forces are derived by the equilibrium imposition. The section fibre division on the two main axis of a member cross section allow to account for different confinement levels, depending on the transversal reinforcement layout. The biaxial bending coupled to a varying axial load action can also be considered. The shear behaviour can also be introduced with different approaches (Cosenza et al., 2002; Petrangeli et al., 1999).
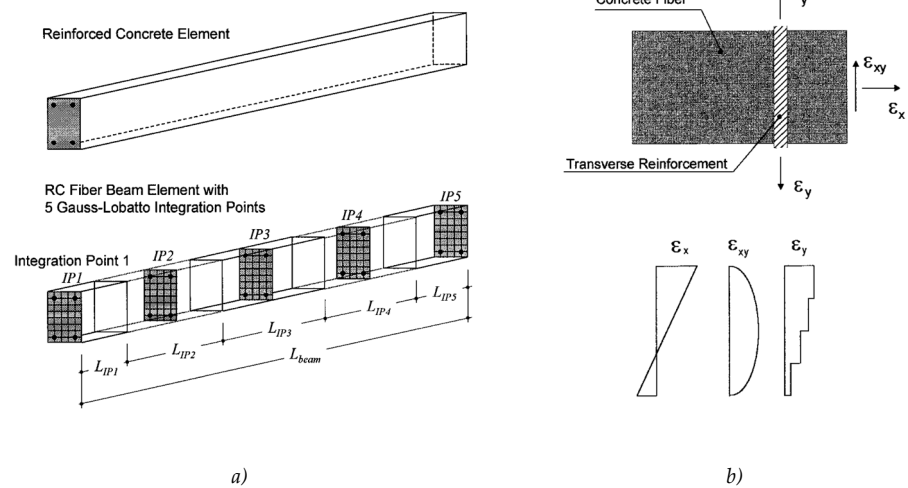
Figure 36: Fibre beam element with 5 Gauss-Lobatto integration points a) (Monti and Spacone, 2000) and focus on a concrete fibre with example of shape function for it b) (Petrangeli et al., 1999).

Typical assumptions in a fibre-based model are the planarity of the section under bending (Bernoulli hypothesis), and the perfect bond between the reinforcement and the surrounding concrete. The second assumption is not adequate in the case of poor bond performance due to cyclic loading, and/or to the employment of smooth reinforcement (such is the case of GLD structures). To solve this significant issue, a refined RC element was proposed to account for the bar slip phenomena in the analytical definition of a numerical model (Manfredi and Pecce, 1998). The rebar equilibrium with the surrounding concrete is imposed, and a linear representation of the bar slip is assumed. Later, these concepts were introduced in a specific fibre element (Monti and Spacone, 2000). These models can account for rebar slip into the element and in the reinforcement anchorage length. The bar slip from the joint region or from the footings can thus be represented.

As already seen, the fibre elements can account for axial load, biaxial bending, and shear action by the only knowledge of the cross-section dimensions and by the definition of appropriate stress-strain laws. The method also allows to account for the tension stiffening effect, and to the bar slip consequences in presence of not adequate anchored rebar. Moreover, it can represent the elastic dynamic behaviour of the structures and the additional deformation and/or possible brittle failure due to bar pull-out. Despite these powerful values, the method can can be considered of doubtful use when the cross-section dimension, the steel reinforcement layout, and the material properties are not well known. In the case of existing building structural

assessment, the approach can thus result too accurate if compared with the available information and their precision.

A lumped plasticity empirical-based approach was proposed in literature for the GLD frame modelling (O'Reilly and Sullivan, 2017). Its schematization is reported in Figure 37.a. The flexural and the shear behaviour are uncoupled since they are assumed to arise at deformation levels strongly different to each other (the shear failure due to infill-frame interaction does not allow significant element deformation). The definition of the numerical model is mainly empirical and it is based on the specific experimental database available in the literature (Di Ludovico et al., 2014; Melo et al., 2015; Verderame et al., 2008b, 2008a).

a)

b)

c)
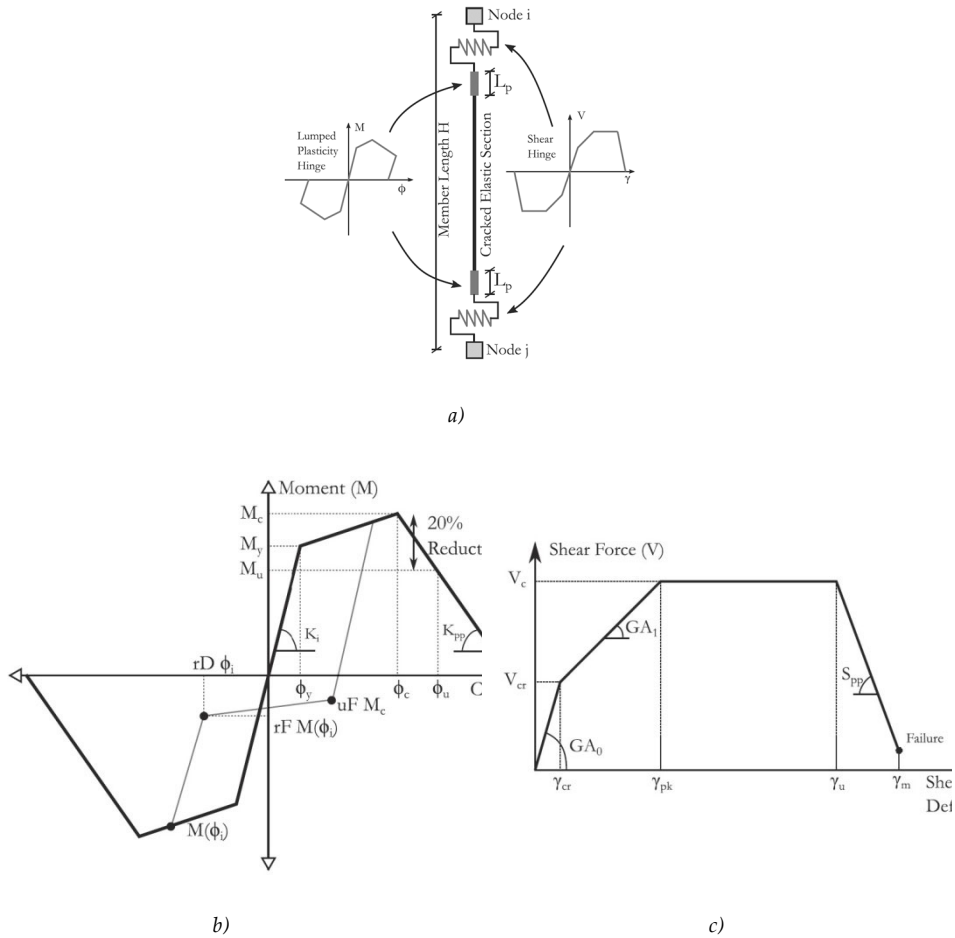
Figure 37: Schematization of a lumped plasticity member modelling a) and focus on the proposed constitutive laws for flexural b) and shear c) hinges (O'Reilly and Sullivan, 2017).

The flexural behaviour of the columns is represented by a tri-linear degrading moment versus curvature backbone (Figure 37.b). The points characterizing the behaviour are the yielding, the capping, and the ultimate one. The first main point is identified by the curvature value defined in Eq.(46) (Paulay and Priestley, 1992), and by the relative bending moment calculated by the means of a sectional analysis. The peak strength (capping moment) is the median value obtained by the reference database; on the other hand, the ultimate curvature is calculated by a plastic hinge approach based on non-detailed column chord rotation capacity (Melo et al., 2015). The hinge length is the one suggested for the member reinforced with deformed rebars (Paulay and Priestley, 1992) and subsequently confirmed for a beam with plain rebar (Melo et al., 2011).

$$\varphi_y = 2.1 \frac{\varepsilon_y}{h} \tag{46}$$

$$L_p = 0.054h + 0.022 f_y d_{bl}, \qquad [m, MPa] \tag{47}$$

$$\varphi_u = \frac{\theta_{um,c}}{L_p} 0 \tag{48}$$

In the definition of the yielding φ_y and ultimate φ_u reference curvatures, the different terms assume the following meanings: f_y and ε_y are the steel yielding stress and strain, d_{bl} is the longitudinal reinforcement diameter, h is the member cross-section height in the plain of bending, L is the member length, L_p the plastic hinge length and $\theta_{um,c}$ the ultimate column rotation capacity.

A simplified way to calculate the ultimate curvature point is suggested, according to the aim of represents structural behaviour also in the case of few available information. By the fitting of reference tests results, the capacitive ductility is defined by the following equation (linear dependence on the axial load ratio v):

$$\mu_\varphi = 22.7 - 47.4v \tag{49}$$

The deformation level at the peak force is defined by a degrading stiffness, assuming a bending action in the ultimate point related to a 20% loss of strength (common Codes choice). This stiffness value is a statistical result too, and it is expressed as a ratio of the initial cracked slope $K_y = M_y/\phi_y$:

$$K_{pp} = a_{pp} K_y \tag{50}$$

$$a_{pp} = -0.1437v - 0.0034 \tag{51}$$

The detrimental effect of the axial load on the deformation capacity and the strength degradation are underlined in the proposed modelling. The mathematical formulations adopted for the ductility capacity and the post-peak stiffness clearly show this.

The uncoupled shear hinge (Figure 37.c) is based on a mechanical based approach, suggested in the literature (Priestley et al., 1994) and enhanced by empirical evidences (Mergos and Kappos, 2012, 2008; Zimos et al., 2018). The backbone of the force-displacement proposed relationship accounts for an elastic initial behaviour; then, a loss of stiffness is assumed until the reach of the member shear strength. The peak force is constant during the development of a certain deformation capacity, which depends on the member detailing. Finally, a strength degradation is represented.

Beam-Column joints modelling

The approaches to model the joint shear strength and the relative deformability are several. A summary of the different techniques allows to divide the model approach in the following groups (Sharma et al., 2011):

- Lumped plasticity model;
- multi-spring model;
- finite element simulation.

The most simply approach obviously consists in the representation of the non-linear behaviour by the definition of a lumped hinge. Treating MRF structures, the most convenient adopted relationship is based on the joint representation in term of bending moment versus rotation $M - \theta$. The lumped hinge has to be located between the column and the beam member (beam side); whereas the joint geometry is simulated with rigid elements (Figure 38). To define this specific hinge a non-linear relationship must be chosen. It should be characterized by a backbone behaviour and a cyclic hysteretic rule, which is strongly influenced by the degradation observed under reversal loading. The fitting of the experimental results is one of the most followed way to calibrate the relationships between the joint generalized action and the relative deformations. The limit of this approach is the dependency on the experimental database used in the calibration, and the consequent difficulties in the extension of the rule to a wide number of generic situations.

Multi-spring models allow to better represent different causes of joint deformation. They are based on the use of rotational and axial springs, which separately model different mechanisms. A complete vision on the mechanism that characterize the joint behaviour is available in the literature (Lowes and Altoontash, 2003).
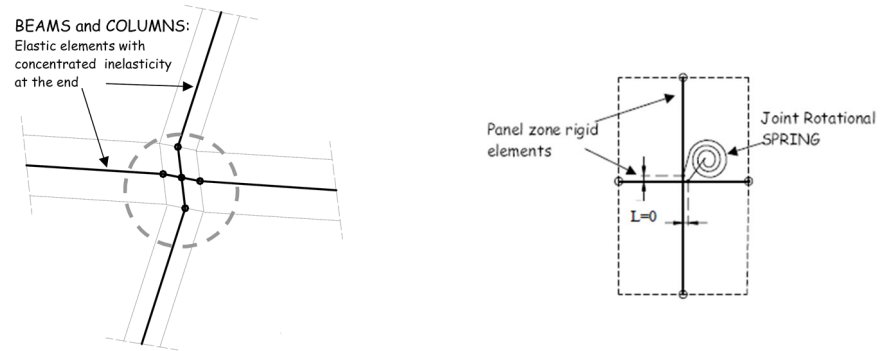
Figure 38: Lumped plasticity approach (Calvi et al., 2002a).
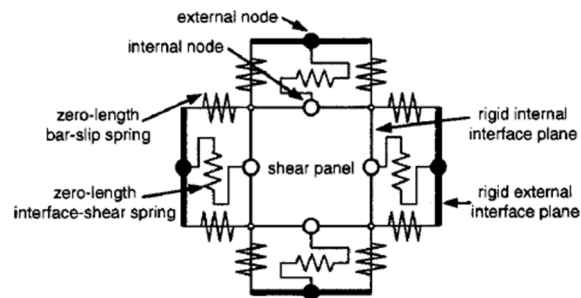
Figure 39: Multi-spring joint model: eight axial springs represent the anchorage slippage, four shear springs model the interface sliding and a rotational one simulates the joint shear deformation (Lowes and Altoontash, 2003).

A couple of axial springs at the member-joint interface can simulate the reinforcement bar bond-slip effect. In the same region a zero-length shear spring can model the interface shear behaviour. Finally, a zero-length rotational spring can simulate the joint shear deformation (Figure 39). The defect of this approach is that it requires the calibration of a several number of springs for each considered joint. Simplification are so suggested to it. For under-designed joints, it seems reasonable evaluate the overall storey drift accounting for joint shear deformation (Sharma et al., 2011). Therefore, the joint influence on the storeys lateral displacement can be represented as the sum of a rotational contribution (beam and column side) and of a horizontal displacement (due to panel shear deformation). The approach is schematized in Figure 40. A horizontal axial spring must be located at the column end, and a rotational one must be placed between the column and the beam. The former relates column shear force to column shear deformation. The latter schematizes a moment-rotation relationship. Note that the model approach only

accounts for joint shear deformation, the member non-linear behaviour must be modelled outside the joint region.

To avoid experimental based calibration, an analytical procedure to obtain the joint springs characteristics was presented (Sharma et al., 2011). The joint shear strength is calculated according to the PSL approach. Once the principle concrete stress versus joint deformation $p_t - \gamma_j$ relationship is defined (Calvi et al., 2002a; Priestley, 1997; Sharma et al., 2011), it is possible to calculate the column shear action and the beam bending moment by the joint equilibrium imposition. The adopted stress-strain relationships must represent the specific joint configuration in an adequate way. The authors (Sharma et al., 2011) analysed the case of non-confined panel region with top bent-in deformed rebar and bottom reinforcement adequately anchored (Figure 40.c) or not (Figure 40.d).

More complex method (like finite element analysis) are able to consider several aspects of the non-linear response of the joint region. On the other hand, they are time-demanding in their construction and they require a significant effort during the numerical analysis. Because of this it is rational not to consider them suitable for a seismic assessment of a structure.

According to the aim of this work, in the following are discussed in the detail the approach proposed for the modelling of non-detailed GLD frame joints (Calvi et al., 2002a; Metelli et al., 2015; O'Reilly and Sullivan, 2017). Longitudinal reinforcement crossing the panel region and beam hook-end anchored in the joint region are considered. Smooth reinforcement is obviously treated. The considered models are based on lumped plasticity approach; hence, the proposal regards the definition of a moment-rotation relationship $M - \theta$. This must be associated to a zero-length spring located between the beam end node and the column. The analysis of the joint strength capacity has been already outlined in Section 2.4. The attention is herein put on the deformation level related to the reach of specific Limit States (different damage amplitude). The hysteretic rule associated with the cyclic response of the joint is also discussed.
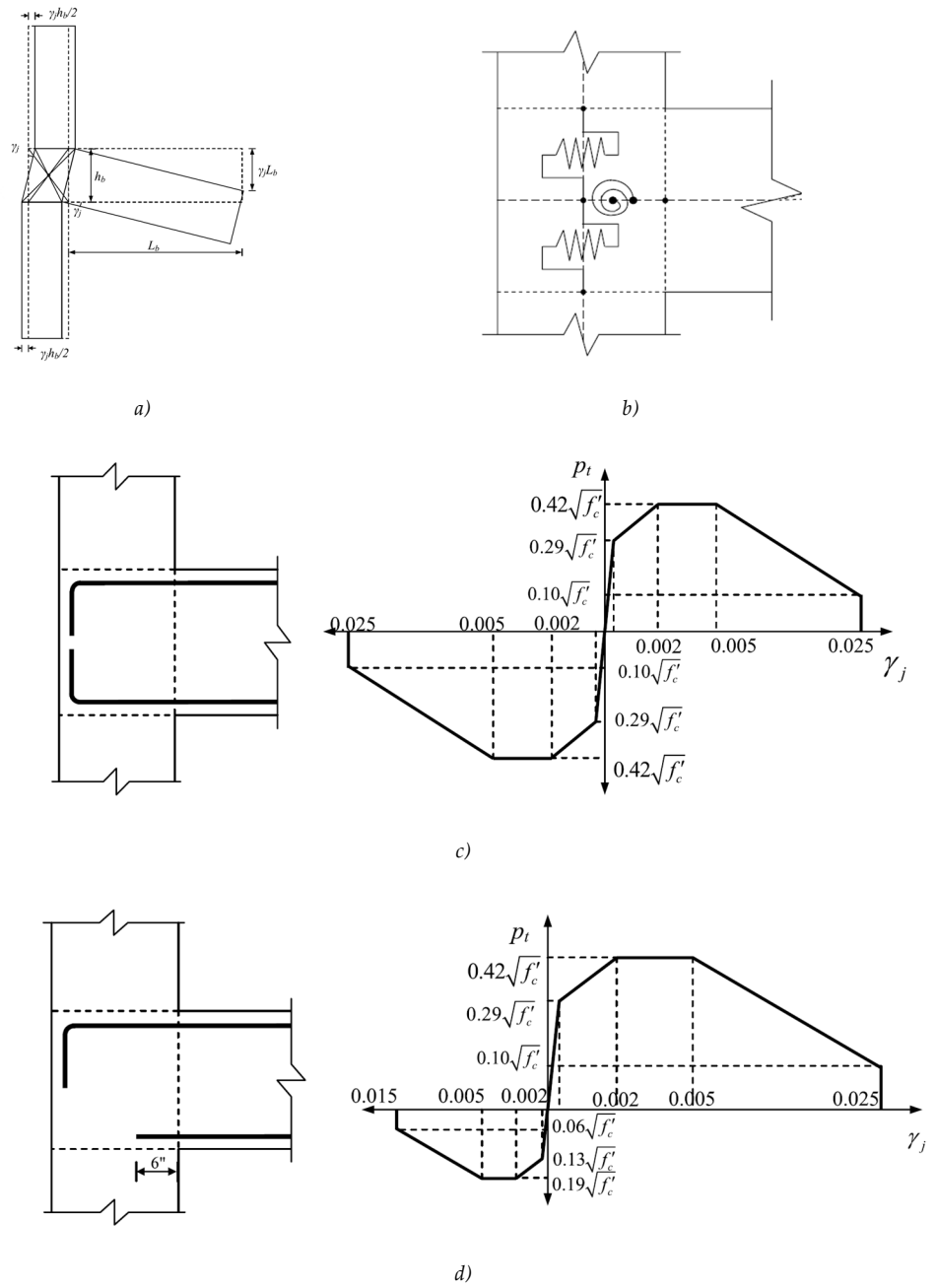
Figure 40: Joint shear deformation effect on a T-joint sub-assemblage a) and relative modelling philosophy b). Concrete principal stress versus deformation relationships for specific beam reinforcement arrangements c) and d)
(Sharma et al., 2011).

In the lumped plasticity approach, the reference relationship between the joint shear strength (expressed in term of principal stresses) and the joint shear deformation γ_j is translated in an equivalent joint moment-rotation behaviour (Calvi et al., 2002a). The assumption is founded on the concept that the joint shear deformation corresponds with the joint hinge rotation. The model defined for the case of plain reinforcement is an extension of the previous suggestions directed to joint with deformed rebar (Priestley, 1997). A comparison between them is reported in Figure 41, with specific application on an external joint. T-joint shear reference strength is associated with the first panel diagonal cracking ($p_t = 0.20\sqrt{f_c}$). For the interior connections a higher value ($p_t = 0.29\sqrt{f_c}$) is suggested for the first cracking, and a hardening branch up to a principle stress $p_t = 0.42\sqrt{f_c}$ reflects their higher shear strength prior to the joint fail (Calvi et al., 2002a). The assumed skeleton curves are reported in Figure 42. Regarding the value of deformation capacity, they are defined only for the exterior joints case (Pampanin et al., 2003). These limits are calibrated on the experimental evidences already discussed (Pampanin et al., 2002). Four different limit states are considered (Table 4). Although the experimental evidence showed a strength degradation after the cracking (Figure 41.b), the proposed model shows a ductility capacity in term of join rotation (Figure 42). Hence, the deformation capacity must be limited by the suggested value of the equivalent hinge rotation at the incipient collapse. The hysteretic behaviour is not mathematically defined; however, a rule able to represent the pinching effect related to smooth rebar slippage and the panel shear cracking effects is suggested (Pampanin et al., 2003).

a)

b)
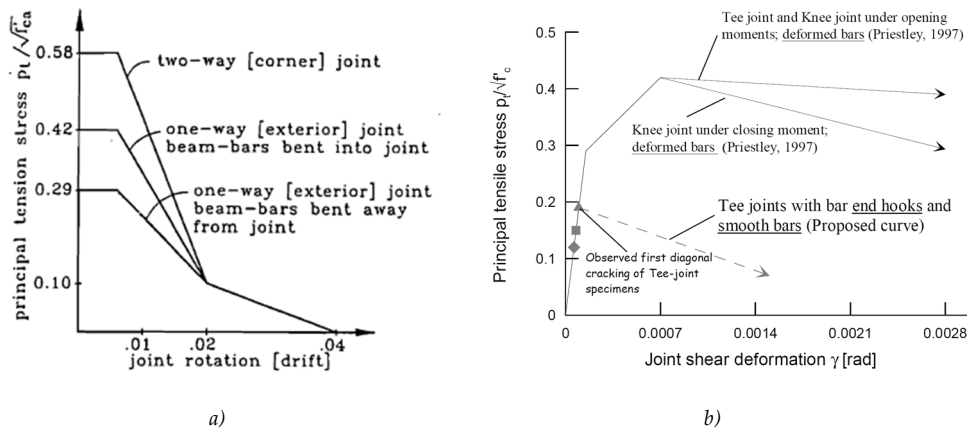
Figure 41: Original PSLM proposal for non-confined joints strength capacity a) (Priestley, 1997) and comparison with the application for smooth reinforcement with hook-end anchorage b) (Pampanin et al., 2002).
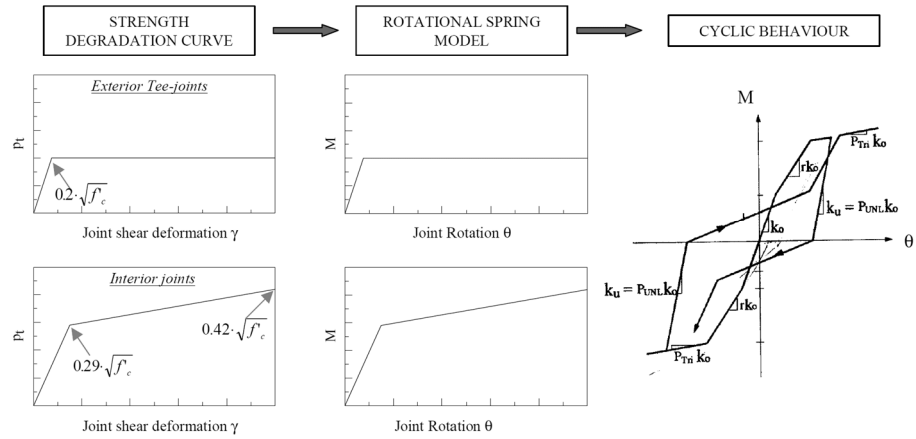
Figure 42: Modelling concept for joint shear behaviour, (Calvi et al., 2002a; Pampanin et al., 2003a).

A more recent similar approach accounts for more experimental evidences (O'Reilly and Sullivan, 2017). Both principle concrete stresses and limit state deformation levels are calibrated by a statistical fitting on 10 experimental tests on T-joint specimens, which arrangement was consistent with the peculiarities of the GLD structures. Contrary to the indication of the previous analysed model (Pampanin et al., 2003; Priestley, 1997), the beam shear contribution is added to the definition of the normal stress acting in the joint (O'Reilly and Sullivan, 2017; Sharma et al., 2011). This results in a different set of coefficients representing the joint shear strength. The main introduction of this proposal is related to the consideration of the strength degradation. Its representation is based on the fitting of the cyclic response of the reference specimens. The difference with the other suggestion (Pampanin et al., 2003) is shown in Table 4.

Limit state	(Pampanin et al., 2003)		(O'Reilly and Sullivan, 2017)	
	k	γ	k	γ
Cracking	0.200	0.02e-2	0.135	0.02e-2
Extensive damage	0.200	0.50e-2	0.135	1.27e-2
Critical damage	0.200	1.00e-2	ND	ND
Incipient collapse	0.200	1.50e-2	0.050	2.00e-2

Table 4: Backbone curve definition for the GLD frame T-joint modelling in term of principle tensile stresses (PSLM model) [$p_t = k\sqrt{f_c}$] and relative deformations [radians].

Respect to the joint models presented till now, a more detailed insight through the mechanisms that characterize the joint panel deformation is proposed by the means of a component-based model (Metelli et al., 2015). A multi-spring representation is considered (Figure 43). The joint panel shear deformation is divided from the contribution due to the relative rotation that develops at the joint-member interface. Only external T-Joints are considered. The model provides a rotational hinge placed between the beam end and the column axis, to represent the panel shear strength and stiffness. Other three rotational springs are instead located at the beam- and column-joint interfaces; these represent the deformation increment due to the reinforcement slip into the panel region. The main difference with the other proposal (above discussed) is the model definition on mechanical concepts. No statistical calibration is required, and the representation can be suitable for the application on different joint geometry and reinforcement arrangement.
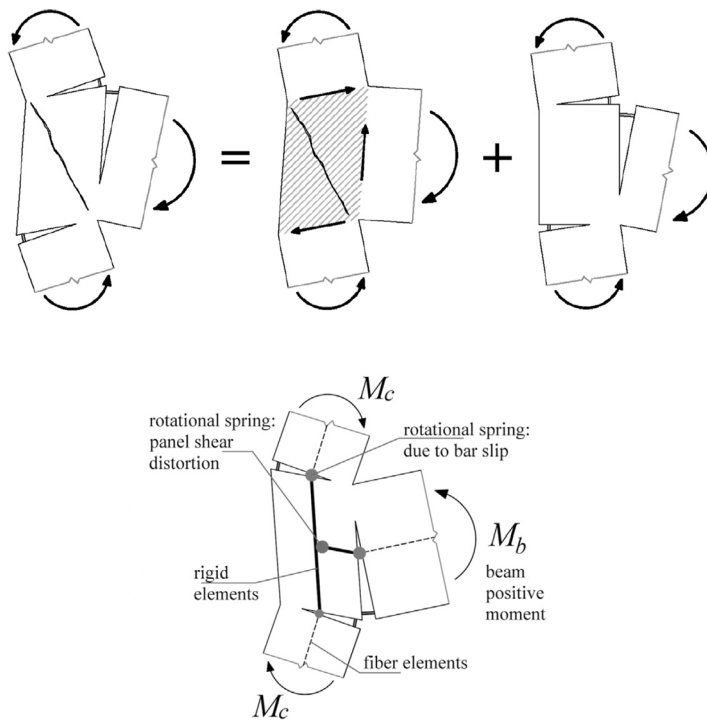
Figure 43: Component based modelling of a joint: division between joint panel shear deformation and interface rotation due to anchorage bond slip in the joint region (Metelli et al., 2015).

The joint shear strength is calculated with the MSSTM, previously discussed (Section 2.4) and the relative deformation are obtained with a geometrical vision on the panel deformed shape (Figure 44.c). By the combination of the horizontal γ_h and vertical γ_v shear distortion, the deformations of the joint panel at the peak force and at the ultimate state can be estimated as it follows. Remembering the steeper joint strut inclination proposed by the authors in Eq.(39-41):

$$\gamma_j = \gamma_h + \gamma_v = \frac{1}{2}(\bar{\varepsilon}_c + \varepsilon_t)(tan\,\theta_j + cot\,\theta_j) \tag{52}$$

$$\bar{\varepsilon}_c = \zeta\varepsilon_c \tag{53}$$
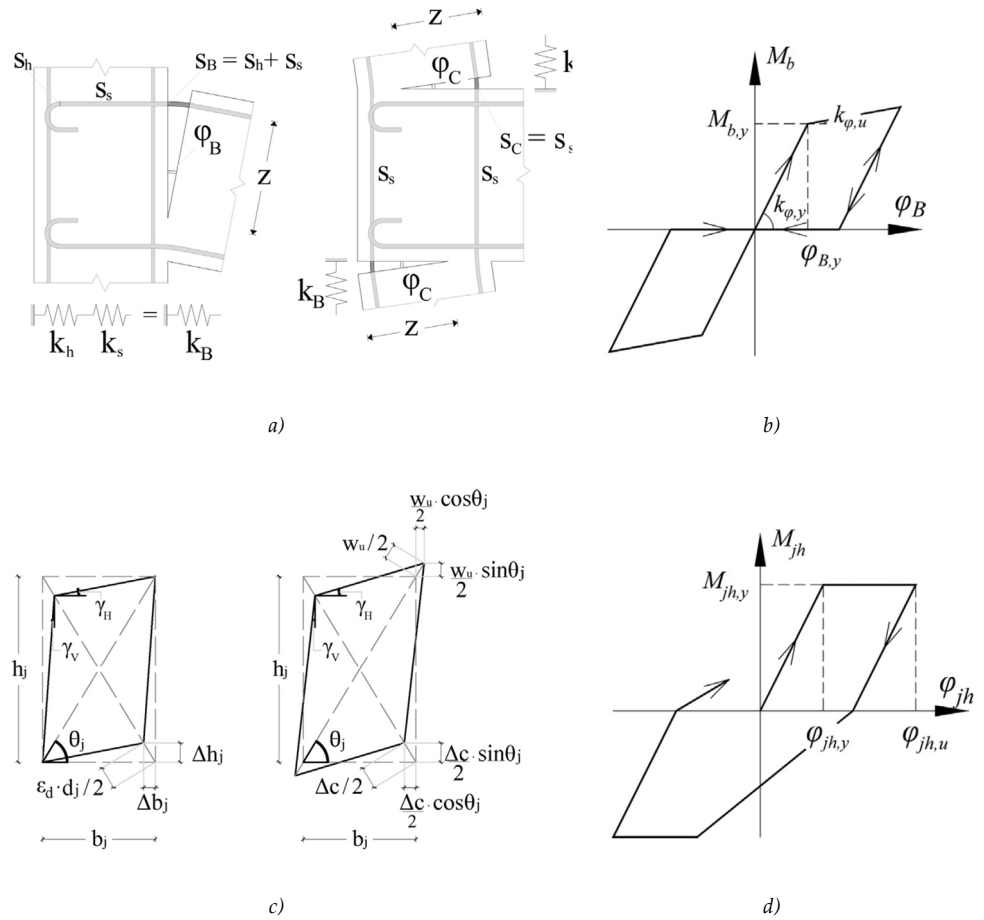
Figure 44: Slip deformation at the joint-member interfaces a), joint panel shear distortion c),and relative hysteretic rules for the modelling of the slip mechanism b) and of the shear one d) (Metelli et al., 2015).

63

According to the softened strut and tie model (Hwang and Lee, 1999), the concrete deformation can be expressed by the multiplication of the softening factor ζ and the reference uniaxial concrete strain (i.e. ε_{c0} at the peak strength and ε_{cu} at failure). Neglecting tensile strain in the elastic field and assuming (based on experimental evidences) a crack width $w_u = 2mm$ at the incipient collapse:

$$\gamma_{j,0} = \frac{1}{2}\zeta\varepsilon_{c0}\left(tan\,\theta_j + cot\,\theta_j\right) \tag{54}$$

$$\gamma_{j,u} = \frac{1}{2}\zeta\left(\varepsilon_{cu} + \frac{w_u}{d_j}\right)\left(tan\,\theta_j + cot\,\theta_j\right) \tag{55}$$

The shear strain at the peak strength and at the incipient collapse are finally defined by Eq.(54) and Eq.(55) respectively. Note that the softening coefficient ζ is found to be close to the value $\zeta = 0.55$ for all the specimens analysed (Metelli et al., 2015).

On the other hand, the bond-slip components are calculated by the imposition of the bar equilibrium between axial and bond stresses. Rigid-plastic relationship for the bond-slip mechanism is assumed. Beam rebar hook-end is considered with an axial bi-linear spring which stiffness is fitted on experimental results, as it is outlined in Section 2.1 and visible in Figure 12. To simplify the modelling, the uniaxial bar-slip relationship is then transformed in a moment-rotation element, with reference to the cross-section geometry of the column and the beam elements.

An example of the beam and column bar stress at failure is shown in Figure 45. It is worth noting that the model (Metelli et al., 2015) assumes that the bond stress is capable to equilibrate the reinforcement axial stress in the only joint height (Figure 45.b). This is doubtful, since the smooth rebar bond performance is very poor and the inadequacy of the straight length anchorage in the panel zone is well outlined in the literature (Braga et al., 2012; Calvi et al., 2002a; Fabbrocino et al., 2004).

Regarding the cyclic behaviour of both the mechanisms, the use of a bilinear slip rule and oh the Takeda rule are suggested for the bar-slip and the panel shear behaviour representation (Metelli et al., 2015). The first hysteresis (Figure 44.b) presents an elastic field followed by a little hardening up to failure. The unloading stiffness is equal to the loading one, hence in-cycle strength and stiffness degradation are not considered. On the other hand, cyclic degradation is implicit in the slip rule. The Takeda hysteresis (Figure 44.d) presents a backbone curve with an elastic field up to a moment equivalent to the joint shear strength, and a successive perfect plastic branch. Also, in this case no strength degradation is modelled, but the hysteretic rule account for cyclic stiffness degradation. The reloading is indeed directed to the point of maximum deformation reached at the previous cycle. Both the chosen hysteretic rules provide a global joint response characterized by pinching, due to anchorage bar slippage and to the joint cyclic degradation.

Modelling of a frame structure

The herein proposed joint modelling is independent from the non-linear behaviour of the member concurring in. Some authors choose to model only members fix-end rotation due to the additional deformation in the joint panel caused by the longitudinal rebar slip (Cosenza et al., 2002; Melo et al., 2011). The addictive deformation component is then modelled in the member-joint interface providing an additional rotation in the beam and column ends. The component based model above presented (Metelli et al., 2015) could result a way to account for this. The approach neglects joint panel cracking, hence also the shear failure of the joints. The significance of modelling the joint shear strength is though clearly outlined by the analysis of the seismic response of multistorey frames (Calvi et al., 2002a; Cosenza et al., 2002; O'Reilly and Sullivan, 2017).

a)   *b)*
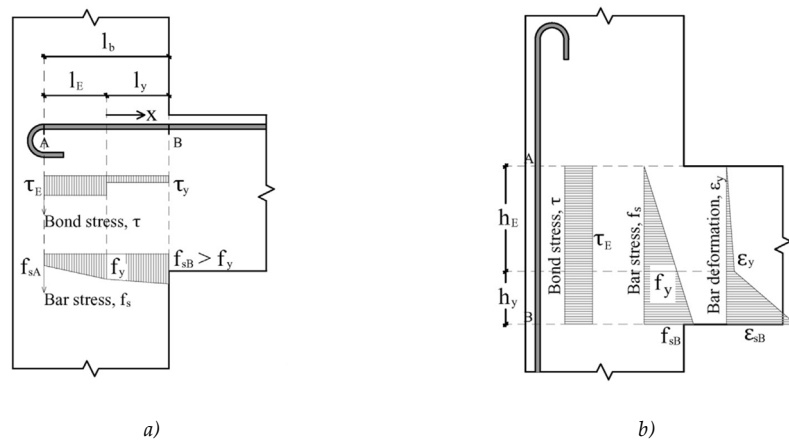
Figure 45: Bond and axial stress distribution on the beam a) and column b) rebar into the joint region; (Metelli et al., 2015)

The failure of the external T-joints allows a redistribution of the deformation demand on the lower and upper inter-storey, thanks to the formation of a shear hinge that inhibits increment of column flexural deformation demand. A structure with many deficiencies in the detailing can fail not necessarily in the most predicted non-ductile mechanism (O'Reilly and Sullivan, 2017). The joint deformation can indeed alter the global structural behaviour. The relevance to adopt an adequate modelling technique, account for joint strength and deformation, is visible in the comparison of Figure 46. It is clear that a simulation pursued with a standard fibre model do not represent the real (Calvi et al., 2002b) structural response; indeed, it does not account for the joint shear behaviour. On the other hand, a lumped plasticity technique accounting for joint shear behaviour (O'Reilly and Sullivan, 2017) can catch the structural response.
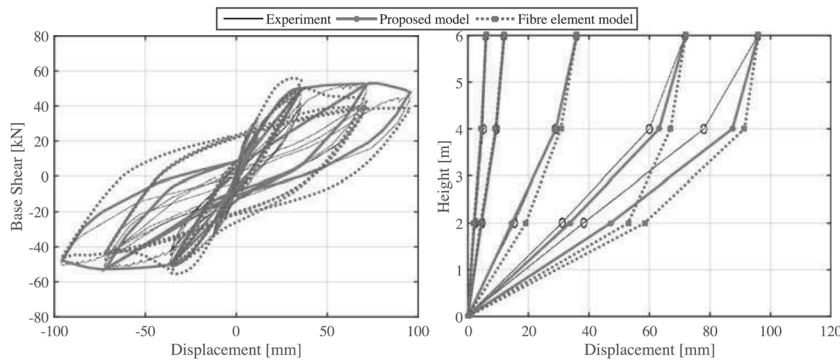
Figure 46: Comparison between a classic fibre model and a lumped plasticity one which account for joint shear behaviour (O'Reilly and Sullivan, 2017): application to an experimental test GLD frame (Calvi et al., 2002b).

It can be noticed that a fibre-based modelling results in a different prediction of the initial elastic response (Cosenza et al., 2002). A different evaluation of the structural stiffness could so affect the lumped plasticity models prediction. In Figure 47.a is visible the comparison between the prediction obtained from DRAIN-2DX (Prakash et al., 1993) lumped plasticity model and a fibre-based approach (Cosenza et al., 2002). The former is clearly stiffer. With reference to the same regular under-designed RC frame (Cosenza et al., 2002), the role of the reinforcement typology (smooth or deformed bars) is also shown (Figure 47.b). Note that the drift capacity of the structure reinforced with smooth bars is greater. This is true only in presence of adequate anchorage of the plain rebar (i.e. hook-end). Effect of bond-slip phenomena are also demonstrated by the authors with reference to building dynamic response (Magonette et al., 2004).

a)   b)
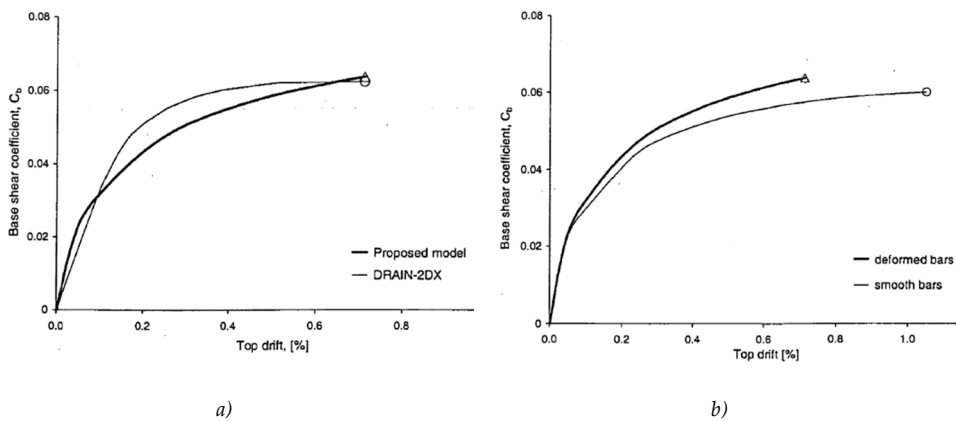
Figure 47: Assessment of an underdesigned real building with pushover analysis: influence of the modelling technique a) and of reinforcement type b); (Cosenza et al., 2002).

2.6 Shear transfer across cracks through dowel mechanism

In the previous section the behaviour of RC members and of their connection has been investigated in the detail. Their non-linear response under cyclic loading is clearly underlined, and it results characterized by strength and stiffness degradation, due to different several causes. Plastic hinge formation under bending action and joint shear mechanism have been presented, with particular attention to the elements reinforced with plain rebar. Little attention has been instead oriented to beam and column capability to transmit their shear action to the joint panel, across member-joint interface. Earthquake motion causes the opening of crossing cracks in the frame elements. Shear transfer across these is mainly governed by the concrete friction and interlocking, and by the longitudinal reinforcement (Hofbeck et al., 1969; Maekawa and Qureshi, 1997). The former mechanisms are though subjected to cyclic degradation, since concrete spalling and crushing affects the cyclic response of RC members, and general degrading is noticed. Therefore, concrete effectiveness in shear transfer across cracks can be debatable, and the dowel effect of the longitudinal reinforcement can assume a prominent role. Experimental results on members reinforced with plain rebars showed uplift at the columns base (Verderame et al., 2008a), squat beams sliding failure (Marefat et al., 2009) and frame beam elongation under cyclic actions. Hence the possibility to transfer shear action across a completely opened crack is to be considered. In this case, the dowel action is the only resistant mechanism

In the following a brief State of Art about dowel mechanism is presented. It was studied by the means of analytical (Gelfi and Giuriani, 1987; Vintzēleou and Tassios, 1986), experimental (Brenna et al., 1990; Dei Poli et al., 1992; Dulacska, 1972; Hofbeck et al., 1969; Soroushian et al., 1986; Vintzēleou and Tassios, 1987) and numerical tools (El-Ariss, 2007; He and Kwan, 2001). The concept is then extended to the case of rebar subjected both to shear and axial load, to understand the real dowel mechanism capacity in presence of coupled and cyclic axial and shear actions (Maekawa and Qureshi, 1996a, 1996b; Moradi et al., 2012; Soltani and Maekawa, 2008; Xu et al., 2014). All the presented works are relative to deformed reinforcement. Indeed, according to the author knowledge, the dowel mechanism is not treated in the literature. At the sectional level the coupled action effects could be the same; on the other hand, the damage induced in the surrounding concrete by the deformed bar ribs under pull-out action can significantly affect the shear resisting mechanism. A difference in the dowel capacity of smooth bar can so be expected.

Shear transfer in a cracked section

Element capacity to transmit shear action on a pre-existing plane (shear transfer) was originally investigated with attention to connection between cast-in-place and pre-

cast structure. Nowadays the same theme results however of great interest since cracks opening characterize every RC structure. 38 push-off specimens (Figure 48.a) were tested in absence of external force normal to the surface (Hofbeck et al., 1969). They were characterized by the presence or not of a pre-existing crack on the shear plane, by different dowel reinforcement amount and grade, and by different concrete strength. The dowel action of the reinforcement crossing the crack was inhibited or not. By the application of a sliding on the shear plane, it was concluded that:

- pre-existing cracking cause lower strength and higher slip in the shear transfer mechanism;
- the reinforcement transversal to the shear plane influences the mechanism only by its confining capacity (expressed in term or reinforcement ratio and yielding capacity), and not by its layout (i.e. steel type, bar diameter and spacing);
- the concrete strength improves the mechanism resistance, and it fixes an upper limit to the confinement level effectiveness;
- the dowel effect plays a significant role in shear transfer on a pre-cracked element (20÷30% of the total strength in absence of transversal load).

Concerning the dowel effect of crossing reinforcement, two mode of failure can be observed:

- crushing of concrete and yield of the reinforcement;
- concrete splitting.

The development of the first or the second failure mechanism is mainly governed by the confinement due the presence of transversal reinforcement, and by the distance between the dowel and the element edge (i.e. concrete cover). Experimental test can be used to set a minimum distance over which the failure is governed by the former ductile mechanism, which comprehension can be based on mathematical models. Empirical formulations are instead available for the latter. A short literature review on the topic (Vintzēleou and Tassios, 1986) and a specific experimental campaign (Vintzēleou and Tassios, 1987) showed that concrete cover from 6 to 8 times the bar diameter avoid splitting failure mode. The shown limit to the splitting failure is larger than the common value of longitudinal reinforcement concrete cover; furthermore, adequate stirrups spacing to avoid splitting failure is not common in non-conforming existing elements. Because of this, in presence of cyclic excitation, sliding resistance provided by the dowel mechanism can be related only to the rebar which act on the concrete core, neglecting the ones that act on the cover. Only literature reference on dowel mechanism in absence of splitting failure are herein presented.
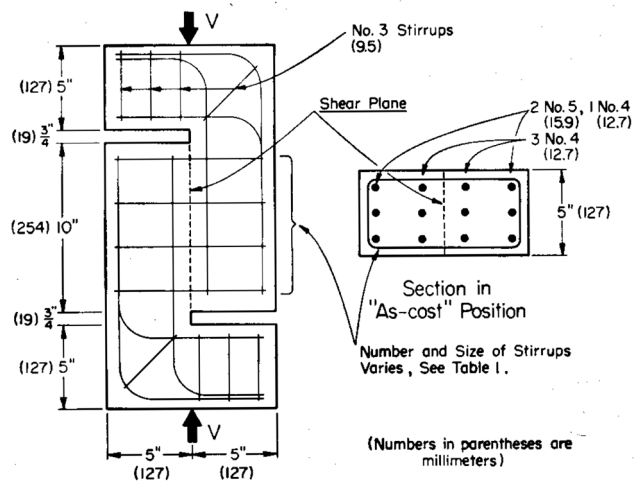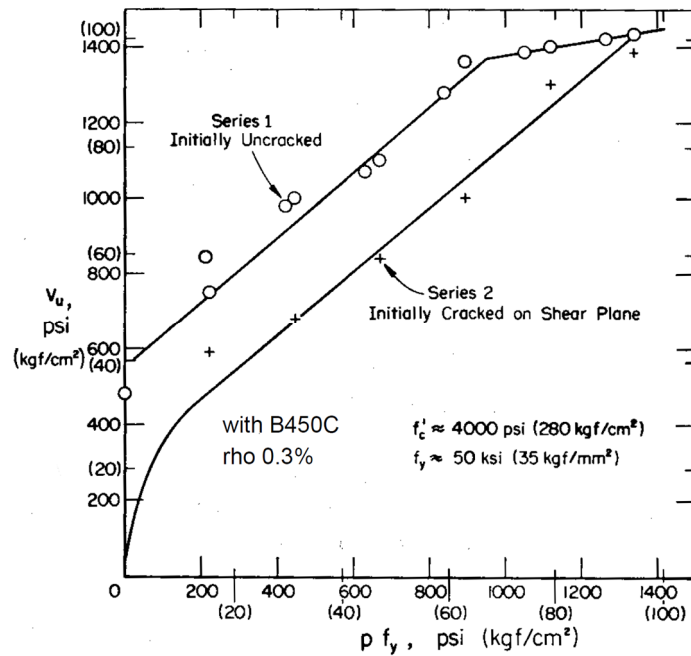
Figure 48: Push-off specimen a) and results on companion samples with and without pre-existing crack b) (Hofbeck et al., 1969). Ultimate shear stress versus mechanical transversal reinforcement ratio is considered for the plot.

Beam on Elastic Foundation (BEF) model

The classical model of the Beam on Elastic Foundation (BEF) (Timoshenko and Lessels, 1925) is herein summarized. To approach a rebar that crosses an RC crack, the reference scheme is the one in which a semi-infinitely beam is eccentrically loaded on its end. An eccentricity equal to $a = w/2$ is considered, with w crack opening. A schematization of the reference scheme is shown in Figure 49, and a contextualization on a crack plane is visible in Figure 54.a. The model is based on completely elastic behaviour both for the beam (rebar) and the foundation (surrounding concrete). The former is identified by a flexural stiffness EJ, the latter is schematized with a series of vertical axial spring of stiffness k_t. Each spring is independent from the others and it reacts on the problem depth d_b with the following rule, where $y(x)$ is the beam deflection:

$$\sigma_t(x) = k_t y(x) \tag{56}$$
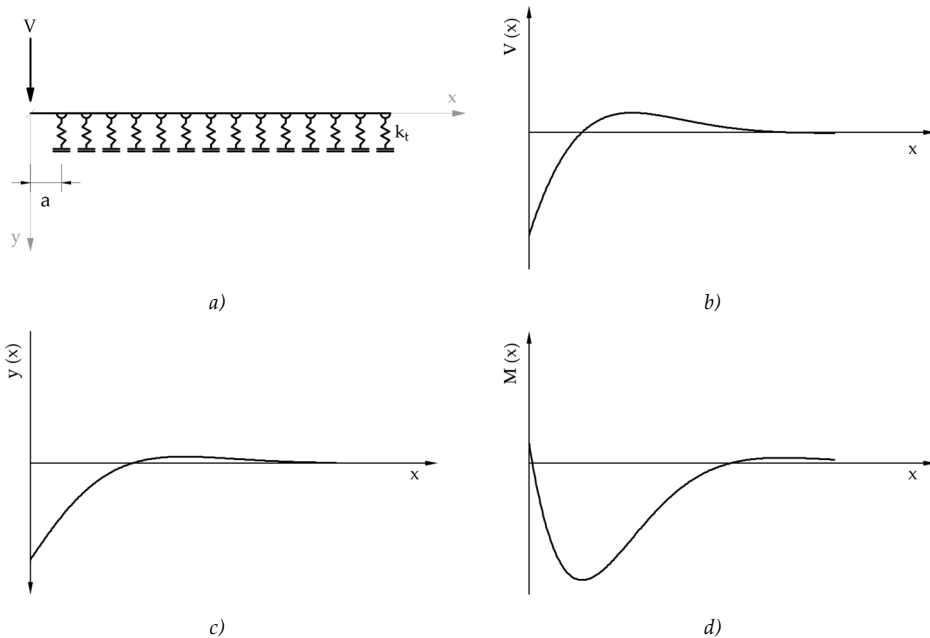
Figure 49: BEF model: schematization a) and example of deflection shape c), shear action b) and bending action d).

Ignoring the elastic shear deformation of the rebar, the solution of the classical problem is:

$$y^{IV}(x) + \frac{k_t d_b}{EJ} y(x) = 0 \tag{57}$$

Eq.(57) can be rewritten by the definition of the parameter that represents the ratio between the stiffness of the beam and the foundation soil:

$$\lambda = \left(\frac{k_t d_b}{4EJ}\right)^{\frac{1}{4}} \tag{58}$$

$$y^{IV}(x) + 4\lambda^4 y(x) = 0 \tag{59}$$

The analytical solution is:

$$\begin{aligned} y(x) = \\ e^{-\lambda x}(C_1 \sin(\lambda x) + C_2 \cos(\lambda x)) + \\ e^{\lambda x}(C_3 \sin(\lambda x) + C_4 \cos(\lambda x)) \end{aligned} \tag{60}$$

Four condition have to be imposed to solve the problem: i) null deflection at long distance from the load application point, ii) symmetry of the problem, iii) external bending (M) and iv) shear action (V) acting at the beam embedded length end. For the sack of simplicity, in the following is reported the analytical solution in absence of load eccentricity ($a = 0$). However, for the general case the solving is similar.

$$y(x) = \frac{2\lambda V}{k_t d_b} e^{-\lambda x} \cos(\lambda x) \tag{61}$$

Shear and bending actions are defined by the derivative of the deformed shape (Eq.(61)):

$$V(x) = Ve^{-\lambda x}(\sin(\lambda x) - \cos(\lambda x)) \tag{62}$$

$$M(x) = -\frac{V}{\lambda} e^{-\lambda x} \sin(\lambda x) \tag{63}$$

Finally the point and the value of the maximum bending moment is obtained by the imposition of null shear action:

$$x_{max} = \frac{\pi}{4\lambda} \tag{64}$$

$$M_{max} = M(x_{max}) = -\frac{\sqrt{2}V}{2\lambda} e^{-\frac{\pi}{4}} \tag{65}$$

For the analysis of the dowel behaviour of a bar embedded in concrete, the main issue results in the definition of the foundation modulus. To define it, an experimental (Dei Poli et al., 1992; Soroushian et al., 1987) and/or an analytical (Gelfi and Giuriani, 1987) evaluation is required. It is worth noting that the subgrade stiffness value was found to be very scattered and influenced by the magnitude of the action acting in the dowel (Dei Poli et al., 1992). Moreover, the validity of the model is restricted to the elastic behaviour, which can result not consistent with the analysis of cracked section in presence of significant load. The incapability of the model in predicting the dowel behaviour was explicated in the literature, because of the main role played by concrete and steel non-linear behaviour (Soroushian et al., 1986).

Experimental investigation on dowel acting on concrete core

The dowel contribution to the shear transfer across a crack can be evaluated by the inhibition of the concrete role in the experimental push-off test presented in Figure 48. A specific specimen with artificial crack, on which the friction is avoided by the interposition of brass sheets, is now considered (Dulacska, 1972). The crossing reinforcement is placed with an angle δ on the horizontal direction, thus the steel rebars are subjected both to tensile and shear load, due to their inclination. Different concrete grade, crossing rebar size, and reinforcement inclination effects are investigated. A total amount of 15 specimens were tested. The experimental results allowed to define formulations for the dowel strength and for the sliding evaluation on the shear plane. Set d_b the reinforcement diameter, f_c and f_y the concrete cubic strength and the steel reinforcement yielding stress, the followings were suggested (dimension in *in.* and *ksi*). Also, a possible presence of an axial force N in the dowel is considered.

$$\rho = 1 - \frac{4N}{\pi d_b^2} \tag{66}$$

$$V_u = 0.2\rho \, d_b^2 \sin\delta \left[\sqrt{1 + \frac{f_c}{0.03\rho f_y \sin^2\delta}} - 1 \right] \tag{67}$$

$$\Delta = \frac{3V}{d_b 10^6} \sqrt{\frac{1}{f_c} \tan\left(\frac{V}{V_u}\frac{\pi}{2}\right)} \tag{68}$$

V_u is the mechanism strength, V the actual shear acting on the plane, and Δ the relative sliding displacement. Note that with a null inclination (i.e. steel reinforcement normal to the shear plane), such as the case of longitudinal reinforcement in flexural cracks, the Eq.(67) can be rearranged in the following one (expression in MPa for sake of simplicity):

$$V_u = 1.27 d_b^2 \sqrt{f_c f_y} \qquad\qquad (69)$$

The above equation Eq.(69) is the most used for the classical dowel mechanism interpretation.

By the plot of the author original proposal of Eq.(67) an ellipse of a skew angle δ is obtained. This represents a dominion of the coupled axial and transversal loads acting on the reinforcement rebar, which crosses the shear plane by an inclination δ on its normal. With reference to Figure 50, the horizontal axis represents the shear load carried by the dowel mechanism, whereas the vertical one the shear resisted by the axial force in the same reinforcement rebar. Established a load pattern by the ratio between the two reference load types, a vector describes the reach of the failure point, which is identified by the couple of action $(T_f; N_f)$. This is obviously lower than the couple $(T_{f0}; N_{f0})$, due to the effect of the coupled action. T_{f0} is the dowel strength under pure shear load ($\delta = 0$) and N_{f0} is the rebar tensile axial load ($\delta = 90°$).

a)   *b)*
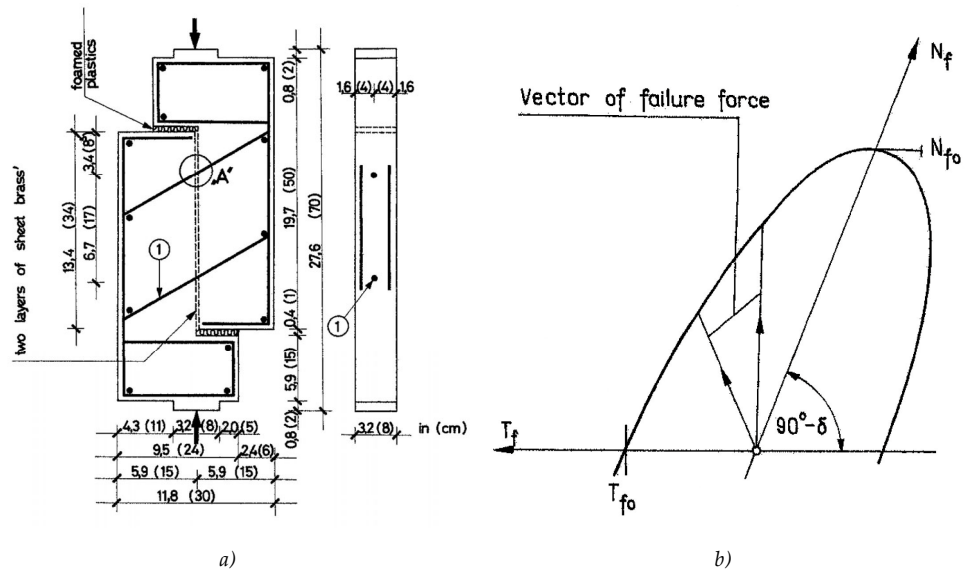
Figure 50: Push-off specimen in presence of a steel bar crossing the shear plane with an inclination δ a) and failure dominion b) for coupled shear T_f and axial N_f loads (Dulacska, 1972).

Further experimental tests investigated about the role of the dowel diameter (Soroushian et al., 1986). A range from 0.5 to 1.0 inch is considered. The maximum strength was exhibited before a split crack formation. It was in the plane formed by the dowel load and the dowel bar. After, the dowel mechanism response presents a resistance drop, which magnitude is proportional to the dowel rebar size. BEF model is used to give a mathematical base at the estimation of the mechanism strength. The

73

reference simplified scheme is reported in Figure 51. The calibration of the non-reactive concrete length c is required. It was done on literature available tests results (Dulacska, 1972) by the means of Eq.(70). With the proposed model the ultimate strength V_u can be estimated with Eq.(72). The distance L between the point of load application and the position of the plastic hinge formation (point of maximum acting bending moment) is derived by the BEF reference. The resistant flexural strength of the rebar $M_{b,y}$ accounts for the presence of axial load N; the approximated indication of Eq.(71) is considered. Finally, the inclination of the dowel rebar α is considered null.

$$c = \frac{0.05 f_y d_b}{f_c} \tag{70}$$

$$M_{b,y} = \frac{f_y d_b^3}{6}\left(1 - \left(\frac{4N}{f_y d_b^2}\right)^2\right) \tag{71}$$

$$V_u = f_{bc}\frac{(L-c)^2}{2} + \frac{M_{b,y}}{L} \tag{72}$$
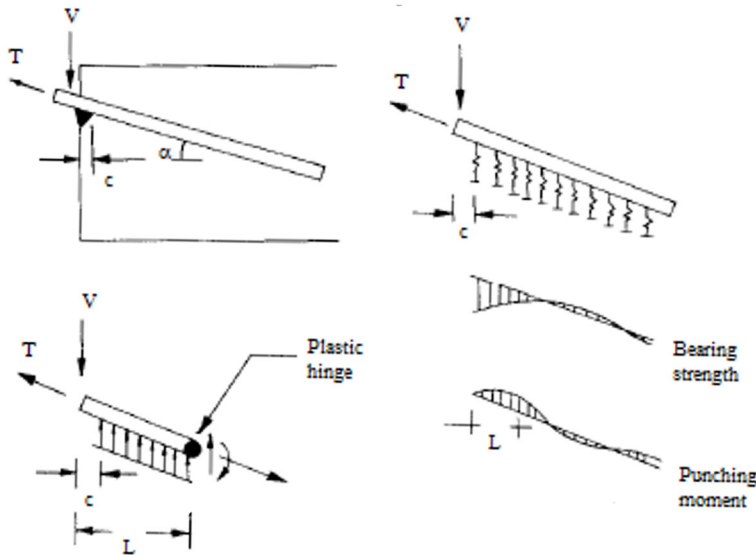
Figure 51: Schematization of the dowel mechanism referring to the BEF model (Soroushian et al., 1986).

The definition of the concrete bearing strength f_{bc} is required. It is dependent on several parameters. The influences on concrete strength f_c, rebar diameter d_b, rebar distance from the edge w, and normalized embedded rebar length l_1/l (where l_1 is the embedded bar length and l the length of the concrete block) were shown (Soroushian et al., 1987). The mathematical formulation of the proposal is expressed in Eq.(73). It is immediately clear how the bearing strength capacity increases with the increase of the concrete quality and with the decrease of the rebar diameter.

$$f_{bc} = 8 \left(\frac{w}{d_b}\right)^{\frac{1}{3}} \sqrt{f_c \frac{l}{l_1}} \qquad (73)$$

Successive works simplify the issue, by the attribution of a concrete bearing capacity equal to five times the concrete compressive strength. The approach is both theoretical (Vintzēleou and Tassios, 1986) and experimental (Biolzi and Giuriani, 1990). These values result higher than the previous (Dulacska, 1972) proposal ($f_{bc} = 4f_c$).

Cyclic test were very useful to understand the response of the dowel mechanism in presence of load reversal (Vintzēleou and Tassios, 1987). The specimen is represented in Figure 52.a. Concrete strength, rebar diameter, concrete cover and imposed load level influences were investigated. No transversal reinforcement is provided in the specimen. The experimental evidences showed a significant strength and stiffness degradation under cyclic loading. The former is observed to decrease in increasing number of cycles, and a stabilization is observed after 5 full reversal loading (see Figure 52.b). Cyclic residual strength can be evaluated to be the 70% of the initial resistance, whereas the in-cycle strength reduction shows a further reduction of the 70%. Therefore, it is possible to evaluate a residual strength V_{ur} equal to the half of the strength exhibited during a monotonic loading V_u:

$$V_{ur} \cong 0.7^2 V_u \cong 0.5 V_u^2 \qquad (74)$$

The stiffness degradation can be estimated in 50 percent after 10 reversal. As it is for other shear-sensitive mechanisms, low energy dissipation was measured during the test. The damping coefficient was found to be around 4.30%, the same decreased to the 60% of the initial one after only 3 reversal loading. Both strength and stiffness degradation can be considered independent from concrete cover, bar diameter and concrete strength. Repeated not reversal loading shows a lower magnitude of the phenomena.

a)   b)
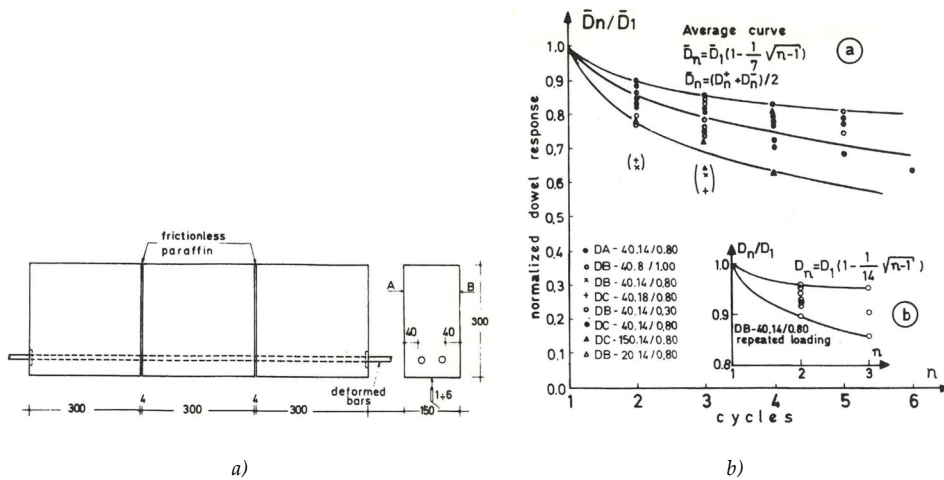
Figure 52: Reference specimen for dowel mechanism investigation under cyclic loading (dimension in [mm]) a) and experimental results in term of strength degradation b) (Vintzēleou and Tassios, 1987).

Dowel load-displacement constitutive relationship

One of the earlier predictive tools for the representation of the dowel mechanism was calibrated on experimental evidence. An empirical definition of the dowel mechanism in term of load-deflection relationships was proposed (Soroushian et al., 1986), with reference to 18 specimen data. It is based on the strength capacity of Eq.(72) and on the experimental calibration of the shear sliding values at the peak force. The suggested relationship is the following (*mm* and *MPa* units):

$$s_u = 2.43e^{-5}V_u + 0.24 \tag{75}$$

The model is also able to predict the resistance drop after split crack formation with a linear degrading branch. It is visible in Figure 53. In the same graphs it is also possible to observe the main role played by the bar diameter and by the axial load level on the mechanism ultimate load.

$$V = s_u \left(\frac{V}{V_u}\right)^{0.5}, \qquad s < s_u \tag{76}$$

$$V = V_u \left(1 - \frac{s - s_u}{0.4/d_b - s_u}\right) \geq 0.4V_u, \qquad s > s_u, \tag{77}$$
$$[lb, in]$$

76

An analytical suggestion was proposed to assess the dowel capacity in composite beams (Gelfi and Giuriani, 1987). This approach requires the equilibrium imposition on the schematization of Figure 54.d. Perfect elastic-plastic behaviour for both steel and concrete under local compression (Biolzi and Giuriani, 1990) were assumed. Furthermore, a simplified uniform radial distribution of the concrete bearing stress on the bar surface (Figure 54.c) is considered. The concrete balances the applied load on a length L_{eff}, which is the distance between the point of maximum bending action in the rebar and the embedded end of it:

$$L_{eff} = -a + \sqrt{a^2 + \frac{d_b^2 f_y}{3 f_{bc}}} \qquad (78)$$

$$V_u = d_b L_{eff} f_{bc} \qquad (79)$$

where f_{bc} is the concrete bearing capacity. It is assumed according to experimental (Biolzi and Giuriani, 1990) and analytical (Vintzēleou and Tassios, 1986) evidence. A non-linear formulation of the mechanism load-deflection relationship is also proposed and validated by the same authors (Gelfi and Giuriani, 1987). It has the form of Eq.(80). The definition of the asymptotic strength value V_u and of the initial stiffness k are required. The former value is the one proposed by the authors in Eq.(79), the latter is analytical evaluated and simplified by the formulation in Eq.(81), where E_c is the concrete elastic modulus.

$$V = V_u \left[1 - e^{-\frac{k}{V_u} \Delta} \right] \qquad (80)$$

$$k \cong 0.5 E_c d_b \qquad (81)$$
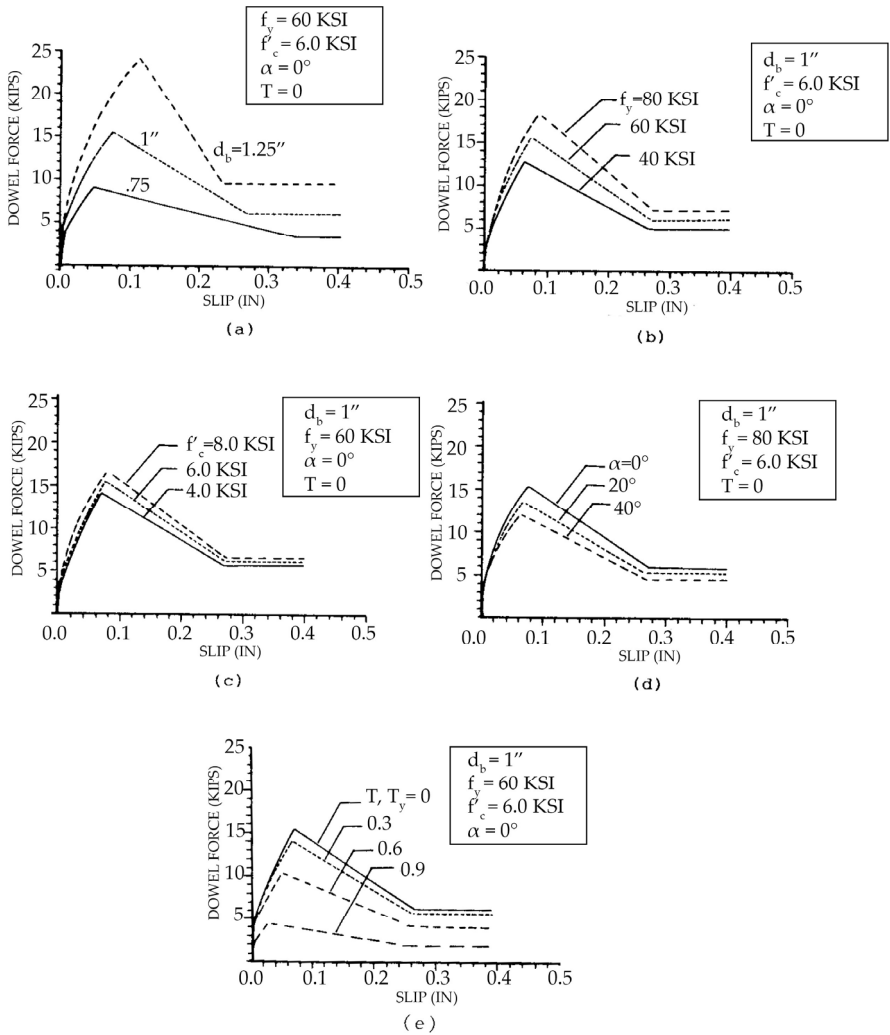
Figure 53: Dowel load-deflection model results varying rebar diameter a), yield strength b), concrete strength c), dowel inclination d), and axial load e) (Soroushian et al., 1986).
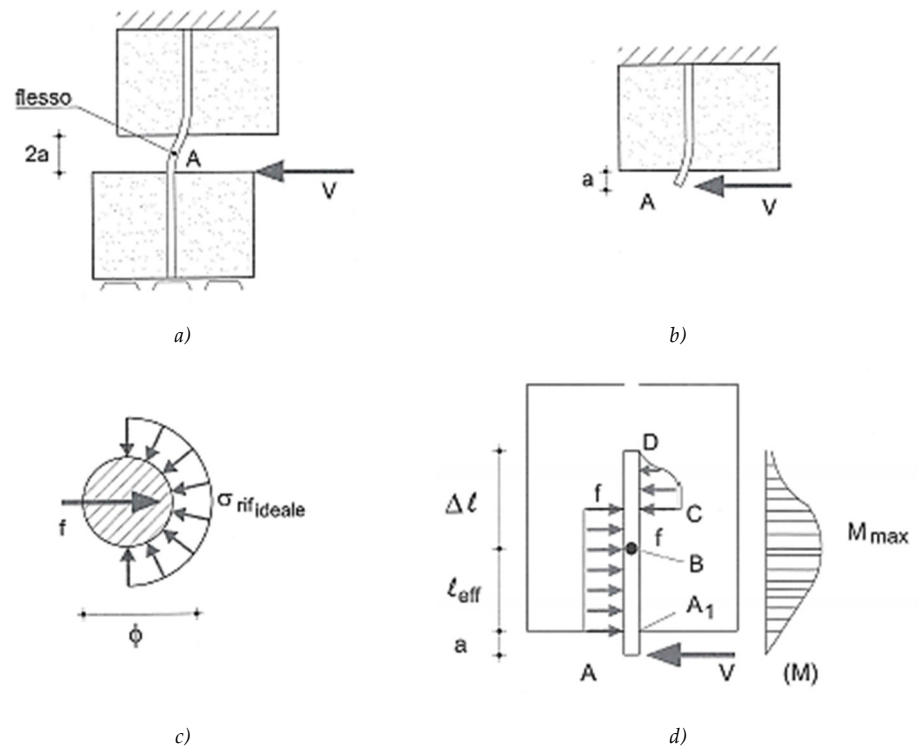
Figure 54: Physical model of a bar crossing a crack subjected to relative sliding on its faces a), simplification due to proble 79ymmetry b), concrete bearing stress assumption c), and model to estimate the dowel capacity of rebar dowel mechanism (Gelfi and Giuriani, 1987; Giuriani, 2012).

The soil stiffness to implement in a BEF model can be related to the rebar diameter and to the concrete strength (Soroushian et al., 1987):

$$k_c = 127 \frac{f_c}{d_b^{\frac{2}{3}}} \tag{82}$$

The values derived from Eq.(82) are found to be very close to the experimental results with acting load near to the failure ($0.70V_u < V < 0.90V_u$) (Dei Poli et al., 1992). For low acting load the real stiffness is instead found to be way larger, over the double. On these basis it was suggested to model the subgrade stiffness k_t accounting for a damage index expressed in term of normalized load (Dei Poli et al., 1992). The proposal is reported in Eq.(83). The reference stiffness k_{ts} and the dowel strength V_u were adopted from literature reference, herein reported in Eq.(82) (Soroushian et al., 1987) and Eq.(69) (Dulacska, 1972).

$$k_t = \omega k_{ts} \tag{83}$$

$$\omega = \begin{array}{c} 2.12, \quad V/V_u < 0.4 \\ \{0.544 + 0.026\,cosh[8(V/V_u - 0.4)]\}^{-\frac{4}{3}}, \quad V/V_u > 0.4 \end{array} \tag{84}$$

An alternative way considers a damage index dependent on the ratio between the displacement and the bar diameter (W_1/d_b) (Brenna et al., 1990):

$$k_t = \omega k_0 \tag{85}$$

$$k_0 = 600\frac{f_c^{0.7}}{d_b} \tag{86}$$

$$\omega = \left[1.5\left(a + \sqrt{d^2(40W_1/d_b - b)^2 + c^2}\right)\right]^{-\frac{4}{3}}$$

$$a = 0.59 - 0.011f_c$$

$$b = 0.0075f_c - 0.23 \tag{87}$$

$$c = 0.0038f_c + 0.44$$

$$d = 0.0025f_c + 0.58$$
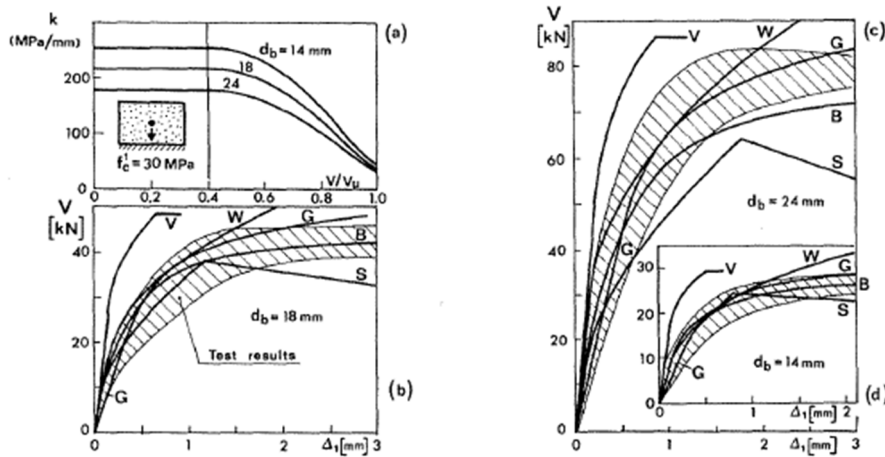
Figure 55: Subgrade stiffness versus dowel normalized load a), and suggested models for the dowel mechanism in term of load versus displacement b), c), d): (Dei Poli et al., 1992) (G), (Brenna et al., 1990) (B), (Vintzēleou and Tassios, 1986) (V), (Walraven and Reinhardt, 1981) (W) and (Soroushian et al., 1986) (S).

More recently, another formulation was suggested (Moradi et al., 2012). It compares the BEF elastic models with the consideration of the concrete damage (Soltani and Maekawa, 2008). It results:

$$k_s(\delta) = \begin{cases} 220f_c^{0.85}, & DI \leq 0.02 \\ \dfrac{220f_c^{0.85}}{[1 + 3(DI - 0.02)^{0.8}]^4}, & DI > 0.02 \end{cases} \tag{88}$$

where the damage index DI is expressed in term of normalized displacement:

$$DI = \frac{\delta}{d_b} \tag{89}$$

A representation of the cyclic dowel response was also suggested in the literature (Vintzēleou and Tassios, 1986). A qualitative schematization of the model is visible in Figure 56.a. The strength degradation is expressed as a function of the imposed number of cycles; the $n - th$ cycle loss of strength ΔV_u is normalized over the monotonic capacity V_u. It is function of the concrete Δf_c and steel Δf_y degradation. A fitting on the authors experimental campaign (Vintzēleou and Tassios, 1987) is then pursued, in absence of load eccentricity, and ignoring the steel contribution to the dowel strength degrade. The final formulations are:

$$\left(\frac{\Delta V_u}{V_u}\right)_n = \lambda\left[\left(\frac{\Delta f_c}{f_c}\right)_n + \left(\frac{\Delta f_y}{f_y}\right)_n\right] \tag{90}$$

$$\frac{V_n}{V_u} = 1 - \frac{1}{7}\sqrt{n - 1} \tag{91}$$

Based on new experimental responses of dowel rebars subjected to cyclic and repeated loading, a new more complex approach was followed (Moradi et al., 2012). A schematization of the non-linear load-deflection behaviour is reported in Figure 56.b. This last proposal was also extended to the more generic case of axial pull-out coupled with shear sliding action.

81

a)

b)
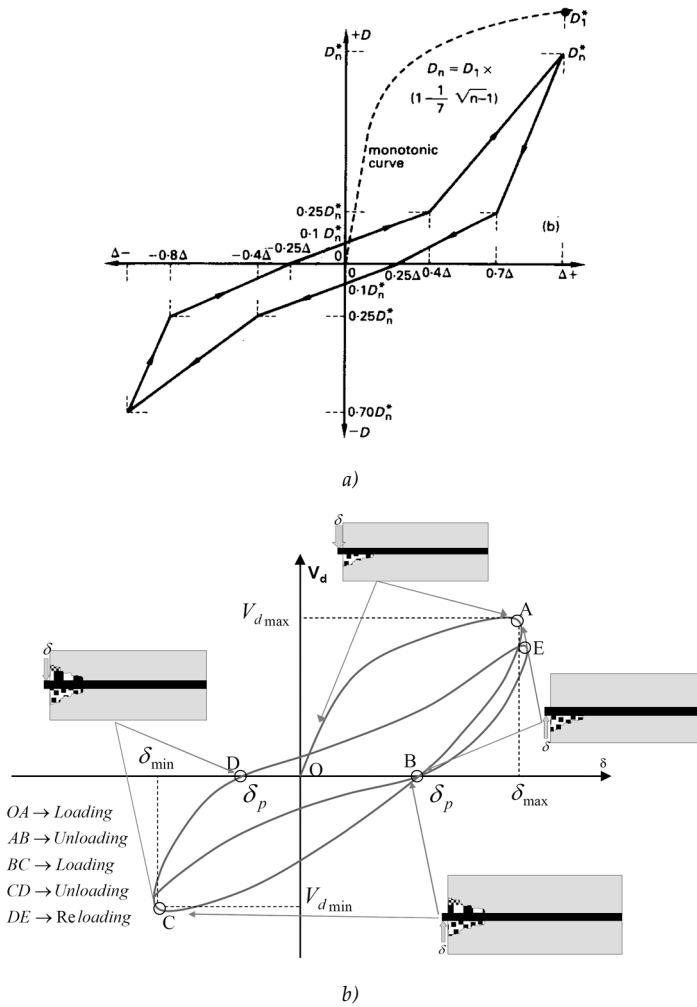
Figure 56 Formalistic model for the cyclic response of dowel in presence of cyclic loading (Vintzēleou and Tassios, 1986) and its recent update (Moradi et al., 2012) b).

Longitudinal rebar under coupled axial and shear action

The most comprehensive analytical tool to predict the dowel behaviour of a longitudinal rebar embedded in concrete is the BEF model. Its application clearly shows that the failure of the dowel mechanism is due to a formation of a plastic hinge in the rebar. The peak in the bending moment and in the relative curvature are located at a certain distance from the load application point (Figure 49). This concept is reiterated by the formulation of the dowel capacity available in the literature (Dulacska, 1972; Gelfi and Giuriani, 1987; Soroushian et al., 1986; Vintzēleou and

Tassios, 1986), which well predict the experimental results representing the mechanism with a limit-analysis application. Treating a flexural failure, it is very easy to understand that the presence of the axial stress in the rebar reduces the mechanism capacity. Furthermore, this was experimentally investigated (Dulacska, 1972) and analytical suggested (Soroushian et al., 1986; Vintzēleou and Tassios, 1987). A deep insight into the coupled action of rebar pull-out (axial mechanism) and transverse sliding (shear mechanism) on a crack was suggested (Maekawa and Qureshi, 1996a). The reference authors imposed a combined axial and transversal displacement path, with reference to the specimen represented in Figure 57. By the application of a shear load, the axial displacement is obtained thanks to the crack dilatancy in presence of rough surface or construction joint. Shear displacement, crack opening, rebar slip and local curvature were measured.

Figure 57: Specimen designed to account for coupled axial and shear load a) and its details in the crack zone b) (Maekawa and Qureshi, 1997, 1996a).

The effect of the coupled action is immediately understood by the analysis of Figure 58. The dowel rebar fails at an axial stress level lower than the yielding one, due to the coupled action effects. The sliding on the crack causes the curvature of the rebar, therefore a bending action act in it. At this point both longitudinal (slip S) and transverse displacement (sliding δ) increase. The reduction of axial capacity was found to be very correlated with the crack roughness and with the longitudinal reinforcement ratio. Indeed, it increases with the increase of both the parameters. No dependency on the rebar diameter was found. According to BEF model, the authors found a concentration of curvature demand out of the crack region; they also observed that the shear load effect is fulfilled in a bar embedded length equal to 5 times its diameter (Figure 58.c). In the crack region, the bar presents strain lower than the reference yielding ones; however, the computed axial stress was constant between the points of curvature peak, and they result lower than the yielding reference (Figure 58.d). It is also possible to observe that the damage in the crack zone, due to the pull-out mechanism of the deformed bar, causes a softening of the

mechanism. This could result in a loss of the stiffness in the shear resistant behaviour, with respect to the same in absence of axial load.

With base on the summarized observations, it is possible to conclude that the pull-out behaviour is significantly influenced by the imposition of a shear displacement along the crack crossed by the considered rebar. Therefore, the authors (Maekawa and Qureshi, 1996b) defined the pull-out and the dowel behaviour mutually interactive; furthermore, they propose an analytical model to account for this. The proposal is based on available bond-slip law (Shima et al., 1987), which accounts for concrete strength and bar diameter. The modifications to account for the coupled action are related to the local behaviour. They provide the definition of a bond deterioration zone and of a length of curvature influence. The first accounts for the concrete degradation near to the crack plane, by the consideration of a lack of bond capacity and a progressive linear tendency to the max value of resistant tangential stress (Figure 59.a). The second defines the length in which a proposed curvature profile is fitted on experimental tests. Furthermore, the latter parameter increases to account for a higher influence length due to higher applied load.

a)

b)

c)

d)
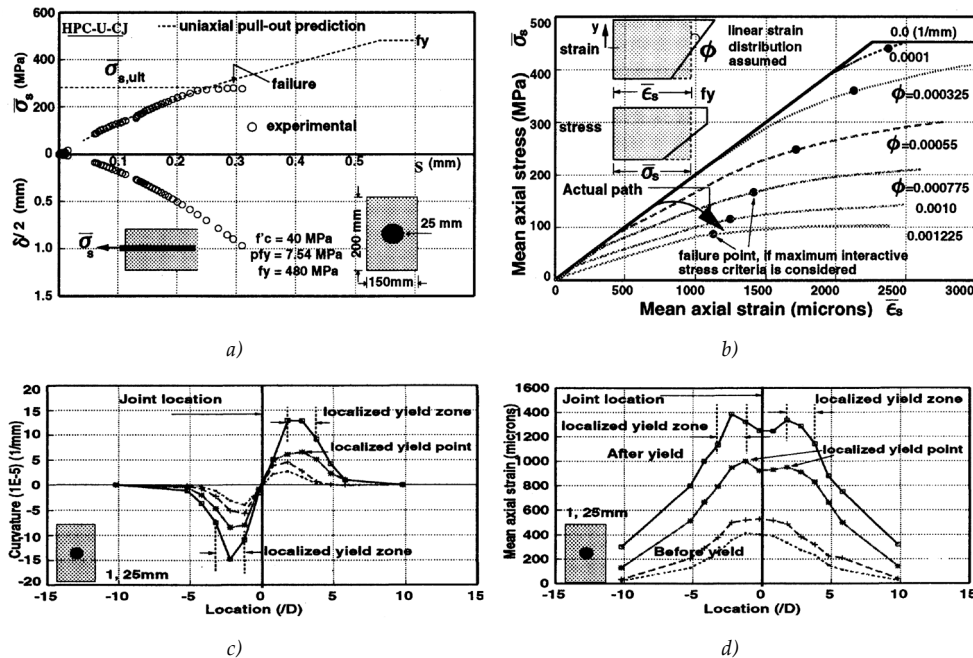
Figure 58: Experimental results in term of pull-out load versus bar slip on a specimen with smooth crack a), and general effect of induced curvature on a steel section subjected to axial stress b). Measured curvature profile c) and computed axial stress d) on the same specimen (Maekawa and Qureshi, 1997).

84

a)   b)
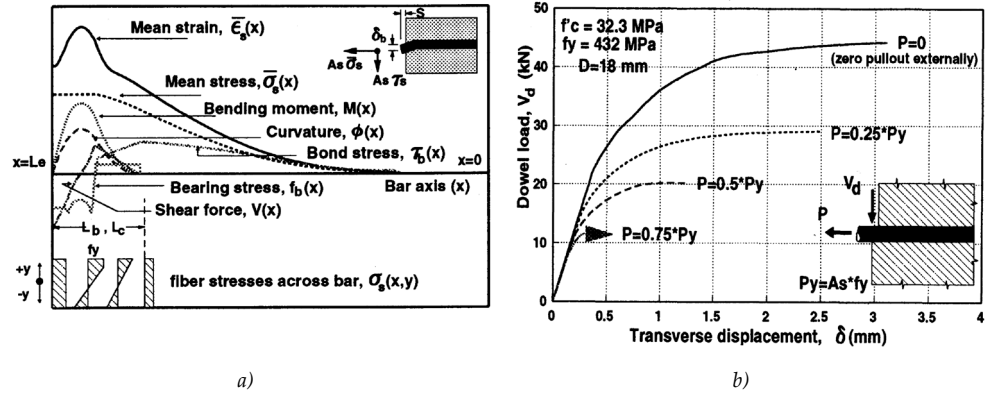
Figure 59 Proposal to account for axial pull-out and shear sliding on a crack, and influence of axial force on the dowel mechanism according to the authors analytical model (Maekawa and Qureshi, 1996b).

From a mathematical point of view, fixed a reference point $x = 0$ on the shear plane interface, the bond stress in the zone of bond deterioration L_b are defined as follows:

$$\tau_b(x) = \begin{cases} 0, & x < \dfrac{L_b}{2} \\ \dfrac{\tau_{b,max}}{L_b}x, & \dfrac{L_b}{2} < x < L_b \end{cases} \qquad (92)$$

Out of this zone the reference slip proposal (Shima et al., 1987) is adopted, with S bar slip, $c = 3$ and $k = 0.73$:

$$\tau_b(\bar{\varepsilon}_s;\ s) = \tau_{b0}(s)g(\bar{\varepsilon}_s) \qquad (93)$$

$$\tau_{b0} = f_c l\{ln(1 + 5s)\}^c \qquad (94)$$

$$g(\bar{\varepsilon}_s) = (1 + 10^5\bar{\varepsilon}_s)^{-1} \qquad (95)$$

$$s = 1000\frac{S}{d_b} \qquad (96)$$

Regarding the zone of curvature influence, it is defined with reference to the BEF model. The initial value L_{c0} is indeed defined by 3 times the distance of the maximum bending action defined by Eq.(64) in the classical model. This value is then extended by the definition of a damage index DI, function of the actual displacement δ:

$$L_{c0} = \frac{3\pi}{4}\left(\frac{4EJ}{k_t d_b}\right)^{\frac{1}{4}} \qquad (97)$$

85

$$k_t = \frac{150 f_c'}{d_b} \tag{98}$$

$$DI = \frac{1 + 150 S/d_b}{d_b} \delta \tag{99}$$

$$L_c = \begin{array}{l} L_{c0}, \quad DI \leq 0.02 \\ L_{c0}\{1 + 3(DI - 0.02^{0.8})\}, \quad DI > 0.02 \end{array} \tag{100}$$

Finally, the proposed curvature profile is defined:

$$\phi(x) = \begin{array}{l} -\dfrac{3\phi_{max}}{L_c^2}\left[3\left(\dfrac{L_c}{2} - x\right)^2 - L_c\left(\dfrac{3}{4}L_c - x\right)\right], \quad x \leq \dfrac{L_c}{2} \\[3mm] \dfrac{3\phi_{max}(L_c - x)^2}{L_c^2}, \quad \dfrac{L_c}{2} < x < L_c \end{array} \tag{101}$$

$$\phi_{max} = \frac{64\delta}{11 L_c^2} \tag{102}$$

Known the bond stress and curvature profiles, compatibility and equilibrium conditions must be imposed to compute the actual force in each rebar section. By the consideration of perfectly rigid-plastic material, the following dominion criterion can be used to find the section x in which the rebar fails:

$$\lambda(x) = \left[\frac{M(x)}{M_0} + \left(\frac{P(x)}{P_0}\right)^2\right] + \left[\frac{V(x)}{V_0}\right]^2 \tag{103}$$

where $M(x)$, $P(x)$, $V(x)$ are the actual value of bending moment, axial force and shear action; M_0, P_0, V_0 are the sectional capacity under non-interactive conditions. The reach of $\lambda(x) = 1$ proves the fail under coupled action, which is found to be always in the point of maximum curvature. The flexural mechanism is thus confirmed.

On the base of the presented model, an analytical proposal to account for the coupled axial and shear loading on the dowel behaviour was suggested (Moradi et al., 2012; Soltani and Maekawa, 2008). A constitutive relationship for cyclic and repeated loading was also proposed.

2.7 Infill-frame interaction

All the deformation capacities of RC frame elements and beam-column joints, above described, can be reached only in bare frames, where no limitation on structural displacements is imposed to them. In a common context, masonry infills are instead present on the facades and other masonry partitions are located in the internal space. With specific reference to the former, their use is due both to aesthetics and functional reasons. They are indeed able to guarantee internal privacy and good thermal and

acoustic insulation performance. Furthermore, the infill construction system results simple and cost-effective, it is thus largely employed in the building stock. In the Mediterranean area use of clay blocks (hollowed or not) is very widespread; in the United States concrete block are instead used in frame infilling, with the same aims previously presented. The response of an infilled frame subjected to in-plane loading is characterized by the interaction between the frame members and the masonry walls. The combined system response is different from the sum of its single components if they are considered independent to each other. Frame members are flexible, and they fail in combined axial and bending mechanism. On the other hand, the infill is extremely rigid, and its failure occurs in presence of very small displacement by cracking, shear mechanism or local crushing. The interaction between the infill panel and the surrounding elements results in a stiffer response and in different failure modes. Moreover, the brittle failure of the Un-Reinforced Masonry (URM) and the effect of the interaction increases in a significant way the vulnerability of the buildings, also in moderate earthquakes (Braga et al., 2009; Goda et al., 2015; Polese et al., 2015).

Behaviour of URM infills

Figure 60 shows a schematization of the behaviour of an infilled frame subjected to transversal loading. During the strongly non-linear response of the composite infills-frame system, the detachment of the panel from the adjacent members occurs in the corners under tension, whereas it is generally accepted that a compressive strut forms between the other two. In this context different failure modes of the masonry can take place. Examples are reported in Figure 61 for an in-situ campaign after the L'Aquila 2009 earthquake in Italy.

a)   *b)*
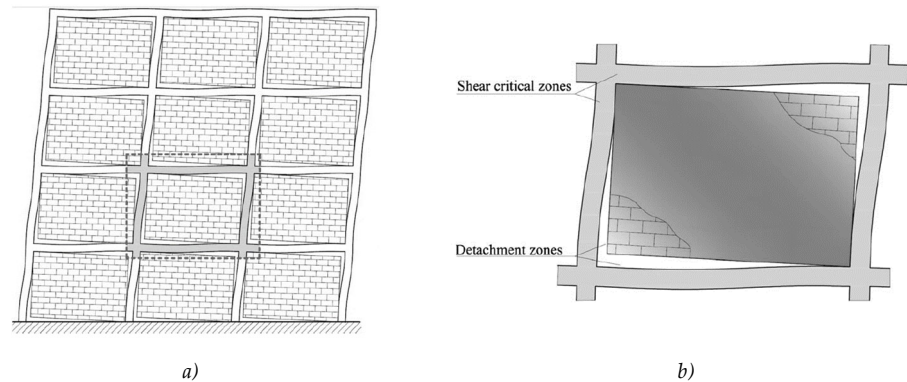
Figure 60: Deformed shape of an infilled RC frame subjected to seismic loads a) and particularization for a single bay b); (Cavaleri and Di Trapani, 2015).

a)   *b)*

Figure 61: Infills damage on buildings in L'Aquila (IT): external leaf expulsion after diagonal in-plane cracking a) and typical X shape cracks due to reversal loading effects b) (Verderame et al., 2009c).

The behaviour characterization of the URM panels is very complex, due to the heterogeneity of its single components, such as block and mortar joints, and to the connections between they and the surrounding frame members.

Generally speaking it is possible to define the following URM failure modes (Asteris et al., 2011; El-Dakhakhni et al., 2003; Ghosh and Amde, 2002; Wood, 1978):

- corner crashing (CC);
- diagonal compression (DC);
- sliding shear (SS);
- diagonal cracking (DK).

The CC mode is reached when at least one of the two loaded panel corner crushes; this type of failure is thus usually related to a masonry of weak blocks surrounded by strong frame members. Diagonal compression DC is instead related to the splitting of the masonry under strut compressive force, followed by out-of-plane collapse under buckling effects. The first mode is the most common, until the second one is related to low thickness walls, typically not employed to guarantee a minimum level of thermal and acoustic performances. The diagonal cracking DK and the sliding shear SS are modes of failure related to a low mortar joints quality; indeed, both present a sliding mechanism on them. In the first case (DK) the contact lengths between the infill and the surrounding frame provide a certain level of confinement, allowing so the panel to carry higher loads after its cracking. Hence, this mode cannot be considered a real collapse mechanism. It is worth noting that all the presented failure modes are relative to walls without openings (a short literature survey about this topic is presented in the following).

URM damage due to in-plane action is also cause of wall high vulnerability respect to out-of-plane (OOP) actions. The strength against transversal loading is mainly related to horizontal and vertical arching in the infill thickness (Abrams et al., 1996), which are balanced by the contact force between the same wall and the surrounding frame (columns and beams, respectively). In presence of damage due to in-plane loading, the arch mechanism is weakened; this reflects in a reduction of the masonry wall stability under out-of-plane action. Therefore, the study of the seismic response of masonry infill cannot disregard the behaviour of the wall under combined in-plane and out-of-plane actions. Several works are available in the literature for the experimental assessment of the OOP capacity in presence of in-plane damage (Di Domenico et al., 2020; Furtado et al., 2016), and for the combined action modelling (Asteris et al., 2017; Mohyeddin et al., 2013; Ricci et al., 2018).
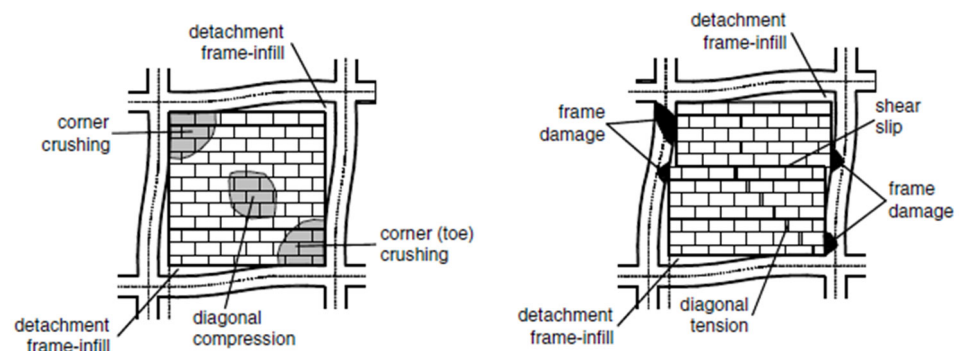
Figure 62: Identification of the different URM modes of failure (Asteris et al., 2011).

Experimental tests on infilled frames

Several experimental programs were performed on different typology of infilled frame. The following were investigated: i) type of the surrounding frame, ii) masonry typology, iii) presence of openings, iv) number of infilled bays, and v) test loading protocol. Only the results consistent with the aim of this work are herein presented. A preliminary objective is the presentation of the earlier experimental evidences that have characterized the base of the infill-frame interaction study (Mainstone and Weeks, 1970). Then, a discussion of RC non-ductile frame interaction with masonry panel is proposed (Al-Chaar et al., 2002; Mehrabi et al., 1996; Stavridis et al., 2012). Only 2D sub-assemblages are considered. Despite their clearly fascination, shaking table test on 3D systems (Hashemi and Mosalam, 2006; Zarnic et al., 2001) are herein not considered, since they are relative to seismic detailed MRF frames.

The first experimental tests were done on solid brickwork infills in presence of concrete-encased steel frames (Mainstone and Weeks, 1970). The role of different infill-frame relative stiffness was investigated on a single bay scaled frame specimen. Moreover, the effects of adjacent infilled bays is also simulated. Experimental

89

evidences showed that the behaviour of the composite system is characterized by an initial non-linear branch, followed by the diagonal cracking of the infill. The load-carrying capacity is however higher respect to the cracking load, cause to the frame capacity in confining the masonry. The peak strength was reached with the failure in compression of the infill followed by a softening behaviour (Figure 63.d). The authors (Mainstone and Weeks, 1970) identified the infilled one-bay system as a lower bound for the behaviour expected in a multi-bay and multi-storey building, because of the stiffening role played by the infill in the near frame bays. The effect was experimentally simulated by the increase in the stiffness of the frame members (but not of its joints), and the conclusion is confirmed. Indeed, the specific samples show a considerably enhanced strength for the infills.
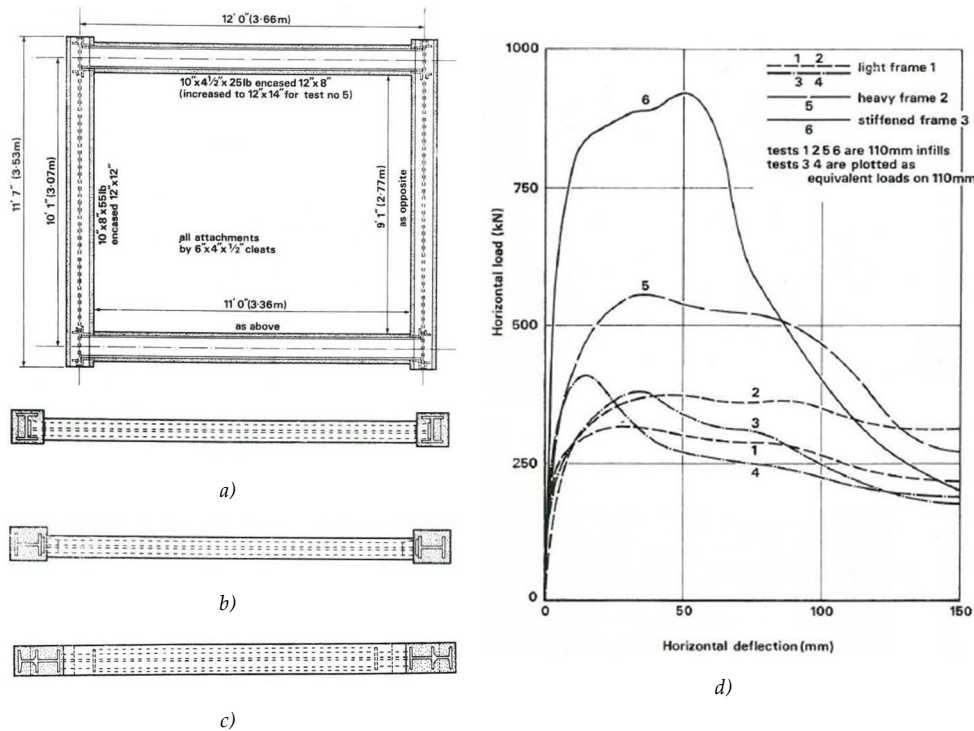
Figure 63: Concrete-encased steel frames with different column stiffness a), b), c), and relative experimental results d) (Mainstone and Weeks, 1970).

Twelve RC frames infilled with concrete masonry were tested by other authors (Mehrabi et al., 1996). The RC members were designed according both to only lateral wind (weak frame) and strong-earthquake load (strong frame). The infills were realized with solid concrete blocks (strong infill) and with hollowed ones (weak infill). The In-Plane (IP) response of the different solutions was investigated. The infilled specimens initiated to crack in the upper loaded corner with an inclination of about 45°. Later, a horizontal sliding crack develops. It is possible to refer to it as a

90

diagonal/sliding crack mechanism (Mehrabi et al., 1996); it is not considered in the classical URM failure modes illustrated in Figure 62. The successive development of the failure modes strongly depends on the frame and infill strengths. For the weak infills the lateral resistance was governed by sliding on the mortar joints, and the infill-frame interaction did not significantly affect the structural response. Therefore, the global strength was the sum of the strengths of the two components (RC frame and masonry infill). Diagonal/sliding failure governed the strong infilled weak frame response, which failure was due to windward column shear cracking. In this case the response to lateral load was characterized by a loss of strength after the peak resistance load (Figure 64.a). Strong infilled strong frame was finally characterized by the diagonal cracking of the wall, related to the complete development of the diagonal strut. The weak frame stiffness was increased by a factor 15 in presence of weak infill and by a factor 50 in presence of strong infill. A significant increase in the composite system strength was also observed. Furthermore, the authors (Mehrabi et al., 1996) found that the vertical load distribution on the infill-frame structure did not influence the response to lateral loading. Nevertheless, the increase of vertical load caused an increase in the structural stiffness and strength. In Figure 64.b is reported the comparison between the experimental results and some analytical models available to estimate the stiffness of the infilled frames (they are discussed in the following). Comparison about the lateral strength are also considered, in term of ratio between the experimental value F_u and the strength of the bare infill F_1 summed to the masonry wall one (calculated assuming a sliding-shear failure according to Mohr-Coulomb criterion).

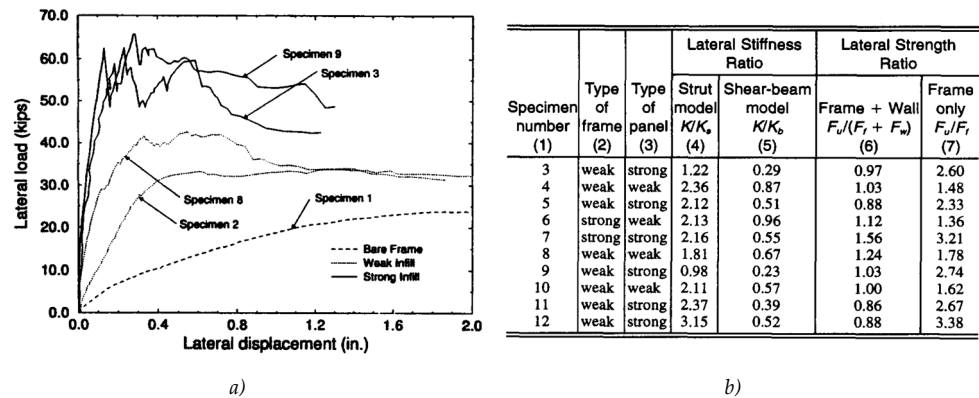| Specimen number (1)	Type of frame (2)	Type of panel (3)	Lateral Stiffness Ratio		Lateral Strength Ratio	
			Strut model K/K_e (4)	Shear-beam model K/K_b (5)	Frame + Wall $F_u/(F_f + F_w)$ (6)	Frame only F_u/F_f (7)
3	weak	strong	1.22	0.29	0.97	2.60
4	weak	weak	2.36	0.87	1.03	1.48
5	weak	strong	2.12	0.51	0.88	2.33
6	strong	weak	2.13	0.96	1.12	1.36
7	strong	strong	2.16	0.55	1.56	3.21
8	weak	weak	1.81	0.67	1.24	1.78
9	weak	strong	0.98	0.23	1.03	2.74
10	weak	weak	2.11	0.57	1.00	1.62
11	weak	strong	2.37	0.39	0.86	2.67
12	weak	strong	3.15	0.52	0.88	3.38

a)　　　　　　　　　　　　　　　　　　b)

Figure 64: Monotonic response of not earthquake-designed RC frames infilled with solid concrete block (strong infill) and hollow ones (weak infill) a), and numerical data about the experimental campaign (Mehrabi et al., 1996).

The above reported experimental evidences allow to conclude that the first major crack in the infill appears at a level drift between 0.17% and 0.46%, whereas a reduction of 80% of the peak strength is reached at a drift level that ranges from 1.00% to 2.00%. Severe shear crack in the columns were not visible at a drift level lower than 0.70%. These indications can be useful to define serviceability and ultimate limit states to consider in the design and assessment process.

Non ductile RC frame interaction with concrete and brick masonry infills was shown by (Al-Chaar et al., 2002). Five 1 storey-1 bay half scale frame specimens, with lack in the seismic detailing and not anchored bottom beam reinforcement in the joint, were analysed. The behaviour was compared with the one of other analogues infilled specimens. Also double and triple bay samples were tested. The loading protocol provided a monotonic push up to 9.00% drift level. The peak and the residual strength and displacement were monitored. The bare frame showed a ductile failure despite the loss of anchorage in the joint region. The mechanism was governed by the formation of plastic hinges, and a shear failure arose in the column at a drift level higher than the 3.00%. Single bay infilled specimens showed a significant increase in strength (2.5 times), both in term of peak and residual values. No evident loss of strength was visible up to the reached displacement (Figure 65.a). The cracking of the masonry was different in the two observed specimens, due to their mechanical characteristics. Higher compression over shear strength of brick masonry reflected in diagonal failure of the infill, with a clear definition of more parallel struts (Figure 67.d). On the other hand, Concrete Masonry Unit (CMU) showed a sliding plane formation prior to the corner crushing (Figure 67.c). The increasing number of infilled bays reflected in an increase of strength and stiffness of the composite systems, but in a non-proportional way. The windward panel showed failure mode like the single bay relative specimen. Anyway, the frame was subjected to shear and flexural cracking far from the joint region, thus the effect of the infill-frame interaction in the determination of the frame internal action is confirmed; the first activated limit state was however the infill cracking (Figure 65.b).

Wall	First major infill crack	Column shear	Joint shear crack	Joint sliding	Corner crushing	Maximum
Model 1	NA	1.4	0.8	NA	NA	9
Model 2	0.7	1.3	1.3	0.7	NA	10
Model 3	1.0	1.0	0.4	NA	NA	9
Model 4	0.3	0.8	1.2	0.8	1.2	7
Model 5	0.7	0.7	1.4	NA	NA	8
Mehrabi (1996)						
Frame (no infill)	NA	NA	1.32	NA	NA	4.9
$h/l=0.67$ weak	0.17	1.82	1.40	0.99	NA	2.6
$h/l=0.67$ strong	0.33	1.32	2.07	1.32	NA	2.3
$h/l=0.48$ weak	0.17	NA	NA	0.41	0.91	2.4
$h/l=0.48$ strong	0.36	1.32	NA	0.91	NA	2.1

a)   *b)*

Figure 65: Load-deflection curve a) and capacity drift at different limit state b) (Al-Chaar et al., 2002; Mehrabi et al., 1996).

a)

b)
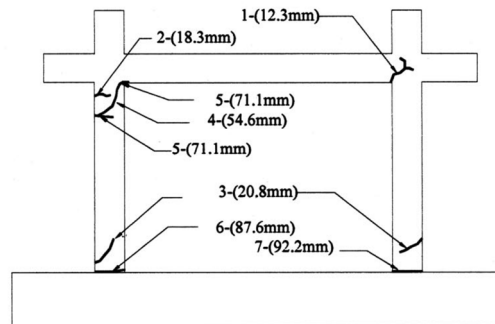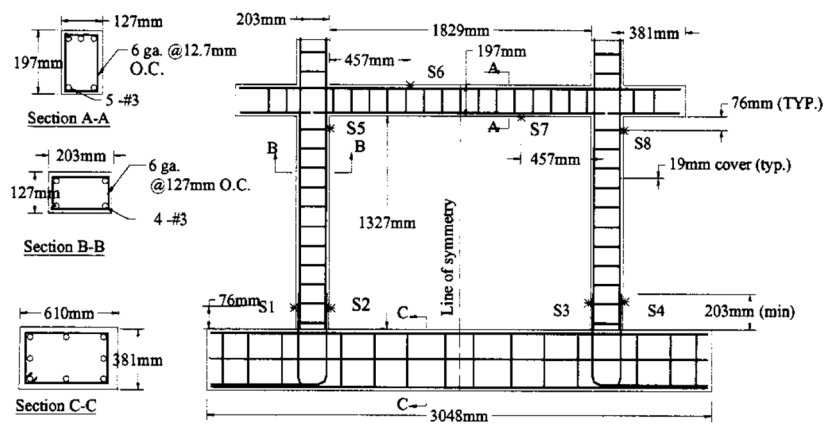
Figure 66: Detailing of the reference bare non-ductile RC frame a) and its crack pattern evolution during IP monotonic loading b) (Al-Chaar et al., 2002). Continue in Figure 67.

93

c)

d)

e)

f)
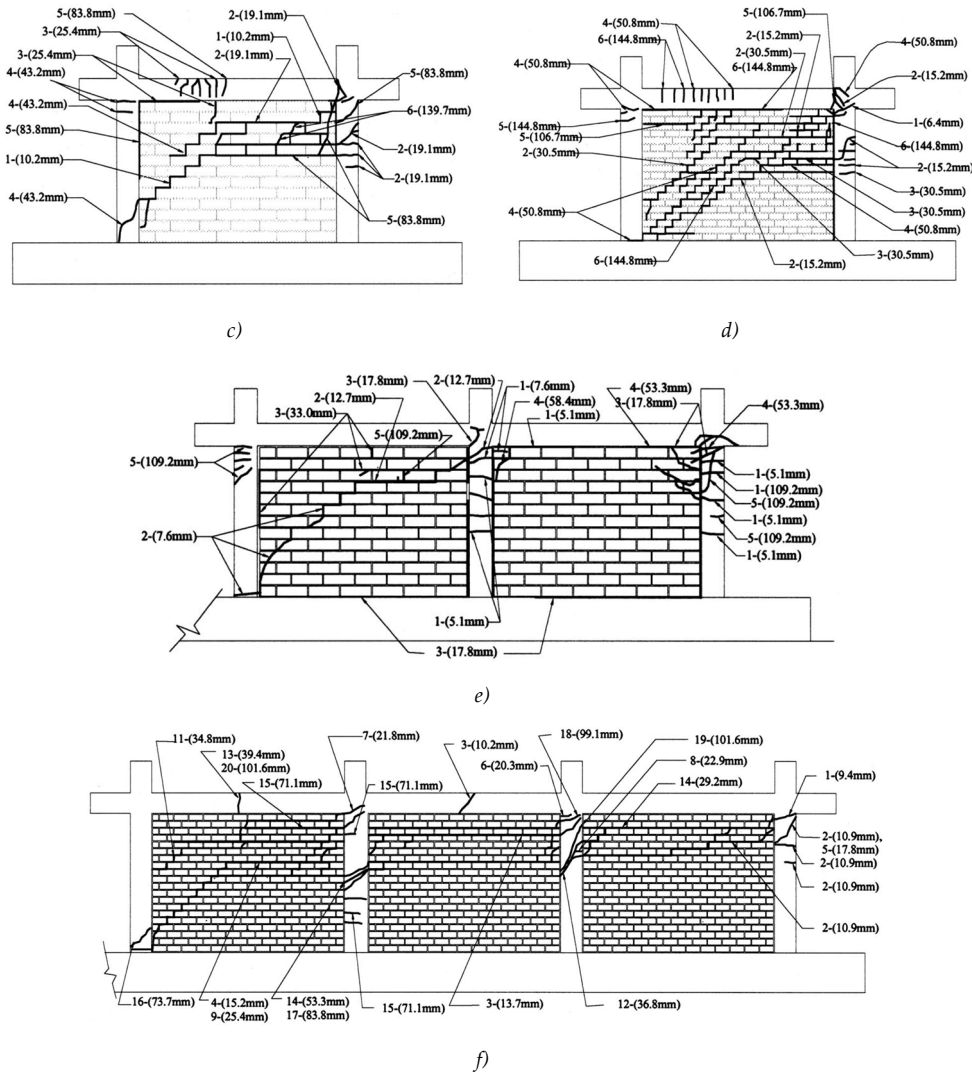
Figure 67: Damage results for concrete c) and brick d) masonry infilled 1-bay specimens; 2 bay concrete masonry e), and 3 bay brick infilled frame f) (Al-Chaar et al., 2002). Continued from Figure 66.

94

A 2-bays 3-storeys non-ductile RC frame infilled with multi-withes brick masonry wall was tested under dynamic loading (Stavridis et al., 2012). The 2:3 scaled specimen was composed by beams and columns high longitudinal reinforcement ratio but presents lack in the shear reinforcement. Very high stirrups spacing characterized the columns, no shear reinforcement was instead placed in the beams. Clay bricks composed the infill walls, which were solid for a bay and presented an eccentric window in the other, over all the three storeys. The development of the observed collapse mechanism can be summarized in the followings:

- minor crack in the infill;
- horizontal and diagonal crack in the infill;
- diagonal cracking of the columns;
- soft-storey mechanism;
- infill collapse;
- structural collapse.

The first cracks appeared at the infill-frame interface in the solid infilled bay (Figure 68.a), whereas they start from the window corner in the other one. These low damage type, related to low seismic demand, required only minor cosmetic repairs. The successive infill cracking (Figure 68.b) did not jeopardize the structural integrity but it altered in a significant way the hysteretic response, which became non-linear. Then, the sliding on the horizontal cracks caused high shear action demand on the columns (Figure 68.c-d), showing a great change in the structural response. In the initial phase it behaved like a unique cantilever (overturning moment resisted by the columns and shear action by the infills), after the walls damage a clear soft-storey mechanism was instead shown and the column failed in a brittle mode (Figure 68.e-g). During the development of the damage, the fundamental period of the structure gradually increased, due to the inelastic deformations and to the energy dissipation by the damaged structure. Only minor damage was measured in the second storey and no damage was visible in the third, according to the development of a soft-storey mechanism. The beams did not show significant axial deformation, but the frame joints rotated respect to the slab. The infill with opening was more vulnerable respect to the solid one, as it was shown by its out-of-plane failure.

Other dynamic results about the seismic response of a 2-bay 2-storeys structure with solid panel at the ground level and openings presence in the first storey are available in the literature (Buonopane and White, 1999).
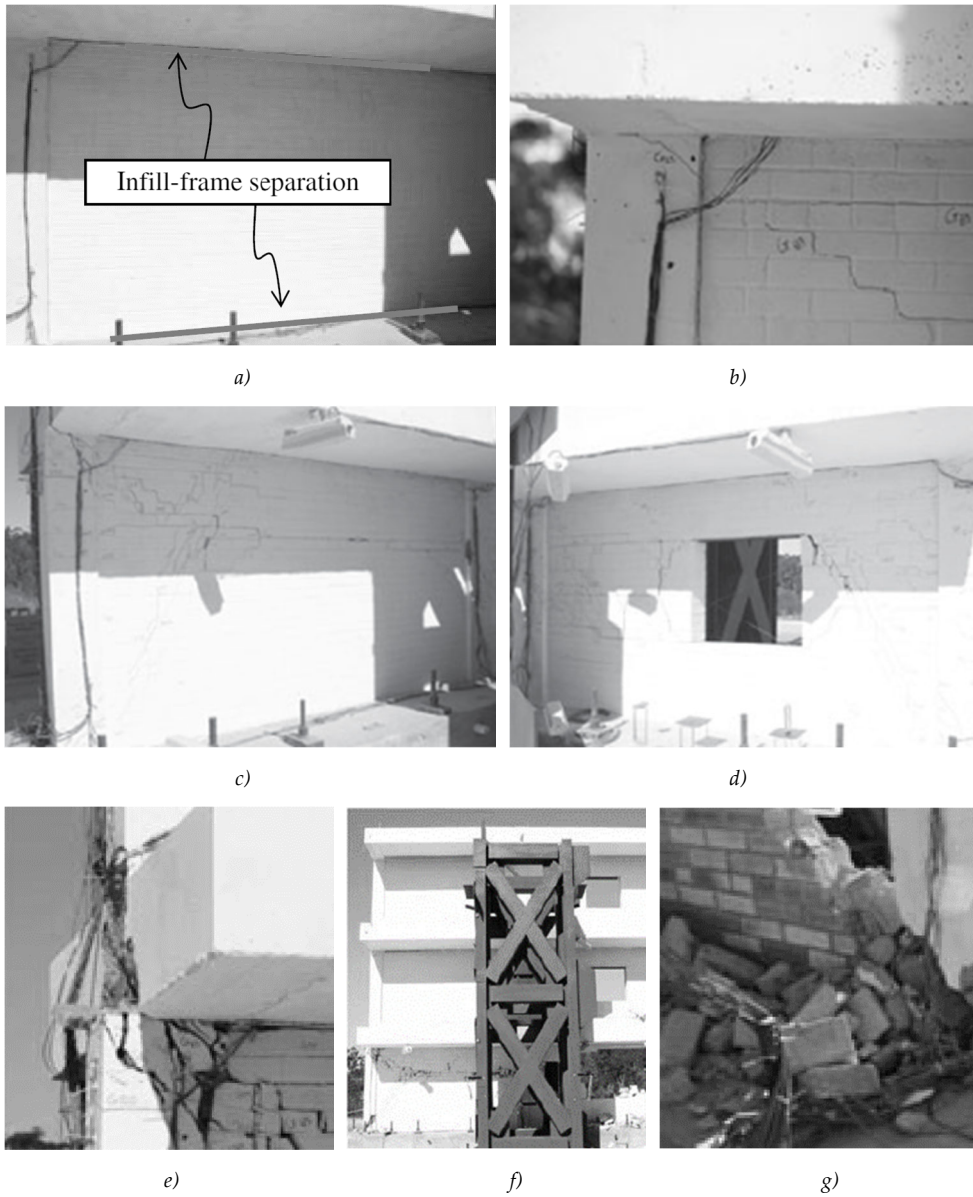
Figure 68: Damage evolution of the infilled frame tested under dynamic loading. Minor initial cracks a) and their successive development b) in the solid infilled bay, more severe crack pattern exhibited in presence of higher demand for the solid infill c) and for the wall with opening d), and global structure representation at the collapse e), f), h) (Stavridis et al., 2012).

Infilled frame stiffness

A first equivalent model to define the stiffness of an infilled frame was proposed by (Fiorato et al., 1970). The composite system is compared to a shear-beam characterized by the stiffness K_b, result of the composition between a shear K_{sh} and a flexural K_{fl} values. The former is calculated assuming only the infill contribution and a uniform distribution of stress in it; the latter is related to the frame role. Defined E_c the column frame modulus of elasticity, and I_c its second order moment of area, A_w, h_w and $G_w = E_w/2(1 + v)$ the masonry horizontal cross section area, height and shear modulus respectively, the following can be written:

$$K_{sh} = \frac{A_w G_w}{h_w} \tag{104}$$

$$K_{fl} = \frac{3E_c I}{h^3} \tag{105}$$

$$K_b = \frac{1}{1/K_{sh} + 1/K_{fl}} \tag{106}$$

Later, it was demonstrated that the stiffness and strength capacity of an infill panel, as they are the action induced in the surrounding members, are strongly dependent by the contact stress length between the panel and the frame elements. This is mainly governed by the followings (Mainstone and Weeks, 1970):

- stiffness of the frame members and joints;
- infill stiffness;
- any restraints to deformation of the frame from adjacent infills;
- lack of initial fit between the infill and the surrounding frame (e.g. shrinkage effect or poor construction detailing).

The contact length dependence on the relative infill-frame stiffness was outlined in analogy with the problem of Beam on Elastic Foundation (BEF) (Stafford-Smith, 1967). The author related the contact length α with the non-dimensional stiffness λ in the following way:

$$\lambda = \left(\frac{E_w t_w sin(2\theta_w)}{4EIl'}\right)^{\frac{1}{4}} \tag{107}$$

$$\frac{\alpha}{l} = \frac{\pi}{2\lambda l} \tag{108}$$

where E_w is the infill modulus of elasticity (assumption of isotropic material), t_w, l' and θ_w are the infill thickness, characteristic dimension (height h_w or length l_w) and diagonal slope respecitvely; E is frame members Young modulus, I the second order

moment of area of the same and l is the member (column h or beam L) length. According to the algebraic form of Eq.(108), it is possible to represent in a graphic way the relationship between the contact length and the infilled frame diagonal stiffness. An example is reported in Figure 69. It is clearly visible that the relative stiffness parameter strongly influences the contact length amplitude, but only for its small values ($\lambda l < 5$ like suggested by the author). On the other hand ($\lambda l > 5$), the diagonal strut stiffness is mainly governed by the infill contribution. Due to the dependence of the infill strength from the contact length, it is also possible to represent the load carrying capacity in the form of the curve of Figure 69.a.

a)   b)
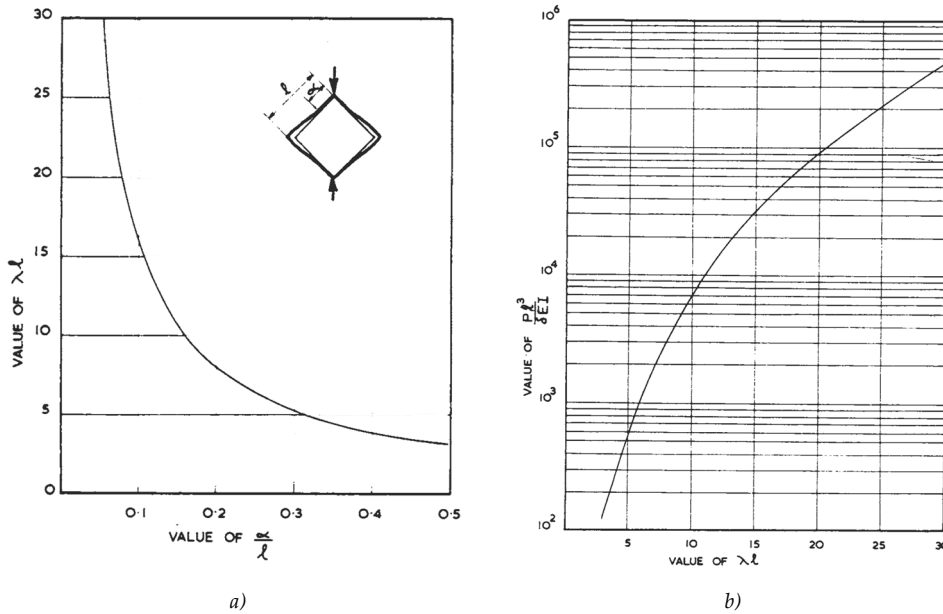
Figure 69: Plot of the contact length amplitude α and of the infill diagonal stiffness according to the relative infilled frame stiffness dependence (Stafford-Smith, 1967).

Some experimental results (Mehrabi et al., 1996) were compared with the stiffness of two equivalent model available in literature (Figure 64.b). The experimental reference is the secant value related to the response point at the 50% of the peak strength. It was demonstrated that the structural stiffness obtained by the strut model (Stafford-Smith, 1967) is, in general, the half of the experimental measured value. The other comparison is with the equivalent beam model (Fiorato et al., 1970) (Eq.(106)). It overestimates the experimental stiffness, probably due to the not considered cracking effect in the definition of the schematic representation.

URM panel strength

Several empirical formulations were proposed in the literature for the assessment of the Unreinforced Masonry panel strength (Bertoldi et al., 1993; Buonopane and White, 1999; Flanagan and Bennett, 1999; Liauw and Kwan, 1983; Wood, 1978). They associate the infill masonry properties and the confining frame strength and stiffness to the masonry panel strength. In the following only the more comprehensive approach is presented.

The reference model (Bertoldi et al., 1993) was based on the relative infill-frame stiffness λ (Stafford-Smith, 1962) and on a set of empirical coefficients available in Table 5. These were used to define the masonry strength, according to the different failure modes previously discussed: Corner Crushing (CC), Diagonal Compression (DC), Sliding Shear (SS) and Diagonal Cracking (DK). The equivalent strength is then assumed to be related to the minimum of the calculated values; mathematical formulation of the proposal from Eq.(109) to Eq.(112).

Known σ_v the vertical compression stress due to gravity loads, f_{wv} the vertical compression strength of the infill, f_{wu} the sliding resistance of the mortar joints and f_{ws} the shear resistance under diagonal loading, the followings can be defined:

$$\sigma_w(CC) = \frac{1.12\, f_{wv}\, sin\,\theta\, cos\,\theta}{K_1(\lambda h)^{-0.12} + K_2(\lambda h)^{0.88}} \qquad (109)$$

$$\sigma_w(DC) = \frac{1.16\, f_{wv}\, tan\,\theta}{K_1 + K_2\lambda h} \qquad (110)$$

$$\sigma_w(SS) = \frac{(1.20\, sin\,\theta + 0.45\, cos\,\theta)f_{wu} + 0.30\sigma_v}{b_w/d_w} \qquad (111)$$

$$\sigma_w(DK) = \frac{0.60 f_{ws} + 0.30\sigma_v}{b_w/d_w} \qquad (112)$$

$$\sigma_w = min\big(\sigma_w(DC);\ \sigma_w(CC);\ \sigma_w(SS);\ \sigma_w(DK)\big) \qquad (113)$$

Parameter	$\lambda h < 3.14$	$3.14 < \lambda h < 7.85$	$\lambda h > 7.85$
K_1	1.300	0.707	0.470
K_2	-0.178	0.010	0.040

Table 5: Empirical parameters to define the infill masonry strength (Bertoldi et al., 1993).

The proposed model is very useful in the definition of the modelling technique of masonry infilled frames since it allows to well define an equivalent strut (Asteris et al., 2011; Crisafulli et al., 2000; Decanini et al., 2004b; Di Trapani et al., 2015). Nevertheless, a great number of mechanical parameters are required to define the strength relative to each mode of failure; therefore, several experimental results on masonry specimens must be available.

Effects of infill-frames interaction

The main consequences of the infill-frame interaction are the increment of the composite system stiffness and strength, and the change in the frame members internal actions. Regarding the former aspect, the consequent reduction of the building natural period usually reflects in a higher seismic load. Moreover, if the infill panels reach their maximum strength and then fail partially or wholly, the higher forced introduced in the system are suddenly transferred to the frame members. The distribution of the infills in the building façades also influences the global dynamic response. Torsional effects are introduced if the infill disposition in plan or elevation is irregular; hence, the displacement demand on the frame members could be amplified. On the other hand, the increase in strength due to masonry infill presence can be related to a safer structural system in presence of low earthquake actions; to such an extent that some researchers suggested the infill design to resist horizontal loads (El-Dakhakhni et al., 2003; Ghosh and Amde, 2002; Mehrabi et al., 1996; Saneinejad and Hobbs, 1995). At the serviceability level, a significant energy dissipation can occur thanks to the infill panels, in form of sliding on the mortar joint planes, microcracking, and other mechanisms well defined after the diagonal cracking. Therefore, it is possible to consider the masonry infills as a first line of defence in buildings subjected to earthquake loading (Kappos, 2000).

The strong action transmitted from the infill to the frame members results in a completely different distribution of the frame internal actions, with respect to the case of the bare frame. In this situation plastic hinges can form out of the expected regions, under the effect of the transversal force introduced by the infill strut. Shear failure can also arise in the column and beam elements. Under strong seismic actions, the structural safety can be governed by the only frames system only if it is adequately designed accounting for the infill-frame interaction. On the other hand, treating existing RC buildings, the adequacy of the columns and the beams in resisting the infill induced action is surely debatable. Lack of detailing and non-conforming seismic design cannot be neglected, and frame brittle failure can arise also in presence of low earthquake demand. Therefore, the expected increase in strength due to the infills presence can be avoided by the premature fail of the members. This is a typical case of the herein studied GLD frame buildings, which performance under horizontal loads are very poorer.

100

The typical low-ductility collapse mechanisms, induced by the infill-frame interaction, are well known in the literature. Furthermore, they were well recognized during in-situ inspection after the past earthquakes. They can be summarized in:

- soft-storey mechanism;
- short column mechanism;
- column or beam shear failure;
- column failure under combined tensile axial and shear load.

The evaluation of the shear induced in the frame member by the interaction effect is very argued to be experimentally measured (V. Bolis et al., 2019). The only available information was found by the means of an adequate modelling of the composite system. Some examples of interesting works can be found in the literature (Bolis et al., 2017; Cavaleri and Di Trapani, 2015; De Risi et al., 2019). It is noteworthy to observe that the shear failure of the existing elements can also occur in presence of structural strengthening by shear wall introduction in the structure. The stiffening effects of the masonry infill on the retrofitted structure is lower in presence of high stiffness shear wall (Kose, 2009); nevertheless, the high vulnerability of the existing RC columns can be insufficient to guarantee a minimum level of safety (Valentino Bolis et al., 2019). Nowadays this topic is of particular interest in the earthquake engineering research, since in the past year several reinforcement techniques were proposed without considering their effect on the local behaviour of the existing frame members.

Performance of infill panels under earthquake actions

Different observed infill damage levels can be related to the reach of specific Limit States (LS), as they are intended in several codes (CEN Eurocode 8, 2005; FEMA 273, 1997; FEMA E-74, 2015; Norme Tecniche per le Costruzioni, 2018). From a practical point of view, the damage can be related to economic loss and to the guarantee of a safety level. In the literature different reference on the topic are available. Twelve different Limit States were defined including not only infill damage but also RC surrounding frame members one (Meharbi and Shing, 2003). On the other hand, an easier proposal identifies four different stages related only to infill behaviour (Calvi and Bolognini, 2001), dividing i) no damage ii) light damage, iii) severe damage and iv) very high damage observed in the masonry wall. In the following more recent proposals are reported. They are useful for the structural assessment of infilled frames, since they are associated to well described level of damage and to evaluable economic loss.
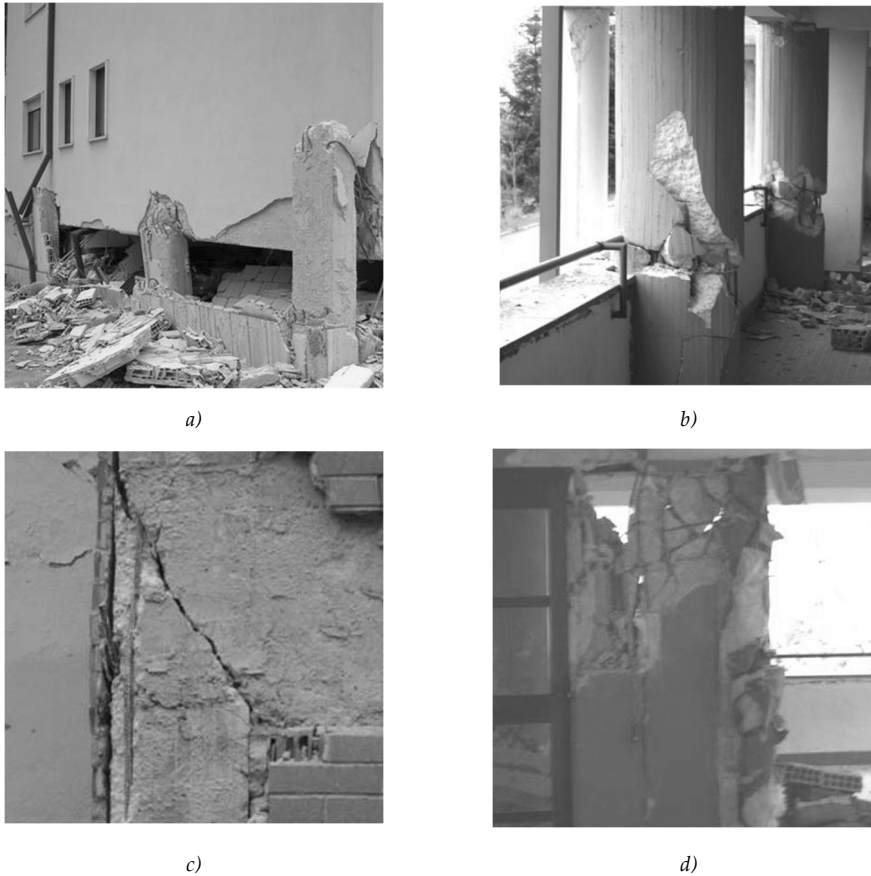
Figure 70: Damages on building following the seismic event of L'Aquila (IT) 2006: soft-storey a) and short-column b) mechanisms, joint and element local shear failure b-c); (Verderame et al., 2009c).

The damage of the infills due to load in their plane has a significant role (Hak et al., 2012), both at Ultimate Limit State ULS and at serviceability one (Damage Limitation DLS). In the first case detrimental effects due to in-plane action can initiate principle of out-of-plane instability, with consequent dangerous effect on the life safety. On the other hand, non-economically interventions can be required to repair damage related to lower seismicity levels (DLS). With reference to experimental tests on an URM infilled RC frame (Calvi and Bolognini, 1999), an equivalent infill strut can be numerically calibrated to represent the empirical evidence (Hak et al., 2012). The numerical information was then associated to specific interstorey drift levels. The work results in a definition of three different Limit States, which are summarized in Table 6. Regarding a weak masonry infills (8cm single-leaf clay horizontal hollowed with mortar plaster on both its faces), a drift limitation equal to 0.30% at the DLS and

an upper limit of 1.00% are suggested for the design process. Therefore, it is shown that a high ductility class frame cannot express its deformation capabilities in presence of masonry infills. The results of the approach also shows that the Code (CEN Eurocode 8, 2005) indications are uncapable to ensure a well define level of safety, no clear approach to the structural analysis of infilled frames is indeed defined.

Limit State	Drift	Description
Operational	0.20%	Undamaged infills
Damage Limitation	0.30%	Infill damage economically repaired
Life Safety	1.00%	Severe damage in the infills with reparability economically questionable; lives aren't threatened

Table 6: (Hak et al., 2012) definition of the principle Limit States for infilled frame structures.

The above presented work (Hak et al., 2012) was later improved (Sassun et al., 2016). Four different limit states were defined on the bases of empirical observed damage. Solid or hollowed clay or concrete block masonry infills were considered, in presence of RC or steel frame (a wide experimental test results database was used as a reference). The authors correlate a specific level of damage, which wants to represent the reach of a Limit State (Table 7), with the test measured level of drift. The suggestion is conceptually summarized in Figure 71. Thanks to the proposed approach, specific drift values can be expressed in term of fragility curves, and in term of economic loss. The latter were expressed by the means of numerical data in the reference paper (Sassun et al., 2016).
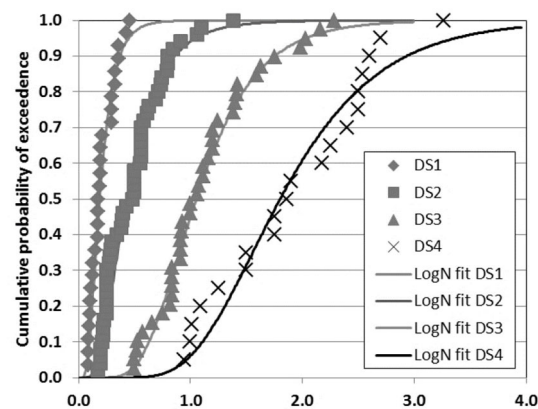
LS	All	Solid clay brick	Vertical hollowed clay brick
DS1	0.18	0.14	0.16
DS2	0.46	0.33	0.44
DS3	1.05	0.96	0.97
DS4	1.88	2.00	1.33

a)   b)

Figure 71: Fragility curves for infills a) and mean value for the drift level associated at each Limit State for different clay brick masonry infill panels; (Sassun et al., 2016).

Code	Limit State	Description
DS1	Operational	The infill is considered slightly damaged. The occurrence of this level of damage, usually subsequent to the detachment of the masonry panel from the RC frame at the intrados of the top beam and along the (upper) height of the columns, can be characterized by a very light and superficial cracking in the masonry panel, or by cracks in the plaster. A "Cosmetic" damage without the need for repair, does not belong to this damage state.
DS2	Damage Limitation	The infill is damaged but can be effectively and economically repaired. Damage of the infill panel, through the formation of bi-diagonal cracking, involving both the joints and the units or diagonal step-wise cracking affecting mainly the bed and the head-joints, is expected to occur. Sliding in the bed-joints may also occur. Very limited crushing and spalling of a few units can be assumed to occur.
DS3	Life Safety	The infill is severely damaged and repairability is economically questionable, however, lives are not threatened. Detachment of large plaster area, significant sliding in the mortar joints and further development of cracks in the units can be expected to occur. In addition, crushing and spalling of brick units are more widespread on the panel. The wall is not repairable at reasonable costs, however the position and the weight of masonry portions falling down is so limited as to exclude the risk for the loss of human lives. In case of openings in the infill, the window is considered not damaged, however it has to be removed and installed again.
DS4	Near collapse	The infill is close to collapse. A large amount masonry panel area is assumed to be affected by crushing/spalling of blocks/bricks and the panel is close to collapse. The window is considered damaged and it has to be replaced.

Table 7: Re-arrangement of the definition of the limit state for infill masonry panels (Sassun et al., 2016).

Influence of openings

Architectural and functional reasons are cause of openings presence in the infills. Door or window presence in an infilled bay characterizes further complications in the seismic response evaluation of the composite system. Technical installations are also cause of discontinuity in the regularity of a masonry panel, which reflects in possible different failure mechanism respect to the ones above mentioned. Due to the strong variability in the opening geometry and location, the study of their influence on the seismic response of infilled frames is an argued topic in the research. A further complication to the already mentioned modelling difficulties is introduced, in term of the definition of the interaction problem and in term of damage assessment. Therefore, a unique conclusion cannot be identified to account for their role.

A work on 1:3 scale 1-bay 1-storey infilled RC frame is herein considered (Kakaletsis and Karayannis, 2007). The RC member were designed to avoid their brittle failure, the attention is so put on the infill behaviour. Strength, stiffness, ductility, and energy dissipation capacity of bare, fully infilled, and different openings configurations were studied. The experimental campaign results are herein plotted in term of capacity curve and damage assessment. In Figure 72 the reference systems behaviour is reported; in Figure 73 and Figure 74 the influence of window and door position is respectively investigated. Summarizing the author conclusions, the presence of an opening reduced the stiffness and the strength of the infilled frame in a significant way, but the interaction between the infill and the opening was not however negligible. Damage distribution in the masonry wall changed, with the possibility to increase the vulnerability of the system respect to both in-plane and out-of-plane actions. Due to the higher influence on the diagonal strut resisting mechanism, a central opening more influenced the seismic response respect to an eccentric one. A summary of the experimental results is available in Table 8, in term of secant initial stiffness K_0, maximum lateral load V_u, displacement at the maximum load δ_u, maximum normalized energy dissipation $W/2\delta$, displacement at maximum normalized energy dissipation δ_w, and cumulative energy dissipation $\sum W$.

Other experimental tests on similar specimens are shown in the literature (Anil and Altin, 2007). An investigation on a 3-bay 3-storeys RC frame in presence of different location and geometry of the openings (Al-Chaar et al., 2003), and a review of the seismic behaviour of partially infilled frame (Surendran, 2012) were treated.

Sample	K_0 [kn/mm]	V_u [kN]	δ_u [mm]	$W/2\delta$ [kN]	δ_w [mm]	ΣW [kNmm]
B	8.34	44.27	13.95	19.08	18	8316
S	20.71	81.46	8.31	51.36	12	13101
WX1	17.84	72.71	18.97	31.19	18	12411
WX2	15.19	72.19	12.20	35.70	12	11386
WO2	14.55	66.56	10.00	36.00	12	11931
DX1	13.54	64.69	12.51	29.76	12	11067
DX2	12.70	61.04	12.07	29.08	12	11189
DO2	13.10	61.56	10.82	24.67	12	8498

Table 8: Numerical results of the (Kakaletsis and Karayannis, 2007) tests.

a1)

a2)

b1)

b2)
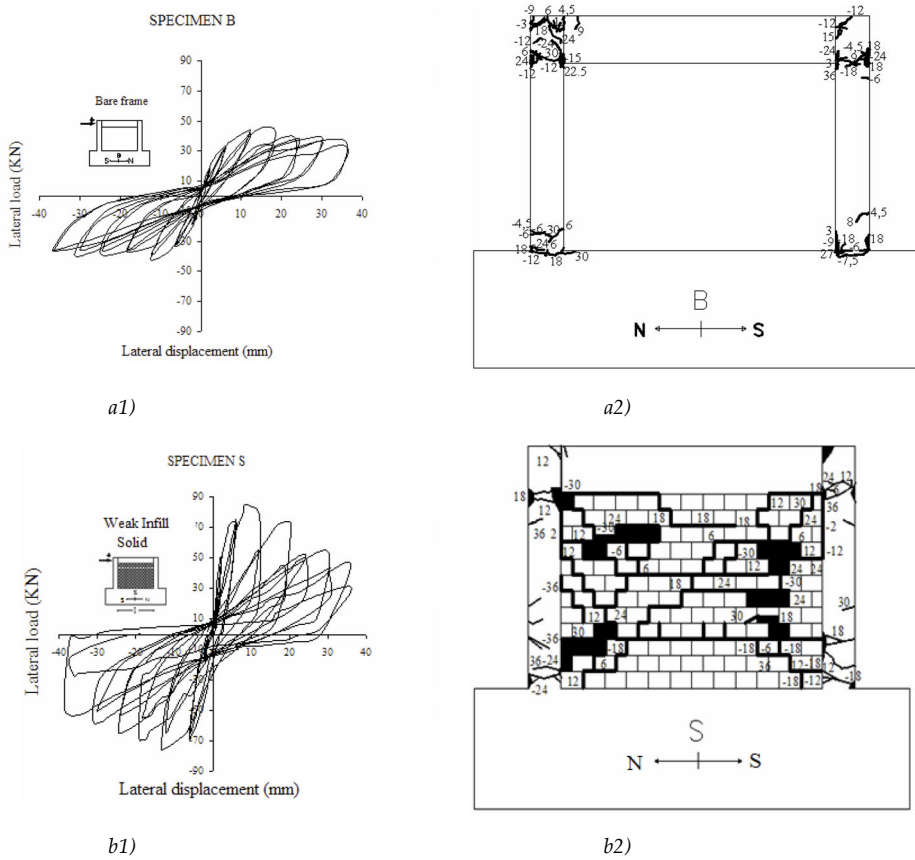
Figure 72: Result of cyclic tests on 1:3 scaled RC bare a) and fully infilled b) frames in terms of capacity curves 1) and damage assessment 2) (Kakaletsis and Karayannis, 2007).

106

a1)   *a2)*

b1)   *b2)*

c1)   *c2)*
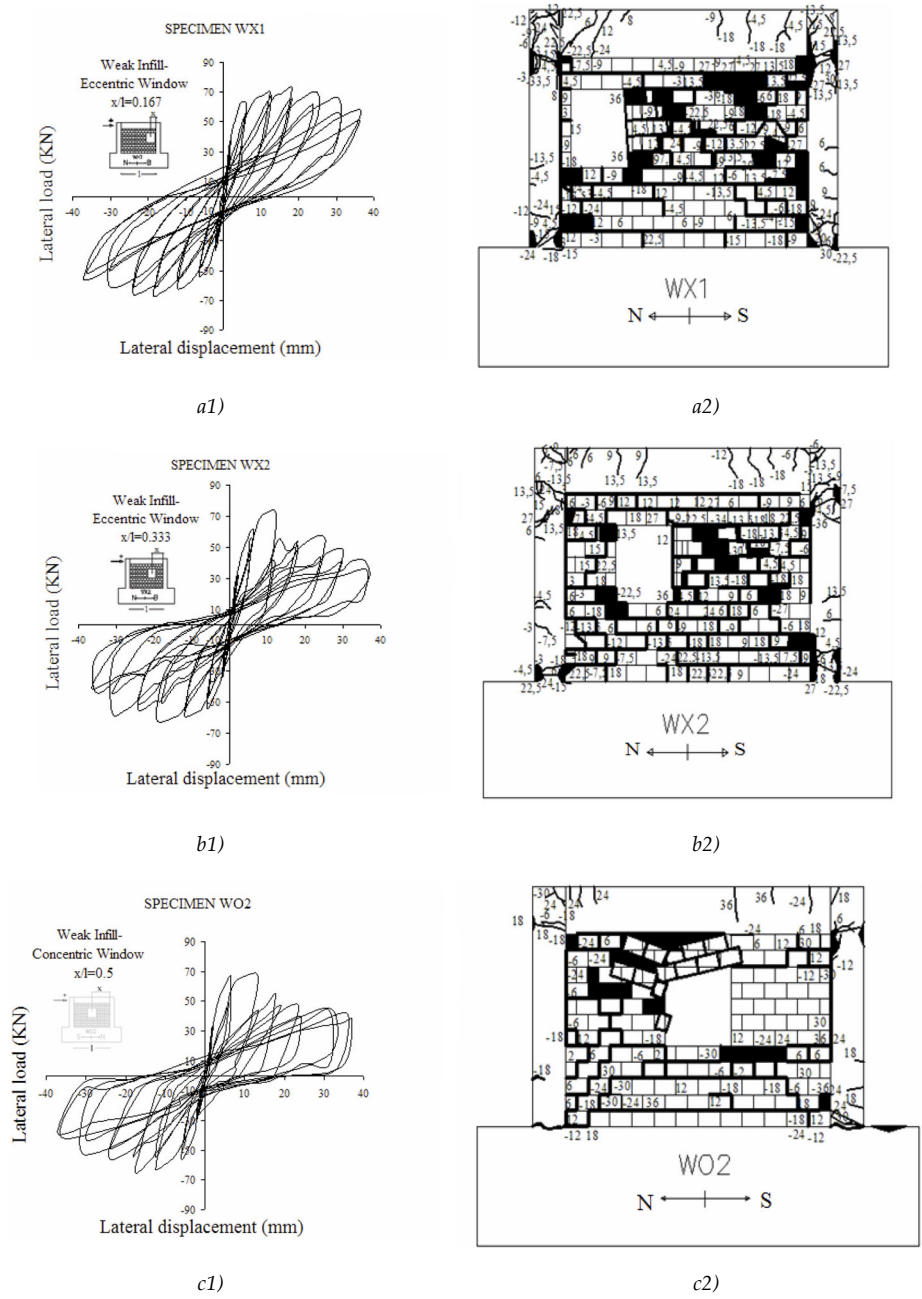
Figure 73: Influence of window opening position in the IP response of an infilled frame (Kakaletsis and Karayannis, 2007).

a1)   a2)

b1)   b2)

c1)   c2)

Figure 74: Influence of door opening position on the IP response of an infilled frame (Kakaletsis and Karayannis, 2007).

108

2.8   Mitigation of infill-frame interaction

Different construction techniques have been experimentally tested in order to significantly reduce the masonry infill In-Plane (IP) stiffness and to guarantee high Out-Of-Plane (OOP) strength for both low (8cm) (Bolis et al., 2020) and high (25cm) (Preti et al., 2014; Preti and Bolis, 2017) thickness walls. They result as being very effective in ensuring a stable response up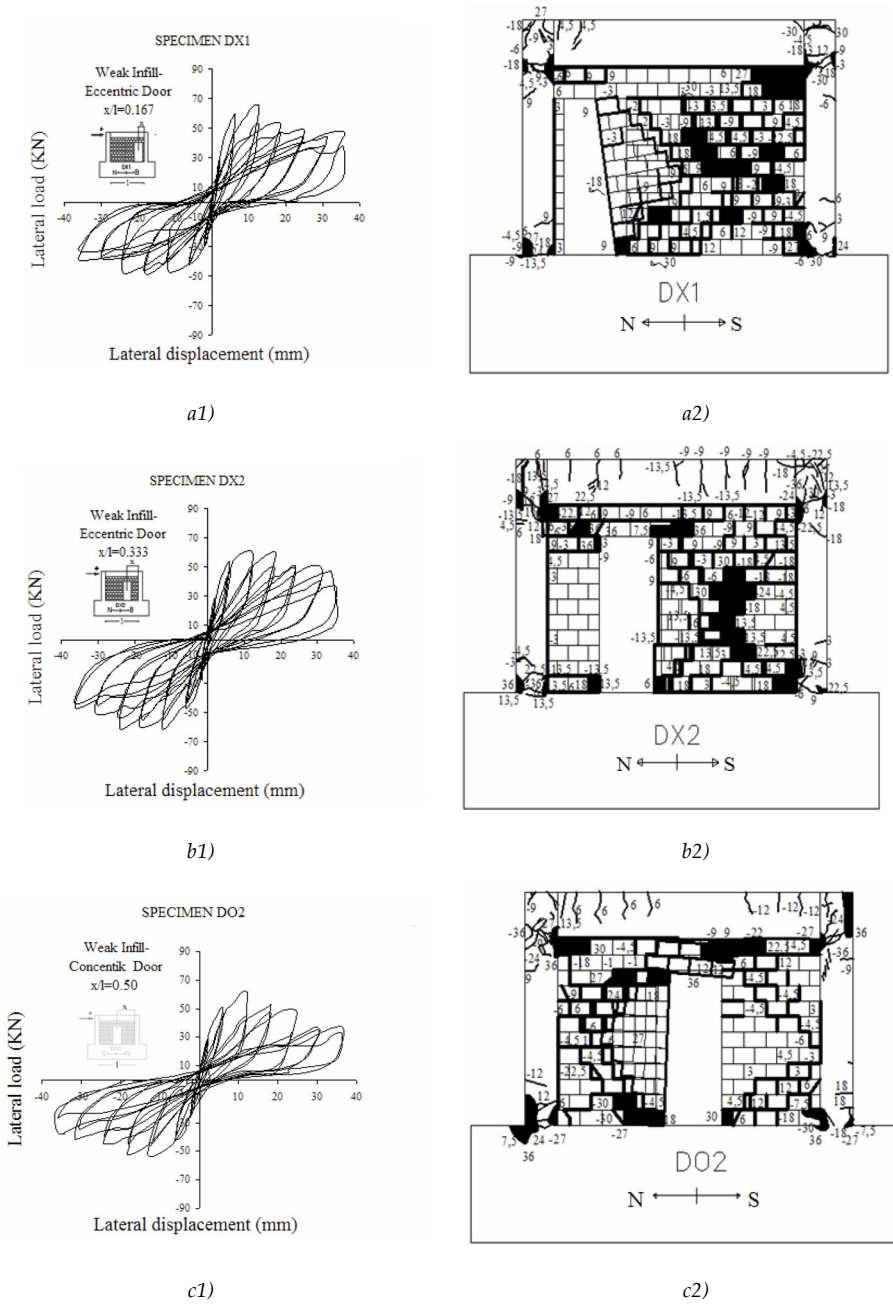 to the high interstorey drift level, showing a very reduced damage entity. The experimental evidence also indicates the possibility to apply these techniques to an existing masonry infill and they result compatible with the presence of openings. In the following a focus on these opportunities is proposed. Their application opens to the possibility of studying a bare frame in the assessment of an existing building and in the design process of a strengthening intervention (Valentino Bolis et al., 2019).

Sliding joints

The stiffness and strength capacities of a masonry wall are strictly dependent on its geometry, which allows for a shear panel mechanism formation. Considering the non-tensile strength of the masonry material, an equivalent model to understand the infill behaviour under In-Plane (IP) loads considers the formation of a main diagonal strut (Bertoldi et al., 1993; El-Dakhakhni et al., 2003; Mainstone and Weeks, 1970; Paulay and Priestley, 1992; Polyakov, 1960; Saneinejad and Hobbs, 1995). By introducing horizontal sliding joints on the masonry wall extension, different sub-portions of the wall are formed and, since they are free to slide over each other, a significant reduced stiffness is expected. The basis of the concept is described in (Preti et al., 2012), from which the schematic representation of Figure 75 is extracted.
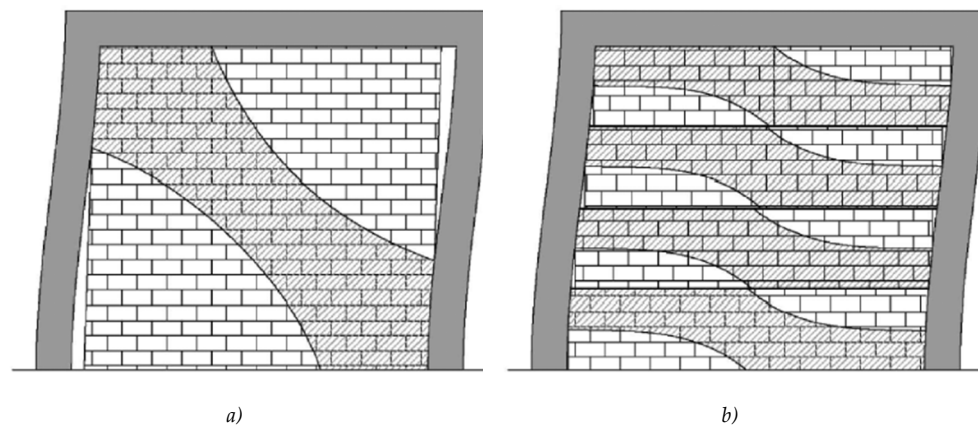

a)   b)

Figure 75: Conceptual division of a masonry infill into minor sub-portions, identification of the IP induced stress on it (Preti et al., 2012).

Due to practical reasons, the construction technique presented both for fired clay and adobe walls (Preti et al., 2014, 2012) is not doable in an existing building context, since the realization of horizontal joints results too complicated. The concept is thus extended in a vertical joint configuration scheme, whose application feasibility on an existing wall has been proved in (Preti and Bolis, 2017). Specific solution arrangement and local construction details are shown in Figure 76. The partitioning of the wall is ensured by means of vertical elements that allow the relative sliding; these are pinned to the base and the top beams with specific joints. A gap between the infill top and the upper beam is guaranteed, to permit vertical deformation due to the bending action in the frame member. The IP response of the engineered wall is characterized by the rocking mechanism of the sub-portions (Figure 76.a), on which i) self-weight, ii) friction stress along the vertical joints, iii) upper beam confinement due to compatibility reasons (in absence of top gap) act respectively. The listed contributions define the low strength of the whole wall system, which is defined in the order of a few kilo-Newtons in (Preti and Bolis, 2017). The OOP strength is guaranteed by masonry bridging between the vertical elements (sliding joints), which are simply supported on the frame horizontal members. The investigated wall thickness is equal to 12cm, to represent the external leaf configuration typically observed during on-site investigation. Thicker infill can be however treated in the same way, whereas for the low thickness walls the hybrid solution technique (presented in the following) results as being more suitable. Different arrangement of the sliding portions also permits to accommodate the presence of openings.

The experimental tests showed a very ductile and symmetric response, which is clearly visible in Figure 77.a; it is worth noting that the experienced drift levels are higher than the acceptable deformation demand on an existing structures. Furthermore, the very low resistance characterizing the solution response avoids the possibility of brittle failure mechanisms in the existing RC surrounding elements. It is noteworthy to observe that the analysed specimen geometry is consistent with a common building frame bay. The strength values outlined in the graph of Figure 77 (net infill contribution thanks to the pinned scheme of the testing frame) are thus representative of the proposed technique effectiveness in reducing the infill-frame interaction effects. If the top gap is not guaranteed, a greater force is resisted by the system, since the additional contribution of a confinement alters the rocking behaviour (mechanism iii) in Figure 76.b). Practical consequences are shown in Figure 77.b, where the infill hysteresis in the presence of a low (rock wool) and high (mortar) stiffness gap filling are presented.
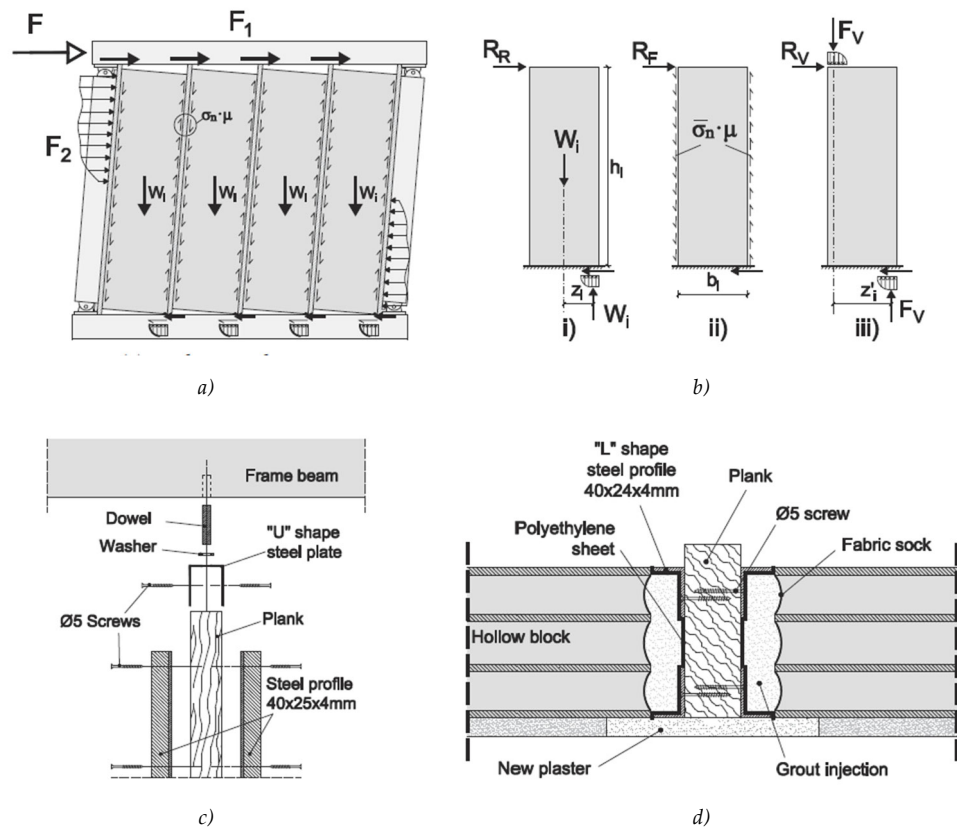
Figure 76: Conceptual organization of a masonry infill with vertical sliding joints a-b) and construction details for the application in an existing infill c-d) (Preti and Bolis, 2017).
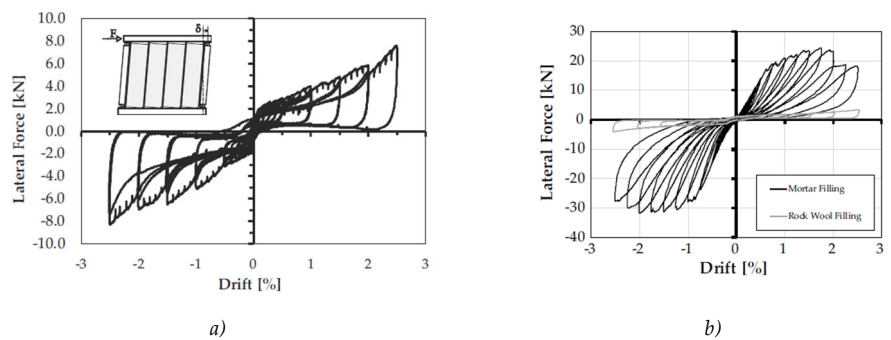

Figure 77: In-Plane response of the weakened existing masonry wall tested: presence of top gap a) and its filling with different stiffness materials b) by (Bolis et al., 2017).

Hybrid isolation

The seismic response of a frame results significantly affected by the infill interaction since the latter is built in contact with the beam and column members. The isolation technique is based on a void guarantee between the masonry and the concrete of the frame elements on the lateral and the upper infill edges. The solution effectiveness is strictly dependent on the void thickness, since it must accommodate all the frame deformations required by the seismic action. On the other hand, the same loss of contact is reason of very high vulnerability against the OOP mechanism. A correct compromise is thus to be followed, to ensure both a reduction of the infill-frame interactive mechanism and a stability against the transversal action. A major role is played by the specific top joint, which must allow for IP sliding between the infill and the upper beam and, at the same time, to ensure an effective restraint for a vertical arch mechanism. The latter is identified as the main resistant one for the OOP bending. A vertical deformation must be guaranteed in the same top joint, for beam bending deflection accommodation.
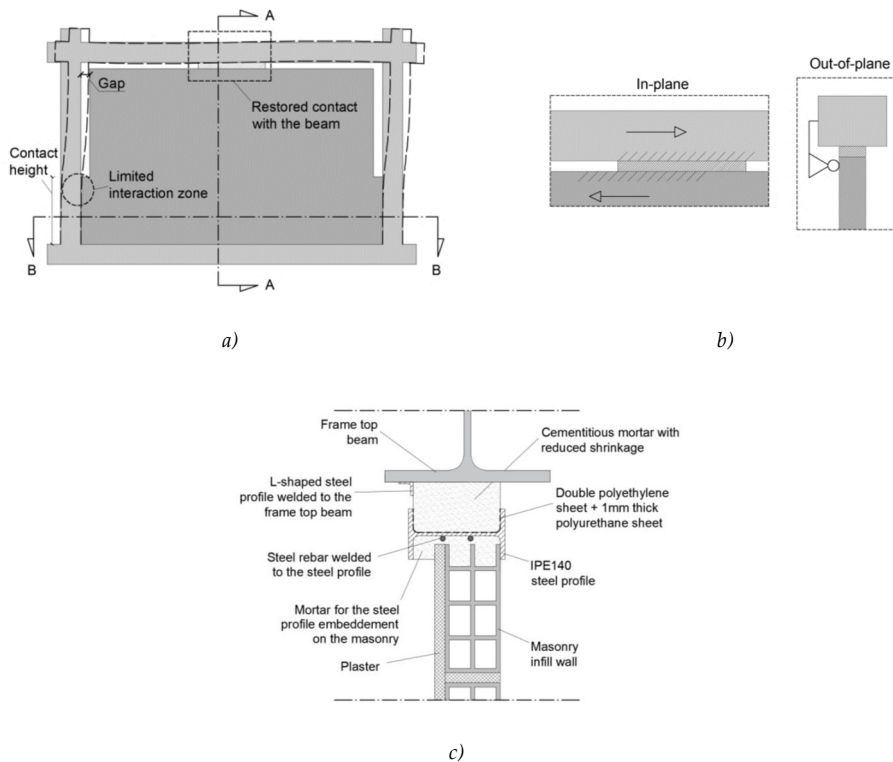

a)

b)

c)

Figure 78: Concept of the hybrid isolation technique for existing low thickness masonry infill (Bolis et al., 2020).

The concept of the solution is schematized in Figure 78. The lateral cuts on the masonry-infill interfaces are not created full-height, a partial infill-frame interaction at the wall base is thus introduced and the masonry damage is expected in the lower infill region. The choice is pursued to find a trade-off between the ideal isolation concept and a low invasiveness aim; especially, the uncut region needs to preserve the possible existing technological systems location. In the same region a further resistant horizontal arch mechanism can form in balancing the OOP action.

Experimental In-Plane response showed different behaviours, with respect to the explored drift levels and to the exhibited damage entity. Up to a 0.5% drift level the response is substantially elastic, after this deformation a strength degrading is instead observed, due to the formation of a horizontal crack which divides the lower adherent infill portion from the upper isolated one. By imposing higher drift level, significant but repairable damage occurs in the lower corners, under the action of contact stress against the frame column deformation. The damage development allows to identify a clearly horizontal sliding joints on the previous formed crack, and the stiffness and the strength of the infill is significantly reduced to about 10kN. The hysteresis assumes the connotates of a friction-based mechanism. The passage from the pre-cracking behaviour to the post-cracking one is visible in the focus on the IP response (Figure 79.b). The damage effects on the overall behaviour is instead visible by the observation of the second IP test (IP-2). The three different loading phases are separately considered, since OOP tests were performed between them. Their results show the engineered infill capacity in resisting a peak equivalent acceleration of about $4g$, and a residual one higher than $2g$, which follows an increase of the IP damage level. After the second OOP test, a further decrease in the infill In-Plane strength was noticed (IP-3).

Opening presence does not avoid the isolation technique application if the top joint is characterized by enough length to ensure the vertical arch mechanism activation out of the opening dimensions. The technique is well adaptable for low thickness internal infill leaf or for partitions. Thermal and acoustic performance of the infill cannot be reduced by the cut on the masonry wall edge, their filling with low stiffness polymeric material is so suggested to however ensure sufficient building performances. The specimen geometry was the same as the previous analysed masonry wall engineered with vertical sliding joints. The exhibited strength is comparable only after the formation of the horizontal sliding crack in the low thickness specimen. At lower drift a higher strength was instead noticed and the verification about column safety condition against shear forces is thus necessary.
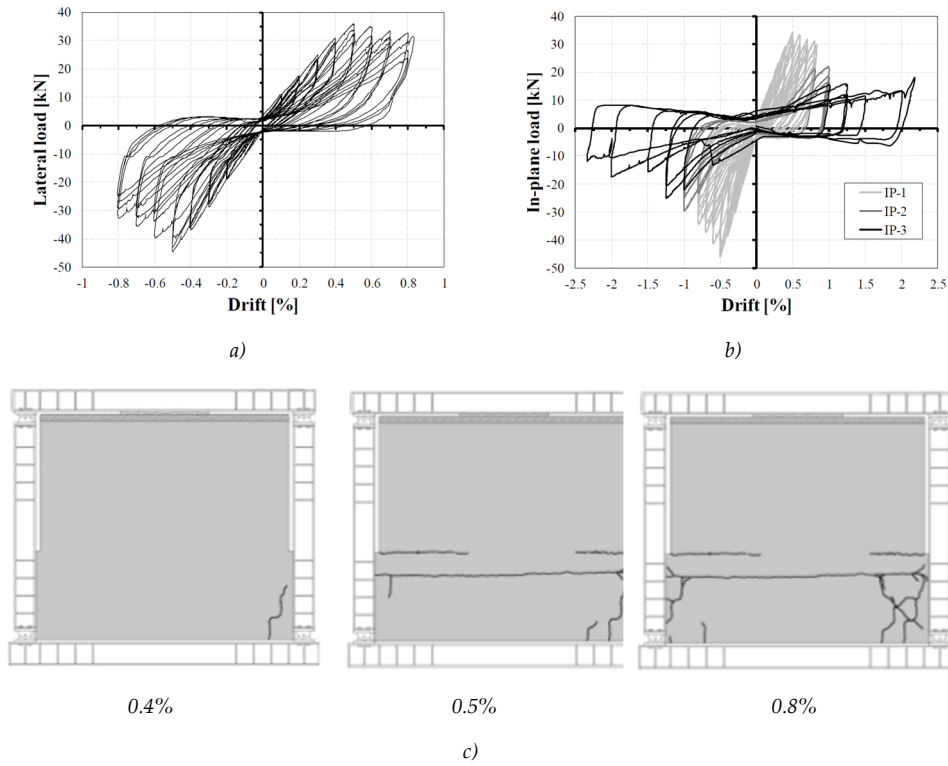
a)

b)

0.4%

0.5%

0.8%

c)

Figure 79: IP response of 8cm thickness masonry infill partially isolated from the surrounding frame: focus on the pre-cracking behaviour a) and on the post-cracking ones b); damage amplitude and crack pattern at increasing imposed drift level (Bolis et al., 2020).

3 EXPERIMENTAL TESTS ON THE BOND PERFORMANCE OF PLAIN REBAR SUBJECTED TO CYCLIC LOADING

3.1 Introduction

To understand the seismic behaviour of existing concrete structures reinforced with plain rebar, a deep knowledge about the bond performance of smooth bars and of their anchorage detailing is fundamental; several experimental evidences have indeed shown like the poor bond capacities of this reinforcement type influences, in a very significant way, the structural response (Beschi et al., 2015; Braga et al., 2009; Calvi et al., 2002b; Pampanin et al., 2002; Russo and Pauletta, 2012). The main mechanisms governing the bond stress acting on a smooth rebar are: i) adhesion between the bar surface and the surrounding concrete and ii) small concrete particles micro-interlocking (Feldman and Bartlett, 2005); the former characterizes the reach of a peak strength, after which the latter results the main source against slip. Since micro-interlocking degrades also under cyclic loading, like clearly shown by experimental tests on a short anchorage length (Verderame et al., 2009b), significant bond strength degradation is expected during a seismic excitation; consequently, a greater bar-slip is expected too, which may turn into a strategic resource when deformation capacity is required to survive the earthquake demand. Moreover, beyond the reinforcement yielding, a gradual reduction of the rebar transversal section, due to Poisson effect, affects the bar-slip response, causing possible further loss of bond performance. Finally, in the critical regions, such as the beam-column joints, rebar straight length isn't enough to guarantee an effective anchorage; end hook and/or bar bent are so employed to improve the anchorage performance. In this case the bar slip depends not only on the bond performance, but also on the plastic deformation demand to the bar sections to allow its straightening.

Pull-out tests on a straight smooth rebar of short anchorage length are available in the literature (Fabbrocino et al., 2005; Feldman and Bartlett, 2007; Verderame et al., 2009). However, only one of them (Verderame et al., 2009b) investigates the effect of a cyclic loading; in these work, the bar behaviour is interpreted assuming a constant bond stress distribution along the bar surface, thanks to its short length. A 80cm hollow square cross section bar was also tested under pull-out force (Feldman and Bartlett, 2007), showing the bond stress profile significantly varies along the bar length; more in detail, the peak bond strength results to penetrate into the concrete depth (on the bar direction) under the increase of the axial stress.

To clarify all the discussed aspects, the results of a specific experimental campaign are reported in the present chapter. Straight long length anchorage, hook-end and bent rebars axial stress-slip behaviour is analysed, with reference to both the elastic (before the yielding) and the plastic field (beyond the yielding).

In the following the geometry of three different specimen types is described, explaining the significance of each of them in a structural context, and their experimental response to a specific loading protocol is shown and discussed; finally, an analytical interpretation of the stress-slip behaviour of straight and hook ended anchored plain rebar is proposed, to be used in the structural modelling of plain rebar structure under seismic loading.

3.2 Specimens description

With reference to a generic reinforcement detailing in a structural frame joint region, like the one shown in Figure 80, it is possible to identify the different bar shapes commonly employed in existing buildings for the smooth rebar anchorage. Three different specimen types are considered in the herein presented experimental campaign, one for each anchorage specific shape. With a self-balanced external load frame, the rebar head is moved in displacement control, simulating an excitation consistent with the one introduced by flexure in a structural member during a seismic event.

SL-type: Straight length bar

H-type: Only hook anchorage

HS-type: Hook-end rebar

B-type: Bent rebar

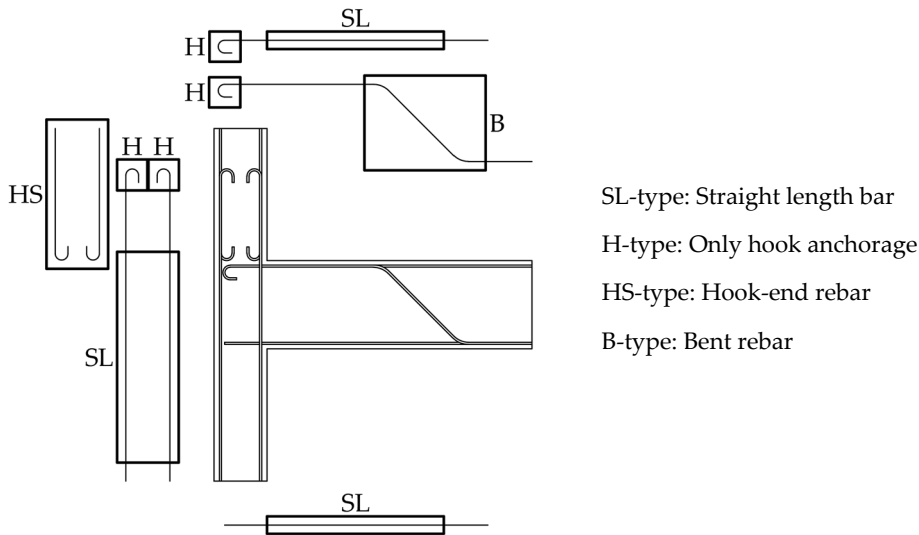*Figure 80: Example of the tested anchorage types for plain bars in a generic beam-column T-joint reinforcement arrangement.*
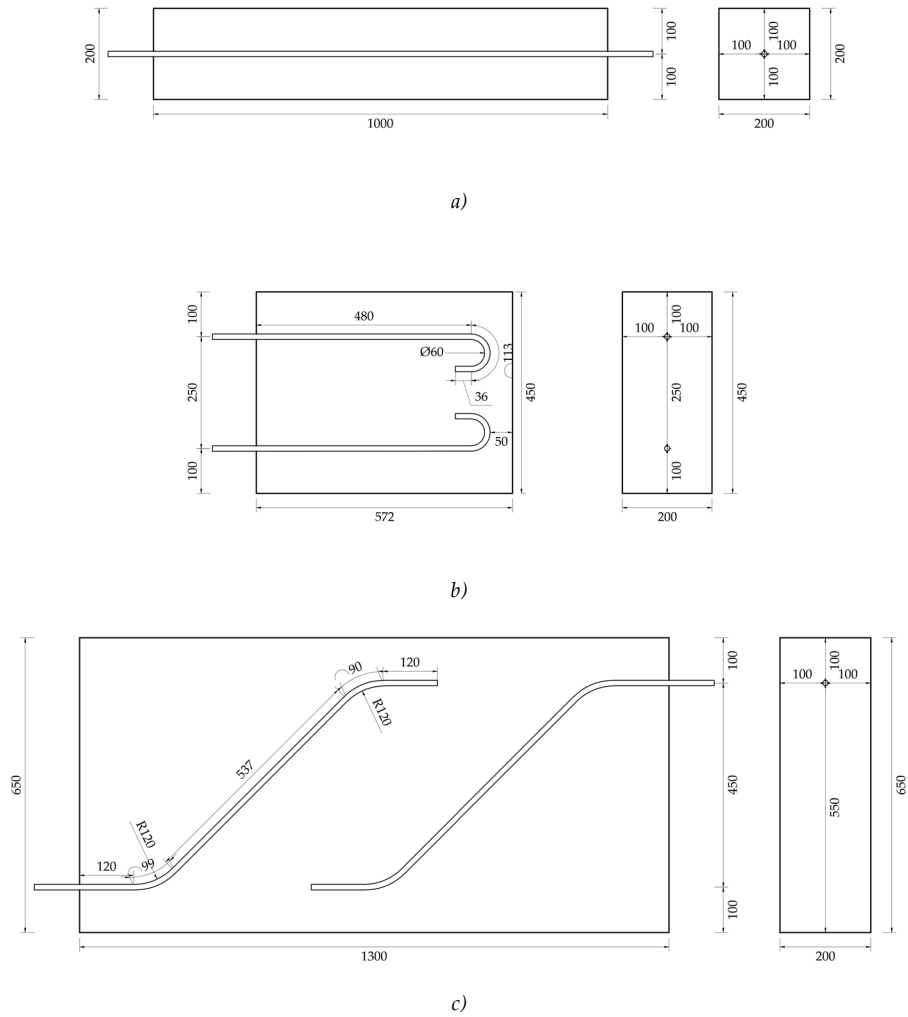
a)

b)

c)

Figure 81: Geometry of the reference specimens: Straight length bar SL-type a), Hook-end anchorage for the H- and HS-sample types and Bent rebars c). Dimensions refer to bar centreline.

Anchorage typologies and geometry

Hot rolled smooth rebar of diameter $d_b = 12mm$ is used in the reference samples; the choice is consistent with the most employed bar in the reference structures (Verderame et al., 2001); moreover, it allows to compare the test results with available similar ones (Fabbrocino et al., 2005; Verderame et al., 2009b). In a single concrete block one or two testing rebar are located for sample construction simplicity reasons; in any case, only one of them is loaded and it is supposed the other one does not affect the response, since a significant distance between them is guaranteed. On the other hand, the choice also allows to investigate different bond conditions effects, since it is possible to qualitatively consider the lower bar in good bond conditions and the upper one in bad bond condition, thanks to the specimen height. Brittle failure (concrete splitting), like that observed in (Fabbrocino et al., 2005) end-type sample, is prevented by a minimum concrete cover of 100mm in all the specimens types herein presented, so it is not under investigation.

The simplest solution of a straight rebar with no end specific detailing is considered for the specimens called SL-type. These are made by a concrete block with square cross section and length of 1000mm, in which a single bar is embedded (Figure 81.a). The aim is to investigate the bond performance over a significant rebar length, on which it is expect a non-constant bond stress distribution. In two out of four samples, three couples of strain-gauge are located along the rebar (Figure 85.a), at regular spacing, with the aim of measuring differential axial stress on the embedded length. In this way bond stress capacity can be evaluated on the partial lengths. The approach is the same already followed in the literature (Feldman and Bartlett, 2007). However, in that case a spacing lower than 100mm is guaranteed between the applied strain-gauges, thanks to the use of a bar hollowed square cross section. Here, the strain gauges are attached on the bar surface, thus the bond length is interrupted by the cage of the gauges (Figure 86), and a less discretized stress reading is possible. On the other hand, cyclic load effects on the rebar response are herein considered. The specific anchorage type is representative of the bar embedment into column or beam lengths. An analogous behaviour can be also noticed in the joint region, where a short embedded straight length is present.

The hook-end H- and HS-type specimens are representative of the T-joint beam reinforcement anchorage and of columns overlapping on a cold joint. The geometry of the specimens is referred to the latter case, more in detail Italian reference code (RD 2229, 1939) indications are followed. The $40d_b$ straight length (code imposed overlapping) is embedded (HS-type) or not (H-type) in concrete and an hook device follows it; the last is characterized by an inner bending diameter of amplitude $5d_b$ and a $3d_b$ final straight length. In the H-type samples, the adhesion between the bar surface and the surrounding concrete is prevented by a plastic pipe, like shown in Figure 82.b.

118

Finally, the typical bent shape (B-type specimens) is considered, since it was frequently used for the beam reinforcement crossing a joint region over the support. The role of this specific anchorage shape is to contribute to the shear resistance about the beam support (RD 2229, 1939; Santarella, 1956) and to move the rebar tensile resistance contribution for bending from the beam bottom at the beam midspan (sagging), to the top side on the support (hogging). On the other hand, a significant improvement in the anchorage capacity is expected, since not only tangential stress acts on the bar surface.

<table>
<tr><td align="center">*a)*</td><td align="center">*b)*</td></tr>
</table>

Figure 82: HS-type sample a) and H one with plastic pipe application b); pre-casting phase.

Type	Bar for block	Block number	Total bar	SG app. Bar
S	1	4	4	2
H	2	1	2	0
HS	2	2	4	0
B	2	2	4	2

Table 9: Reference specimens for smooth rebar anchorage evaluation; number of testing samples and indication of bars on which strain gauges (SG) are applied.

Load frame

A self-balanced steel frame is used to impose the axial load on the rebar head; its schematic view is shown in Figure 83. The apparatus is designed to impose a refined displacement control, thanks to a 3.5mm thread loading screw; the introduced load reacts on a steel plate, which is connect, by means of 3 circular struts, to another plate which reacts on the concrete block. When pull-out action is imposed, that is tensile force on the testing bar, the inner plate directly reacts on the concrete block face. On the other hand, when push-in action is imposed (compressive force on the testing rebar), it is balanced by the outer steel plate, which is connected with the frame by four 12mm threaded bars. These were lightly prestressed to avoid the plates detachment from the concrete surface but limiting the compression on the sample concrete to negligible values.

The smooth rebar sample is anchored to the loading apparatus through a commercial mechanical joint, composed by a hollow cylinder in which three high hardness steel screws punch the rebar surface under a specific tightening torque. A specific tensile test was performed to confirm that the joint allows the rebar failure out of the disturbed zone.

The rebar head-joint is fixed, thanks to a specific connector, to a load cell able to read both tension and compression loads; the latter is then fixed by a torsion-free joint to the loading screw. It is noteworthy to observe that the frame moving components are able to slide on the parallel struts by the means of low friction device (bronze material), whereas all the frame weight and loading torque are transmitted by the steel plates on external supports; in this way no bending or torque action affect the bar state of stress.
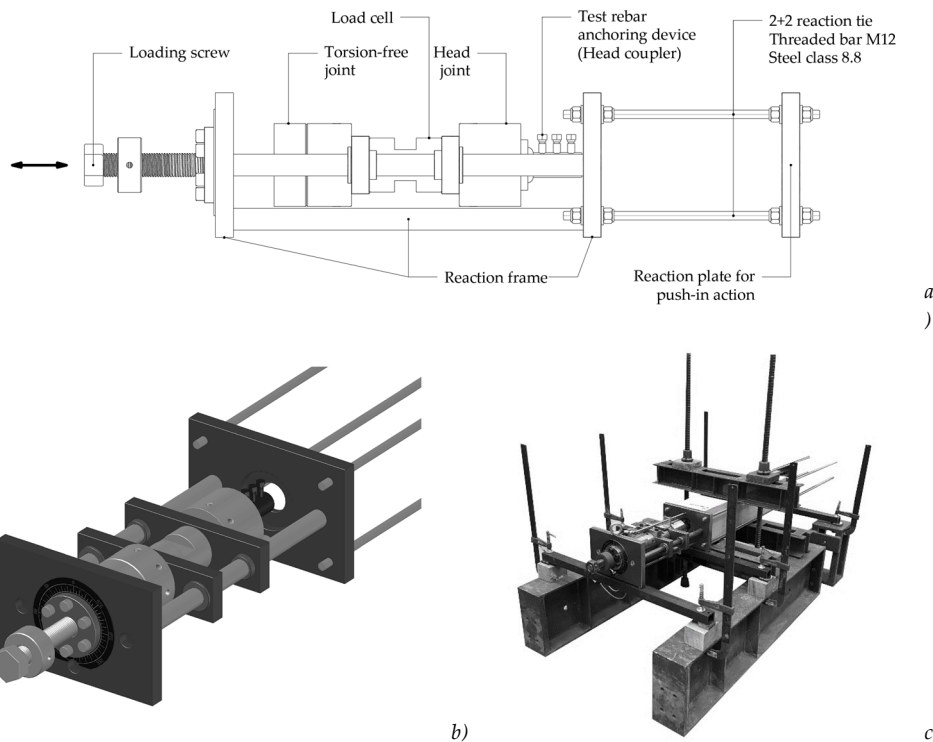

Figure 83: Schematization of the load frame a), 3D representation b) and application on a SL specimen c).

Instrumentation

Two different families of instruments are used for the herein expressed campaign: load and displacement transducers to monitor the bar axial stress-slip behaviour and strain-gauges to measure the axial strain along the rebar embedded length.

The main parameter to monitor during the tests is the rebar head slip out from the concrete block, which in a structural context is directly related to the member crack opening. For this aim, three LVDTs are placed between the fixed and the sliding part of the frame. They are located in order to catch eccentricity effect on the two main directions. A qualitative representation of the instrument's arrangement is shown in Figure 84. A compromise was taken with the transducers reading on the steel plate in contact with the concrete surface, instead of the concrete surface itself. As already mentioned, the plate was prestressed on the concrete member to avoid relative movements, which were monitored to be negligible throughout the test. Moreover, since the load frame is characterized by a very high axial stiffness, it should not significantly affect the evaluation of the bar slip. The obtained data are so considered adequate in representing the bar slip.
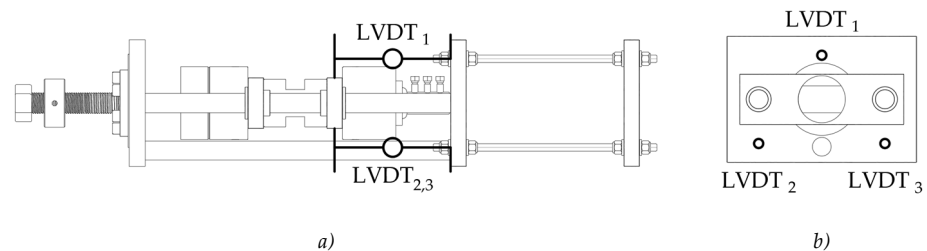

a)   b)

Figure 84: LVDTs disposition on the load frame a) and their arrangement respect to the rebar axis b).

The applied load is measured by a load cell, which acts both in tension and in compression; axial stress along the rebar is instead read by couples of strain-gauges. For two SL-type samples, 3 couples of strain-gauges are located at a regular spacing to monitor differential loading; in this way, the bond performance on the interval length can be evaluated. Furthermore, on two bent rebar samples, the extensimeter measures are taken at mid-length of the bar inclined segment and on the tile after the second bend, to monitor if the axial stress penetrates until these points. No bar strain measures are provided on the hooks or bends, to avoid disturbance. The disposition of the Strain-Gauge (SG) is schematized in Figure 85. Their application modifies the bar surface, the steel-concrete contact is thus inhibited on a finite length across the gauge application point; in this way the bond strength assessment is related only to the not disturbed bar lengths. For the aim, a plastic pipe of 40mm diameter is placed around the instruments and the void between it and the rebar is filled by low strength

121

viscous polymer (silicone), which also allow to prevent water infiltration during the casting phase. According to the schematization in Figure 86, the bond stress action is inhibited 60mm before the gauge application point and 20mm beyond it, for a total length of 80mm. The polymer mechanical properties do not affect the bond action in the interested zone, its stiffness is indeed negligible and the friction coefficient between it and the rebar is very low; to accommodate bar slip, a loose electrical cable length is provided, in this way no cable embedded length results activated. In the B-sample a steel plate is placed at the rebars free end; otherwise, if axial stress penetrates until this point, no strain (thus stress) can be read, since no mechanism would be able to balance it.
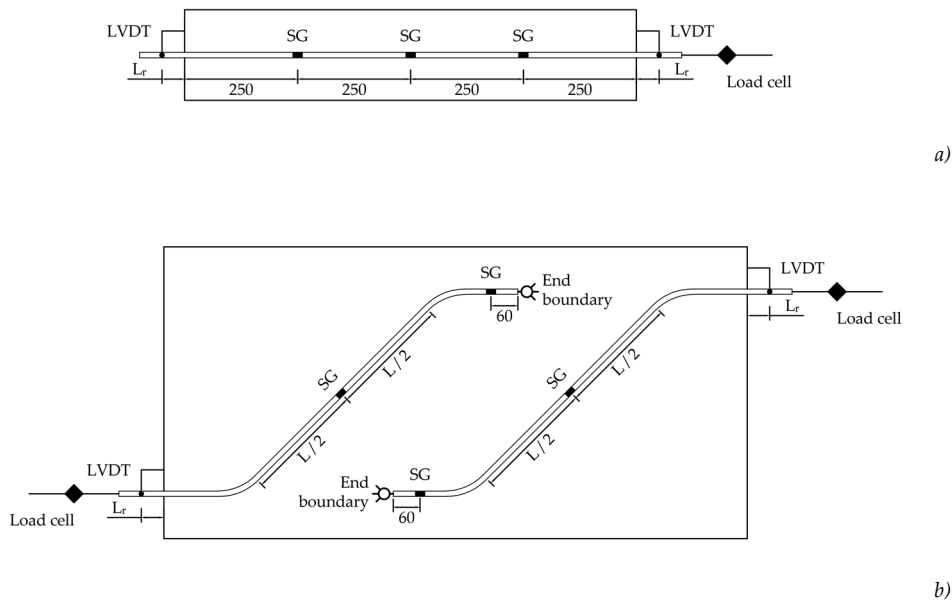

a)

b)

Figure 85: Instrumentation of the S-type a) and B-type b) specimens, with attention to the strain-gauge location.
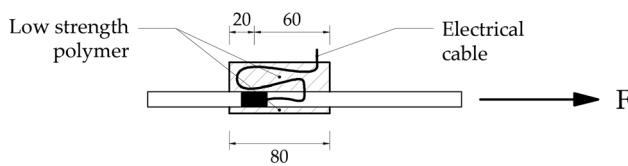

Figure 86: Detailing of the strain gauge isolation from the surrounding concrete.

3.3 Materials

The mechanical properties of the employed materials are representative of existing RC constructions. All the different casting can be classified in the category C16/20, according to (UNI EN 206, 2016). To represent the bond condition of plain reinforcement, structural steel of the type S275 (UNI EN 10025-2, 2005) is used; B, H and HS specimens are realized with similar steel batches, straight bar are instead characterized by higher yield stress. More details in Table 12.

Concrete

The reference mix design is based on a low strength cement and by a high water-content; in this way the compressive strength simulates the properties of a typical existing concrete (RD 2229, 1939), which significantly influence the bond performance. The specific concrete mix design is reported in Table 10: Portland cement CEM I-32.5 R (EN 197-1, 2007), 0.6 water over cement ratio and three different aggregates size characterize it. The slump (EN 12350-2, 2009) is 170mm for all the casts, except for SL one, which results in 100mm due to a water dosage accidental mistake in the concrete mix.

Cement content 32.5 [kg/m³]	Water [l/m³]	w/c	D1 (0-4mm) [kg/m³]	D2 (4-10mm) [kg/m³]	D3 (8-20mm) [kg/m³]
300	193	0.60	1129	470	282

Table 10: Bond test specimens concrete mix design.

Compressive tests on almost two cylinders for each casting were done, according to (UNI EN 12390-3, 2003); the results show a low homogeneity of the concrete. Since the bond strength is strongly related with compressive concrete strength, three different mean values are considered (one for each specimen type). The same approach is followed also for the definition of the reference Young modulus, established according to (UNI EN 12390-13, 2013); for the casting B2 only a cylinder sample is available for the specific analysis, the relative CoV index is not thus calculated. The assessed elastic modulus can be well predicted according to (Priestley et al., 2007) indications:

$$E_c = 5000\sqrt{f_c}$$

Parameter	Cylindrical strength f_c [MPa]			Young modulus E_c [MPa]		
Casting	Mean [MPa]	CoV	Assumed	Mean [Mpa]	CoV	Assumed
S	24.71	1.99%	24.71	25490	2.68%	25490
H	19.53	5.39%	19.53	22810	6.87%	22810
B1	23.02	1.10%	22.52	24870	4.78%	25175
B2	22.01	3.03%		25480	NA	

Table 11: Bond test concrete characterization by compressive strength and elasticity modulus; mean values and relative Coefficient of Variations.

Plain bar steel

Uniaxial tensile tests on the different steel batches adopted were performed according to (UNI EN 10080, 2005). Yielding and failure stress, elastic modulus and elongation at the maximum load are defined respectively for all the embedded hook-end and bent rebars, whereas only a representative sample is analysed for the characterization of the straight bars, which have been all extracted from the same steel bar the testing sample was cut from. The length of the testing bars is 400mm ($33d_b$). The results, in term of load-displacement (total bar elongation) relationship, are shown in Table 12; the main mechanical properties are also reported.

It is possible to conclude that the behaviour of the hooked and bent employed rebar well represents the properties of the smooth reinforcement employed in the construction from the second World War to the Seventies (Verderame et al., 2001). The SL samples bar is instead stronger. The mean steel modulus of elasticity can be assumed equal to 200000MPa.

X	SL	H	B
f_y [MPa]	442	361	363
f_t [MPa]	535	519	520
A_{10} [%]	13.70	20.16	18.98

Table 12: Uniaxial tensile test on the bars employed in the bond tests; Straight Length (SL), Hook-end (H and HS) and Bent (B) types.

3.4   Loading protocol

The load is applied along the bar axis, firstly as a pull-out action, simulating the tension on the rebar due to bending, then, cyclic effects are simulated pushing the rebar in its original position. The aim is to represent the boundary condition in crack opening and its successive closure.

In presence of hook-end and bent rebar the same load pattern is followed; in the elastic field two cycles at 3 different tensile levels are imposed, then, after reaching

yielding, increasing slip amplitude is imposed at each cycle (Figure 87.a). A summary of the investigated reference performance levels is reported in Table 13. Due to non-linear stress-slip behaviour, the recovery of null slip occurs under a compressive force acting in the rebar; in presence of unbounded straight length the load reversal is not applied to avoid buckling, which can be anticipated being the bar not laterally restrained by the surrounding concrete.

In presence of straight embedded bar length the test was pushed monotonically up to a displacement amplitude of 2 or 3mm, depending on the specimen response, just beyond the peak of bond resistance or rebar yielding (Figure 87.b). The protocol is summarized in Table 13 e Table 14.

	Reference stress level (In tension)	Number of cycles
Elastic field	$0.20f_y$	2
	$0.40f_y$	2
	$0.80f_y$	2
	$1.00f_y$	2
Plastic field	Reference slip magnitude (In tension)	Number of cycles
	$5mm$	1
	$10mm$	1
	$15mm$	1
	$20mm$	1
	$30mm$	1

Table 13: Load pattern followed in the H, HS and B specimen tests.

Specimens	Reference slip magnitude	Number of cycles
SL1-SL2	$3mm$	2
	$6mm$	2
	$12mm$	2
	$18mm$	2
	$24mm$	2
SL3-SL4	$2mm$	2
	$4mm$	2
	$8mm$	2
	$16mm$	2
	$24mm$	2

Table 14: Loading protocol for straight embedded bar (specimens SL).

a)   *b)*
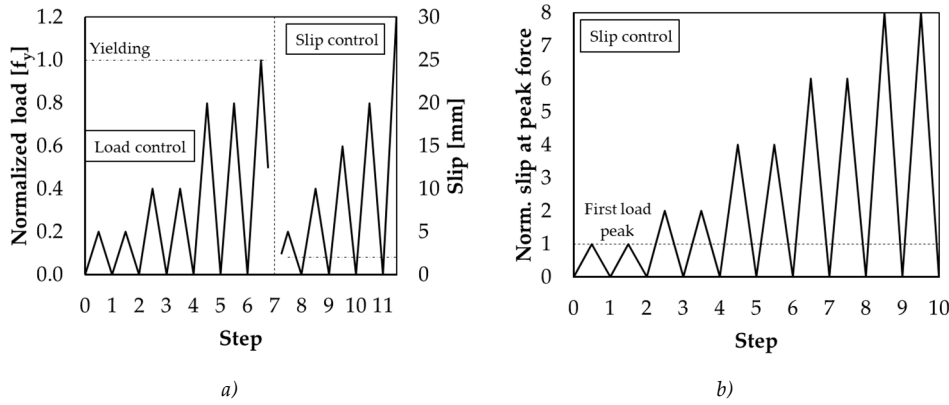
*Figure 87: Graphs about the shaped rebar loading protocol, with reference to shaped bar a)
and straight one b) tests.*

3.5   *Experimental results*

The main result of the tests is expressed in term of bar axial load versus slip. A reference axial stress σ_0 is derived through the reading of the applied load N_0:

$$\sigma_0 = \frac{4N_0}{\pi d_b^2} \qquad (114)$$

where $d_b = 12mm$ is the rebar diameter.

Considering the location of the transducers previously described and represented in Figure 84, the reference measure s_r is defined by the following:

$$s_r = 0.5\left(s_{r1} + \frac{s_{r2} + s_{r3}}{2}\right) \qquad (115)$$

where s_{r1} is the reading of the LVDT placed over the bar axis, s_{r2} and s_{r3} are instead the output of the instruments couple symmetrically placed under it.

The axial load results entirely applied at a distance L_r from the first bar embedded section; more in detail, in the section below the first punching screw of the bar head joint (Figure 88). Consequently, to know the real slip of the first bar section out of the concrete embedment, the elastic elongation on the free rebar length L_r is subtracted from the instrumentation reading:

$$s = s_r - \varepsilon(\sigma_0)L_r \qquad (116)$$

where s and s_r are the head bar slip and the displacement of the reference section respectively, $\varepsilon(\sigma_0)$ is instead the strain associated to the axial stress σ_0. For the SL-type samples, the slip measurement is done also on the bar tail (Figure 85.a), by the mean of another LVDT. In this case no correction is needed, since no axial stress can act on the free bar end.
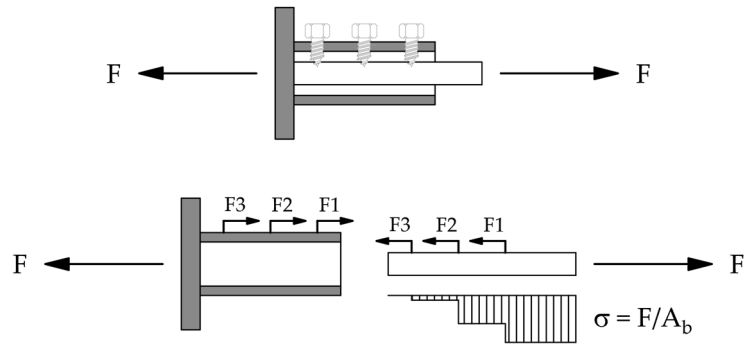
126

Figure 88: Schematization of the tensile force transmission between bar head and the punching joint.

Bar strain reading is translated in stress data through the application of the reinforcement steel elastic modulus E_s. For each monitored internal section (Figure 85), a mean value between the two gauges reading ($\varepsilon_1; \varepsilon_2$) is considered, thus:

$$\sigma_g = \frac{\varepsilon_1 + \varepsilon_2}{2} E_s \qquad (117)$$

where the readings of the strain data in the same bar section are significantly different to each other, the instrument whose data are the less representative is not considered and only a gauge is assumed for the stress calculation. Indeed, no flexure is expected to act in the rebar. This is the case of SL4 specimen, with reference to the couple of gauges placed at the sample half length. On the other hand, if both the gauges placed on a bar section read not consistent values, the stress experimental data are missing (a bent bar in midway on its inclined length).

Straight bar

In straight embedded bar samples, the applied axial load is balanced only by bond stress acting between the steel and the surrounding concrete. Because of this, the strength of the SL-type samples is strongly affected by the embedment total length, which is equal to 1000mm in the case of SL1 and SL2 specimens and equal to 760mm for the instrumented SL3 and SL4 rebars. The first ones allowed to reach the bar yielding axial force in tension N_y, the second ones a maximum load of about 30kN ($\simeq 0.60 N_y$). The slip magnitude at the reach of the peak strength was equal to $s = 1.21mm$ in SL3 case and to $s = 1.09mm$ for SL4 one. During slip recentering, the yield stress in compression is not reached by any bar. Indeed, the maximum compressive peak force was registered for the SL2 sample at a slip $s = 0.22mm$, it results $N_{min} = 94\% N_y$. In the other cases, the peak compressive force was related to the mobilization

127

of the reduced peak bond strength after the load reversal. The load versus slip behaviour is visible in the graphs of Figure 89; more details in Table 15.

The envelope of the experimental response assumes a non-linear shape characterized by a progressive loss of the tangent stiffness. After this, full embedded length specimens show a plastic plateau extended up to a slip level of about 6mm; SL3 and SL4 rebars exhibit instead an initial higher rate of strength degradation and a successive tendency to an asymptotic strength value. These behaviour confirm the evidence outlined in (Verderame et al., 2009b). SL1 and SL2 bars show strength degradation too, but it follows bar plasticization. In any case, the beginning of the load decay is related to the incipient slip of the bar tail.

Bar	N_{max} [kN]	$s (N_{max})$ [mm]	N_{min} [kN]	$s (N_{min})$ [mm]
SL1	51.39	2.53	-40.13	5.26
SL2	49.96	4.24	-47.11	0.22
SL3	33.91	1.21	-33.74	0.34
SL4	31.24	1.09	-26.01	0.75

Table 15: Numerical data about the peak strength point registered during SL-type specimens testing.

Regarding the cyclic behaviour, an unloading non-linear branch can be identified. Its shape is very close to the loading curve one; therefore, a gradual stiffness degradation follows a first stiffer unloading. On the other hand, the description of the re-loading phase is more complex. However, it is possible to conclude that before the triggering of the bar end slip, the reloading curve is secant to the point of maximum displacement reached during the previous cycle (Figure 89 and Figure 90). After the incipient slip of the last embedded section, the following can be concluded:

- a strength lower bound for the cyclic max strength N_c can be identified cycling at a slip level already explored in previous cycles, under tension or compression force;
- increasing the already exhibited slip, a strength recover is observed and an upper bound N_r, related to reloading phase, is observed;
- slip magnitude and number of cycles seem not to affect the amplitude of the above described strength values (N_c and N_r).

An estimation of the two limits above identified is reported in Table 16, in terms of absolute and relative strength values.

In Figure 91 bar head stress versus bar end slip behaviour and bar head versus bar end slip relationships are reported. The head and end displacements are linearly related to each other. More in detail, it is possible to identify a head slip value at which the bar end section begins to move; moreover, after this activation, a rigid sliding of the rebar can be noticed. Loading and unloading phases seem not to alter the slope of the relationships shown in Figure 91.a. In other words, during the load

reversal, the end bar section does not slip until the bond stresses over all the embedded length are mobilized. This is clearly visible from the observation of the vertical branch of the head slip (Figure 89) and of the end slip (Figure 91).

Sample	Cyclic strength Nc		Reloading strength Nr	
	Abs. [kN]	Rel. [Nmax]	Abs. [kN]	Rel. [Nmax]
SL1	12	0.23	22	0.43
SL2	12	0.24	19	0.38
SL3	6	0.18	15	0.44
SL4	8	0.26	12	0.38

Table 16: Estimation of the reloading strength limits for the different bar samples; qualitative definition of the force magnitude and relative comparison with the peak strength reached in the first tensile loading.
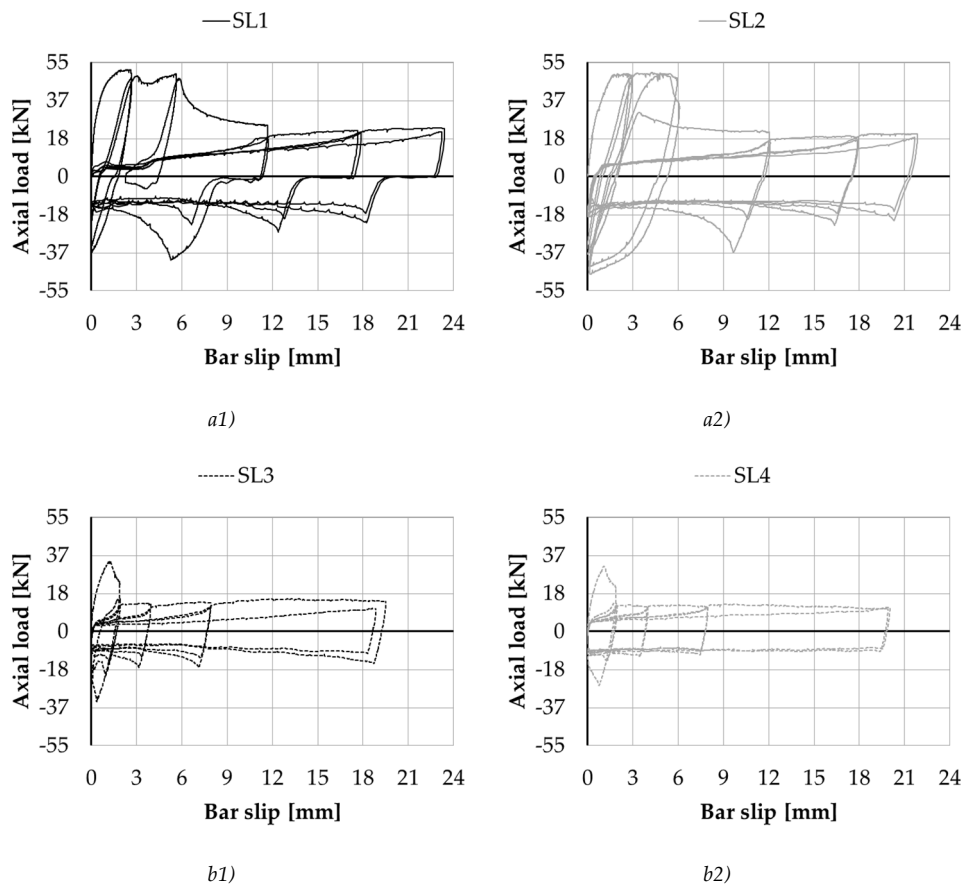

a1)   *a2)*

b1)   *b2)*

Figure 89: Stress-slip behaviour of the SL-type specimens: full embedded length samples a) and instrumented (partial unbounded length) ones b).
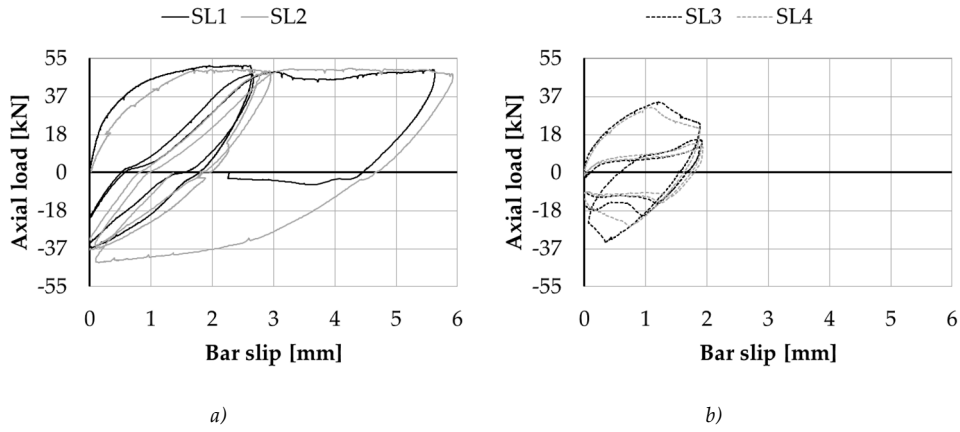
129

Figure 90: Focus on the bar head stress-slip behaviour of the straight embedded bars.
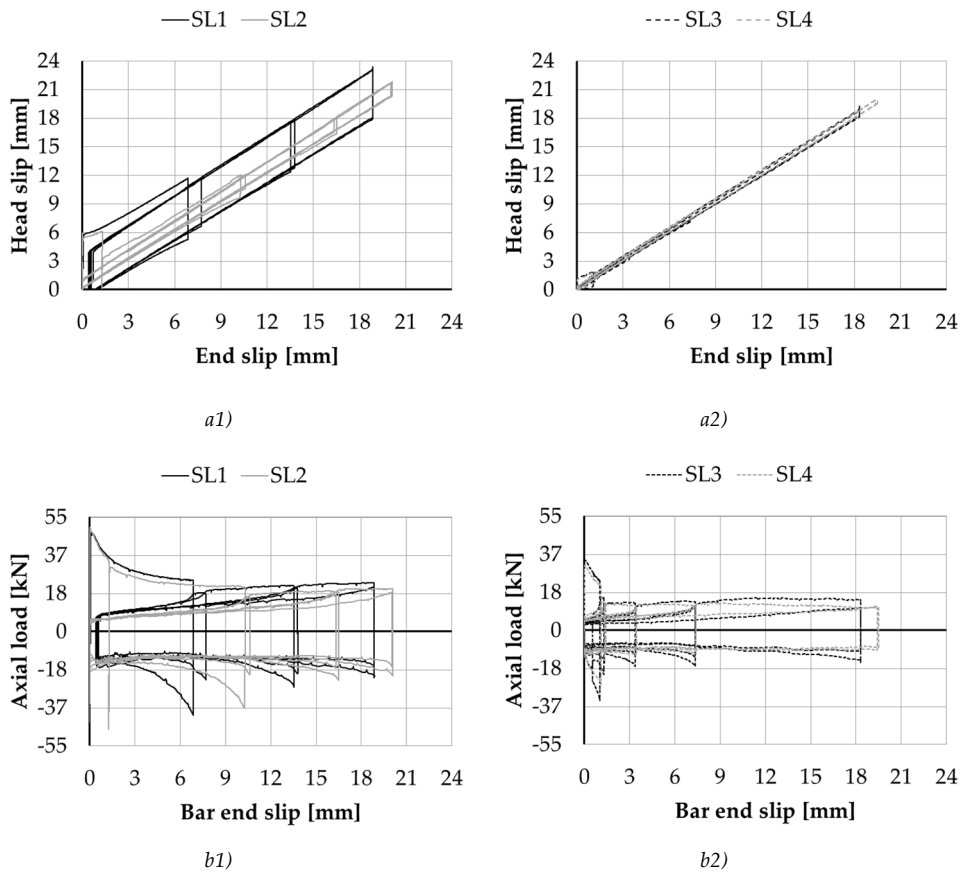

Figure 91: End slip relationships with bar head slip a) and load b); full 1) and partial 2) embedded length specimens.

With reference to the location along the rebar length, the three couple of strain gauges placed on the specimens SL3 and SL4 are called G25, G50 and G75, indicating their distance (in centimetres) from the rebar head. In Figure 92 the stresses along the rebar length versus its head slip are plotted. They are characterized by the same main shape, exception for the last couple of gauges G75, which measured low stress level and did not show load inversion. The overall behaviour is consistent with the one previously discussed, with reference to the axial load versus bar head slip. A peak stress is reached during the first loading phase and a reloading and residual values are defined in the successive cycles.

It is interesting to compare the magnitude of the stresses with respect to the relative bar head slip in the point of maximum strength, for peak tensile (Max) and compressive (Min) loads respectively. The reference for the relative comparison is set on the applied stress σ_0. The stress reading in the G25 position returns stress values higher with respect to the applied one, both for SL3 and SL4 specimens. Since this is not physically possible, a data conversion error has to be accepted and major attention is put on the stress penetration beyond the G25 location, in term of relative values. An increasing bond performance capacity is noticed, moving from the load application point to the bar end; indeed, the differential stress read between the gauges increases in this direction. The conclusion is observed only for tensile action, because at the reversal loading no stress inversion is read in the couple G75. The slip at the maximum strength point is the same for all the stress measurement. The load degradation is thus suffered, after the incipient movement of the last embedded section, along all the rebar length.
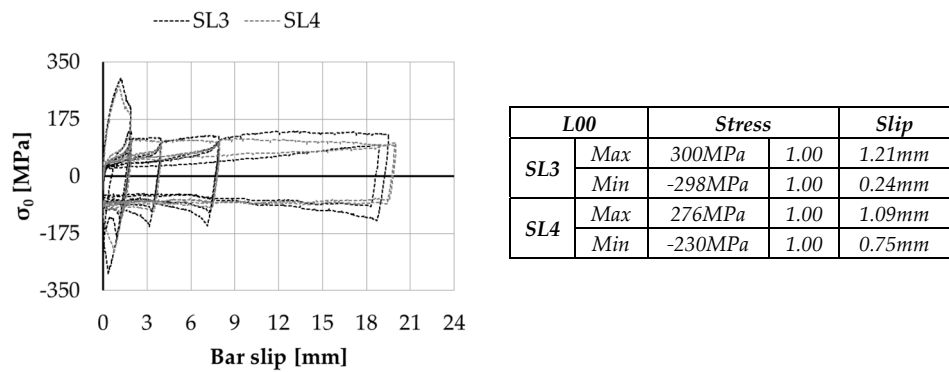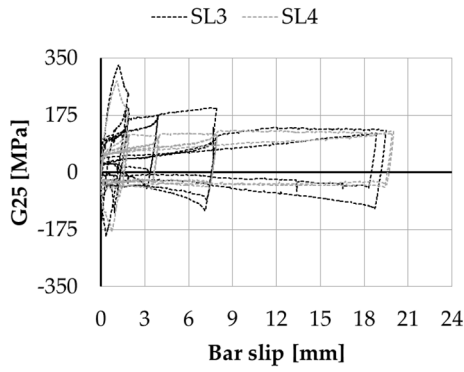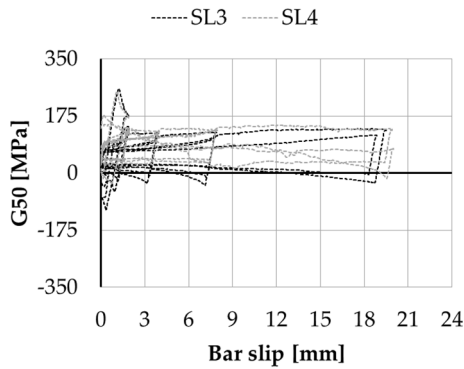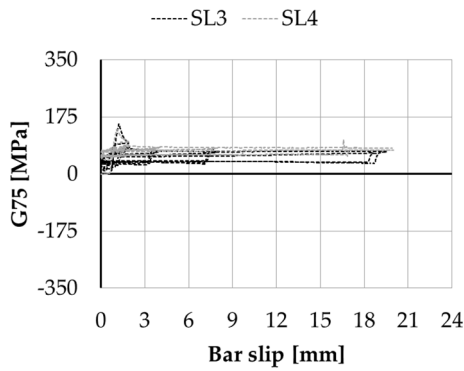

L00		Stress		Slip
SL3	Max	300MPa	1.00	1.21mm
	Min	-298MPa	1.00	0.24mm
SL4	Max	276MPa	1.00	1.09mm
	Min	-230MPa	1.00	0.75mm

Figure 92 (Pt. 1 of 2)

131

L25		Stress		Slip
SL3	Max	329MPa	1.10	1.23mm
	Min	-196MPa	0.66	0.34mm
SL4	Max	279MPa	1.01	1.09mm
	Min	-182MPa	0.79	0.75mm

L50		Stress		Slip
SL3	Max	258MPa	0.86	1.23mm
	Min	-115MPa	0.38	0.34mm
SL4	Max	250MPa	0.91	1.09mm
	Min	-33MPa	0.14	0.75mm

L75		Stress		Slip
SL3	Max	153MPa	0.51	1.24mm
	Min	-1MPa	0.00	0.37mm
SL4	Max	136MPa	0.49	1.11mm
	Min	0MPa	0.00	0.01mm

(Pt. 2 of 2)

Figure 92: Stress-slip relationships along the rebar length: experimental graph and identification of the point of maximum and minimum stress reading (in term of absolute and relative value).

It is interesting to compare the magnitude of the stresses with respect to the relative bar head slip in the point of maximum strength, for peak tensile (Max) and compressive (Min) loads respectively. The reference for the relative comparison is set on the applied stress σ_0. The stress reading in the G25 position returns stress values higher respect to the applied one, both for SL3 and SL4 specimens. Since this is not physically possible, a data conversion error has to be accepted and major attention is put on the stress penetration beyond the G25 location, in term of relative values. An increasing bond performance capacity is noticed, moving from the load application point to the bar end; indeed, the differential stress read between the gauges increases in this direction. The conclusion is observed only for tensile action, because at the reversal loading no stress inversion is read in the couple G75. The slip at the maximum strength point is the same for all the stress measurement. Load degradation is thus suffered, after the incipient movement of the last embedded section, along all the rebar length.

Hook-end bar

The first analysed experimental evidence is relative to the behaviour of the hooked rebar in presence of unbounded straight length (H3 specimens), in order to better understand the response of the other ones (HS1 and HS2 samples). In the following the bar embedded in the concrete block bottom is identified by Good Bond condition (GB), whereas the upper encased one is identified by Bad Bond condition (BB). The reference nomenclature is:

$$H3 - GB \quad H3 - BB$$

$$HS2 - GB \quad HS2 - BB$$

$$HS3 - GB \quad HS3 - BB$$

H3 specimens shows an initial non-linear response. A stiffer behaviour was exhibited at the low slip magnitude, then a gradual loss of stiffness and the final reach of a plastic plateaux were noticed. The relative load, slightly higher than $40kN$, is consistent with the yielding stress shown in the characterization of the steel mechanical properties and it is reached in presence of a slip $s \simeq 2.5mm$. H3-BB sample exhibits hardening after the reach of $12mm$ bar slip. The maximum resisted load is $59kN$, also in this case consistent with the result of the uniaxial tensile test on the bare bar. The response confirms the effectiveness of the hook in ensuring the rebar full anchoring. The sample H3-GB did not follow the reference loading protocol and the relative test was stopped at low slip magnitude, due to practical issues in the testing phase. Anyway, the behaviour of both the H3 specimens were very similar, like clearly visible in the focus of Figure 93.b.

The unloading phase showed residual slip also in presence of bar elastic behaviour. Cycling at $\lambda = 0.8$ (with $\lambda = \sigma_0/f_y$ non-dimensional bar stress) more than $0.5mm$ residual slip was observed, a third of the imposed slip magnitude was so not recovered. Unloading and re-loading stiffness seemed not to be affected by the number and magnitude of imposed cycles, as a matter of fact the relative graph slopes were the same during all the test. Both were higher than the slope of the secant line at the yielding point, therefore a different governing mechanism could be identified with respect to the one related to the first loading phase. Observing the curve envelope, no strength decay was observed.

It is worth noting that the herein reported stress-slip curves are very different respect to the ones outlined in (Fabbrocino et al., 2005, 2004), due to the consideration of a diverse reference displacement. The latter plot the slip of the hook head, whereas the former show the slip of a section placed 480mm far from the hook; therefore, the influence of a bare bar straight length must be considered.
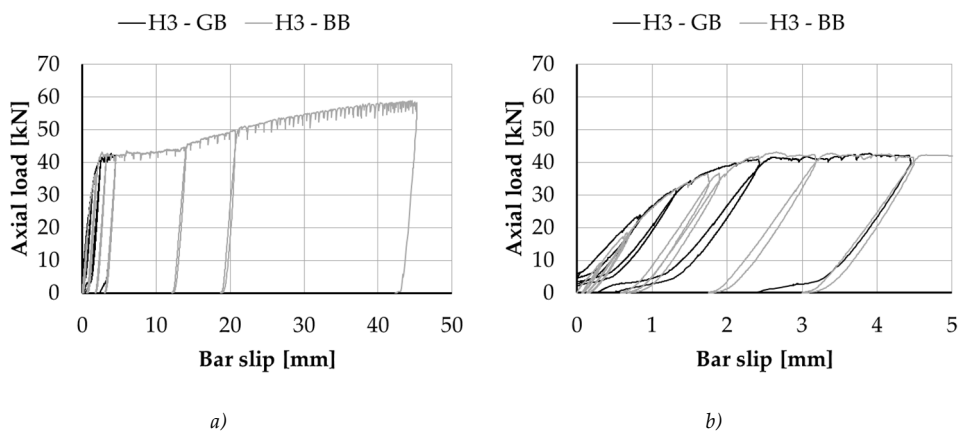

Figure 93: Experimental response of H3 samples: full investigated behaviour a) and focus on the low slip level b).

H1 and H2 specimens differs from the previous described H3 one because of the embedment of the straight length, which precedes the hook device. Thanks to this difference, a slightly higher resisted force can be expected. Moreover, compressive axial load can be introduced in the rebar. With reference to the envelope under tensile loads, the plot of the experimental results showed the same features observed for the sample H3. The non-linear load-displacement loading branch is more visible for the bar located in the upper part of the concrete block, where worse bond condition can be expected. The same bars present a significantly lower stiffness and a slight lower strength; the latter can be however considered consistent with the yielding stress value characterizing the plain bar mechanical properties. To assess if the cyclic load affects the stiffness and strength capacity of the anchored rebar, less cycle number is imposed to the H1-BB and H2-GB specimens. In both the cases cyclic degradation is

not observed. On the other hand, the role of the bond conditions is confirmed, indeed, H2-GB sample shows performance comparable with H1-GB response and the envelope of the H1-BB response is very similar to H2-BB one. The lower bars (GB) reach yielding stress in presence of a slip $s \simeq 1.0mm$, the upper ones (BB) in the range $1.5mm \leq 2.0mm$.

The recovery of the imposed slip in tension shows a compressive stress versus bar slip behaviour less stiff than the one observed in presence of tensile load. Thanks to the high plastic deformation imposed to the bar in the loading phase, a compressive strength higher than the yielding load was however reached. On the other hand, it was not possible to clearly identify a yielding plateau and a successive hardening phase. During the tensile load imposition, the concrete surrounding the first bar embedded length was subjected to damage, as it is reported in Figure 95. The resulting higher bar free length caused the buckling of the rebar, which is related to sudden loss of strength. This is visible in the graphs 1) of Figure 94, with reference to the load reversal in the range $15mm \leq s \leq 20mm$. After this, the imposition of the compressive load was stopped and a last loading phase under tensile action was done. Unloading and re-loading stiffness did not show significant degradation due to cyclic effects.
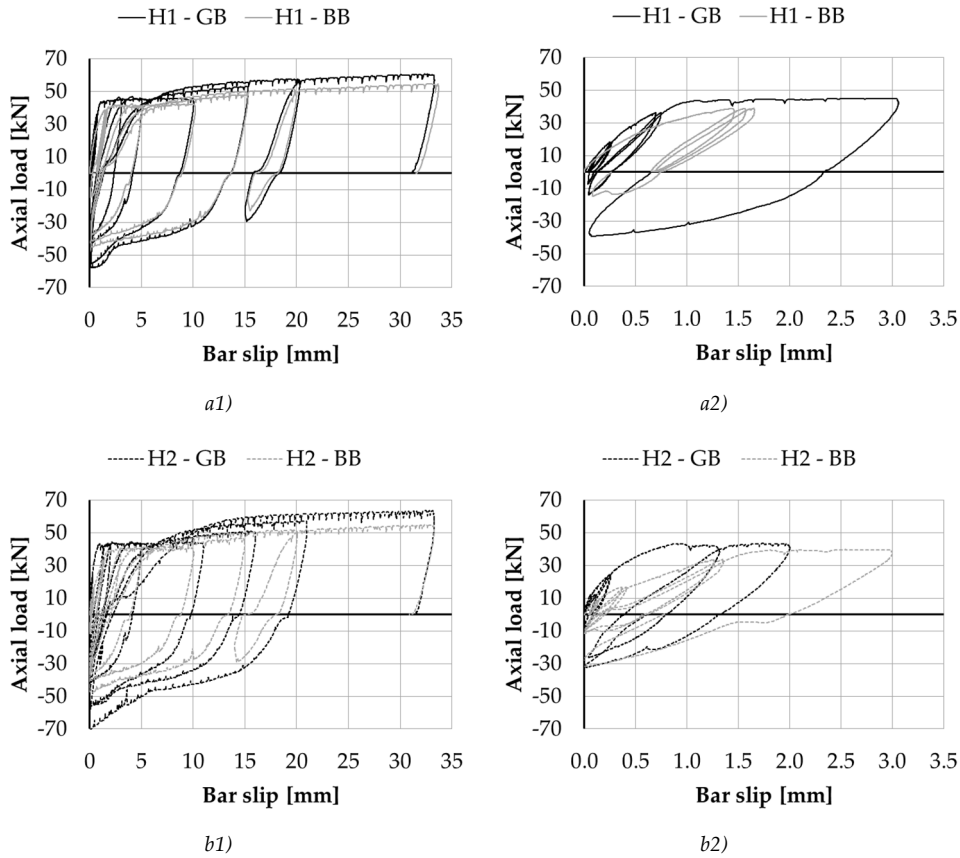
a1)

a2)

b1)

b2)

Figure 94: Stress-slip response for hook ended embedded plain rebar: H1 a) and H2 b) specimens behaviour, with reference to high 1) and low 2) investigated slip magnitude.
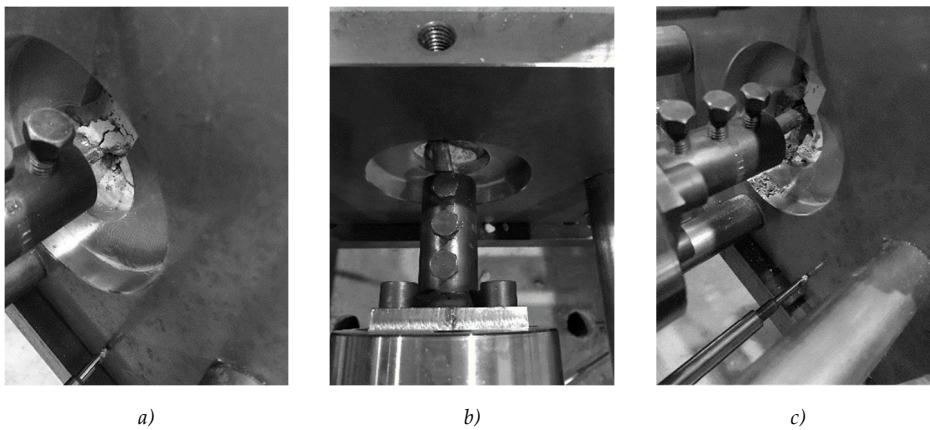

a)

b)

c)

Figure 95: Concrete damage under tensile loads and bar buckling: B1-GB a), B2-GB b), B1-BB c) examples.

Bent rebar

The herein analysed bars cross the concrete block from its top to its bottom and viceversa, therefore they can be qualitatively considered both in good and bad bond conditions. In the following the codes GB and BB are relative to the bar head, or rather to the load application point.

The observed overall behaviour was very closer to the one exhibited by the hooked bars. The elastic cycles were enveloped by a non-linear curve, which reached its yielding at a load mean level consistent with the bar yielding stress (363MPa) and in presence of a slip always lower than $1.50mm$. It is possible to conclude that the loading elastic stiffness of the B-type samples was close to the HS type ones. It is worth also noting that the bar inclined straight length was 540mm long, whereas the HL straight length was 480mm long; these are thus similar to each other, especially in the case of the instrumented B2 rebars. In presence of strain gauges application (geometrically detailed in Figure 85), no significant difference is outlined in the experimental assessed response. Contrary to what was observed for the hook-end bars, the steel hardening started at a slip level lower than 5mm. Furthermore, B1-BB and B2-GB samples reached a maximum strength $N_{max} \simeq 59kN$ before to exhibit a strength degradation; the peak force, reached in the slip range $15mm \leq s \leq 20mm$, is consistent with the steel mechanics characterization.

In presence of compressive load, a very low stiffness was exhibited during the slip recovery. In spite of this, the rebars however reached the yielding stress during the load reversal; the minimum reached force was higher than 50kN in magnitude. Investigating slip value higher than 10mm, the load reversal showed bar buckling. This phenomenon was visible through the observation of the complete response of the specimens B1, which showed significant loss of load in the two last compressive cycles (Figure 96.a1).

In Figure 97, the stresses read at the half of the bent length and on the bar end are reported as a function of the imposed head stress σ_0. The former are identified with the code HG (Half-length Gauge), the latter with the code EG (End-length Gauge). Cause to wiring error, no plot data about the bar strain on the half-length of the sample B2 - BB were available. It is possible to observe a clear relationship between the head load and the one read on the bent length; indeed, the increasing of the former is linearly related to the increase of the latter. The unloading was represented by a very stiff behaviour. In presence of tensile load, the first gauges couple was activated at the lower stress level; on the other hand, in presence of compressive action, they did not work until the bar explored yielding in the loading phase (see detail in Figure 98). More difficult is the interpretation of the end gauges reading; they worked only in tension and with a maximum load of about 100MPa for the sample B2-GB and of about 30MPa for the B2-BB specimen. Both activated only after the reach of a bar head slip higher than 5mm.
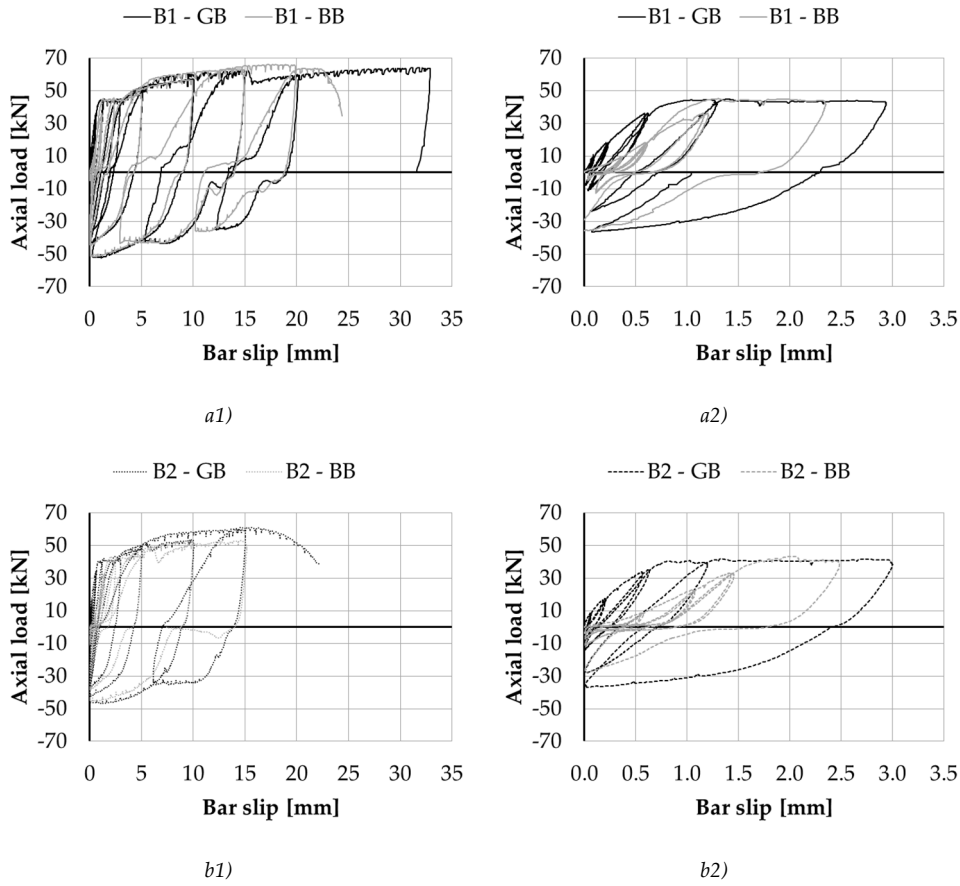
137

a1)

a2)

b1)

b2)

Figure 96: Stress-slip response of the bent rebars: B2 - GB a) and B2 - BB b) overall behaviour 1) and focus on cycle at low slip magnitude 2).
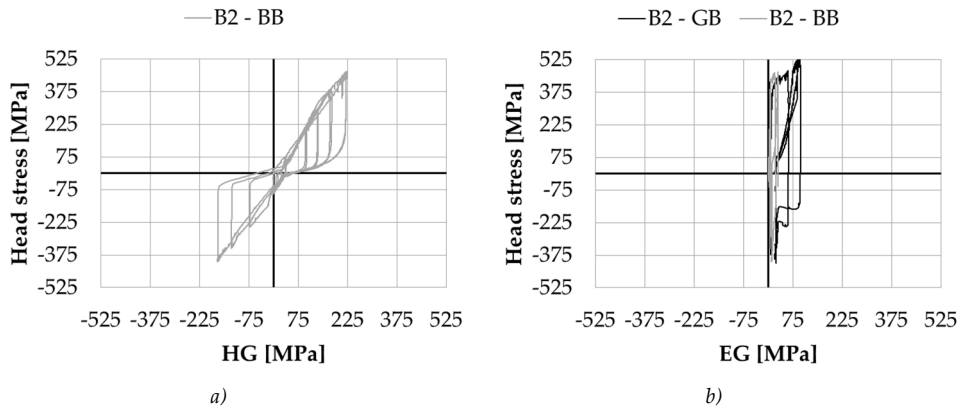

a)

b)

Figure 97: Stress at a) the half of bar bent length (HG) and b) in its end (EG).

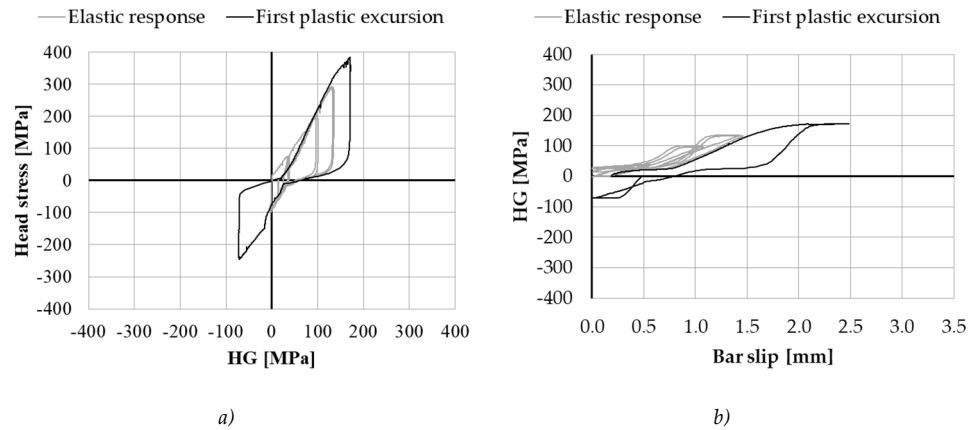a)   b)

Figure 98: Focus on strain gauges reading about the elastic response of the sample B2-BB: bar head load versus half gauge stress a) and half gauge stress versus slip measurement b).

3.6   Analysis of the experimental results

Range of interest slip

It is worthy to set a reference slip range representative of structural application. (Verderame et al., 2008b, 2008a) experimental tests on standard geometry columns showed crack width at yielding in the range of $2mm \leq w \leq 3mm$; the maximum opening in presence of a global drift $3.00\% \leq \theta \leq 4.00\%$ was instead in the range $6mm \leq w \leq 8mm$. On the other hand, for beam members, the yielding drift demand can be assumed in the range $1.00\% \leq \theta \leq 3.00\%$ (Marefat et al., 2009); the relative crack width is then estimated depending on the element properties. Assumed a standard beam cross section height $H\_b = 40 \div 50cm$, a reference crack width can be however assumed lower than 10mm.

Because of symmetry (Figure 99), the crack width w estimation and the bar slip from a concrete block s can be related by the following:

$$w \simeq 2s \qquad\qquad (118)$$

Therefore, an interesting slip range can be fixed in $s \leq 5mm$. Anyway, the experimental tests previously described explored a wider range of slip. The choice allowed to better investigate the experimental behaviour of the anchored bar in the elastic and plastic field, ensuring a good representation of the crack opening during the cyclic actions. At the same time, the exploration of high slip level also allows the study of the anchorage effectiveness.
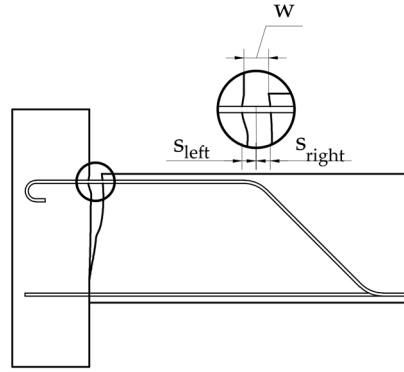
Figure 99: Correlation between bar slip on a crack side and its width (w).

Straight bar

To analyse in the detail the experimental results of the SL specimens, in term of load versus slip behaviour, each relationships plotted in Figure 89 and Figure 90 is enveloped. A mean response for both the full embedded length samples (SL1 and SL2) and of the partial embedded length samples (SL3 and SL4) is then calculated. The first loading branch analysis is divided from the cyclic response since the degraded re-loading bond performance does not allow to reach the first loading stiffness and strength. Graphic results about the procedure are reported in Figure 101. As already observed, the full-length specimens (called L1000 in the following) exhibited a stiffer and more strength behaviour with respect to the partial embedded length ones (L760 in the following). Furthermore, the formers balanced the bar yielding force, whereas the latter no.

Considering Code (Model Code, 2010) and literature available (Verderame et al., 2009a) proposals, it is possible to assign the following bond strength capacities. With reference to the first loading response and to the re-loading one respectively:

$$\tau_{bp} = 0.30\sqrt{f_c} = 1.49 MPa \qquad (119)$$

$$\tau_{br} = 0.09\sqrt{f_c} = 0.45 MPa \qquad (120)$$

By the imposition of the bar axial equilibrium (Figure 100), it is then possible to identify a reference re-loading strength:

$$N_r = \pi d_b \tau_{br} L_e \qquad (121)$$

where $d_b = 12mm$ is the bar diameter and L_e is the total embedded length. The predicted values for the L1000 and L760 cases are reported in Figure 101.b2. The comparison with the experimental response shows a very good strength prediction for the partial embedded length, a stronger reloading characterizes instead the SL1

and SL2 samples. It is also possible to predict the complete load versus slip response, by the assumption of: i) constant bond stress along all the rebar embedded length and ii) rigid-perfectly plastic bond-stress relationship. According to Figure 100 the following can be deduced:

$$s = \frac{\sigma_0 L_e}{2E_s}$$

(122)

where σ_0 is the bar head axial stress and E_s the reinforcement steel modulus of elasticity. In other words, the slip is assumed to be the integral of the bar strain on the embedded length L_e, on which the bond stresses are sufficient to balance the applied load.
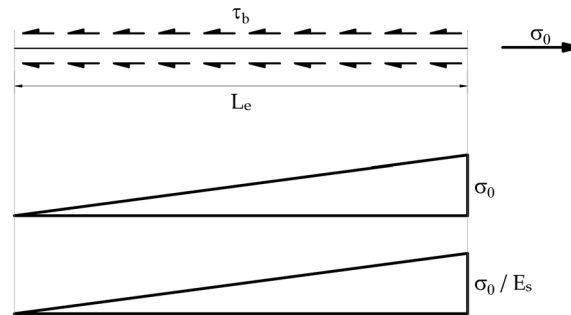

Figure 100: Stress and strain profile acting on a straight embedded bar subjected to constant bond stress.

A graphic comparison between the analytical prediction and the experimental envelopes is shown in Figure 101.b1. Both the application on L1000 and L760 show a too stiff prediction. It is clearly visible at all the investigated slip level, especially near to the peak strength point. The predictive curves are stopped at the minimum force between the yielding one (SL1000), and the maximum load balanced by the bond strength on the embedded length (SL760). In the second case, the analytical maximum resisted load is higher than the experimental one. A lower bond capacity is thus expected.

With the same hypotheses, it is possible to estimate the experimental bond strength capacity $\tau_{b,exp}$ (assumed as constant along the embedded length) by the following:

$$\tau_{b,exp} = \frac{N}{\pi d_b L_e}$$

(123)

where N is the experimental observed peak (N_{max}), cyclic (N_c) and re-loading (N_r) force, which have been previously defined. Numerical values about the max capacity are reported in Table 17. A similar calculation is done about the cyclic and reloading strength; it is reported in Table 18.
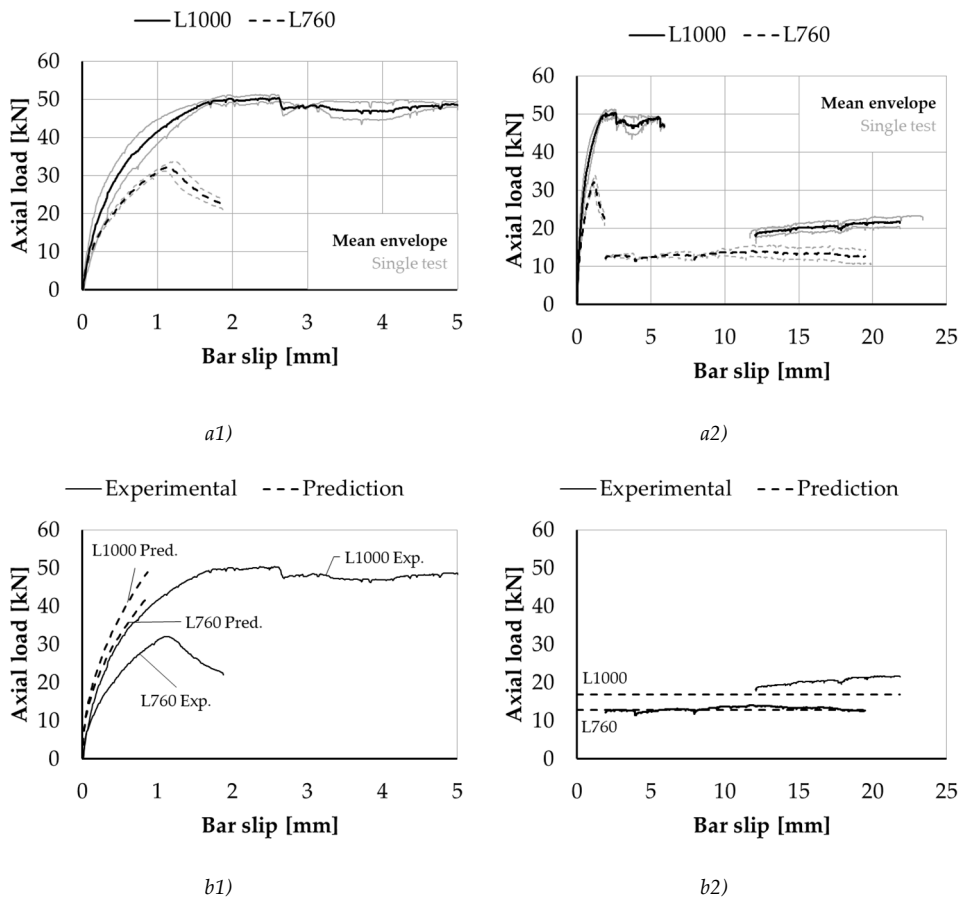
a1)

a2)

b1)

b2)

Figure 101: Analysis of SL experimental load-slip envelope a) and its comparison with analytical prediction b); single test response in thin grey lines and mean envelope in black bold line.

Since the literature proposals above reported are based on a short-embedded length, they should be considered representative in the case of SL3 and SL4 rebars, where four short length are involved in the bar equilibrium. On the other hand, their effectiveness in assessing SL1 and SL2 capacities must be discussed, because a longer embedded length is involved in the bar equilibrium. Despite this, the estimated peak bond strength outlined for the L1000 bars are consistent with the Code (Model Code, 2010) suggestion of Eq.(119); whereas the peak bond stress calculated for L760 bars are significantly lower. Regarding this, it is noteworthy to observe that the reference specimen analysed in the literature (Verderame et al., 2009b) presents a short unbounded length at the concrete block ends (Figure 102.a), the reacting material is thus confined on all the embedded bar length. On the contrary, in the herein

described specimens, the bond stresses can also act near the block ends, concrete damage on the first embedded sections can thus be expected. Assumed that a significant difference between the two types of specimens consists in the number of bar embedment discontinuity, like clearly schematized in Figure 102.b, it can be argued that the concrete damage characterizes a loss in the effective reacting length. On the other hand, the experimental cyclic and re-loading bond stress capacities are consistent with the literature proposal (Verderame et al., 2009a).
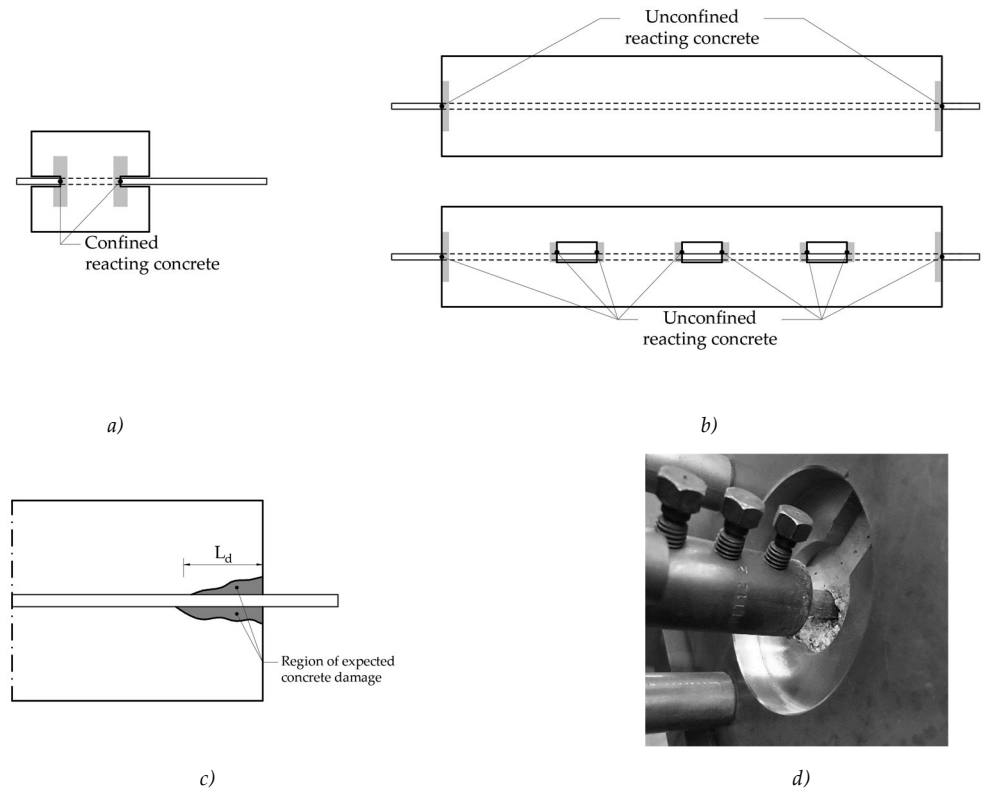

Figure 102: Identification of the boundary condition of the reacting concrete on the embedded bar edge: (Verderame et al., 2009b) a) and SL b) specimens. Schematization of the expected concrete damage in the same region c) and experimental evidence d).

Sample	N_{max} [kN]	L_e [mm]	$\tau_{bp,exp}$ [MPa]	$\sqrt{f_c}$
SL1	51.39	1000	1.36	0.274
SL2	49.96	1000	1.33	0.267
Mean L1000	50.37	1000	1.34	0.269
SL3	33.91	760	1.18	0.238
SL4	31.24	760	1.09	0.219
Mean L760	32.12	760	1.12	0.225

Table 17: Estimation of the peak bond stress acting on the SL embedded bar (hypothesis of constant stress).

Sample	Nc [kN]	Nr [kN]	Le [mm]	$\tau_{bc,exp}$ [MPa]	$\sqrt{f_c}$	$\tau_{br,exp}$ [MPa]	$\sqrt{f_c}$
L1000	12	19-22	1000	0.32	0.06	0.50-0.58	0-10-0.12
L760	6-8	12-15	760	0.21-0.28	0.04-0.06	0.42-0.52	0.08-0.11

Table 18: Estimation of the cyclic and re-loading bond strength acting on the SL samples (hypothesis of constant stress).

Shaped rebars (H and B samples)

In Figure 103 is shown the envelope of the shaped bar experimental response, with emphasis on the role of the steel-concrete bond condition. For sake of simplicity, in the following the Good Bond condition (GB) is relative to the lower bar of a concrete block, whereas the Bad Bond condition (BB) relates with the upper one. Considering the bent rebar, which cross from the concrete block top to its bottom, the condition is defined referring to the bar loading end. The graph a) show the H1 and H2 samples response; a mean curve is defined for both the GB and BB condition, respectively identified by a continuous and a dotted line. Strong difference in term of stiffness could be noticed for the two different bond conditions. The non-linear loading branch of the BB bars shows a more tendency of these specimens in loosing stiffness at increasing load level. Similar conclusions can be treated also for the bent bars. In this case, though, a lower stiffness is noticed at the low slip level in bad bond conditions (concave curve). This observation could be related with an initial sliding of the rebar which develops prior to the bar straightening, contrary to what happens in GB condition. The conclusion can be also confirmed by the bar strain reading on the Half-length gauge, previously described. More in general, an expected higher porosity of the upper concrete can justify a reduced stiffness of the anchored rebar and a possible initial sliding.

By the comparison between the hook-ended rebars and the bent ones, no significant difference were shown by the bars in good bond condition, like clearly visible in Figure 103.d. Different tangent rate is instead observed in BB conditions, with specific reference to the elastic field; on the other hand, the secant stiffness at yielding is almost the same. Finally, the hook specimens with unbounded straight length (H3) can be assumed as a lower limit for the load-displacement behaviour stiffness. Interesting considerations can be treated about the difference in the stress-slip response of straight embedded and shaped anchored rebars. The stiffness of hook ended rebar in good bond condition (GB) is very similar to the one exhibited by SL1000 specimens, whereas the initial elastic branch of the hooks in bad bond condition (BB) is very close to the SL760 bars one, (Figure 104.a). Bent rebar in bad bond condition shows a lower stiffness with respect to the straight embedded rebars. No significant conclusions can be treated about strength, since the analysed samples are characterized by different yielding stress.
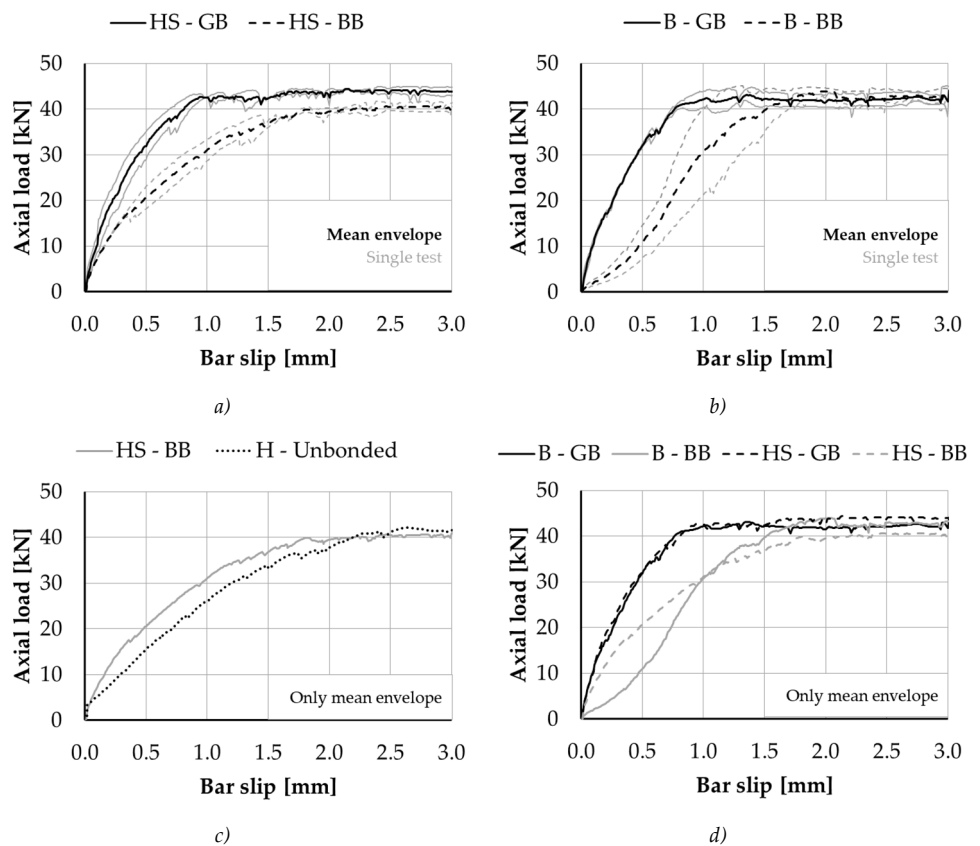
(Pt. 2 of 2)

Figure 103: Envelopes of the shaped bar load versus displacement behaviour.
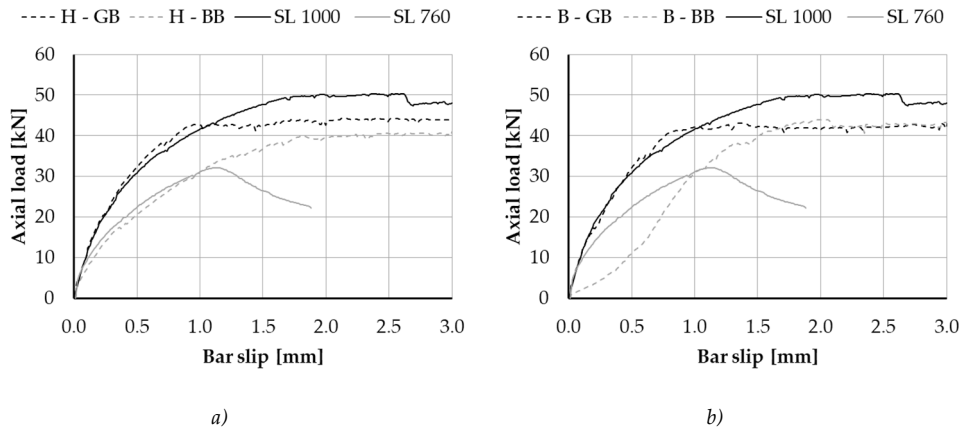
Figure 104: Comparison between straight embedded rebar and hook-end a) or bent b) ones: stress-slip response.

Prediction of the hook stress-slip behaviour

In the following, a simplified analytical model is proposed to represent the hook-end stress-slip behaviour. It is completely based on friction mechanisms, which allow to balance the axial stress applied at the hook head. The resource of friction resistance is assumed originated by more than one mechanism. The first one is related to the micro-interlocking acting between the bar surface and the surrounding concrete (Figure 105.1). It does not depend on the bar bending stiffness as it assumes that it behaves as a rope. The approach is the same discussed for the straight bar; it is qualitatively represented in Figure 100 and detailed in the following Chapter 5. The relative bond strength is called τ_b. On the other hand, the specific hook shape and the bar bending stiffness allow to identify supplemental resources for the anchoring capacities. The bar straightening is required for the hook extraction (Figure 105.2, and the concrete pressure works against it and balances the applied axial load (Figure 105.3). Consequently, an increment of the friction stresses acting on a bar side improves the anchorage load capacity.

A simplified representation of the three different identified mechanisms is reported in Figure 105, their mathematically definition is herein also treated.
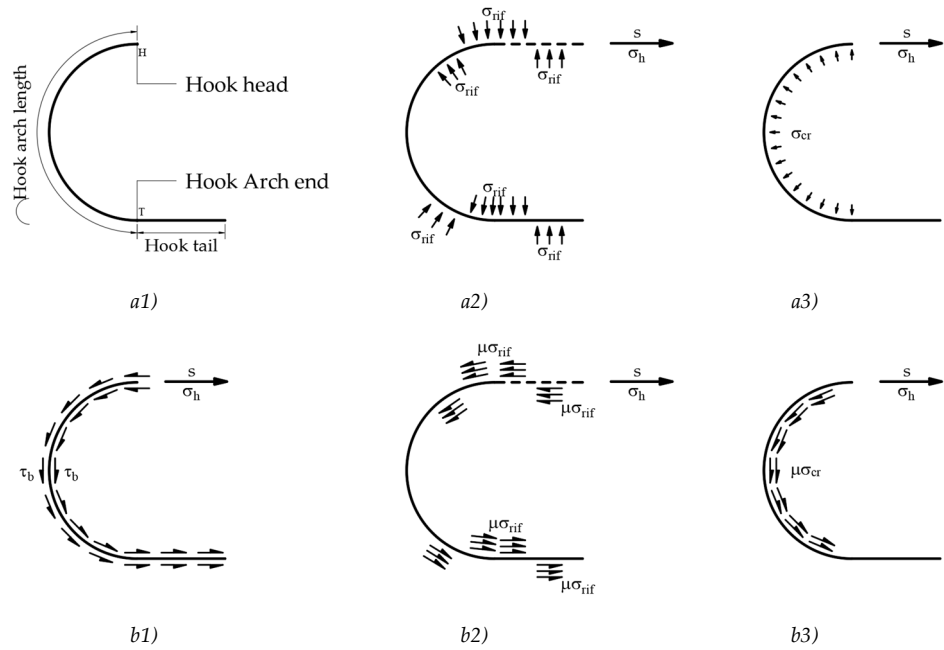
Figure 105: Identification of the Hook resistant mechanisms: rope analogy 1), bar straightening 2), and arch equilibrium 3). Concrete pressure acting on the bar length a) and relative friction stresses on the same b).

Neglecting a transient initial phase, it is possible to consider the development of the concrete bearing stress near the arch length ends (Figure 105.a2). This effect is directly related to the straightening action induced in the hook. It causes bending action on the rebar, which maximum value is in the initial (head) and in the end section of the hook arch length. In other words, where plastic deformations of the rebar are required for its pull-out. Note that the rebar (when it is in tension) is subjected to straightening at about the hook head section and forced to bending at the hook end section. For the sake of simplicity, in first approximation, such bending can be assumed as due to a couple given by the opposite bearing stress distributions σ_{rif}, before and after the hook head (and end) section. Out of the zone interested by such bending effects, a radial concrete pressure profile σ_{cr} balances the axial stress applied on the hook head. This profile is assumed constant (for simplicity) on the overall considered length, and its magnitude is directly related to the hook applied axial stress σ_h:

$$\sigma_{cr} = \sigma_{ch} = \frac{\pi d_b \sigma_h}{8R_i} \qquad (124)$$

where σ_{ch} represents the equivalent constant stress resulting from the projection (on the bar hook vertical diameter) of the stress required for the bar horizontal

translational equilibrium; R_i is the inner radius of the hook, typically equal to $2.5d_b$ (RD 2229, 1939). In this case, the bar to concrete radial stress σ_{cr} is not expected to reach the concrete bearing strength. Both the concrete normal stress involved in the straightening mechanism (σ_{rif}) and the one involved for the rebar global equilibrium (σ_{cr}) allow an increase of the frictional performance, improving the bar anchoring capacity.

Increasing the applied axial stress on the hook head, four different resistant phases can be considered (Figure 106): i) plastic deformation of the hook head due to the straightening tendency, ii) development of concrete radial stress on the arch length, iii) another plastic mechanism located in the arch length end. All the listed contributions cause an increase of the bond strength capacity acting on the entire device length, which is related to bar-concrete microinterlocking. The activation of the first (i) and the second (ii) mechanisms is required to develop the bar anchoring capacity; the third iii) is expected to activate only in presence of poor concrete mechanics or low steel-concrete friction coefficient. If the axial stress is not balanced along the whole arch length, a last resource iv) is available on the hook tail, which is treated as a common straight bar.
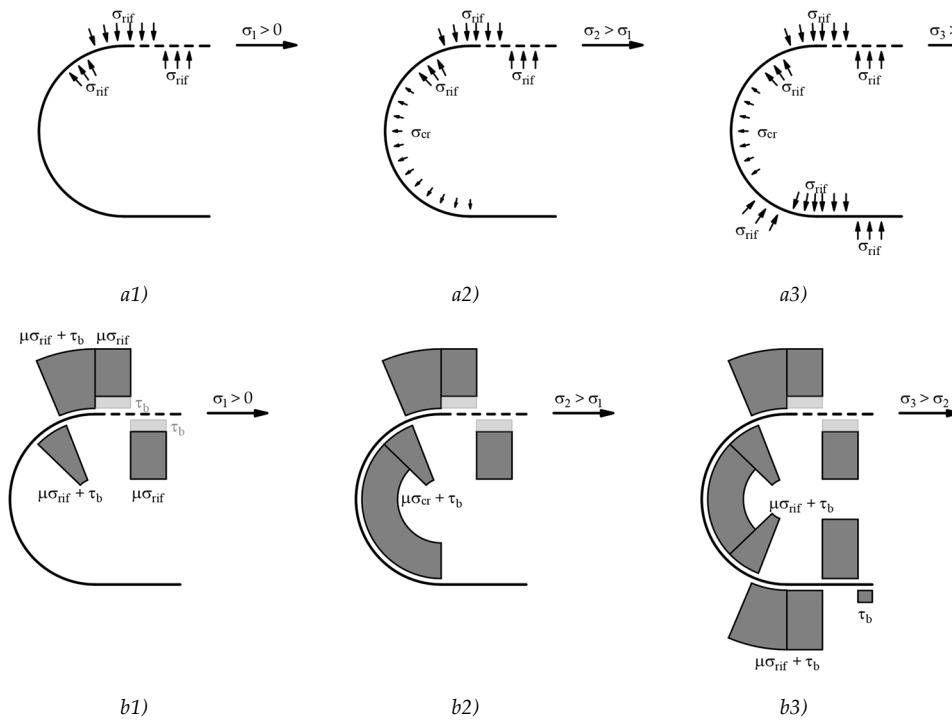

Figure 106: Development of concrete pressure profile a) and bond strength b) along the rebar length at increasing imposed axial stress.

The first presented mechanism (i) is now analysed, with reference to the schematic representation of Figure 107. A conceptual straightening of the hook head is considered. The bar is simultaneously subjected to coupled axial and transverse load, the latter due to bar normal stress on the concrete duct sides. Therefore, it is possible to refer to a dowel mechanism analogy, considering the effect of the coupled loading (see the analytical discussion in the following Chapter 4. Here, the variable is the length over which the concrete bearing stress activates to bend the portion of the bar extracted. At the incipient imposition of the hook slip, the axial load in the rebar are small; thus, the bar hook head section retain its full flexural capacity. Accordingly, it is possible to define an ideal effective length L_{eff0} over which the concrete bearing stress are triggered (Point 1 in Figure 107.b):

$$L_{eff0} = \sqrt{\frac{4M_H}{\sigma_{rif} d_b}} \qquad (125)$$

On this length the concrete bearing stress are assumed to act in the shape of a stress block profile, to reproduce the flexural yielding at the hook head (point H):

$$M_{pl} = \frac{d_b^3 f_y}{6} \qquad (126)$$

$$L_{eff0} = d_b \sqrt{\frac{2f_y}{3\sigma_{rif}}} \qquad (127)$$

Considering an increase of the axial load, the effective length reduces, due to the lower flexural resource. Anyway, it is possible to consider a further introduction of a certain axial stress in the anchoring device, thanks to a local bar hardening. Furthermore, the applied axial load at the hook head slightly diminishes due to the friction induced stress. Finally, the simplified distribution of the concrete stress reacting to the bar straightening could reduce its magnitude after the rebar plasticization. For the sake of simplicity, it can be however assumed the simplified calculation scheme reported in Figure 107.a.

With reference to a general axial stress $\sigma_h < f_y$, a bending bar strength reduction $M_{pl}(\lambda)$ is expected. Assuming the region of bearing stress to remain unchanged, the plasticization moves in another section, just outside the hook head cross section (Point 2 Figure 107.b). The bending action is now induced by the concrete bearing stress acting on a lower length $L_{eff}(\lambda)$; with $\lambda = \sigma_h/f_y$:

$$M_{pl}(\lambda) \simeq M_{pl0}(1 - \lambda^2) = \frac{f_y d_b^3}{6}(1 - \lambda^2) \qquad (128)$$

$$L_{eff}(\lambda) \simeq L_{eff0}\sqrt{1 - \lambda^2} = d_b\sqrt{\frac{2f_y(1 - \lambda^2)}{3\sigma_{rif}}} \qquad (129)$$

The above-mentioned mechanism is expected to involve a finite length, function of the hook resisted load:

$$\Delta L_{eff}(\lambda) = L_{eff0} - L_{eff}(\lambda) \qquad (130)$$

The rebar bending stiffness is reduced to the post yielding stiffness on the identified plastic length, and its straightening allows the rebar pull-out from the concrete. The consequent bar slip can be evaluated by the integration of the plastic deformations, which increase with increasing the applied load. The incremental slip results:

$$\Delta s_{h,pl}(\lambda) = \frac{\Delta \lambda f_y \Delta L_{eff}(\lambda)}{E_h} \qquad (131)$$

where E_h is the hardening steel modulus, which can be assumed two order of magnitude lower than the elastic one E_s. Since the reference equivalent dowel scheme herein considered is characteristic for both the bar length HA and HB (Figure 107.a), the calculation above reported must be multiplied by a factor 2. After the reach of the bar yielding, it is necessary that the bar develops all the yielding plastic strain to spread the stress on the hook arch length, allowing the hardening penetration through the hook head (Fabbrocino et al., 2005).
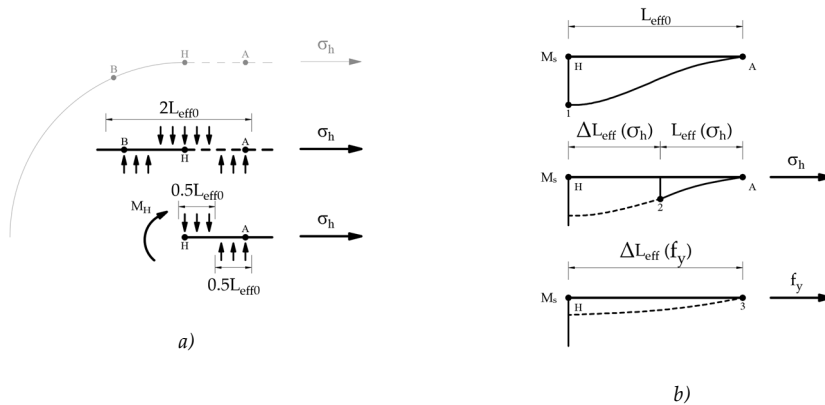

Figure 107: Hook head mechanism in presence of coupled bending and axial load: identification at the hook head a) and focus on the progressive plasticization b).

Remember that hook anchoring effect is possible thanks to the frictional mechanism available on its length, a focus on it is now presented. The bond strength is here assumed as the sum of two contribution: the basic frictional capacity τ_b, which work on the entire bar surface, and the addictive contribution τ_{bf}, which is offered by the

concrete pressure acting on the bar surface. In the head zone, the addictive contribution is related to the concrete bearing strength. On the other hand, along the hook arch length, it is related to the pressure in equilibrium with the hook tensile load (mechanism ii). From a mathematical point of view:

$$\tau_{bf} = \mu\sigma_{cr} \tag{132}$$

where the friction coefficient μ depends on the bar surface roughness and on the concrete mechanical characteristics. A reference value can be assumed in the range $0.25 \leq \mu \leq 0.50$, consistently with literature suggestions (Braga et al., 2001). In the bar equilibrium imposition, it is important to define the surface on which the bond stresses act. The friction resource due to concrete radial pressure works only on the inward part of the bar surface; here assumed with an equivalent depth equal to the bar diameter (Figure 108). On the other hand, the bond capacity τ_b acts on the overall bar surface since it is related to the micro-interlocking between the bar and the surrounding concrete.

The bar slip associated with the friction mechanism is defined by the integration of the bar strain on the hook loaded length. Therefore the total hook slip, that is the displacement of the hook head from its original position, is the sum of the following contributions:

- Integration of the steel strain due to the friction balanced stress;
- plastic strain integration on the progressive plasticity development on the effective length of the hook head.

The main contribution is given by the plastic strain developed in the head zone. This is mathematically expressed in differential way by the following:

$$\Delta s_{h,pl}(\lambda) = 2\frac{\Delta\lambda f_y \Delta L_{eff}(\lambda)}{E_h} \tag{133}$$

The main influencing parameters are the equivalent effective length L_{eff} and the steel hardening modulus E_h. The former is directly related to the steel yielding stress and to the concrete bearing pressure (see Eq.(129)). The influence of the concrete was experimentally observed in the previously presented test results and also in the literature (Fabbrocino et al., 2005). A more deformable response is related to Bad Bond (BB) anchorage condition, probably due to bleeding effect.

A simulation of experimental tests on hook devices (Fabbrocino et al., 2005) is herein proposed. Its results are visible in Figure 109. A good agreement with the experimental results is observed. On the other hand, prediction of the H-samples stress-slip response is shown in Figure 110. The deformation and the slip of the straight bar length before the hook are accounted for. The bond capacity on it is assumed according to (Model Code, 2010); in BB condition the strength outlined in Eq.(119) is halved.
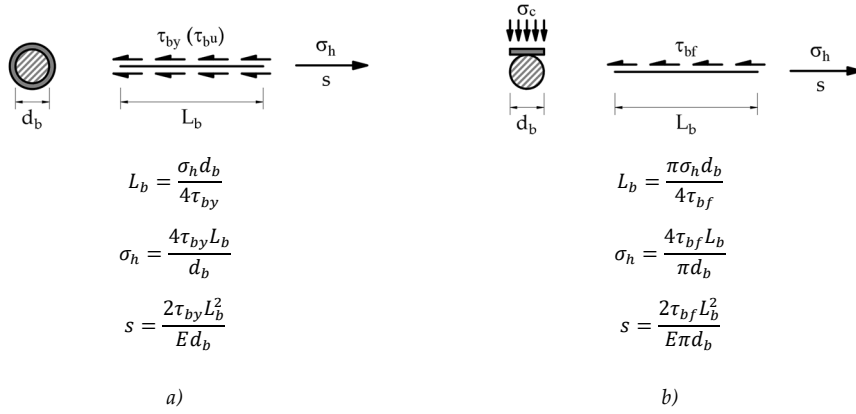
$$L_b = \frac{\sigma_h d_b}{4\tau_{by}}$$

$$\sigma_h = \frac{4\tau_{by}L_b}{d_b}$$

$$s = \frac{2\tau_{by}L_b^2}{Ed_b}$$

$$L_b = \frac{\pi\sigma_h d_b}{4\tau_{bf}}$$

$$\sigma_h = \frac{4\tau_{bf}L_b}{\pi d_b}$$

$$s = \frac{2\tau_{bf}L_b^2}{E\pi d_b}$$

a)

b)

Figure 108: Bar equilibrium and slip evaluation in case of bond stress due to microinterlocking a) and concrete normal pressure b).
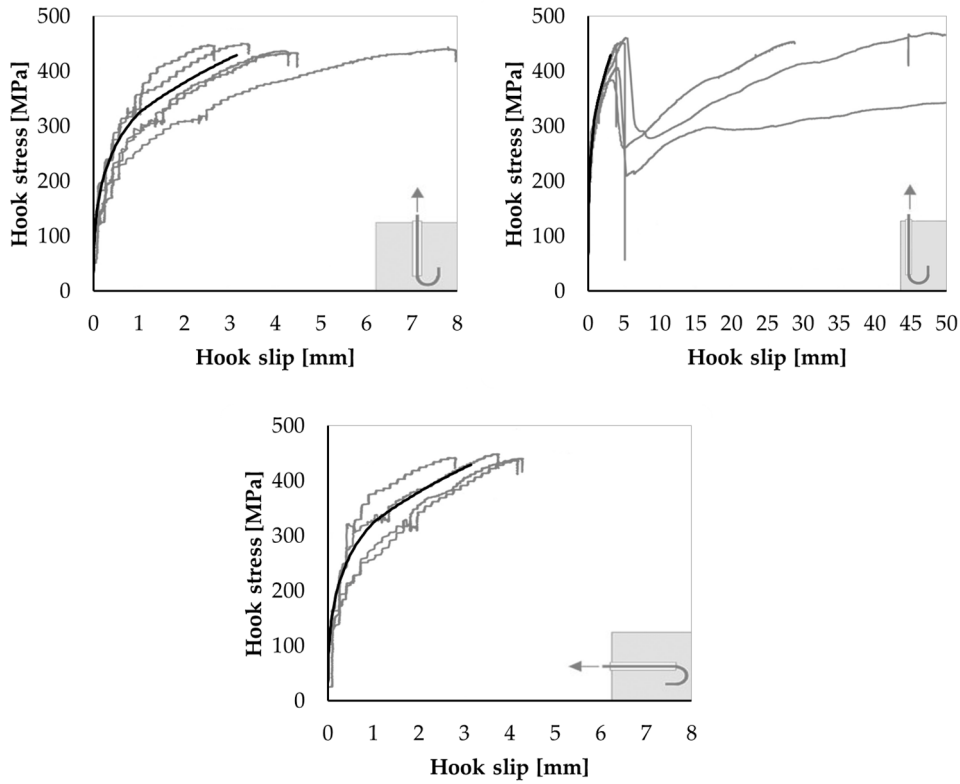

Figure 109: Modelling proposal application on experimental tests about hook stress-slip behaviour (Fabbrocino et al., 2005).
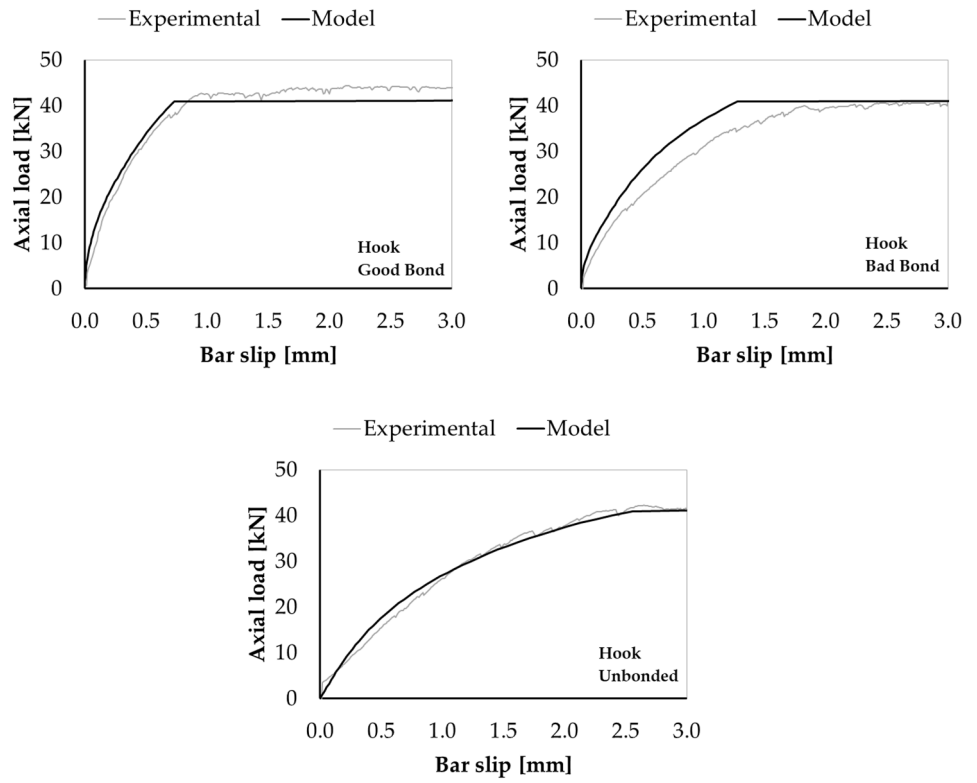
Figure 110: Prediction of the H-samples stress-slip response at low slip level: Good Bond (GB), Bad Bond (BB), and Unbonded condition.

4 EXPERIMENTAL TEST ON EMBEDDED BARS UNDER COUPLED AXIAL AND SHEAR LOADS

4.1 Introduction

Shear transmission on an RC crack is a fundamental aspect to assess the elements capacity in transmitting transversal actions to adjacent members through the joints. As mentioned in the literature survey (Section 2.6), the two main resistant mechanisms are:

- aggregate interlock;
- dowel effect of crossing rebar.

The former is the leading one when significant contact stress acts on the RC interface, due to both axial compressive load and bending actions. The consequent frictional mechanism is very rigid, and it avoids significant sliding on the shear plane, therefore the dowels cannot play a significant role. The aggregate interlock is obviously dependent on the shear plane roughness. This can degrade very quickly during earthquake excitation; thus, the mechanism strength is affected by cyclic deterioration and the dowel strength can gain more importance under repeated loading. Moreover, the plastic elongation of the reinforcement crossing a crack is not always recovered; therefore, the crack closure can be inhibited during the cyclic response (Figure 111). Tensile loads are also cause of crossing cracks in an RC element, such as the case of the windward column or beam in an infilled frames (Figure 112). In these scenarios the dowel mechanism may results the only resource to the shear transfer across a crack; thus, its evaluation is of interest.

In the frame members, as it is for the shear walls, the reinforcement that cross a crack is mainly engaged in bending strength. Consequently, the bars that cross a potential shear sliding surface (i.e. a flexural crack) are simultaneously subjected to both axial and shear loading. Since the dowel mechanism is governed by the formation of plastic hinges in the rebar (Gelfi and Giuriani, 1987; Soroushian et al., 1986; Vintzēleou and Tassios, 1987), the presence of the axial load surely affects the mechanism strength. The influence of this concept is investigated in the following.
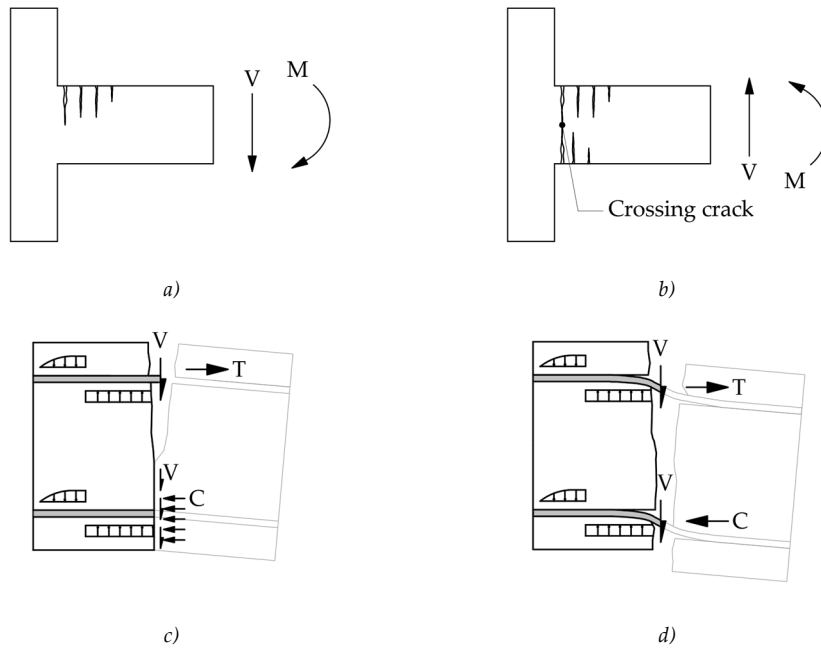
Figure 111: Schematization of a beam subjected to reversal flexural loading at the first cracking a) and in presence of load inversion b): focus on the shear and bending action transmission in presence of closed c) and opened d) crack.

As discussed in the literature review, several experimental tests on rebar dowel effect across a shear plane are available (Brenna et al., 1990; Dei Poli et al., 1992; Dulacska, 1972; Soroushian et al., 1986; Vintzēleou and Tassios, 1987; Walraven and Reinhardt, 1981). However, only some of them take into consideration the coupled action of axial and shear loading; more in detail, only one of them (according to the author knowledge) refers to experimental evidences on the topic (Maekawa and Qureshi, 1996a). The latter reference studies the effect of transversal imposed displacement on the axial pull-out behaviour of a deformed rebar. The authors (Maekawa and Qureshi, 1996a) observe that the bar capacity is strongly dependent on the coupled action; the reduction of the dowel mechanism flexural strength is thus reduced by the presence of an axial load. Nevertheless, the specific experimental test configuration does not allow to independently evaluate the shear and axial capacity of the rebar in presence of a pre-defined fixed value of shear or axial load respectively. Indeed, the two behaviour are related to each-other in that specific test set-up. Furthermore, it is worth noting that the available tests are relative to deformed reinforcement, which ribs can damage the surrounding concrete under pull-out action. Consequently, the mechanical properties of the material that offer the bearing to the dowel pressure can be damaged by the effects of the axial loading.
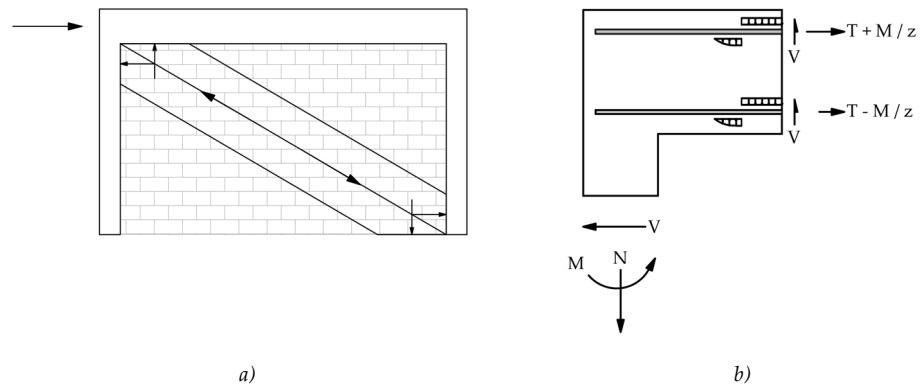
a)   *b)*

Figure 112: Infilled frame under transversal loading: equivalent strut actions a) and focus on the beam situation in the upper loaded corner b).

The experimental campaign reported in the following aims to define the role of the axial stress on the dowel mechanism of reinforcing bars. A total number of 24 specimens are tested. Only ductile failure mechanism is investigated, concrete splitting is indeed avoided by a specific sizing and confinement of the concrete blocks. Therefore, the steel bar fails with plastic hinges formation and the shear load is resisted by concrete bearing stresses, according to a classic dowel mechanism. Most of the specimens are characterized by plain rebar, to investigate dowel mechanism in presence of smooth reinforcement; indeed, a lack of literature experimental results about this topic is noticed. The same choice is also consistent with the aim of the study herein reported, referred to frame structures reinforced with plain rebars.

Strength and stiffness variation of the dowel mechanism are discussed, with reference to the presence of different normal stress in the rebar General consideration about the load-displacement curve are also reported. Most of the tests are done in presence of cyclic not reversal transverse shear loading coupled to tensile axial action, others account for the presence of compressive axial force, cyclic reversal shear load, and both shear and axial reversal action. After the analysis of the experimental evidences, a comparison with the available formulations to predict the mechanism strength and the load-displacement relationships are proposed. A comprehensive method to assess the behaviour of a rebar under coupled axial and shear load is finally proposed.

4.2   Specimen description

The reference specimen is composed by three concrete blocks, separate each other by two 3mm width pre-formed planar cracks (Figure 113). A reinforcement rebar crosses all the blocks and the cracks, being anchored on the outer face of the two end concrete prisms. The axial tensile force is introduced in the specimens by four threaded rods for each external blocks. These transmit the tension force to the concrete by bond stress and they are in contact with an internal confining stirrups with a steel washer (Figure 113.a). Given the low embedded length of the bar in the outer concrete prisms, the bond stress between the concrete and the testing rebar is not sufficient to balance the axial loads, especially in the samples with plain bar. Therefore, a specific external device was provided to ensure the mechanical anchorage (Figure 113.b).
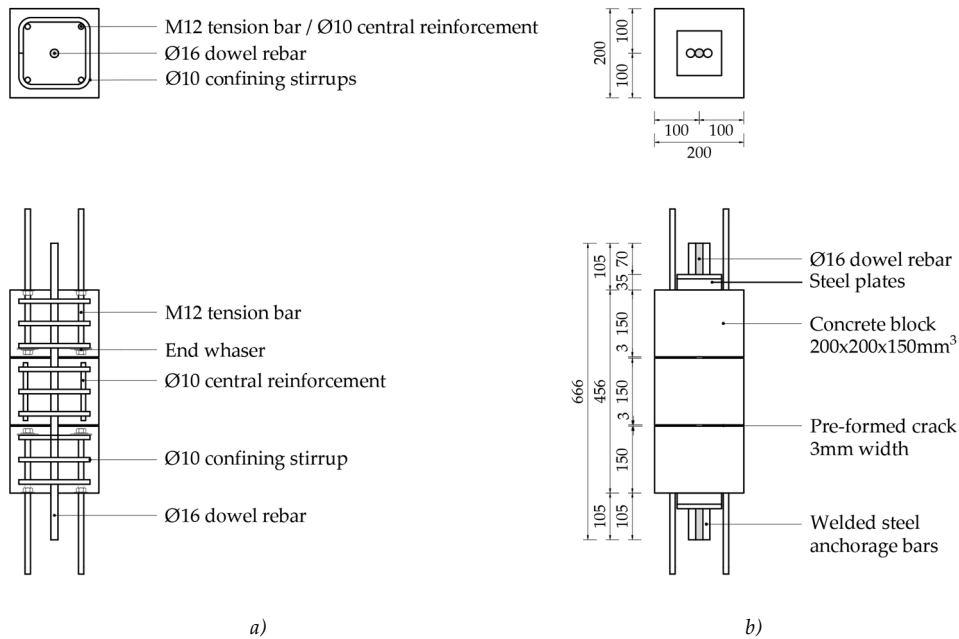

a) *b)*

Figure 113: Reference specimen for the experimental campaign: schematic view of the internal confining reinforcement a) and whole sample b).
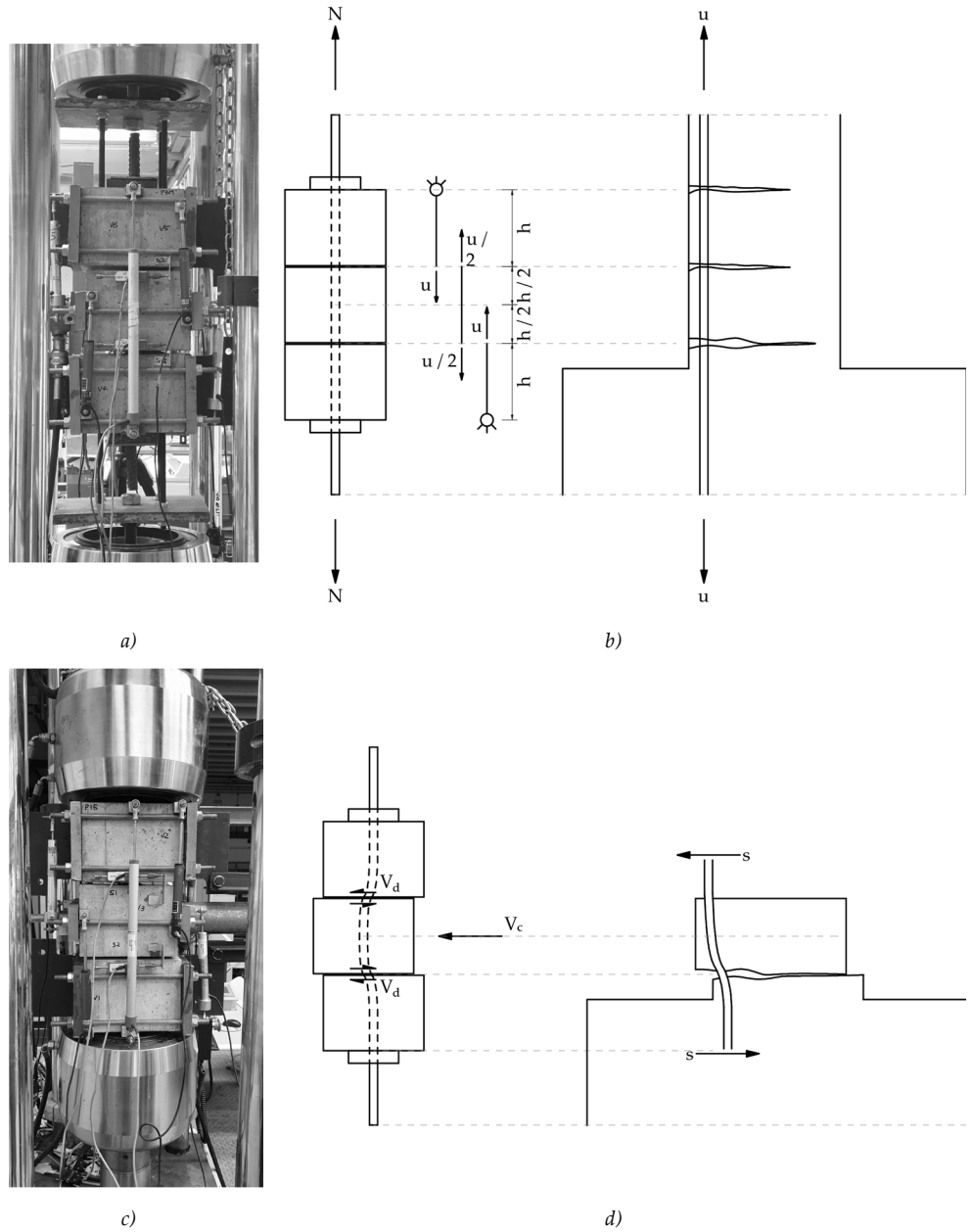
158

Figure 114: Simulation of the axial pull-out a-b) and of sliding induced by transverse loading c-d) for a column rebar anchored in a foundation.

Regarding the transversal load, it is introduced in the specimen by the imposition of a sliding between the central block and the outer two. On the crack no friction can act against the shear force and the concrete surface is very smooth, due to the use of plexiglass panel to guarantee the crack opening during the casting phase. The symmetry of the specimen helps to avoid accidental rotation due to accidental or geometrical eccentricities, which can occur during the shear loading phase. Furthermore, the chosen geometry is able to represent a rebar in a cracked RC member near to an interface, where it is simultaneously subjected to axial pull-out and transverse sliding. In Figure 114 a contextualization on a column-foundation joint is suggested. The bar slip from the outer blocks is higher with respect to the one from the central prism; indeed, the slip from the central block is subdivided in two contribution on both the cracks (because of symmetry).

Axial and shear load application

Regarding the application of the axial load, a distinction must be made between smooth and deformed rebar specimens. For the latter, the axial load is imposed by the head threaded bars, which are connected to a rigid steel plates engaged in a Instron machine, which is able to guarantee the load control (Figure 114.a). The aim of this specific arrangement is to simulate the concrete damage due to axial pull-out mechanism, which is introduced by the ribs of the deformed rebars. In this way the coupled effect of axial and transverse load can be better investigated. On the other hand, for smooth rebar samples, direct application of the tension force can be pursued. Indeed, in these specimens, the slip induced concrete damage can be assumed not significant, due to the poor bond performance of the reinforcement surface type.

A reaction steel frame has been designed for the application of the shear load (Figure 115). Each concrete block is in contact with steel plates on its loaded face. The external ones are connected to a contrast beam by the means of a couple of truss; on the other hand, a jacket actuated by an oil pump in manual control pushes the central prism reacting on the same contrast. The symmetry of the solution, added to the use of truss in realizing the frame and to the application of a spherical hinge between the actuator and the reaction vertical steel beam, allow to avoid loading eccentricities. The jacket load F_a is equally subdivided on the two sliding planes. Note that the system represented in Figure 115 can apply shear load in a single direction, for reversal loading a similar system has to be added on the opposite side of the specimen (Figure 116).

Instrumentation

The axial load is directly read by the Instron machine, which controls time by time its amplitude taking it constant. The shear load is instead read by a load cell, which is put between the actuator and the reaction frame.
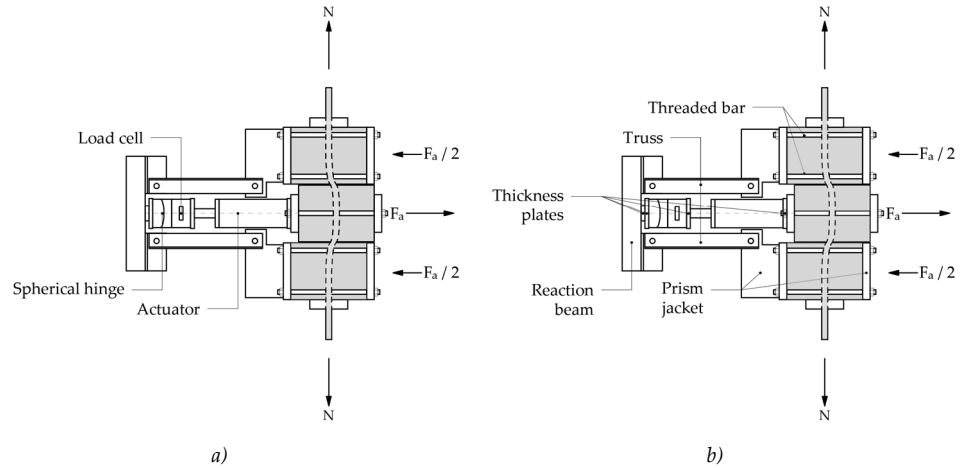

Figure 115: Transverse loading frame: reaction system connected to the specimen a) and relative loading devices b).
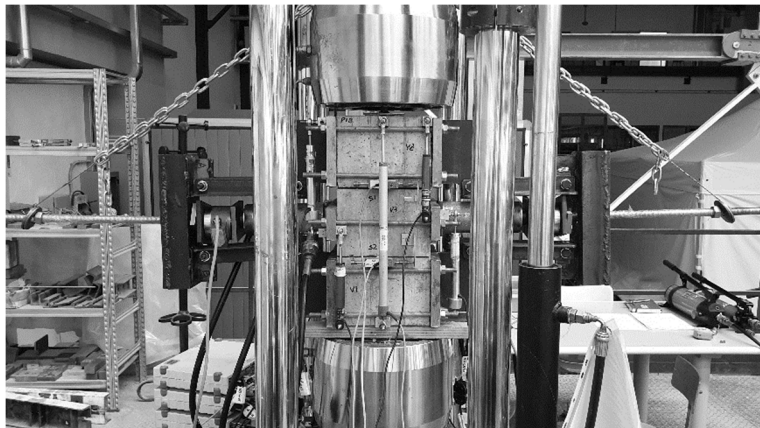

Figure 116: Shear frame arrangement for the cyclic transversal load imposition, pre-test phase.

Vertical and horizontal displacements are measured by potentiometric transducers (Figure 109). On each crack 2 horizontal instruments are placed on the unloaded sides (east and west ones) and parallel to the direction of load application. The choice allows to read the sliding on each shear plane, as the average value measured on the two sides; because of this, the measurement is not affected by concrete prisms torsion around the central rebar. Four vertical transducers are placed across each crack, on all the blocks faces; their position is chosen with the aim to compensate for the vertical rotation of the blocks and to read a mean crack opening. Finally, 2 other transducers connect the external blocks, allowing the measurement of a global crack opening (sum of the two single cracks values). A total number of 14 potentiometer instruments are used for the sample deformation monitoring; a resume is available in Table 19.
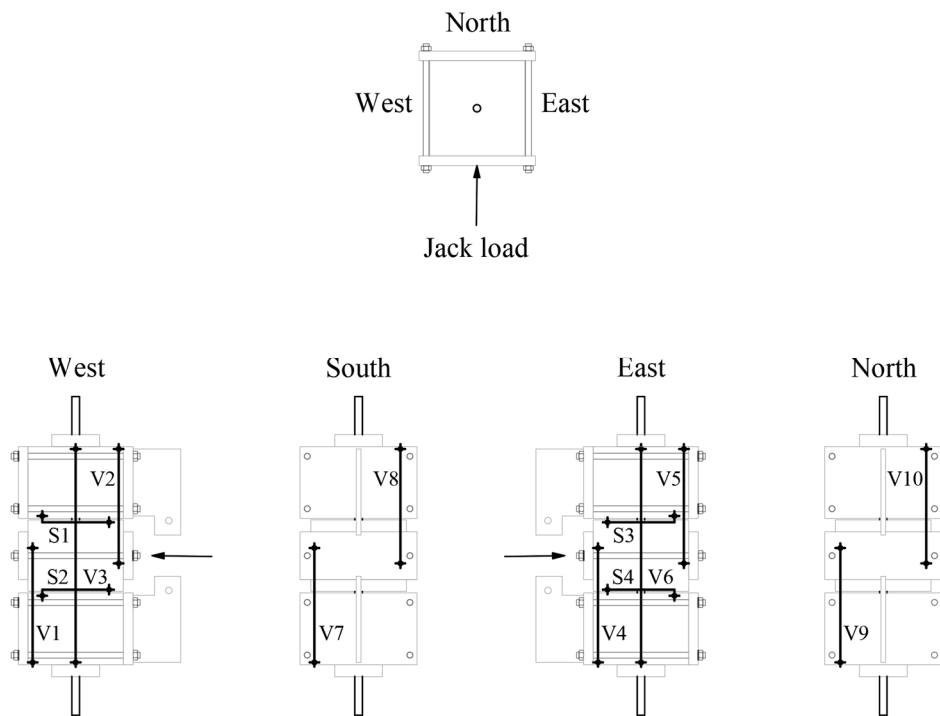

Figure 117: Position of the potentiometric transducers used for the deformation monitoring.

Instrument	Working direction	Crack monitored	Face monitored
S1	Horizontal	Upper	East
S2	Horizontal	Lower	East
S3	Horizontal	Upper	West
S4	Horizontal	Lower	West
V1	Vertical	Lower	West
V2	Vertical	Upper	West
V3	Vertical	Both	West
V4	Vertical	Lower	East
V5	Vertical	Upper	East
V6	Vertical	Both	East
V7	Vertical	Lower	South
V8	Vertical	Upper	South
V9	Vertical	Lower	North
V10	Vertical	Upper	North

Table 19: Summary of the employed instruments, the nomenclature and the position is also reported in Figure 117.

4.3   Materials

The choice of the concrete and of the dowel steel mechanical properties wants to represent as much as possible a typical situation in an existing structure. Normal strength concrete and common reinforcement bar employed in the construction sites are considered, with reference to both the smooth (GLD frames) and the deformed reinforcement (modern buildings).

The concrete mix design is the same for all the specimens but casting at different times causes difference in the characterization process described in the following. Nevertheless, it seems satisfactory to assume the same concrete reference class for all the specimens, identifying a C25/30 concrete according to the Code (CEN Eurocode 2, 2004). On the other hand, two different families of dowel steel are considered. The mechanical properties are the same for all the specimens of the group P (plain dowel) and D (deformed dowel) respectively; indeed, only a steel batch for each specimen type is considered. Nowadays no plain reinforcement bar are available; therefore, the structural steel of the type S275 (UNI EN 10025-2, 2005) is emplyed. On the other hand, ribbed reinforcement of the type B450C is considered for the deformed dowel, consistently with the provisions of the modern Code (Norme Tecniche per le Costruzioni, 2018).

Concrete

The concrete mix design is reported in Table 20. Only basic components are used, according to the aim of represent an existing structure. Portland cement CEM I-42.5 R (EN 197-1, 2007) is employed and high water over cement ratio characterizes a good workability without admixtures use. The siliceous rounded aggregates grain size is identified by three different reference diameters, which limit dimensions is also reported in Table 20. Slump test (EN 12350-2, 2009) result is the same for each of the three casting: 210mm.

Cement content 42.5 [kg/m³]	Water [l/m³]	w/c	D1 (0-4mm) [kg/m³]	D2 (4-10mm) [kg/m³]	D3 (8-20mm) [kg/m³]
340	183	0.54	927	331	581

Table 20: Dowel specimens concrete mix design.

Compressive test on three cylinders for each casting were done, according to the Code procedure (UNI EN 12390-3, 2003). The results show the homogeneity of the concrete. A mean compressive stress equal to 33.69MPa is considered. The Young modulus was also established according to the Code procedure (UNI EN 12390-13, 2013). In this case a greater difference between the three castings was noticed, especially for the P2 series. Despite this a mean value of 30095MPa is however assumed. It is worthy to note that the value of the elastic modulus is very similar to the prevision suggested by (Priestley et al., 2007) ($E_c = 5000\sqrt{f_c}$). According to the Code (UNI EN 206, 2016) the concrete is classified as a C25/30 type.

Parameter	Cylindrical strength f_c [MPa]			Young modulus E_c [MPa]		
Casting	Mean	CoV	Assumed	Mean [Mpa]	CoV	Assumed
P1	34.03	4.20%	33.69	27640	7.67%	30095
P2	33.35	5.84%		32550	17.30%	
D1	33.66	2.83%	33.66	28650	7.31%	28650

Table 21: Results of the concrete characterization in term of compressive strength and elasticity modulus: mean values and Coefficient of Variations. Reference to dowel specimens.

Dowel steel

Uniaxial tensile tests on both the plain and the ribbed dowel bars are performed according to the Code (UNI EN 10080, 2005). The lengths of the specimens were 587mm and 500mm respectively ($37d_b$ and $31d_b$). The test results are shown Figure 118 in term of axial stress versus total elongation, which was measured at the end of the bar. Yield stress f_y, peak strength f_t, and elongation A_{10} on a 10-diameter original length (out of the failure zone) are reported. The yielding and the failure forces of the deformed rebar were respectively the 60% and the 30% higher than the smooth bar

ones. On the other hand, the plastic deformation capacity is strongly higher in the case of the plain bar. It is possible to conclude that the smooth rebar mechanical properties are consistent with the characteristics of the reinforcement employed in the construction of the RC buildings realised from the second World War to the Seventies (Verderame et al., 2001). The steel modulus of elasticity is assumed to be 200000MPa, like confirmed by the plot of the stress versus strain behaviour measured during the test on the smooth rebar before the reach of the yielding phase.
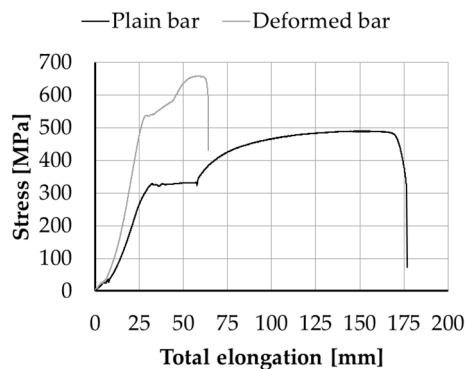
X	Plain	Ribbed
f_y [MPa]	329	538
f_t [MPa]	490	658
A_{10} [%]	19.9	10.2

Figure 118: Uniaxial tensile test on the dowel bars in term of axial stress versus total elongation (at the testing machine cramp).

4.4 Loading protocol

All the experimental tests were performed in axial load control, which was guaranteed by the Instron machine. The shear load is instead introduced by a hydraulic jacket controlled by a manual pump. The latter system allowed to govern the sliding between the central and the outer blocks, but not the load control. The stability in the post-yielding phase was ensured by the high ductility of the tested dowel, which is visible from the uniaxial tensile tests results above reported (Figure 118).

Dowel axial loading

Four different axial stress levels were imposed to the specimens, they are reported in Table 22. To simplify the results understanding, an acronym is used to identify the tests done in the same conditions. The first letter is common for all, the second one shows if the axial load is tensile or compressive one, R specifies the loading reversal for only shear or for both shear and axial load (see in the following); finally, the end number represents the normalized axial load. Three different test types can be

identified, referring to the application of the transverse and axial load (see Figure 119):

- cyclic not reversal shear at fixed axial load levels (NT-NC);
- cyclic reversal shear loading at fixed axial load (NTR);
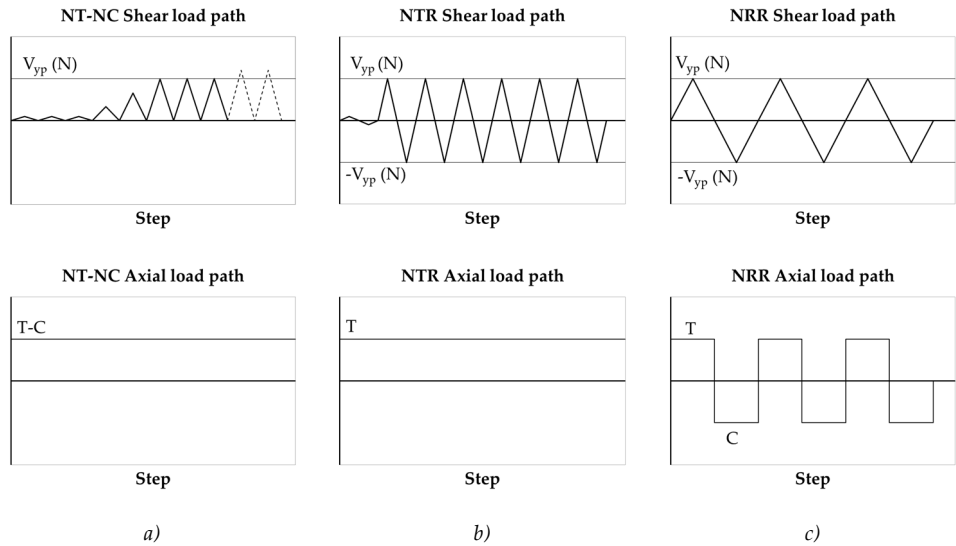- cyclic reversal shear loading at fixed opposite axial load levels (NRR).

Figure 119: Generic shear and axial load path for the three different test typologies: NT-NC a), NTR b) and NRR c).

Shear loading

The shear loading path was chosen after an analytical prevision of the yielding shear $V_{yp}(N)$ capacity. Axial load N detrimental effect on it is preliminary evaluated according to the following:

$$V_{yp}(N) = 1.30 d_b^2 \sqrt{f_y f_c (1 - \alpha^2)} \qquad (134)$$

where d_b and f_y are the bar diameter and the yielding stress respectively, f_c is the concrete compressive strength and $\alpha = 4N/f_y \pi d_b^2$ is the normalized acting axial load. The above formulation, proposed in the literature (Vintzēleou and Tassios, 1987), is a rearrangement of the dowel strength classical formulation (Rasmussen, 1963). In this case, it is corrected to account for the axial load influence on the plastic resistant moment of the rebar (Soroushian et al., 1986). Anyway, the same Eq.(134) is not capable to account for the load eccentricity due to the crack opening, which measure $1.5mm$ in each specimen at the beginning of the test (Figure 113.b). Thus, the

rearrangement of the proposal by Gelfi and Giuriani (Gelfi and Giuriani, 1987) is preliminary considered:

$$V_{yp}(N) = d_b f_{cc} \left[-a + \sqrt{a^2 + \frac{d_b^2 f_y}{3 f_{cc}} (1 - \alpha^2)} \right] \tag{135}$$

with $f_{cc} = 5 f_c$ assumed as concrete bearing strength. The calculated value is used to define the shear load path steps.

Known the reference value $V_{yp}(N)$, the shear action is imposed to the samples by a gradual increase in amplitude. Generally, initial set-up checks were performed at a load level lower than the 15% of the predicted yielding one. Then, single cycles (typically two) at a fraction of the predicted value were imposed. Finally, more than one cycles were performed to explore the plastic response of the system, reaching high ductility level. The presented history is followed only for the NT-NC tests, indeed, full cycles at the reference yielding load were imposed in presence of reversal shear action. The graphic representation of the three different load paths are visible in Figure 119, for the fixed axial load values N and the relative predicted yielding shear $V_{yp}(N)$.

Test	Axial load ratio	Working force [kN]	Specimens
N-00	00%	±00	P1-1 P1-4 P2-1
		±00	D1-1 D1-4
NT-60	60%	+40	P1-2 P1-5
		+65	D1-2 D1-7
NT-90	90%	+60	P1-3 P1-6
		+97	D1-3 D1-8
NT-98	98%	+95	P2-2 P2-3
		+105	D1-5 D1-9
NC-60	60%	-40	P2-4 P2-7
NC-90	90%	-60	P2-5
NR-00	00%	±00	P1-7
NTR-60	60%	+40	P1-8
NTR-90	90%	+60	P1-9
NRR-60	60%	±40	P2-8

Table 22: Axial stress imposed to the different samples during the shear tests.

4.5   Experimental results

The experimental results are reported in term of dowel shear force versus interface sliding displacement. The measured transversal load is the actuator total force F_a, therefore the reference load on each shear plane V_d is defined by the following (Figure 115):

$$V_d = \frac{F_a}{2} \qquad (136)$$

The sliding on each shear planes is calculated from the data collected by the horizontal transducers located across the two cracks: $S1$ and $S3$ for the upper one, $S2$ and $S4$ for the lower one (Figure 117). The reference displacement is then identified in the mean value of the relative measurements:

$$s_{du} = \frac{S1 + S3}{2} \qquad (137)$$

$$s_{dl} = \frac{S2 + S4}{2} \qquad (138)$$

where s_{du} and s_{dl} are the sliding on the upper and lower shear plane respectively. These values can not be the same during the loading phase, due to the inherent features of an experimental test. Consequently, the force-displacement response on the two considered shear planes must be considered in an independent way.
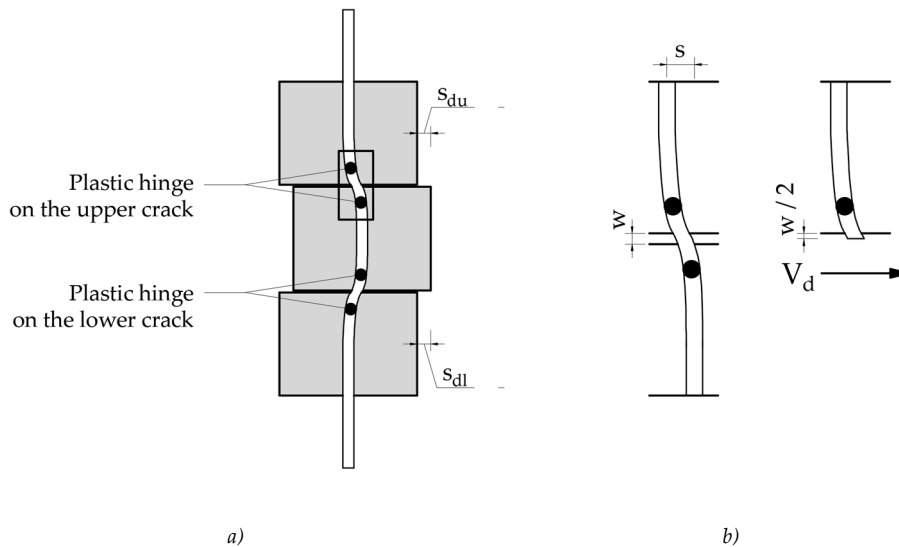

a)   b)

Figure 120: Schematization of the dowel bar flexural deformation a) and focus on a single crack with detailing on the balance force system b).

Figure 120 shows a schematic representation of the dowel mechanism. The shear displacement imposed of the central concrete block, respect to the outer ones, causes the flexural dowel action in the rebar. At the same time the bearing strength of the concrete balances the applied load. At the mechanism yielding two plastic hinges forms at each side of the cracks, causing a significant loss of stiffness in the force-displacement response. The experimental yielding is reached on the two cracks at a different time, the differential mechanism activation causes so a concentration of the plastic deformation demand on the first yielded shear plane. Therefore, the experimental data reported in the following are referred only to the crack which yields first.

To compare the force-displacement relationship of the different specimens, a specific procedure was defined for each single test response data elaboration:

- both the responses of the upper and lower crack are plotted;
- the curve of the first yielding plane is chosen and the other one is discharded;
- the experimental response is enveloped by a single curve, neglecting the different cycles;
- a mean envelope curve is obtained from all the data relative to the specimens tested under the same axial load.

In Figure 121 is reported an example of this.

The presented procedure for the data elaboration is followed for the monotonic cyclic tests (NT and NC). In case of shear cyclic loading and in case of axial and shear reversal loading (NR and NRR tests) only a single test was performed.

The vertical potentiometric transducers are used to monitor the axial loading and the global response of the specimens during the shear test. Their continuous observation allows to identify possible significant eccentricities, which can affect the response. The same instruments are also useful to check a-posteriori the crack opening, with the aim to control a possible crack closure that would cause a possible shear action transfer by friction mechanism.
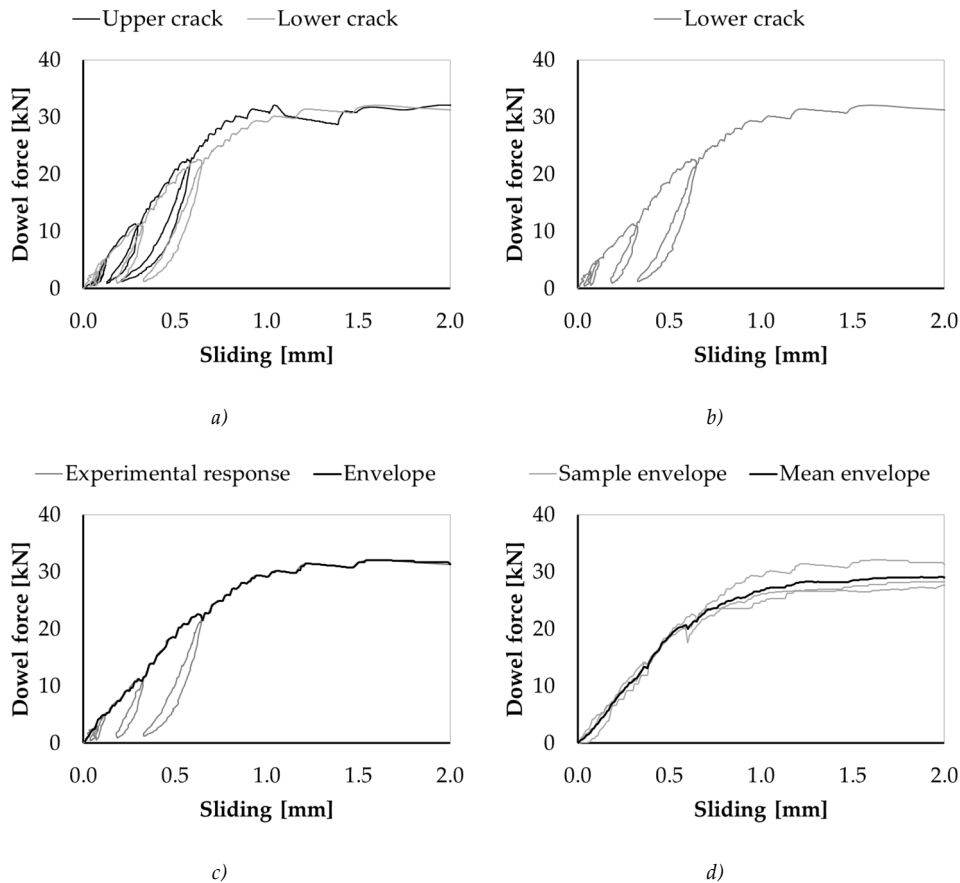
a)

b)

c)

d)

Figure 121: Force-displacement curve elaboration for the dowel mechanism: response on the two cracks of a single specimen up to a sliding displacement equal to 3mm a), reference to the first yielded one b), envelope of the experimental response c), and mean behaviour at a fixed axial load. The shown example is relative to the specimen P4 and to the mean response of plain dowel not axially loaded.

Cyclic non reversal shear load with no axial load

The first focus is on the tests performed in absence of axial load, for which the shear force-displacement behaviour can be identified by a bi-linear relationship. Figure 122 and Figure 123 show the cyclic not reversal loading response of the N-00 tests. In the initial set-up phase the samples response was substantially linear elastic. The successive cycles were basically elastic too, but the response assumed gradual loss of stiffness and the unloading and reloading curves were not aligned to the loading one. Where the change in the stiffness was clearer, it is possible to identify the specimens yielding, after which residual displacements can be well identified in the unloading

phase. Referring to the first part of the response, it is clear that the transition from the elastic to the inelastic field is not well defined (Figure 123). Therefore, the definition of a specific yielding point is not univocal. Nevertheless, it can be defined by the observation of the gradual loss in stiffness or by the development of residual deformation. In the case of the specimens D1-1 and D1-4, the strong correlation between the loss of stiffness and the relative increment of the plastic deformation (in term of shear sliding) was easier to observe, due to the higher number of repeated cycles followed (Figure 123.b).

It is possible to evaluate a resistance of about 30kN in the case of smooth rebar and of about 40kN for the deformed rebar. The role of the different steel mechanical properties was so evidenced in term of mechanism strength. Regarding the shear displacement, the yielding of the former was reached at a sliding level equal to about the half of the latter, which can be assumed to occur at 2.00mm. Anyway, a direct comparison between the P-specimens and the D-one is very complicated, due to the strong non-linear development of the strength capacity, especially for the seconds.
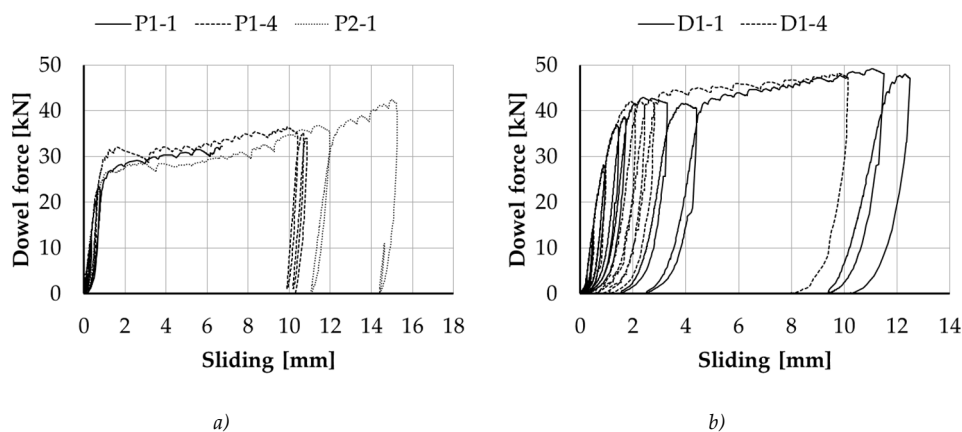

Figure 122: Experimental force-displacement relationships of the N-00 tests for both smooth a) and deformed b) dowel type; only the first yielded crack response is considered.

In the plastic field a constant strength is developed until a displacement level equal to 6÷8mm. After this point a hardening behaviour tries to develop, as it is shown by both the P-specimens and the D-ones. This singularity can be due to the concrete debris around the dowel. An example of it is reported in Figure 124. Entering in the crack, such debris can induce friction or tension in the rebar with consequent kinking effect. Because of the above observations, the hardening behaviour is not considered in the data evaluation.

The unloading response presented an initial stiffer branch and a second re-centring one. The reloading behaviour was secant to the previous reached peak point. The imposed displacement amplitude and the imposed number of cycles did not seem to influence the stiffness of the different loading phases.
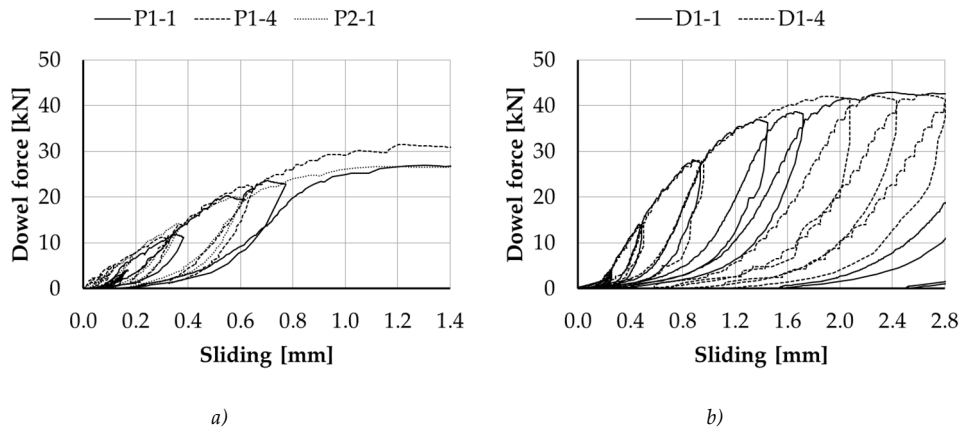
171

a)   *b)*

Figure 123: First part of the N-00 test for smooth dowel a) and deformed one b).

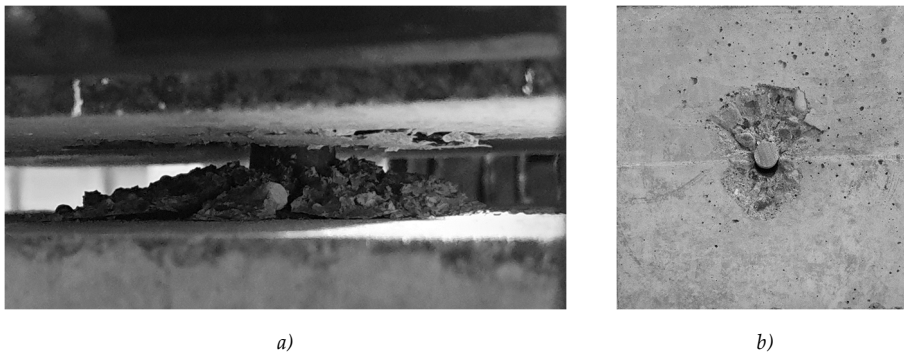*a)*   *b)*

Figure 124: Concrete deposition in the crack width a) and post-test damage on a specimen of the series N-00.

Combined cyclic non-reversal shear and constant tensile axial load

In Figure 125 the full experimental responses of the tests NT-60, NT-90, and NT-98 are shown. A focus on the initial response is instead available in Figure 126, comparing the results of all the specimens tested. Axial load presence did not significantly change the shape of the dowel response; an initial branch distinct from a successive plastic one can be observed again. A great change was instead observed in term of strength and post-elastic stiffness. The axial load characterised a hardening behaviour of the response; its slope increasing with the imposed axial stress.

The mechanism strengths can be assumed equal to 20kN and 10kN for the plain rebar dowel and to 25kN and 15kN for the deformed one, respectively for the test NT-60 and NT-90. In presence of an axial load equal to the 98% of the yielding one (NT-98), the force-displacement response presented an initial stiffness clearly lower respect to the other tests. Assumed a negligible effect of the axial stress on the elastic stiffness,

172

it is possible to assume that the yielding strength of the NT-98 specimens was about zero. Also in this case a higher strength capacity was however exhibited after the mechanism yielding, with reference to the whole imposed deformation range. From the graph in Figure 125 it is possible to observe that a strength similar to the one exhibited by the N-00 series was reached at a displacement of about 10mm, related to very high plastic deformation demand. In presence of a transversal displacement higher than 1mm, all the considered experimental response were in the post-elastic field.
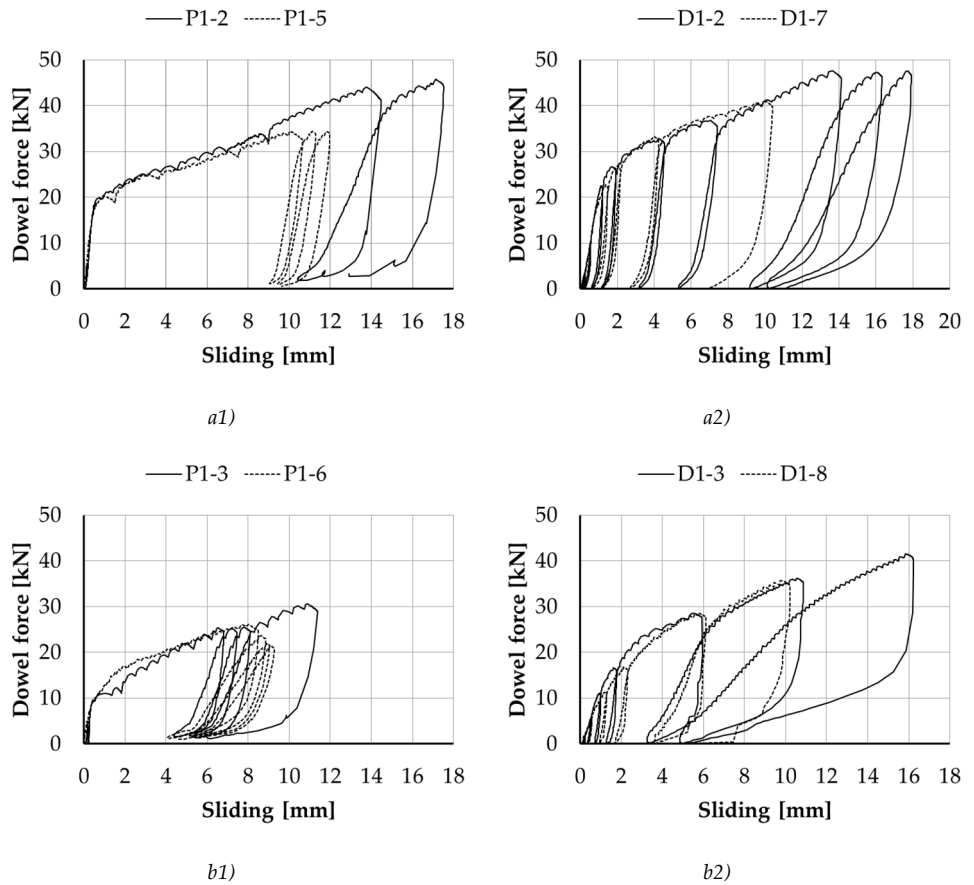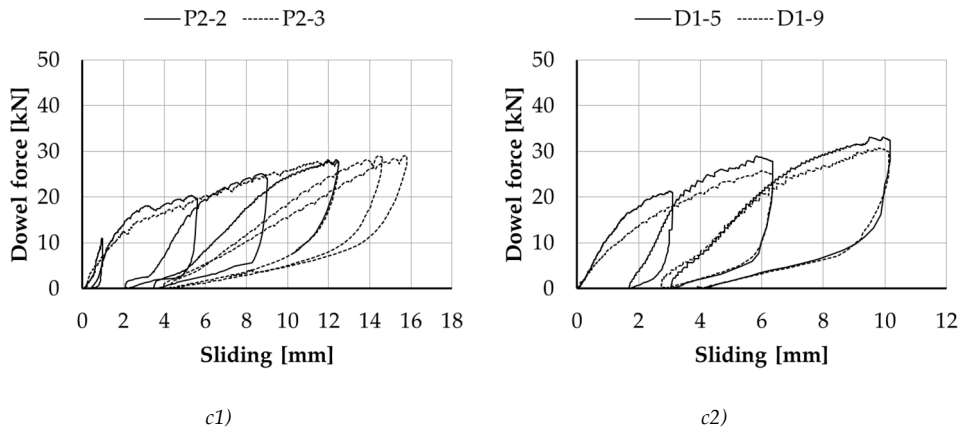

a1)

a2)

b1)

b2)

Figure 125 (Pt. 1 of 2)

173

c1)

c2)

(Pt. 2 of 2)

Figure 125: Shear force-displacement response of specimens with smooth 1) and deformed 2) rebar, respectively subjected to the 60% a), 90% b) and 98% c) of the yielding axial load.

Unloading and reloading stiffness had the same behaviour of the one observed in absence of axial load. The initial stiffer branch characterized most of the recovered force and the re-centring one started at the lower load levels. The latter was more pronounced at the higher sliding values. No strength degradation was observed in the V_d versus s_d response, showing a good ductility capacity of the mechanism. It is worth noting that concrete splitting failure was avoided by a high confinement of the concrete blocks.
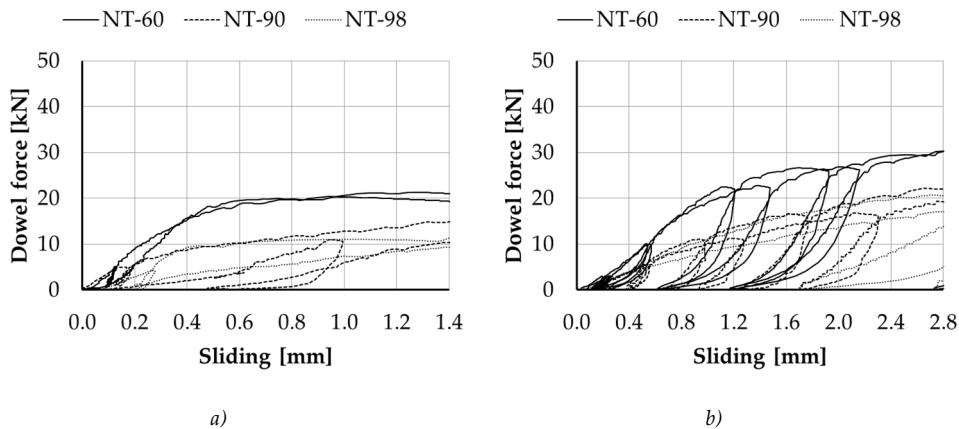

a)

b)

Figure 126: Full response of specimen subjected to different tensile axial load and cyclic not reversal shear loading a); focus on their initial behaviour b).

Combined cyclic not reversal shear and constant compressive axial load

The dowel tested under compressive load were very difficult to control since the shear transversal displacement fosters the buckling of the bar and the consequent closure of the crack. Because of this, the test done in these conditions were very few and only an axial load equal to the 60% of the yielding value was considered.

The responses of the specimens P2-4 and P2-7 are shown in Figure 127. The experimental envelope curve is bi-linear, as for the case of tensile axial load. A yielding shear strength of about 25kN was observed, a value slightly higher respect to the one registered for the series NT-60. The detrimental effect of the axial load on the mechanism strength is however confirmed. The kinking hardening effect is not expected in case of compressive load; on the contrary, a softening response should be related to second order effect. Nevertheless, sample P2-4 envelope curve shows a little hardening at a displacement level higher than 3mm (Figure 127.a). Consequently, an alternative shear strength mechanism may affect the response, such as friction on the concrete interface due to crack closure on the concrete debris. The two specimens yielding resistance was very similar, whereas their initial elastic stiffness was different. The yielding point can be located at a sliding level of about 1.00mm for the stiffer sample and about 1.40mm for the other one. Both the values result higher respect to the one associated with the NT-60 specimen response. The elastic stiffness seemed to be however similar. The lower slope exhibited by the specimens P2-7 force-displacement curve was confirmed by a series of unloading and reloading cycles. The unloading behaviour was consistent with the evidence relative to tensile axial load tests.
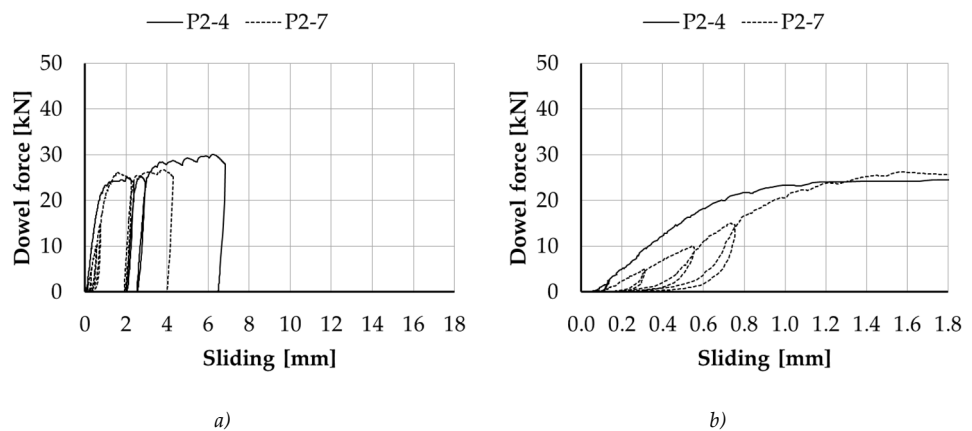

Figure 127: Response of the specimens tested under constant axial compressive load: NC-60 complete behaviour a) and detail on the initial phase b).

P2-5 sample was originally tested with a compression force equal to the 90% of the axial yielding load (NC-90). Its initial response is visible in Figure 128, compared with

the NC-60 curves. The response yielding can be located at a load level slightly lower than 20kN, about the double of the one observed in presence of tensile axial load; the relative sliding is about 0.40mm. Contrary to the experimental response of the series NT-90, the identification of the point of stiffness change   is easier. Since the application of a higher axial load has to be related with a lower shear strength, it is possible to think that the response could be governed by an alternative shear transfer mechanism, as it was noticed for the specimens NC-60.
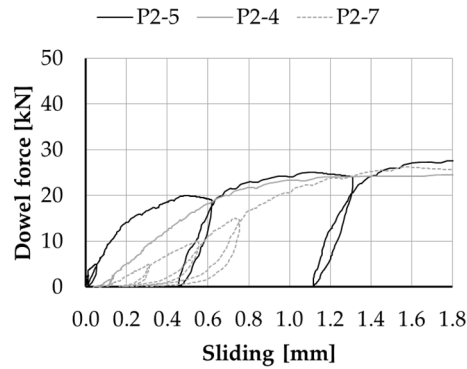

Figure 128: Shear-sliding relationship for the specimen with axial compressive load equal to the 90% of the relative axial yielding (NC-90).

Cyclic reversal shear with constant tensile axial load

Only smooth rebars are tested under cyclic shear reversals. The reference test was performed without axial load, to catch if the dowel behaviour is characterised by in-cycle or cyclic strength and stiffness degradation. The response of the P1-7 specimen showed a good symmetry in term of both strength and stiffness (Figure 129). Furthermore, the first loading cycle presents a behaviour very similar to the one analysed in the monotonic response (Figure 123.a1). The cyclic response was significantly affected by pinching, as it is clearly visible by the observation of the mechanism strength exhibited at a fixed sliding value. This phenomenon characterizes the response only after the first cycle in which a new maximum sliding value is reached; successive loading at the same deformation level showed the same hysteresis loops. The unloading stiffness can be considered constant during all the test. No relevant plastic deformations were visible, since the sliding demand is below the yielding point. Summarizing, the dowel mechanism is affected by cyclic stiffness degradation during reversal shear loading, caused to the imposition of higher sliding values. This peculiarity can be related to the concrete damage under bearing stress caused by the rebar acting against it (Biolzi and Giuriani, 1990), which are not recovered during the unloading process.

176

In presence of axial load, the control of the specimen response after the reach of the yielding becomes more complex. Because of this, the experienced sliding range increases during the test (Figure 130 e Figure 131). A higher deformation demand is however required to observe the cyclic behaviour in presence of an imposed significant deformation. Specimen P1-8 was tested with a constant tensile axial load value equal to the 60% of the yielding one (NTR-60). Its cyclic behaviour is shown in Figure 130. Also, in this case the response up to yielding point is symmetric, but the development of some plastic deformation complicated the response evaluation at the lower sliding level. Yielding strength of the mechanism is reached at a load level of about 20kN and its relative mean horizontal displacement is around 0.50*mm* in both the directions. No strength degradation is observed.
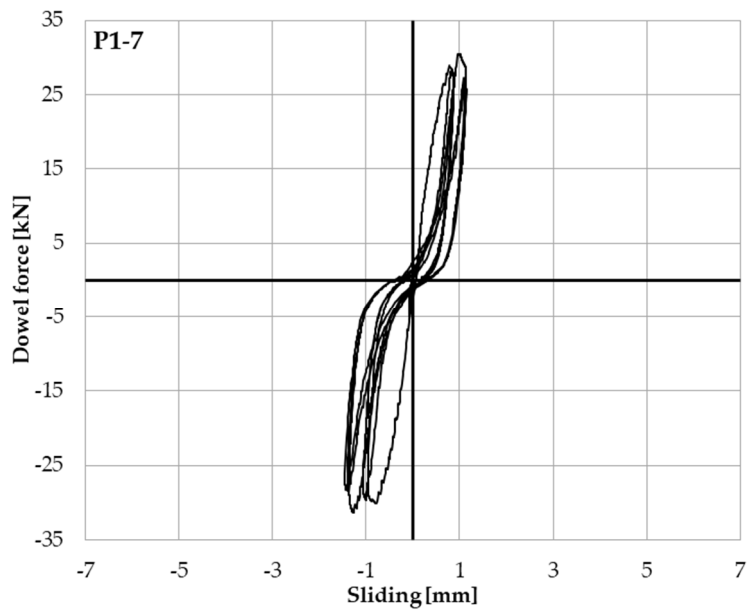

Figure 129: Cyclic response to transversal loading; specimen of the family NR-00.
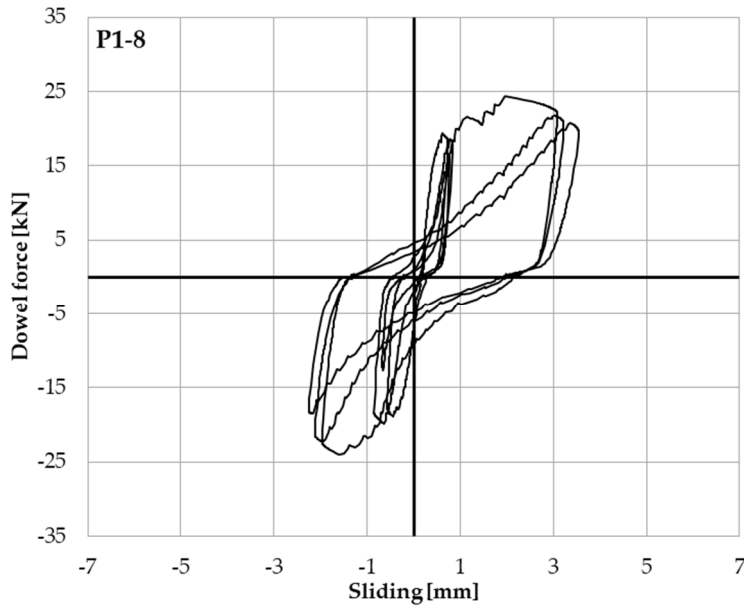
Figure 130: Cyclic shear response under constant tensile axial load equal to the 60% of the yielding one (NTR-60).

With an axial tensile load near to the yielding one (NTR-90), the shear-sliding behaviour showed a clear loss of stiffness at a load level of about 7kN in the positive loading direction. On the other hand, a linear re-loading up to 20kN is followed in the opposite direction. The former observed behaviour was very similar to the monotonic response of the specimen P1-3 (series NT-90 in Figure 125). The latter showed instead that the effect of the combined load makes the identification of a clear yielding point very difficult. Cause to the peculiarity of the shear load frame and to the displacement control by a manual pump, the sample behaviour was very sensitive to the loading rate and the different direction response was difficult to understand. Nevertheless, the detrimental effect of the axial load in the reduction of the mechanism strength is confirmed also in these tests. Moreover, the hardening behaviour due to the kinking effect is clearly visible from the hysteretic response of the specimen P1-8 (Figure 130) and P1-9 (Figure 131). The reloading showed a strong pinching effect, which was clearly visible thanks to the higher plastic deformation impose during the test. A decrease of the unloading stiffness was instead observed increasing the imposed deformation level. A higher re-centring behaviour can be seen at the highest sliding value. This effect is emphasized by the axial load since the kinking effect (discussed in the following) results proportional to the imposed transverse displacement magnitude.
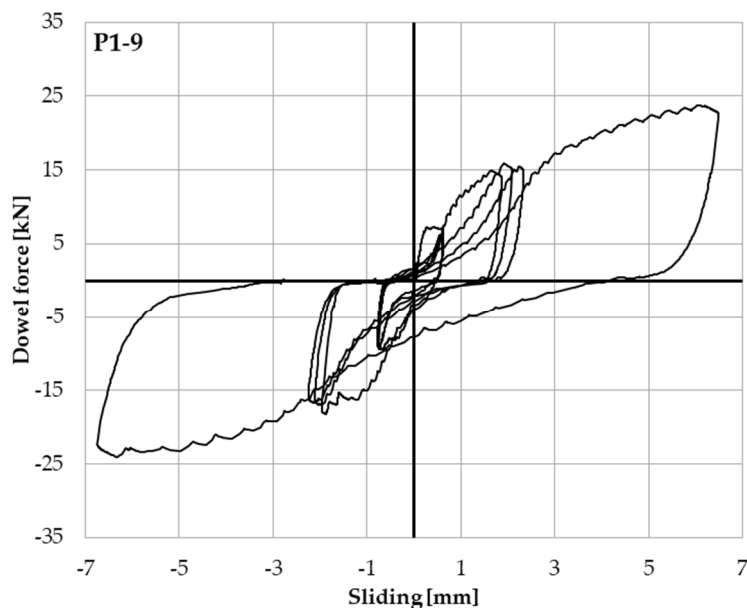
Figure 131: Dowel shear cyclic behaviour under a constant tensile axial load equal to the 90% of the yielding one (NTR-90).

Cyclic reversal of shear and axial loading

The herein presented test is the most comprehensive representation of the behaviour of a longitudinal rebar in an RC element simultaneously subjected to bending moment and sliding on a crack. A coupled cyclic shear and axial load is simultaneously applied. The test was done by the imposition of a fixed axial load value and a successive push up to a nominal yielding shear load. After the shear unloading, the axial load is removed and then inverted, finally also the shear load is reverted, thanks to a transversal displacement imposition by a jacket located on the opposite central concrete block side. To reach a compromise between the significance of the axial load on the dowel mechanism and the comprehension of the experimental results, a testing axial load level equal to the 60% of the yielding value (NRR-60) is chosen to better control the test.

In Figure 132 the experimental response is shown. The positive sliding values are relative to tensile axial load, conversely the negative ones are imposed in presence of a compressive axial stress on the rebar. The first loading was in the positive direction (axial tension) and the behaviour showed a less stiff force-displacement relationship respect to the previous observed ones. The nominal yielding point can be located at a shear load of about 20kN, but the relative sliding value was higher than 1.00mm. For the series NT-60 it was lower than 0.5mm, whereas in the NTR-60 test it was less than 1.00mm. In the opposite direction the response seemed instead to be consistent

179

with the previous analysed evidence, with reference to the same compressive axial stress. The same conclusion drawn for the cyclic response in presence of tensile axial load can be confirmed. It seems reasonable to conclude that the sign of the axial load does not significantly change the yielding strength of the mechanism subjected to cyclic combined shear and axial loading. On the other hand, it is clearly visible that in presence of tensile load an hardening behaviour is guaranteed by the kinking effect, whereas the compression load does not produce a softening plastic branch of the response, like it would be reasonable to assume for the same reasons. The behaviour of the specimens can so be related mainly to the plastic response of the dowel, governed by the formation of two plastic hinges on both the sides of the crack. Obviously, this formation is strongly affected by the axial load value, which influence is reflected in a lower strength exhibited at a reference sliding level.
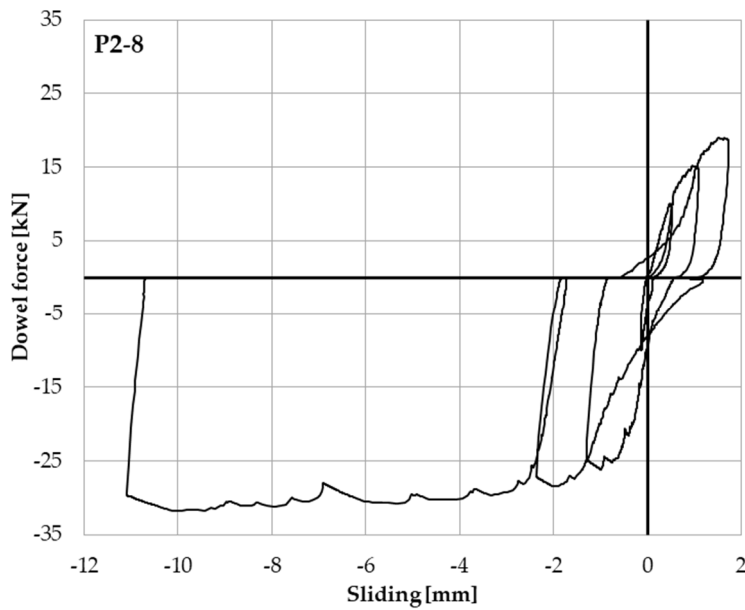

Figure 132: Response to coupled cyclic axial and shear load.

4.6 Analysis of the experimental results

Shear sliding response in presence of different axial load

In the following, a data analysis aimed to quantify the effect of the coupled loading on the dowel mechanism strength is presented. Furthermore, an analytical model to predict the dowel shear versus displacement behaviour is suggested, accounting for the axial load presence. Only cyclic not reversal load in presence of tensile axial stress (N and NT) is considered. Indeed, the test done with reversal shear loading (NRT) and coupled reversal axial and shear loading (NRR) have shown a behaviour very similar to the one herein analysed. Therefore, the following considerations can be extended to all the cases. On the other hand, no conclusions are treated on the force-displacement relationship under combined shear and compressive load (NC).

The experimental evidence shows that the force-displacement behaviour can be well represented by a bi-linear curve. Elastic-plastic envelope is a good approximation of the response in absence of axial loading, whereas a hardening branch can well represent the post-elastic behaviour of the mechanism in presence of a significant tensile axial load. On the other hand, the experimental force-displacement relationship assumes a more complex shape increasing the considered axial load. The evidence is clear observing the following Figure 133 e Figure 134, with main attention on the resume graph e). More in detail, the initial elastic branch presents a stronger non-linear behaviour, therefore the identification of a yielding load on the envelope curves is difficult. To note the axial load role on the dowel mechanism behaviour, two main conclusions can be suggested:

- increasing axial load value, the nominal yielding strength of the mechanism decreases;
- fixed a reference sliding value, the higher the axial stress in the rebar the lower the mechanism resistance.
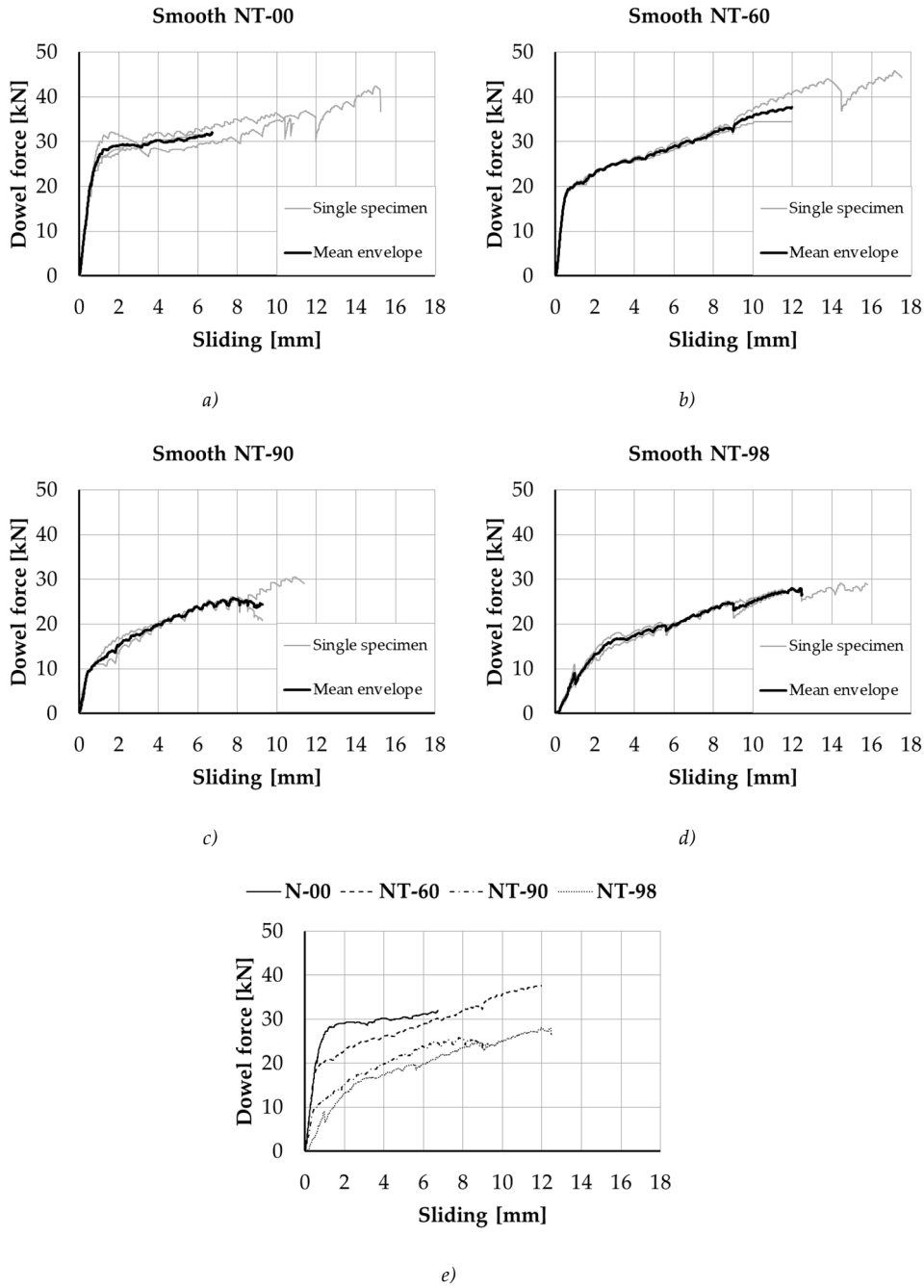
a)

b)

c)

d)

e)

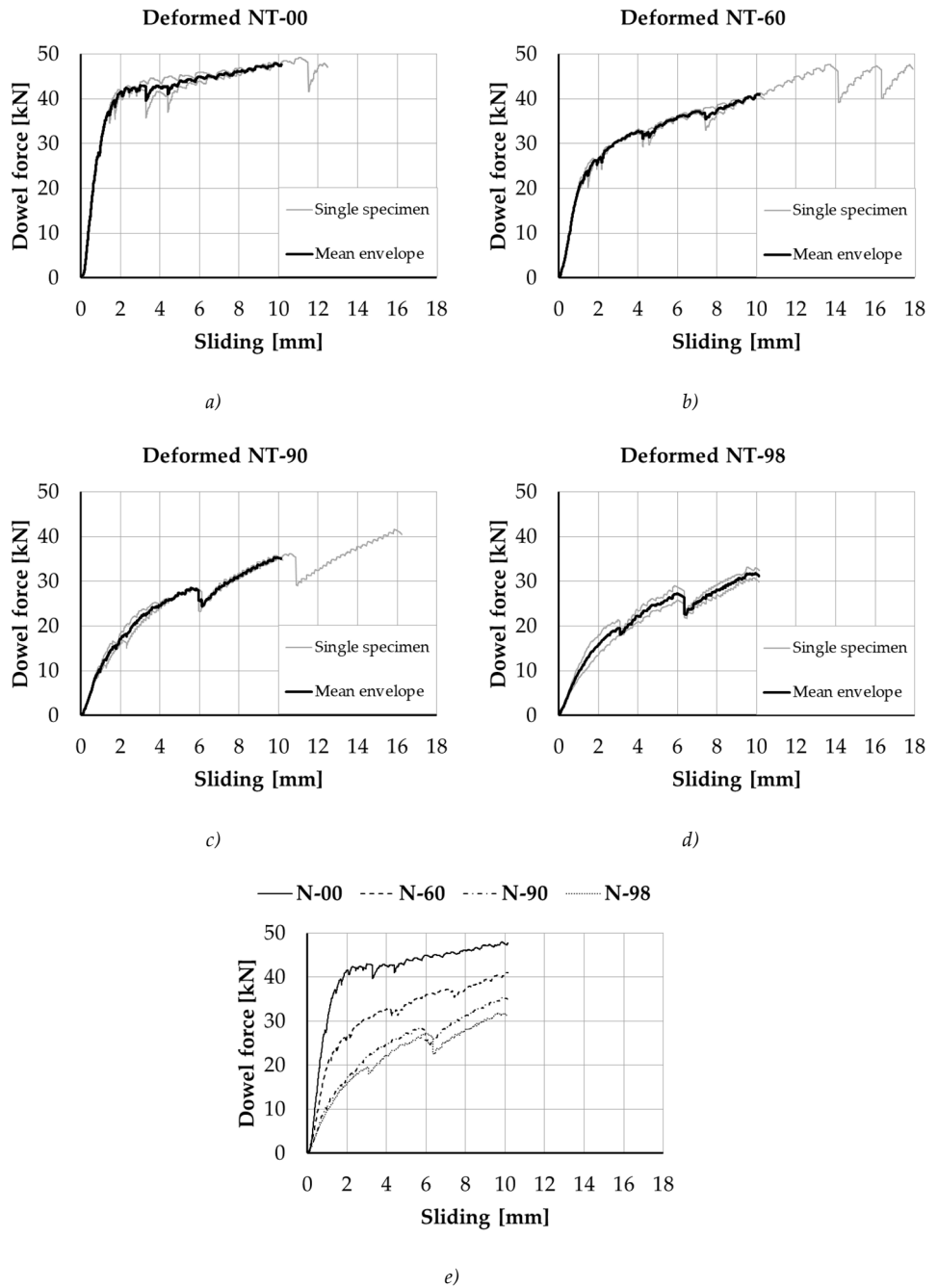Figure 133: Experimental response of smooth dowel rebar in presence of different tensile axial load.

Figure 134: Experimental response of deformed dowel rebar in presence of different tensile axial load.

Comparison between smooth and deformed dowel response

A direct comparison between the behaviour of smooth and deformed dowel is not possible. Indeed, the different bars are characterized by different yielding stress, thus by different dowel mechanism yielding force. With reference to Figure 135, some interesting conclusions can be however treated.

Without axial load, the initial elastic branch of the force-displacement relationships is similar for both the plain and deformed rebar. Increasing the axial stress is instead possible to notice a stiffness decrease for the latter. However, no significant difference is finally observed, in term of stiffness, for the dowel axially loaded near to the yielding point (NT-98). The experimental evidence can be explained by a concrete pull-out damage caused by the ribs of the deformed rebar, which reduces the stiffness of the concrete surrounding the bar and reacting to the transversal displacement (Maekawa and Qureshi, 1996b; Soltani and Maekawa, 2008). This phenomenon can be neglected for the dowel tested in presence of the highest axial load (NT-98), since the mechanism behaviour is mainly influenced by the kinking effect (Figure 135.d).

Except for the null axial load case (N-00), the comparison shows that in presence of deformed rebar the response assumes a stronger non-linear behaviour. This can be observed also at the lower sliding level. Consequently, the identification of a yielding shear load for the mechanism is not immediate, while it is easier in the case of smooth dowel.

Prediction of the mechanism behaviour

To predict the mechanism strength it is possible to refer to a literature proposal (Gelfi and Giuriani, 1987; Giuriani, 2012). Considering a reinforcement rebar across a crack, simultaneously subjected to axial and shear load, a self-balanced calculation scheme is presented in Figure 136. The analysed mechanism is flexural based, and it results characterised by a ductile failure (if splitting mechanism is avoided in presence of sufficient confinement of the concrete). Because of this, it is possible to apply a limit analysis to evaluate the yielding strength of the embedded rebar subjected to transverse load, assuming a rigid plastic behaviour both for the reinforcement steel and for the surrounding concrete.
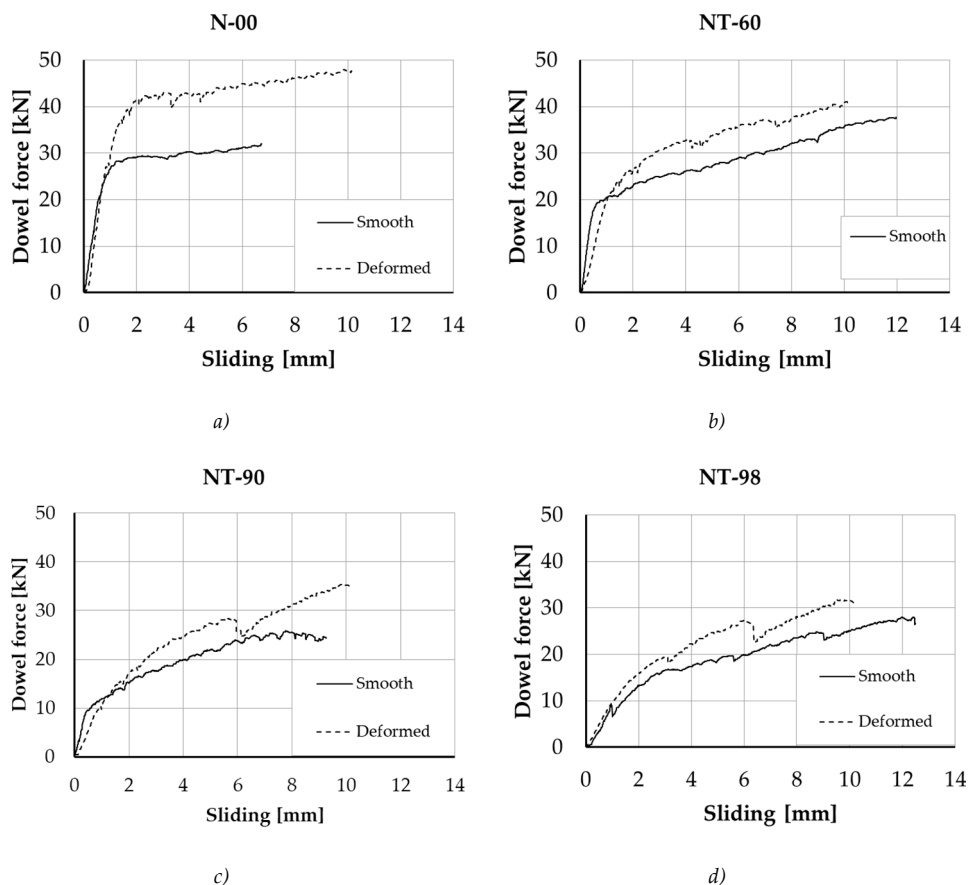
a)

b)

c)

d)

Figure 135: Shear sliding envelope behaviour for the NT series.

The capacity of the mechanism is expressed as a function of the problem geometry and of the material mechanics, considering small deformations. At the mechanism triggering a plastic hinge forms on both the crack sides, at a certain distance L_{eff} from the load point application (contraflexure point). Translational and rotational equilibrium imposition are expressed by the followings:

$$V_{dy} = d_b f_{cc} L_{eff} \qquad (139)$$

$$M_y(N_s) = V_{dy}(L_{eff} + a) - d_b f_{cc} \frac{L_{eff}}{2} \qquad (140)$$

where V_{dy} is the mechanism yielding strength obtained from the herein proposed procedure, d_b is the bar diameter, $f_{cc} = 5f_c$ is the concrete bearing strength (Biolzi and Giuriani, 1990; Vintzēleou and Tassios, 1986), L_{eff} is the effective length required to balance the applied load, a is the shear load eccentricity (assumed to be the half of

185

the crack width for the problem symmetry), and $M_y(N_s)$ is the plastic bar bending strength, related the actual axial load. Rearranging:

$$d_b f_{cc} L_{eff}^2 + d_b f_{cc} a L_{eff} - M_y(N_s) = 0 \qquad (141)$$

The latter term of Eq.(141) is the main parameter influencing the dowel response under coupled action. Indeed, the plastic hinge formation is strongly influenced by the presence of an axial stress in the rebar. Known this, it is possible to quantify the cross-section fibres area $A_n(N_s)$ resisting to it:

$$A_n(N_s) = \frac{N_s}{f_y} \qquad (142)$$

where f_y is the rebar steel yielding stress and N_s the relative axial load. In this condition a maximum bending action $M_y(N_s)$ can be balanced by the yielding of the only outer fibres (Figure 137):

$$A_m = \frac{1}{2}\left(\pi \frac{d_b^2}{4} - A_n(N_s)\right) \qquad (143)$$

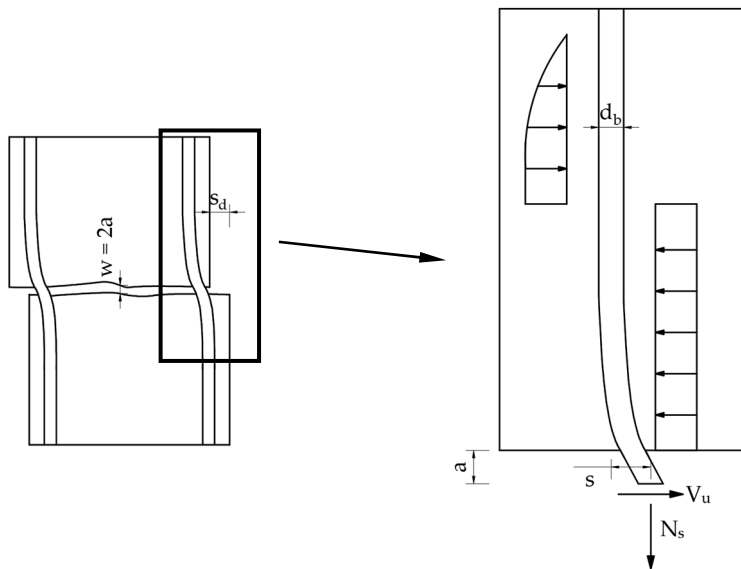$$M_y(N_s) = f_y A_m(N_s) z(N_s) \qquad (144)$$

Figure 136: Representation of dowel mechanism in presence of coupled shear and axial load.

Working on the circular section (Figure 137.a), the following expression can be demonstrated:

$$A_m(N_s) = \frac{d_b^2}{8}(\theta - sin\theta) \qquad (145)$$

To define the plastic bending capacity in presence of a defined axial load, it is necessary to solve the non-linear form of Eq.(146), identifying the angle subscribing the bending available cross section area:

$$\theta - sin\theta - \frac{8A_m(N_s)}{\pi d_b^2} = 0 \qquad (146)$$
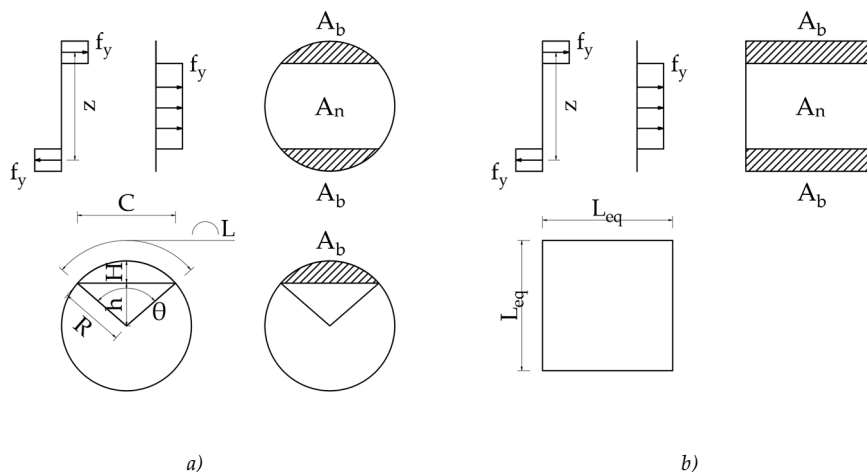
Figure 137: Coupled axial and bending stress distribution in the rebar: limit analysis on the effective circular shape b) and equivalent square section approach c).

An alternative and simpler approach can be defined working on an equivalent square section, for which (Figure 137.b):

$$L_{eq} = \sqrt{\frac{\pi d_b^2}{4}} \qquad (147)$$

In this case the determination of the bending moment capacity, thus of the effective length and of the dowel yielding capacity are direct:

$$L_{eff} = -a + \sqrt{a^2 + \frac{f_y\left(l_{eq^3} - \frac{N_s^2}{l_{eq}f_y^2}\right)}{2d_{bf_{cc}}}} \qquad (148)$$

$$V_u(N_s) = d_b f_{cc} L_{eff}(N_s) \qquad (149)$$

187

Axial load also affects the post-elastic behaviour of the mechanism, offering a re-centring transversal force called kinking effect (only in case of tensile load). Based on the schematisation of Figure 138, assuming the plastic hinges to form at a known distance from the crack interface and linearising the phenomenon, it is possible to define the following hardening stiffness:

$$K_k = \frac{N_s}{2(a + L_{eff})} \tag{150}$$

where, for the sake of simplicity, the imposed distance from the crack side is assumed, in any case, to be the effective length of the mechanism in absence of $L_{eff}(N_s = 0)$. This assumption could be not consistent with the limit analysis above presented, in which L_{eff} decreases with axial stress increasing. Nevertheless, it is worth noting that the crack opening also increases in presence of axial load; therefore, in first approximation, it is assumed a reference constant length.

In presence of axial compressive load, the opposite effect should be noticed, and a softening behaviour can be expected after the mechanism yielding. From a mathematical point of view, Eq.(150) reflects this observation. On the other hand, the experimental evidences do not show a decrease in the dowel strength (series NC-60).
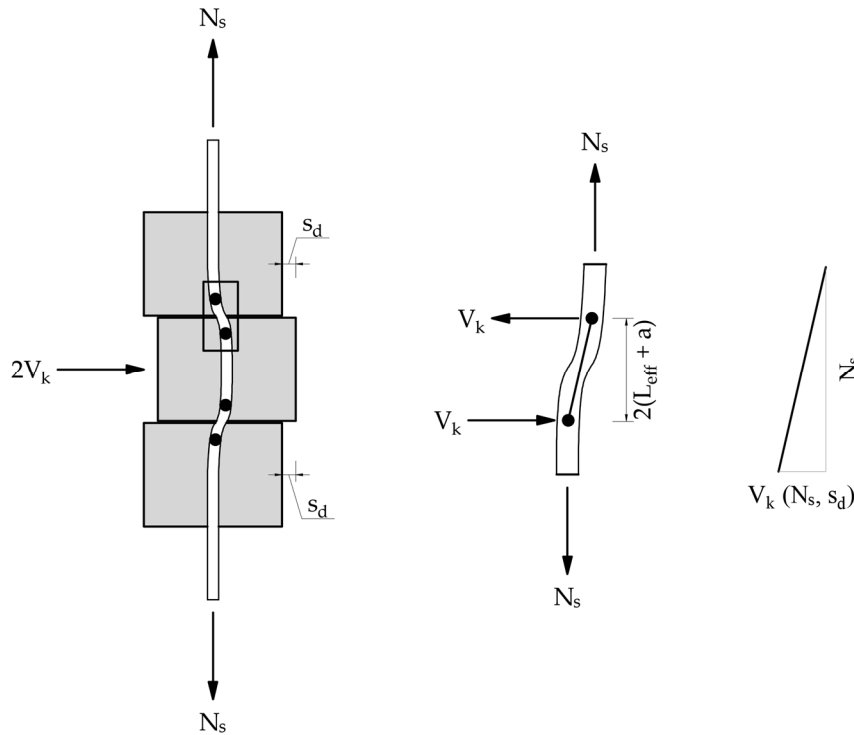

Figure 138: Schematization of the kinking effect contextualized on the reference specimen.

To analytically define a complete force-displacement relationship, the definition of the elastic stiffness is still missing. In the following, a model for its definition is presented. The same literature proposal at the base of the strength evaluation is considered as a starting point (Gelfi and Giuriani, 1987). The concrete around the dowel rebar is schematized assuming independent parallel layer Each of them can be schematized as a plate subjected to a local horizontal load. Referring to Figure 139, the applied force V_i and the consequent deflection are related by the elasticity theory in this way:

$$K_c = \frac{V_i}{\delta} = \frac{\sigma_c d_b E_c}{\beta d_b \sigma_c} = \frac{E_c}{\beta} \qquad (151)$$

where the applied load on each layer V_i is balanced by concrete uniform stress σ_c on the rebar diameter d_b, and β is a coefficient dependent on the rebar spacing. The latter is herein assumed in the following range:

$$\beta = 2.5 \div 3.3 \qquad (152)$$

According to the original proposal (Gelfi and Giuriani, 1987) and in a consistent way with the typical longitudinal rebar spacing in RC existing members ($10 \div 20 d_b$).
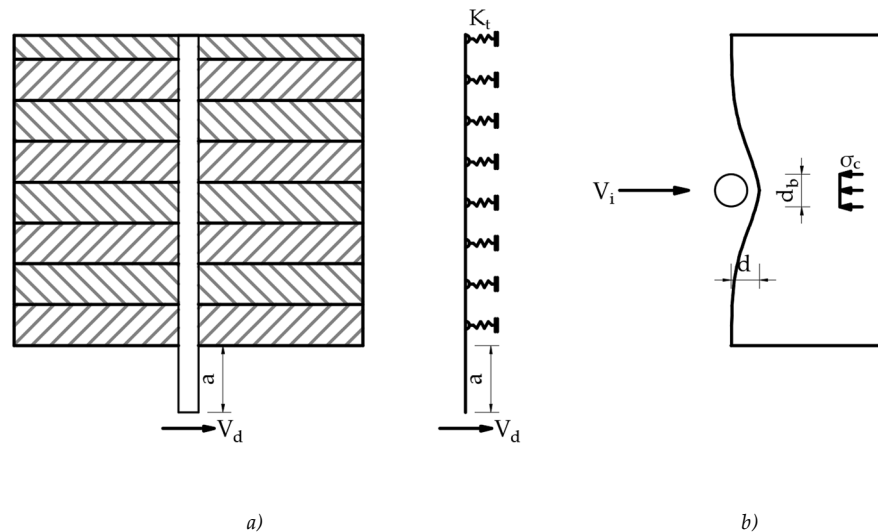

a)   *b)*

Figure 139: Schematization of the concrete around the dowel rebar: EBEF model a) and concrete layer plate under local horizontal force b).

Known the stiffness of the EBEF soil, it is possible to express the initial elastic stiffness of the whole mechanism. The external applied load V_d is thus divided by the maximum transversal deflection $s = 0.5s_d$ (contextualized in Figure 136). The proposed approach also accounts for the load eccentricity a, which is not considered in the original model:

$$s_d = \frac{V_d}{\lambda^2 E_s J_b} \left[\frac{(2 + a\lambda)}{\lambda} + a(1 + a\lambda) \right] \tag{153}$$

$$K_0 = \frac{V_d}{s_d} \tag{154}$$

The parameter λ is the relative stiffness of the EBEF model, which can be particularized for this specific case:

$$\lambda = \frac{2}{d_b} \left(\frac{1}{n\pi\beta} \right)^{1/4} \tag{155}$$

with $n = E_s/E_c$ ratio between the reinforcement steel and surrounding concrete modulus of elasticity. Anyway, the significant non-linear response experimentally observed cannot be represented through a secant stiffness branch. According to herein considered reference suggestion (Gelfi and Giuriani, 1987), the K_0 value above presented is used for the representation of the initial tangent stiffness. A non-linear behaviour is then defined by the following:

$$V_d = V_{dy} \left[1 - exp \left(-\frac{K_o}{V_{dy}} s_d \right) \right] \tag{156}$$

where the load capacity at yielding V_{dy} is defined with the direct formulation based on the equivalent square section (Eq.(147-149)). After the yielding point identification, the response is governed by the only kinking effect contribution, which equivalent stiffness is quantified in Eq.(150).

An application of the proposed model is represented in Figure 140 and Figure 141, respectively for the smooth and the deformed dowel rebar. In the same graphs is visible the comparison with respect to the experimental envelope response. The approach seems to be very good in the prediction of the smooth dowel response, whereas it is less accurate in the case of the deformed rebar. The great difference is in the estimation of the mechanism stiffness. It is noteworthy to observe that the herein presented model does not account for concrete damage, due to deformed rebar pull-out from the concrete. This can significantly influence the response in term stiffness, as it is experimentally observed. A refinement of the method is thus required for the application to ribbed dowel subjected to coupled axial and shear action.

Quantification of the experimental results

Two different ways to quantify the axial stress role on the definition of the dowel behaviour are herein discussed. The first refers to the simplified analytical model above presented, the second one measures the strength data at a fixed sliding value. The results of the two different approaches do not have to be considered exhaustive in the definition of the dowel mechanism capacity. Indeed, a complex behaviour in term of load-displacement response was observed, and it makes very difficult the identification of a yielding and/or failure load value. Nevertheless, the suggested methods can be useful to highlight the coupled action effects. Numerical values about the application are presented in Table 23 for the smooth dowel and in Table 24 for the deformed one. $V_{dy,mod}$ is the analytical calculated mechanism capacity at yielding; on the other hand, $V_{d,st}$ is the experimental strength at the reference drift. The subscript zero refers to null axial load case ($V_{dy,mod0}$, $V_{d,st0}$). A relative comparison is reported to briefly describe the influence of the axial load.

For the plot of the proposed model a target sliding level of 5mm is chosen. Anyway, it has no influence on the accuracy of the tool, since the predicted yielding strength $V_{dy,mod}$ depends only on the rebar geometry and on the material mechanics. On the other hand, the choice of the target sliding at which the mechanism strength is read strongly influences the results of the approach. In this work a conventional choice $s_t = 0.5mm$ is presented; it is worth noting that it does not represent the mechanism yielding. For structural application specific target values can however be set, to well match the expected sliding or to guarantee specific performances.
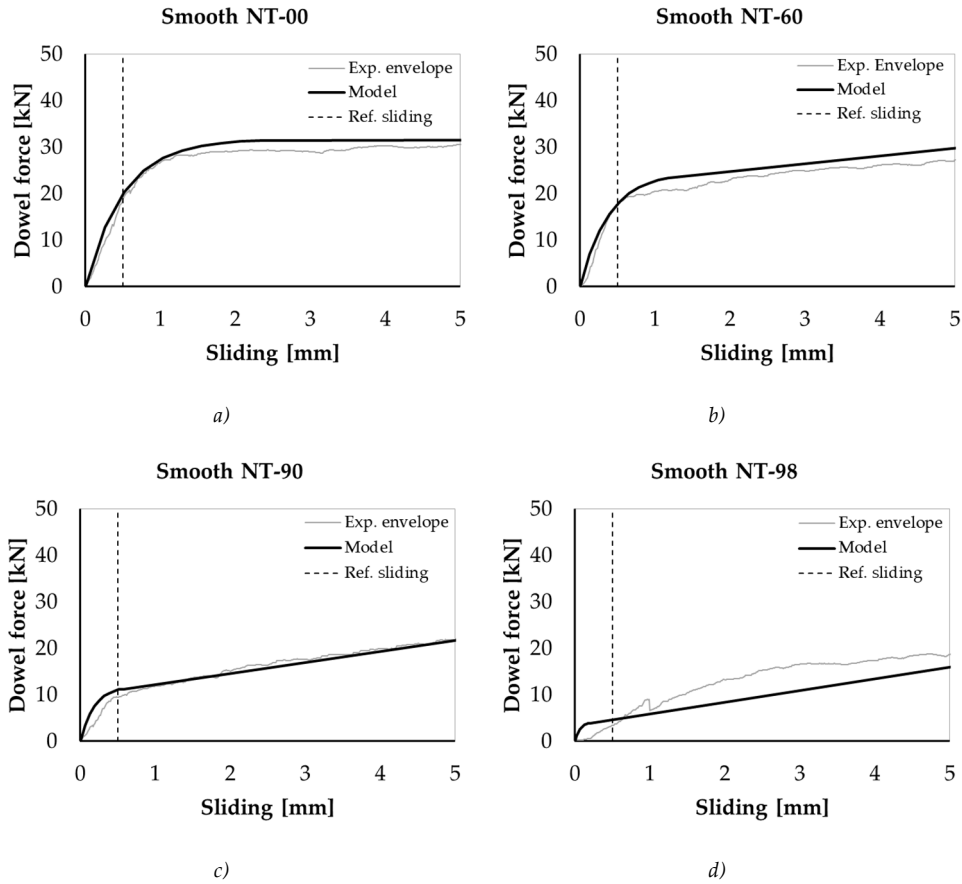
a)

b)

c)

d)

Figure 140: Modelling of the experimental force-sliding mean envelope curve in presence of increasing axial load: smooth rebar dowel. N-00 a), NT-60 b), NT-90 c) and NT-98 d) series.

N [Ny]	$V_{dy,mod}$ [kN]	$V_{dy,mod}$ (N) / $V_{dy,mod0}$	$V_{d,st}$ [kN]	$V_{d,st}$ (N) / $V_{dy,st0}$
0.00	31.76	1.00	18.36	1.00
0.60	24.70	0.78	17.66	0.96
0.90	11.98	0.38	9.53	0.52
0.98	4.11	0.13	3.47	0.19

Table 23: Quantification of the dowel mechanism strength in presence of coupled shear and axial load: smooth dowel.
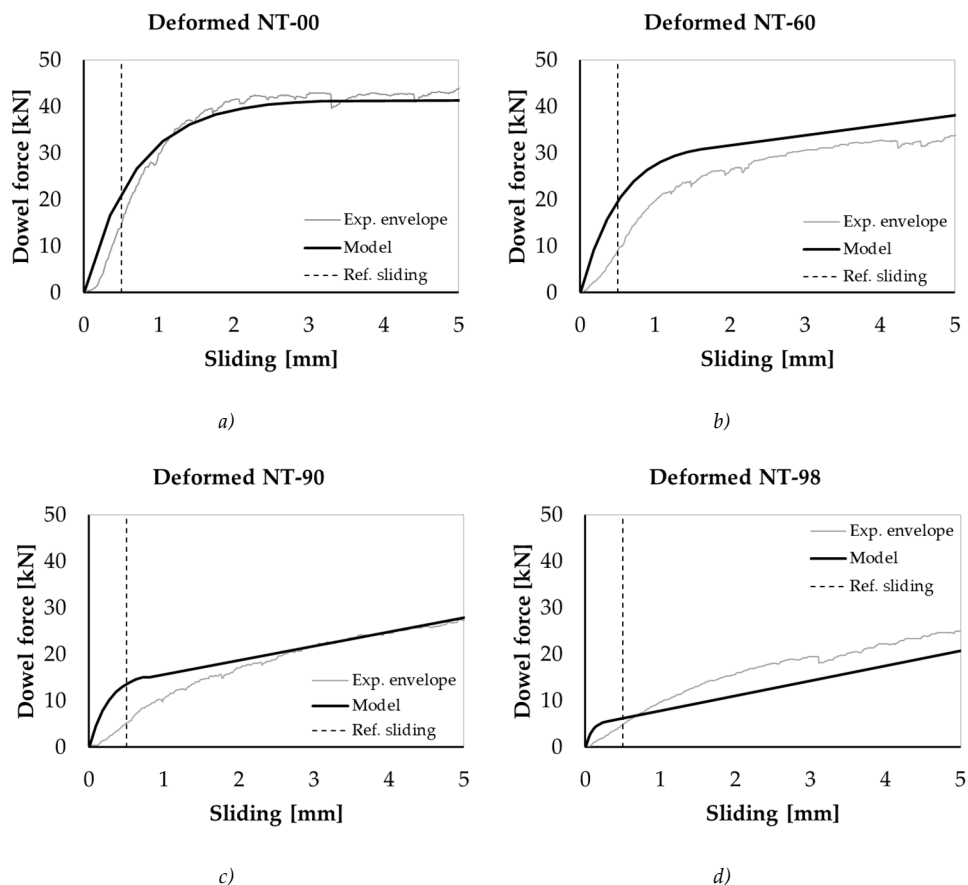
a)

b)

c)

d)

Figure 141: Proposed model for the experimental force-sliding mean envelope curve in presence of increasing axial load: deformed rebar dowel. N-00 a), NT-60 b), NT-90 c) and NT-98 d) series.

N [Ny]	$V_{dy,mod}$ [kN]	$V_{dy,mod}$ (N) / $V_{dy,mod0}$	$V_{d,st}$ [kN]	$V_{d,st}$ (N) / $V_{dy,st0}$
0.00	41.59	1.00	14.15	1.00
0.60	32.54	0.78	8.84	0.62
0.90	16.18	0.39	5.19	0.37
0.98	5.87	0.14	4.82	0.34

Table 24: Quantification of the dowel mechanism strength in presence of coupled shear and axial load: deformed dowel.

Comparison with model available in literature

In the following, the experimental results above discussed are compared with different predictive models available in literature. Firstly an analysis on the

mechanism yielding strength is proposed, in a second time a more comprehensive study of the force-displacement relationships follows. Cause to the difficulty in the definition of an experimental yielding load, a direct comparison on the only different predictive tools is presented. For the experimental data see the previous curves.

The first references available in literature are all based on limit analysis approach and do not account for coupled action and load eccentricity in a direct way (Dulacska, 1972; Soroushian et al., 1986; Vintzēleou and Tassios, 1987). However, Soroushian et al. proposal (Soroushian et al., 1986) is herein taken as a reference, but modified to account for the coupled loads.

$$V_u = f_b \frac{(L-c)^2}{2} + \frac{M_y(N)}{L+a}$$

The load eccentricity a is introduced in the original equilibrium formulation, and the axial load influence is considered in the following way:

$$M_y(N_s) = \frac{f_y d_b^3}{6}\left(1 - \frac{4N_s}{\pi d_b^2}\right)$$

Empirical formulation (Soroushian et al., 1987) for the concrete bearing strength f_{bc} and the stiffness K_c are assumed and implemented in the reference model equations. For more details see the State fo the Art (Section 2.6).

Gelfi and Giuriani original proposal (Gelfi and Giuriani, 1987) allows to account for load eccentricity but not for the combined load effects. The above discussed extensions of the theory, on the circular and equivalent square cross section, are thus implemented for a more comprehensive approach to the problem.

Elastic Beam on Elastic Foundation (EBEF) model is applied in its elastic form and a yielding surface $\lambda(x)$ (Maekawa and Qureshi, 1996b) is considered to identify the yielding shear capacity of the mechanism:

$$V(x) = Ve^{-\lambda x}[sin(\lambda x) - cos(\lambda x) - 2a\lambda sin(\lambda x)] \tag{157}$$

$$M(x) = -\frac{V}{\lambda}e^{-\lambda x}[sin(\lambda x) - a\lambda cos(\lambda x) \\ - a\lambda sin(\lambda x)] \tag{158}$$

$$\lambda(x) = \left[\frac{M(x)}{M_0} + \left(\frac{N}{N_0}\right)^2\right] + \left[\frac{V(x)}{V_0}\right]^2 \tag{159}$$

$$V_{dy} = V(\lambda = 1) \tag{160}$$

where all the employed parameters have been already presented in the literature survey (Chapter 2). Graphic examples of the method application on smooth dowel is represented in Figure 142.
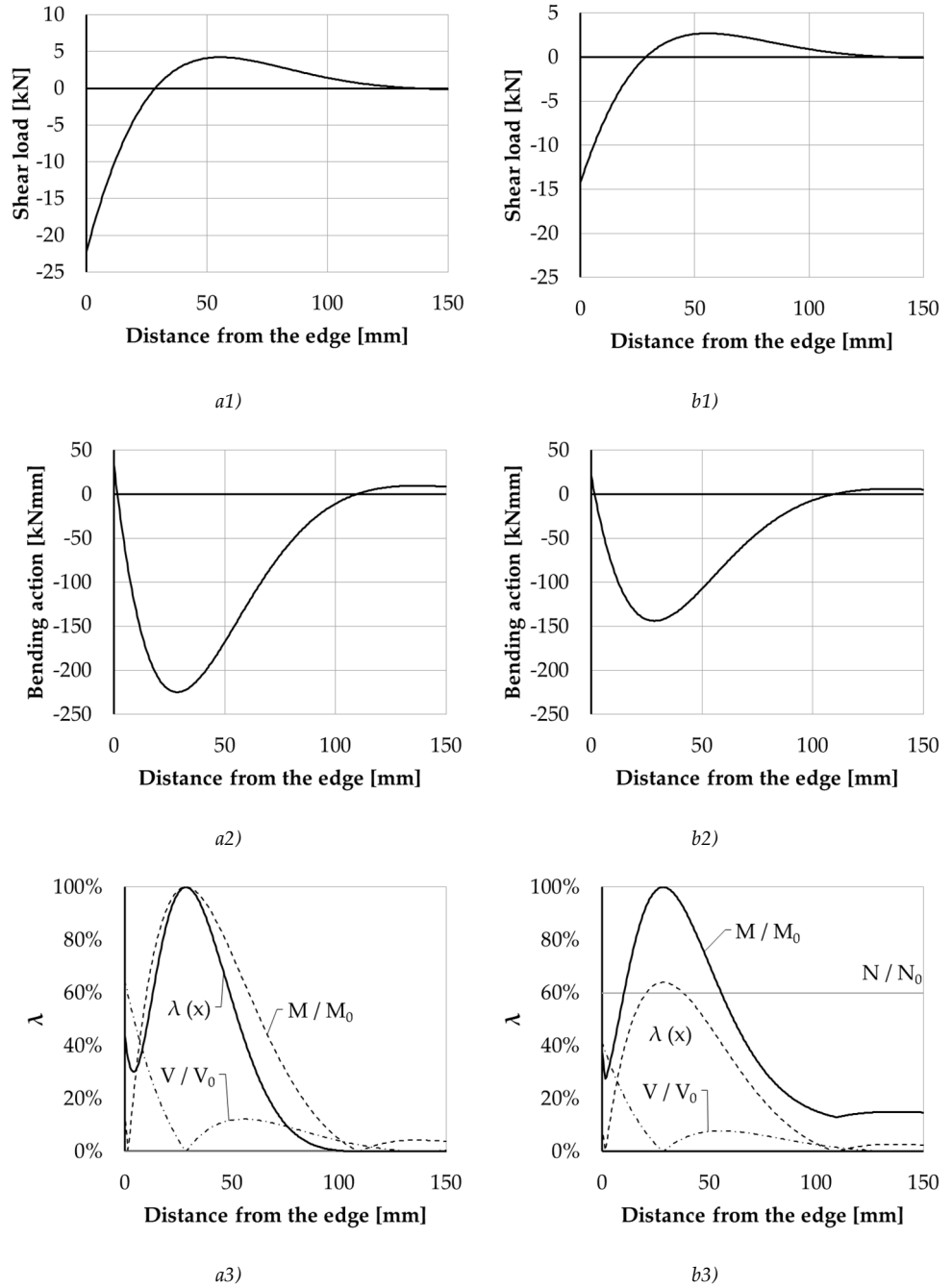
a1)

b1)

a2)

b2)

a3)

b3)

Figure 142: Bending 1) and shear 2) action combined in the yielding surface criterion (Maekawa and Qureshi, 1996b) 3) for a reference specimen in presence of smooth rebar: null axial load a) and 60% of the yielding value b).

195

Finally, the minimum value between the Code formulations for the sliding verification is also considered (CEN Eurocode 8, 2005; Norme Tecniche per le Costruzioni, 2018):

$$V_{dd,1} = 1.3 A_s \sqrt{f_c f_y} \qquad (161)$$

$$V_{dd,2} = 0.25 A_s f_y \qquad (162)$$

$$V_{dd} = min(V_{dd,1}; V_{dd,2}) \qquad (163)$$

where A_s is the rebar cross section area.

In Figure 143 a strength dominion is represented, in term of dowel mechanism yielding load versus normalized axial stress. Except for the first presented approach (adapted from Soroushian et al., 1986), the predictive tools which direct account for axial load presence are consistent in confirming the experimental results. The herein suggested analytical predictive models show results very similar to each other, the simpler approach (related to the consideration of an equivalent square section) is thus preferred. On the other hand, more conservative results can be obtained by the application of the elastic based EBEF model associated to the yielding surface criterion (Maekawa and Qureshi, 1996b). Using the latter, the dominion curve shape is very similar to the previous analysed ones, moreover it shows that the influence of the coupled action is very strong in presence of the highest axial load values. Code indications about the sliding verification at the base of the shear walls (CEN Eurocode 8, 2009; Norme Tecniche per le Costruzioni, 2018) are safety side only in presence of an axial stress lower than the 60% of the yielding one, both for smooth and deformed dowel. It is noteworthy to observe the comparison between the Code prediction and the experimental strength at the reference sliding. In the case of the deformed rebar the latter is significantly lower. This conclusion is consistent with the observed loss of stiffness associated to the dowel mechanism of ribbed bar; on the other hand, the result is strictly dependent on the conventional choice about the reference sliding value. It does not identify the mechanism strength capacity.
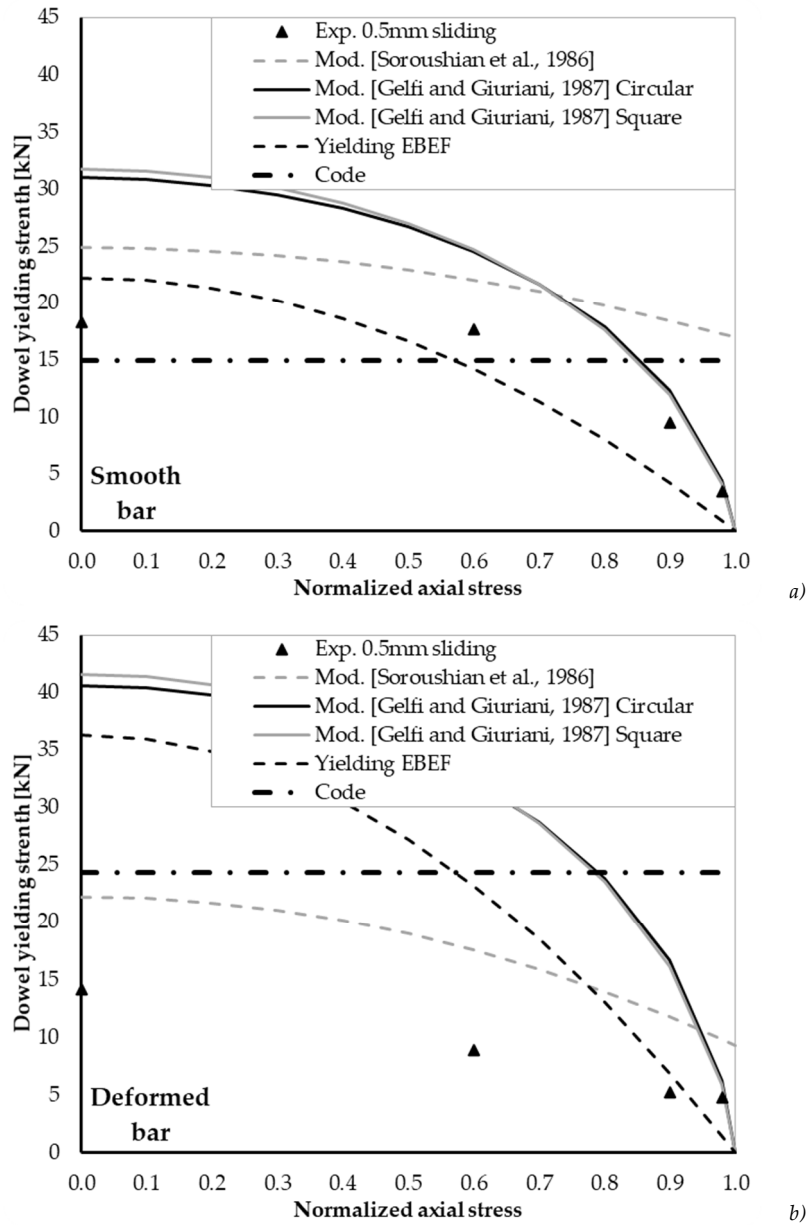
Figure 143: Coupled shear and axial load dominion for smooth a) and deformed b) rebar.

Regarding the dowel force-displacement relationship assessment (Figure 144), the main available tools in the literature are referred to the case of null axial load. The comparison presented in the following is so restricted to this case. The main reference model is the Elastic Beam on Elastic Foundation (EBEF) one. Accounting for the load eccentricity a, it is possible to express the deflection at the free end y_{max} as a function

197

of: the applied load V_d, the bar diameter d_b, its flexural stiffness $E_s J_s$, and the concrete stiffness under bearing loads k_c:

$$y_{max} = y(x = 0) = \frac{V_d}{2\lambda^2 E_s J_s}\left[\frac{(2 + \lambda z)}{\lambda} + (1 + \lambda z)z\right] \qquad (164)$$

$$\lambda = \left(\frac{K_c d_b}{4 E_s J_s}\right)^{\frac{1}{4}} \qquad (165)$$

Under the hypothesis of perfect elasticity conditions, the EBEF model reference model is characterized by a unique value of the soil (concrete) stiffness k_c. In the load increasing phase, due to the progressive concrete damage, this parameter can however assume different values. A secant stiffness to the failure load is suggested in the literature (Soroushian et al., 1987); for the test specimens it results:

$$k_t = 127\frac{\sqrt{f_c}}{d_b^{\frac{2}{3}}} = 116\frac{MPa}{mm} \qquad (166)$$

The proposal is not able to well represent the experimental response (Figure 144). The resulting linear force-displacement relationship exhibits a stiffness too low with respect to the experimental evidence. To solve this representativeness issue, damage models for the concrete stiffness could be implemented (Figure 145). They can be quantified by the ratio between the actual load and the mechanism shear capacity (Dei Poli et al., 1992), or by the consideration of the actual shear displacement (Brenna et al., 1990; Moradi et al., 2012). The mathematical formulations of the proposed laws are reported in the State of the Art (Chapter 2). Applications on the experimental data herein treated are reported in Figure 145. In the same graph is also visible the strong difference with the EBEF proposal, in which a secant stiffness constant value is considered. The modified models catch very well the response of the deformed dowel specimens. With reference to the plain rebar, they are equivalent in representing the initial elastic stiffness of the mechanism, whereas they differently represent the behaviour at the highest load levels. The force-based degrading model (Dei Poli et al., 1992) follows with a very good accuracy the entire initial response branch, the displacement-based ones (Brenna et al., 1990; Moradi et al., 2012) presents instead a delayed loss of stiffness. It is worth noting that these curves are not representative of the mechanism strength, for which assessment is required the application of a specific dominion, like previously discussed.

Gelfi and Giuriani proposal (Gelfi and Giuriani, 1987) well reflects the experimental data. Other refence models are purely empirical; thus, they result significantly dependent on the experimental specimens and on the loading arrangements. One of them well represents the mechanism strength despite it does not account for the load eccentricity (Dulacska, 1972); its elastic response is however too stiff. Another one

does not catch either the load capacity nor the initial response stiffness (Soroushian et al., 1986); furthermore, its post-elastic branch present also softening behaviour, non-representative of the considered specimens.
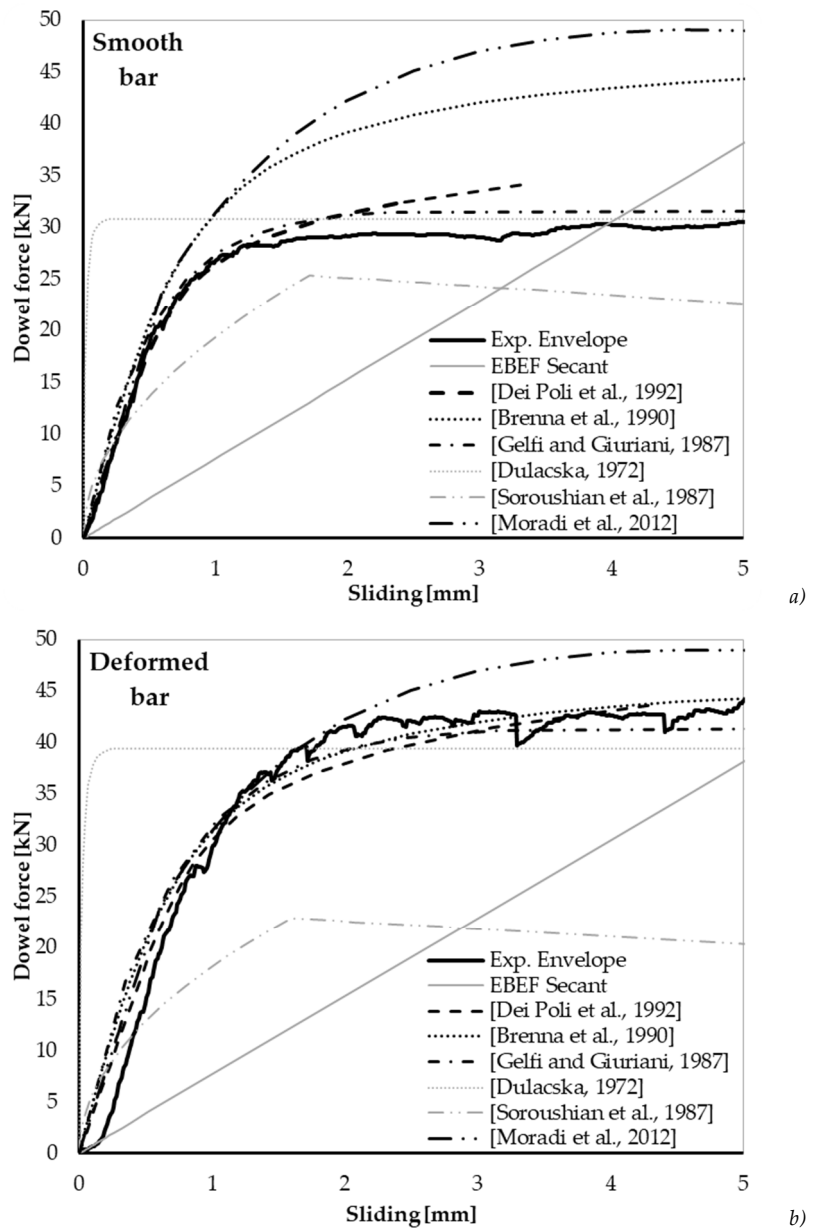

Figure 144: Medium envelope experimental curve in term of load-displacement relationship (bolted line) and literature previsions: smooth a) and deformed b) dowel.
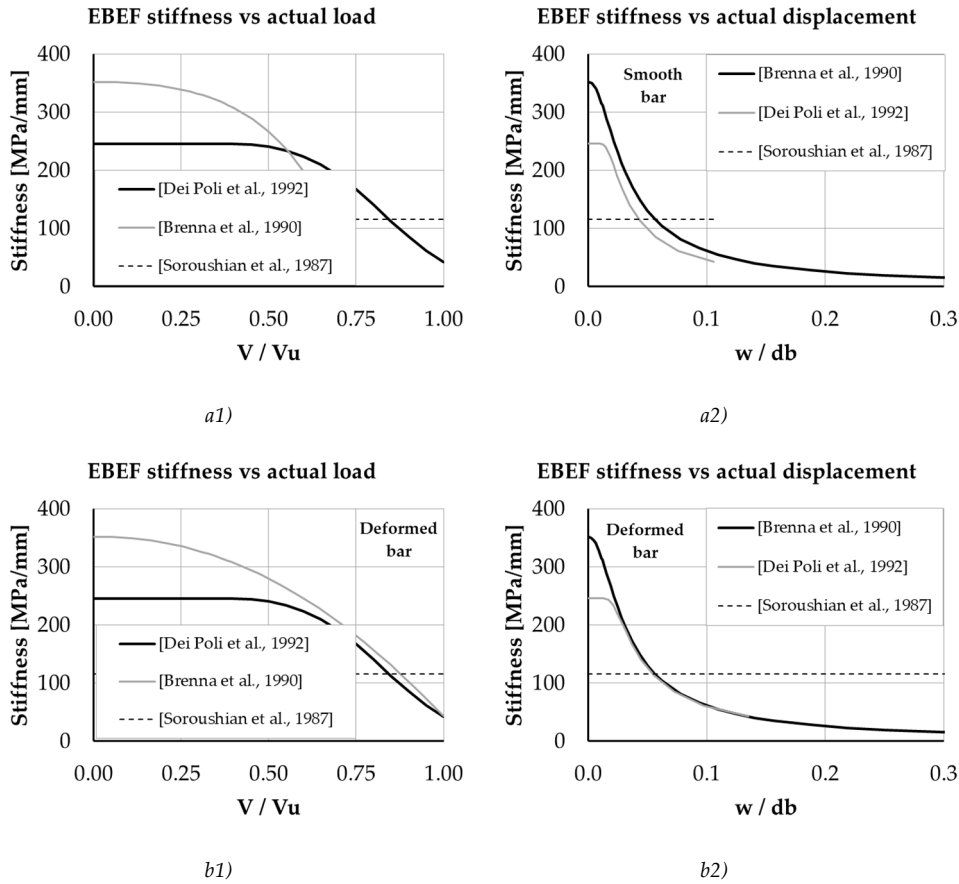
Figure 145: EBEF model stiffness considering and not the concrete degradation with increasing load (plot 1) or displacement (plot 2): curves for the reference experimental campaign in presence of smooth a) and deformed b) dowel.

5 MODELLING OF SUBSTANDARD RC FRAME ELEMENTS WITH PLAIN REINFORCEMENT

5.1 Introduction

In the literature, the non-linear response of RC elements under seismic action was investigated in detail. Experimental behaviour of columns, beams, and beam-column joints subassemblies showed that the poor bond performance of plain reinforcement strongly influences the seismic response of the GLD buildings. To account for this, an analytical approach is proposed in this chapter, for the interpretation of the flexural behaviour of under-designed RC frame elements. It is based on smooth bar stress-slip relationships, which represent the bar pull-out from the crack sides. The increment of flexural deformation due to bar slip from the joint region was analysed by several authors (Braga et al., 2012; Cosenza et al., 2002; Fabbrocino et al., 2004; Metelli et al., 2015; Sharma et al., 2011). Its extension in the element is instead a new proposal to explicitly consider the non-linear behaviour of the frame members. Lumped plasticity approach (Figure 146) is used to model the bar slip from both the joint (or foundation) region and from the frame element. The opening of one main crack at the member end is assumed, since none or negligible plastic curvature occurs along the member length. The model is based on explicit analytical representation of the bar slip phenomena. Sophisticated empirical calibration of lumped hinge hysteresis (O'Reilly and Sullivan, 2017) is thus avoided. Furthermore, the model application is meant to be extended to a general structural configuration.
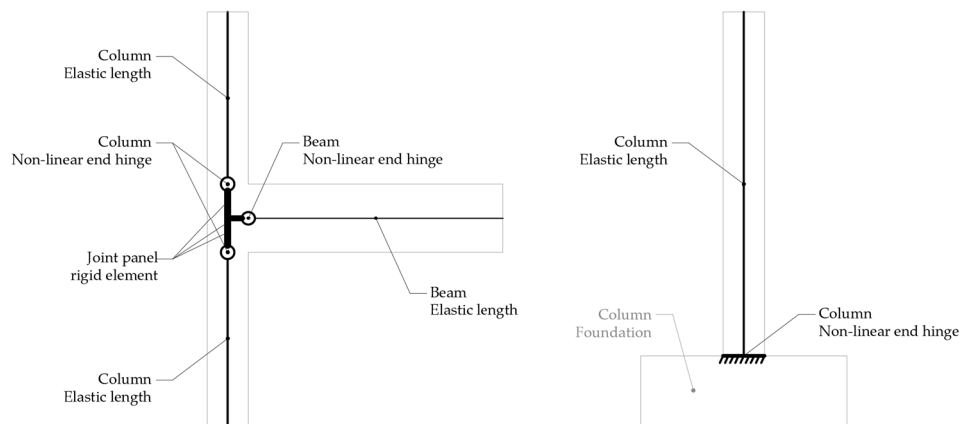

Figure 146: Schematization of the adopted lumped plasticity approach.

Other possible collapse mechanisms, such as member or joint shear failures, affect the GLD seismic response. Therefore, the herein presented model must be combined with other techniques, which account for possible brittle failures. Infill-frame interaction is reason of high shear load on RC members (Al-Chaar et al., 2002; Di Trapani et al., 2015; Mehrabi et al., 1996; Stavridis et al., 2012); since the modelling of this phenomenon is not the aim of the present work, no discussion is herein reported on beam and column failure due to transversal loading. However, specific numerical hinge can be implemented in the modelling. Regarding Beam-column joint shear behaviour, several experimental (Beschi et al., 2015; Braga et al., 2009; Calvi et al., 2002a; Priestley, 1997), theoretical (Hwang and Lee, 1999; Sharma et al., 2011) and numerical (Calvi et al., 2002a; Metelli et al., 2015; O'Reilly and Sullivan, 2017; Pampanin et al., 2003) investigations showed that the panel shear cracking, and the successive shear failure, significantly characterizes the assessment of the structural response. To account for it, several models can be implemented in the frame representation. In the following, the simplest approach of (Pampanin et al., 2003) is considered. It is based on the limitation of the joint shear strength of the panel at its cracking triggering, by the limitation of the equivalent principal tensile stresses in it. The effectiveness of the herein defined proposal is discussed in the next Chapter 6, with reference to experimental tests previously discussed in the Literature Survey (Chapter 2). Further applications are then reported in Appendix C.

5.2   Stress-slip relationships for smooth rebars crossing a crack

A formulation to express the stress-slip relationship of a smooth rebar crossing a crack is proposed and analytically formulated in the following. It is based on the rebar equilibrium between applied bar axial stresses and resisting bond stresses acting on the embedded surface. The behaviour of both straight bars and hook end anchorage devices is presented. The resulting combination of the different defined stress-slip laws is then used to express the behaviour of a general anchored smooth bar.

General approach

Considering a longitudinal smooth rebar anchored in a concrete region, such as beam-column joint panel or foundation element, different anchoring solution can be identified. In Figure 147 the most common cases are presented: a) only Straight Length (SL) presence, b) straight length followed by an end hook (HS) and c) bent rebar (B). Cause to the poorer bond capacities of plain reinforcement, the lower performance is expected to be related with the first layout (SL). On the other hand, the presence of specific rebar bending involves anchorage capacity significantly

higher. An experimental investigation, useful to contextualize the herein presented hypothesis, is reported in the previous Chapter 3.

The analytical evaluation of the straight length anchorage behaviour is based on the following main hypotheses:

- rigid-perfectly plastic behaviour assumption for the bond-slip definition on the SL;
- constant average bond stress acting on the straight embedded bar length.

With the above reported assumptions, the slip of the bar from the concrete block can be calculated through the integration of the bar deformations along the mobilized anchorage straight length. The approach was already suggested in the literature (Metelli et al., 2015; Xu et al., 2014). It differs from other models which consider linear bond-slip relationship along the rebar straight length (Braga et al., 2012; Laterza et al., 2017).

On the other hand, the end anchorage device is treated as a local axial spring of known stress-slip uniaxial relationship. An analytical approach to evaluate the spring behaviour is presented in the previous Chapter 3 (see from page 146). No empirical based non-linear (Fabbrocino et al., 2004) or multi-linear (Metelli et al., 2015) law are herein considered.
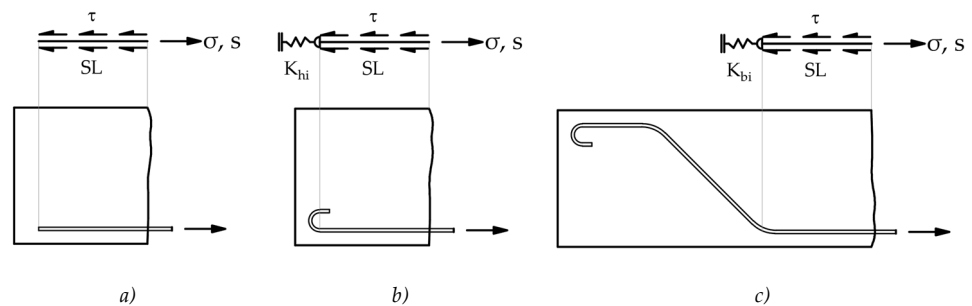

Figure 147: Approach to the modelling of smooth bar anchoring in a concrete block: only straight length (SL) a), hook-end anchoring device b) and bent rebar (c).

Modelling of the embedded bar straight length

The equilibrium of Figure 148.a governs the bar Straight Length behaviour. The external applied normal stress σ_s is balanced by bond stress distribution τ_b on a required anchorage length $h(\sigma_s)$. Cause to the assumption of rigid-perfectly plastic bond-slip behaviour, the anchorage length is linearly proportional to the applied stress:

$$L_{b(\sigma_s)} = \frac{\sigma_s d_b}{4\tau_b} \qquad (167)$$

where d_b is the bar diameter. In conclusion, it is possible to express the bar slip from the concrete block $s(\sigma_s)$ by the integration of the deformations developed on the calculated length $h(\sigma_s)$. Assuming the steel modulus of elasticity E_s:

$$s(\sigma_s) = \frac{\sigma_s h(\sigma_s)^2}{E_s d_b} \qquad (168)$$
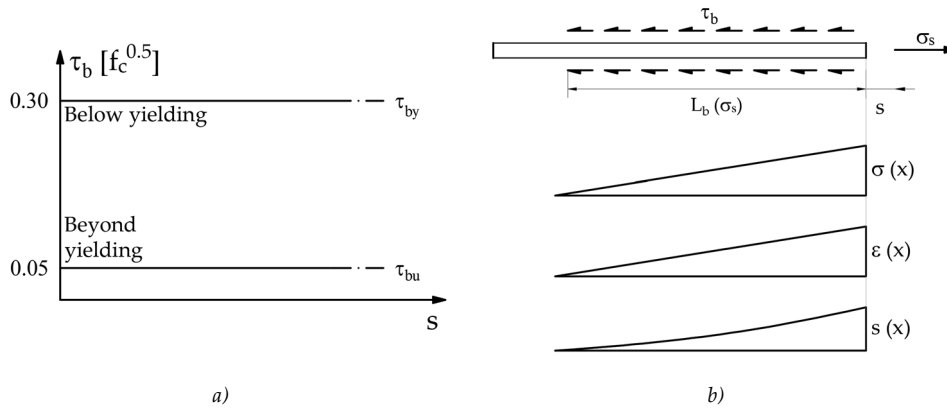

a)   b)

Figure 148: Bar equilibrium on its straight length a) and bond-slip behaviour assumption for the proposed model before and after rebar yielding b).

To completely define the slip amplitude, the bond capacities of smooth bar length must be defined. A reference for the evaluation can be found in the (Model Code, 2010). A strength value before the rebar yielding point is defined and a function to correct it, to account for plastic deformation in the rebar, is suggested for post-yielding elongation. Several experimental tests by (Fabbrocino et al., 2004) showed that the Code proposal, with reference to good bond conditions, is well representative of the peak bond strength. A more comprehensive work by (Verderame et al., 2009b) confirms the above conclusions and extend the evaluation of the bond performances in presence of cyclic excitations, peculiar to seismic action. Further information are available from the experimental campaign presented in Chapter 3.

Concrete bond stress capacity is expressed like a function of the square root of the concrete compressive strength. Figure 148.b shows the bond-slip relationships herein adopted, characterized by the identification of a peak (pre-yielding) τ_{bp} and a residual (post-yielding) τ_{bu} strength. The representation of a gradual loss of bond capacities in the plastic field is neglected. With reference to (Model Code, 2010) indications, it is possible to identify a lower bound for the bond strength imposing of the bar failure ($\varepsilon = \varepsilon_u$),:

$$a(\varepsilon_u) = \frac{\varepsilon - \varepsilon_y}{\varepsilon_u - \varepsilon_y} = 1 \qquad (169)$$

$$\Omega_y(\varepsilon_u) = 1 - 0.85\left(1 - e^{-5a^b}\right) \simeq 0.16, \qquad \forall b \qquad (170)$$

$$\tau_{bu} = \Omega(\varepsilon_u)\tau_{by} \simeq 0.05\sqrt{f_c} \qquad (171)$$

The assumption of this constant reference value implies the neglection of higher capacities for axial stress value slightly over the yielding point. Despite this, the loss of bond performance described by the Code function $\Omega_y(\varepsilon > \varepsilon_y)$ is very pronounced (Figure 149), thus the simplification is herein accepted. It is possible to synthetize the approach with reference to the following formulation:

$$\tau_b = C_b\sqrt{f_c} \qquad (172)$$

where the suggested values for the coefficient C_b are reported in Table 25. A comparison with literature references (Model Code, 2010; Verderame et al., 2009a) and experimental data (described in the previous chapter) is also provided.

Reference	Peak value	Residual value	Post-elastic field
(Model Code, 2010)	0.30	NA	$0.30\Omega_y$
(Verderame et al., 2009a)	0.31	0.05	NA
Experimental tests	0.20÷0.30	0.04÷0.06	NA
Proposal	0.30	0.05	0.05

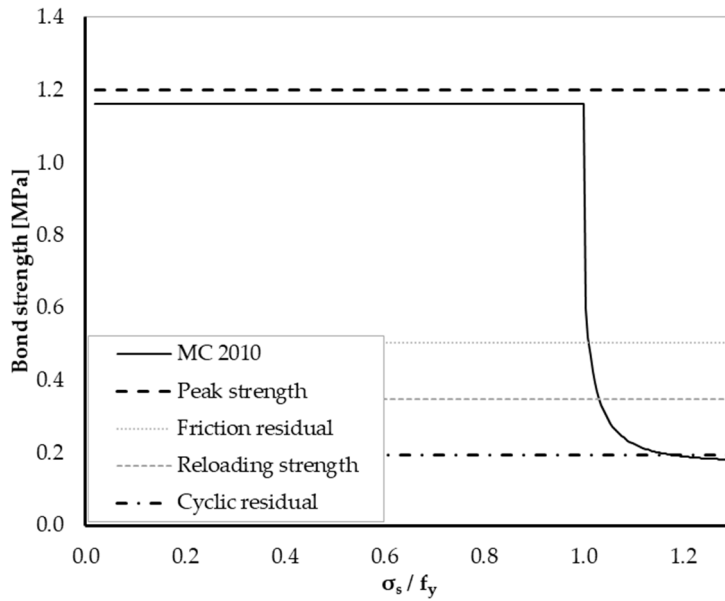*Table 25: Coefficient for the bond strength definition.*

Figure 149: Comparison between Code (Model Code, 2010) proposal for the bond strength definition and empirical based (Verderame et al., 2009a) suggestions for a reference case study.

In Figure 150 a stress-slip response for a common employed 12mm rebar embedded in a low-quality concrete is reported. It is very clear like the non-linear shape of the deformation response gradually loses stiffness in presence of increasing stress level. Moreover, after the yielding point, the overstrength of the rebar is shown only in presence of very high slip values.

The herein discussed proposal is representative of the only monotonic bar SL response. Regarding the cyclic loading, (Verderame et al., 2009b) experimental evidence showed instead a significant degradation of the bond performance under reversal and repeated loading. According to the authors (Verderame et al., 2009a), the bond-slip behaviour of a short length embedment can be well defined by the assumption of four different reference values: i) a first loading peak capacities $\tau_{b,p}$, ii) a frictional residual strength under monotonic excitation $\tau_{b,f}$, iii) a reloading reduced capacity $\tau_{b,r}$ and iv) a cyclic residual strength $\tau_{b,c}$. A graphical comparison for a specific reference case is shown in Figure 149. The two reference values herein assumed for the modelling suggestion are the same as the higher ($C_b = 0.30$) and the lower ($C_b = 0.05$) described bounds. Nevertheless, it is worthy to observe that the cyclic degradation effects are independent from the bar plasticization, a further strength decrease can thus be expected.

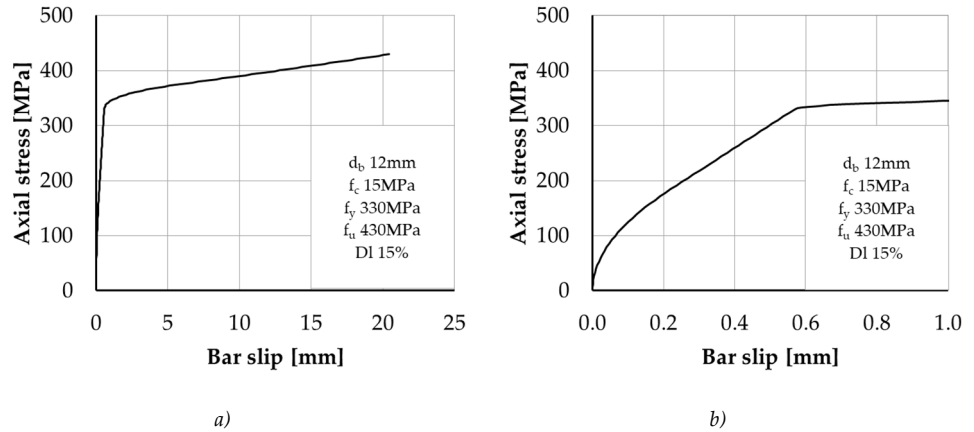*a)*   *b)*

Figure 150: Stress slip response for a common straight bar embedded in a 15MPa resistant concrete: response up to failure point a) and focus on the initial elastic phase b).

Modelling of the hook-end

The previously defined analytical interpretation of the hook stress-slip behaviour is herein considered (see Chapter 3). The ability of the proposal in representing the experimental evidence has been already analysed. Therefore, in the following, only a comparison with other literature available models is reported; in the detail the following proposal are considered:

- (Fabbrocino et al., 2004) empirical calibration of Popov's non-linear function;
- (Metelli et al., 2015) bilinear proposal.

The alternative friction based model suggested by (Braga et al., 2012) is not considered. Indeed, its linear elastic nature is retained to be not adequate in the representation of the hook strongly non-linear behaviour.
A wide experimental campaign is at the base of the (Fabbrocino et al., 2004) empirical calibration of the Popov's equation, which is mathematically described in Eq.(173). It represents both the pre- and post-yielding hook response simulating a gradual loss of stiffness, consistently with the experimental evidence. Fixed the bar failure stress f_u, it is possible to relate the hook stress σ_h and its head slip s_h by the means of the following:

$$\sigma_h = f_u \left(\frac{s_h}{3.90} \right)^{0.30} \qquad (173)$$

On the other hand, (Metelli et al., 2015) suggests to define a bilinear relationship, in which the hook normalized stress is related to the measured slip by the following function:

$$\frac{\sigma_h}{f_y} = K_{hi}s_h, \qquad K_{hi} = \begin{cases} 1.130mm^{-1}, & \sigma_h \leq f_y \\ 0.048mm^{-1}, & \sigma_h > f_y \end{cases} \qquad (174)$$

By the comparison of Figure 151, it is clear that the simplified bilinear approach cannot capture the initial stiff hook response; moreover, after the bar yielding, the predicted hook strength is significant lower than the one suggested by the other two interpretations. The herein presented proposal, which is not empirical calibrated but analytical based, shows a stress-slip law very similar to the suggestions by (Fabbrocino et al., 2005), but it results stiffer at intermediate stress levels.
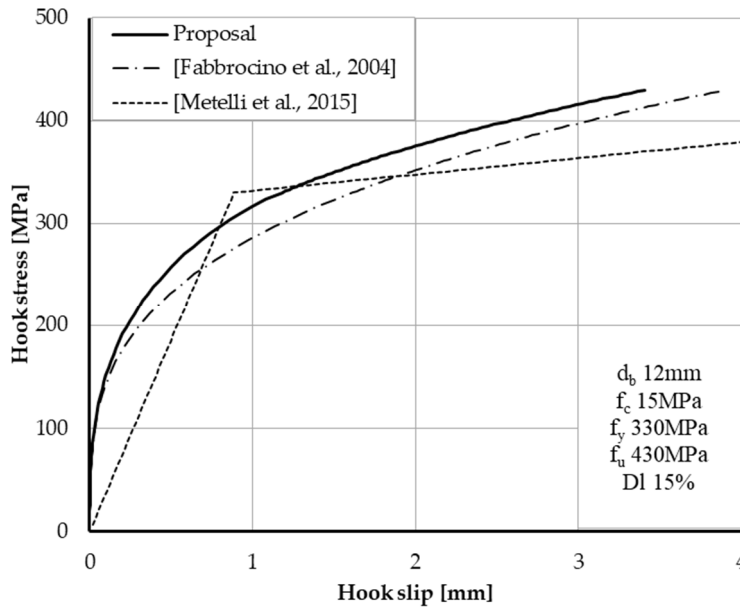

Figure 151: Different bar end hook stress-slip laws predicted for a reference case study (bar and concrete detail in the legend).

Modelling of bent anchorage

No specific modelling is suggested to represent the anchorage performance of bent rebars. Indeed, according to the author knowledge, no pull-out experimental tests, as nor analytically/empirically based or numerical predictive rules are available in literature. The experimental campaign described in Chapter 3 investigated about the behaviour of such solution, but the tested bars are few. The definition of an effective modelling technique is thus premature. However, as a first approximation, it is

possible to refer to the hook analytical stress-slip behaviour. Indeed, the bent anchorage secant stiffness at the bar yielding is similar to the hook one (for more details see the experimental results in Figure 103).

5.3   Cyclic behaviour of anchored smooth rebar

A model for the representation of smooth rebar monotonic stress-slip behaviour has been proposed in the previous section. It can be used for strength and stiffness evaluation of substandard RC frame structures by means of pushover analysis. In the definition of the structural seismic response, a very significant role is however played by the effect of load reversal and by the cyclic strength and stiffness degradation. To account for this, the previously presented model must be extended to the case of cyclic loading. As already mentioned, experimental tests showed that the cyclic loading strongly reduces smooth straight bar anchorage performances. According to (Verderame et al., 2009b), the drop in the strength capacity can be expressed by a reduction factor also higher than 4 (see Figure 149). The mentioned experimental results were obtained by the imposition of a bar slip on a short (10 diameters) straight anchorage length, assuming an equivalent constant distribution of the bond stress along the embedded bar length. In a more common context, the anchorage length is significantly longer; consequently, a different distribution of the bond stress along the rebar surface may be expected (Feldman and Bartlett, 2007). Because of this, the evaluation of the cyclic bar-slip development becomes very complex and its modelling needs further simplifications to be defined.

In the following, an analytical based model to represent the unloading stiffness degradation of anchored smooth steel rebars is presented. A rule to define their cyclic behaviour is also suggested. The application of the presented concepts is herein discussed, whereas the numerical validation of the proposal is presented in the following Chapter 6.

Stress-slip unloading stiffness

The unloading stiffness is the first parameter to be defined for the cyclic response simulation. A simplified approach to the problem can be based on the equivalence with an ideal elastic-plastic material. All the elastic component of the imposed deformation is recovered during the unloading phase, whereas the plastic part equals the residual one. With reference to Figure 152, it is possible to extend the reference behaviour to the stress-slip relationship of a smooth bar. Like previously seen, the relationship between a smooth anchored rebar pull-out force F and the consequent slip s is strongly non-linear. Indeed, it results from a combination of a quadratic form (on the straight length) and of a complex non-linear model (for the end anchorage). Despite this, for the sake of simplicity, a linear unloading branch of slope $K_{un}(s)$ is

proposed. The choice has the aim of simplify a complex definition of the unloading phase branch; moreover, it results of practical use. Only the plastic s_{pl} or the elastic s_{el} component of the general slip s (developed in presence of a pull-out force $F(s)$) has to be defined for the application:

$$s = s_{el} + s_{pl} \qquad (175)$$

$$K_{un}(s) = \frac{F(s)}{s_{el}} = \frac{F(s)}{s - s_{pl}} \qquad (176)$$

By the observation of the half cycle representation in Figure 152.b, it is clearly visible that the unloading stiffness continuously reduces increasing the imposed slip. The observation can be contextualized with reference to both the elastic and the plastic bar behaviour. The loading phase beyond the yielding point is characterized by a quadratic stress-slip law, which tangent slope gradually reduces increasing the slip level. On the other hand, it is possible to observe also the phenomena capacity of develop elastic slip component beyond the yielding point. To justify this assumption, it is essential to remember that the proposed model relates a pull-out force to a rebar slip out from the concrete side of a crack. Since the suggested slip calculation is based on the integral of the steel strain along the anchorage length, the rebar head displacement results from the integration of both elastic and plastic strains. In particular, the former can increase also in presence of bar pull-out force higher than the yielding one, because on the anchorage length the bond reduces the rebar axial stress and so a part of it is subjected to elastic axial stress. A clear representation of the situation is shown in the cases C and D of Table 26.

It is worth noting that working at a stress level lower than the yielding one, the response not necessary re-centre to the zero-force-zero-displacement point. Indeed, the end anchoring device activation involves plastic deformation development also at low stress level (for more details see the analytical stress-slip model of the hook-end). The schemes of Figure 152.b are so followed only when the straight length anchorage can balance itself the applied load.
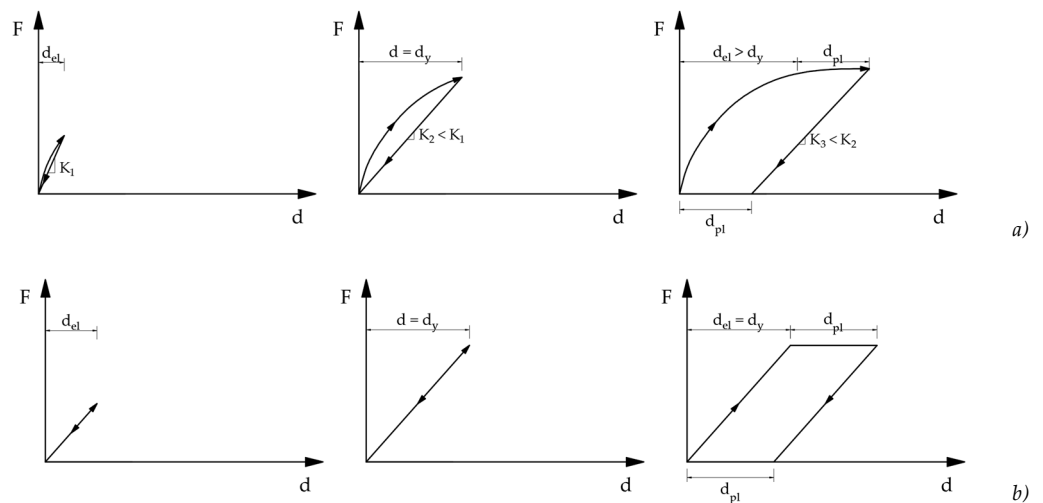
Figure 152: Elastic-perfectly plastic material behaviour a) and extension to a general non-linear Force-displacement relationship b).

Reversal and cyclic loading

Experimental data on the cyclic behaviour of anchored smooth rebar are not available in literature. However, their stress-slip response has been investigated by the specific experimental campaign discussed in the previous Chapter 3. Thanks to these results, a conceptual investigation is herein defined to approach at the study of the bar behaviour in presence of reversal and cyclic loading. With reference to Eqs.(167-168), different anchorage length and slip magnitude can be associated to a specific axial stress level, depending on the assumed bond strength. Considering the reference values suggested by (Verderame et al., 2009a), the bond strength capacity can be defined with reference to: i) loading, ii) reloading and iii) cyclic loading field. Consequently, it is possible to draw the stress-slip qualitative relationships shown in Figure 153. The degradation in the bond strength capacity causes strong variations in the bar slip assessment; in other words, cause to cyclic loading effects, more deformation is required to balance a specific pull-out force and a lower strength is exhibited at an imposed slip level.
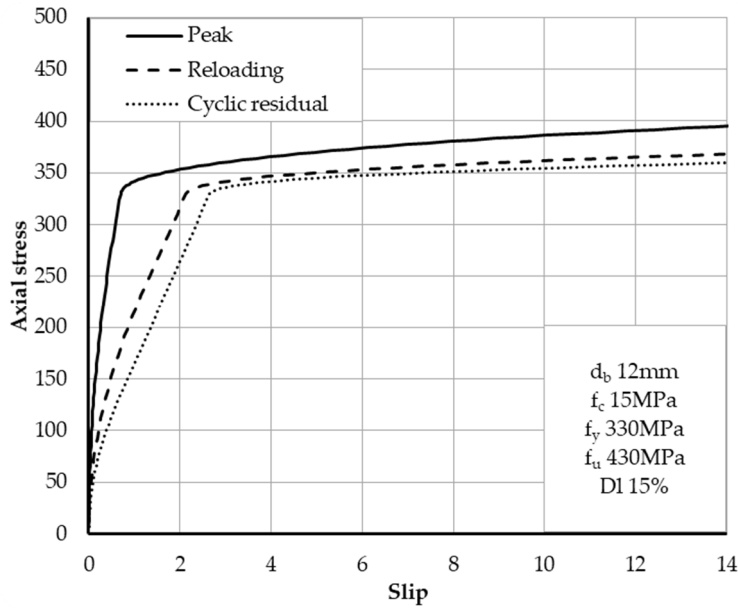
Figure 153: First loading, reloading and cyclic stress-slip relationships for a straight length rebar embedded in concrete; reference to the common concrete and steel parameters already investigated for the other applications.

Because of the above presented effects, significant changes in the cyclic and in-cycle response of a straight embedded smooth rebar is expected. To account for this, the following simplified hypotheses are assumed, where the slip calculation is done according to the previous calculations by the implementation of the literature (Verderame et al., 2009a) suggestions about the bond strength; for details see Eq.(172) and Table 25.

- Slip magnitude at the first loading is calculated with $C_b = 0.30$;
- slip magnitude at load reversal is calculated with $C_b = 0.09$;
- slip magnitude at repeated cyclic loading is calculated with $C_b = 0.05$;
- secant line to a reference axial stress value is used to represent the cyclic response.

Therefore, the modelling of the reloading phase and of the cyclic behaviour of a straight bar embedded in concrete is strongly dependent on both the acting bond stresses and the load or displacement history. Indeed, a secant value is used to approximate the real non-linear behaviour. Example of the first loading complete cycle definition and of the successive reloading is reported in Figure 154.

It is worth noting that the cycling loading is only a reason of bond strength degradation. Indeed, the bar cross section reduction, beyond the yielding stress (cause to Poisson effect), is cause of further degradation. The phenomenon is the

same affecting the monotonic response discussion. Considering cyclic loading out of the elastic bar response, both the detrimental effects of repeated loading and Poisson effect should so be considered. The mathematical application of this combined concept could result too severe in the assessment of the real structure stiffness. Thus, in the application field of this model, a lower bound to the bond strength is however fixed at the following limit:

$$\tau_b = 0.05\sqrt{f_c} \qquad\qquad (177)$$

The above presented models are relative to the behaviour of the only straight rebar length, on which only bond stresses balance the bar axial load. In the case of hook-end anchorage or bent rebar, another specific hysteretic model must be adopted, since the behaviour of the special anchoring devices is strongly related to the bar plastic deformation required for its pull-out. A multilinear hysteresis is proposed for their cyclic response modelling. For the sake of simplicity, the non-linear observed stress-slip behaviour of mechanical anchorage is simplified assuming a secant three-linear backbone curve. It is characterized by the following reference points: i) axial stress penetration over the rebar hook head, ii) bar yielding and iii) bar failure point. The first reference point is well identified in the description of the hook stress-slip analytical model (Chapter 3). The complete plasticization of the hook head is considered for its identification (see the passage between the bar straightening mechanism and the arch one). The unloading and the reloading stiffness are the same of the first loading one.
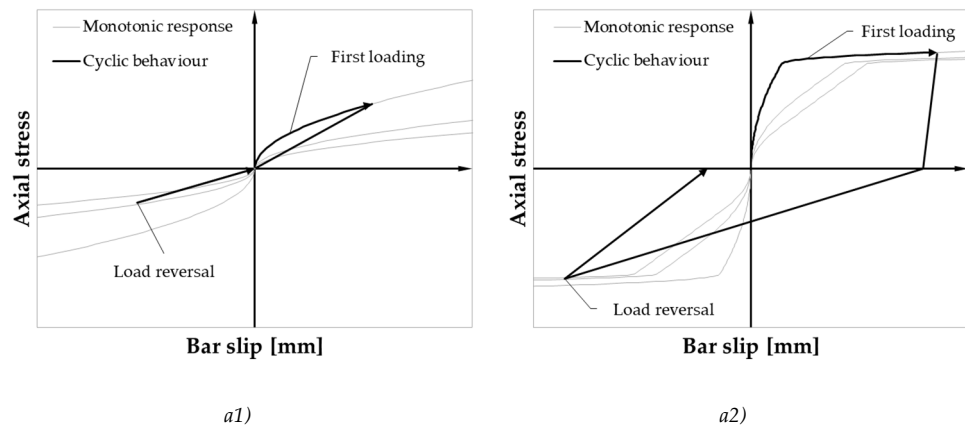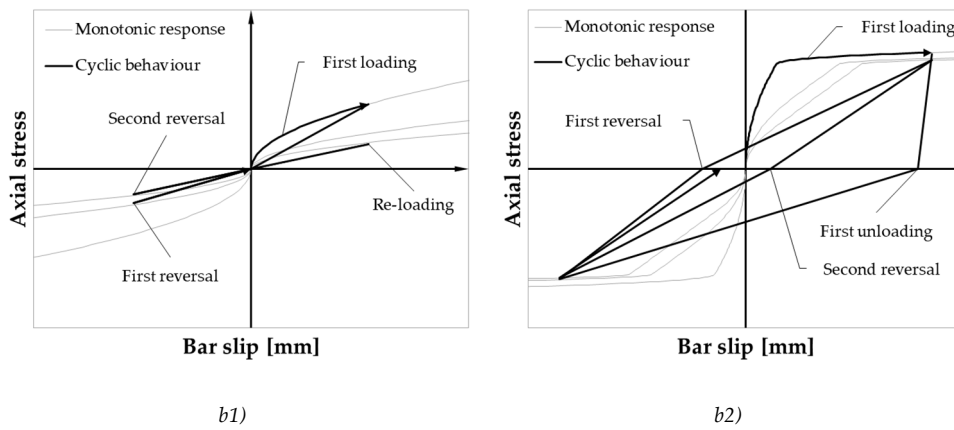

a1)   a2)

Figure 154 (Pt. 1 of 2)

213

b1)   b2)

(Pt. 2 of 2)

Figure 154: Stress-slip behaviour modelling at different target slip values: first loading a) and successive cycles b) in elastic 1) and plastic 2) fields. The gray lines represent the monotonic assessed response in presence of peak, re-loading and cyclic bond strength acting the rebar.
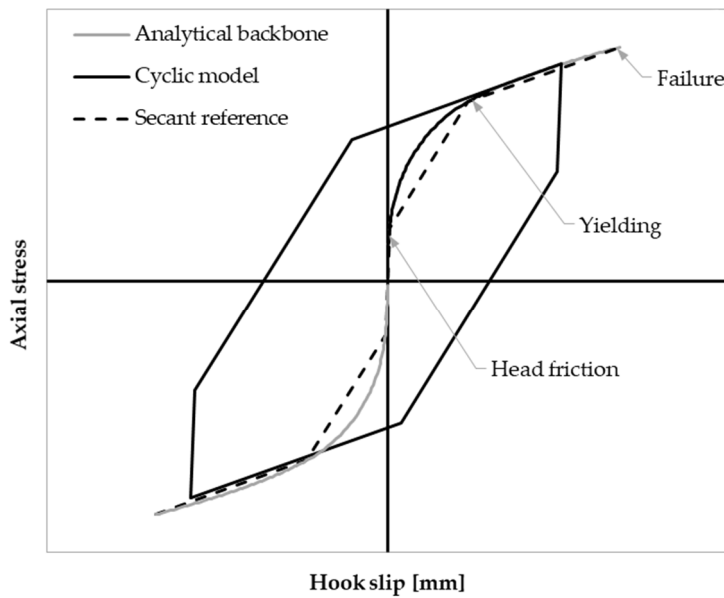

Figure 155: Schematization of the multi-linear hysteresis model adopted for the hook-end and bent rebar subjected to stress-slip cyclic excitation.

5.4 From the bar slip calculation to the structural modelling

A structural model to assess GLD frame building seismic response is herein presented and its underlying hypotheses are discussed in the following. Firstly, a single crack plasticity approach is justified, based on experimental evidences about RC members reinforced with smooth rebar. Secondarily, the application of the previously discussed analytical stress-slip model is suggested for the evaluation of the crack opening, thus of the structural subassembly rotational capacity.

The information herein reported are sufficient to define the numerical modelling of single members, structural sub-assemblages, and whole planar frame. The implementation of the same in a specific modelling code is discussed in the next Section 5.6.

Hypothesis on GLD elements crack pattern

Due to the poor bond performance of smooth reinforcement, GLD frame elements present crack patterns characterized by very few cracks of significant opening. Contrary to what happens in RC members reinforced with deformed bar, none or little crack spreading is experimentally observed and the flexural behaviour is very similar to a rocking member one (Arani et al., 2013, 2010). Schematic representation of the expected deformed shape of a column and its crack pattern are shown in Figure 156.

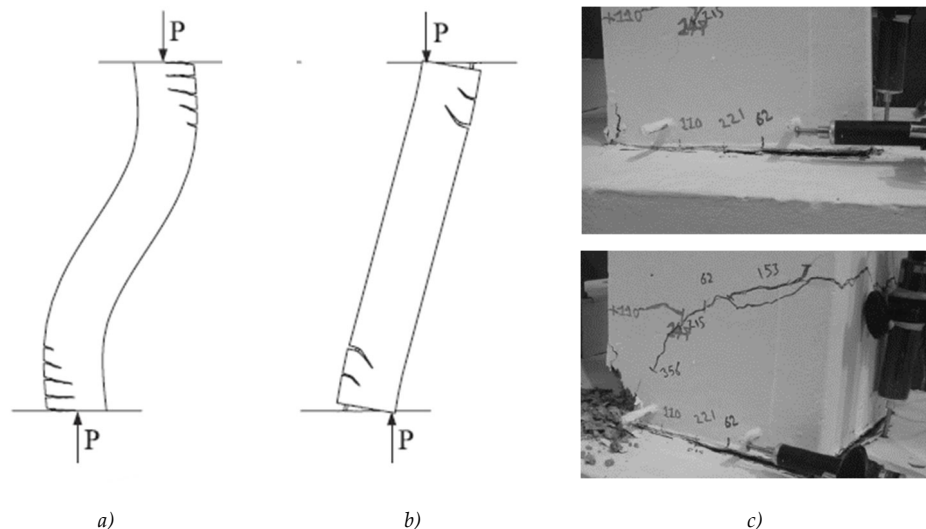a)   b)   c)

Figure 156: Different crack pattern for a column subjected to transversal differential displacement at its end: case of deformed a) and smooth b) longitudinal reinforcement. Experimental observed crack opening during an experimental test (Arani et al., 2013) c).

The experimental evidences show the main contribution of the foundation-column interface crack opening to the definition of the column member drift magnitude θ_d. Thus, a linear relationship can be drawn between the crack opening (or column base rotation θ_b) and the experimental observed top column displacement (or element drift θ_d). Generally speaking, it is possible to assume the following approximation:

$$\theta_b \simeq \theta_d \qquad (178)$$

where the column base rotation and the element drift, with reference to Figure 157, are respectively expressed in the following way:

$$\theta_b = \frac{d_2 - d_1}{D} \qquad (179)$$
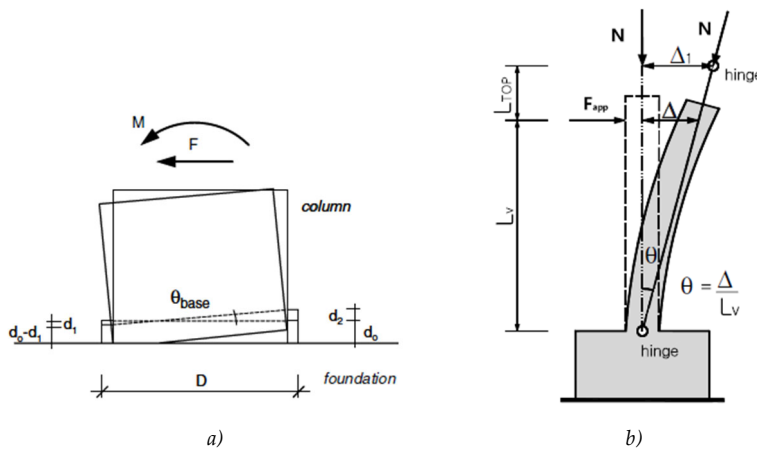
$$\theta_d = \frac{\Delta}{L_V} \qquad (180)$$

Figure 157: Physical definition of the column base rotation due to crack opening a) and of the drift of a member subjected to lateral loading b); (Di Ludovico et al., 2013).

The formation of a single crack at the column base is undeniable in presence of overlapped reinforcement at the column base (Verderame et al., 2008b); on the other hand, more cracks open in presence of continuous reinforcement. Despite this, the same authors (Verderame et al., 2008b) demonstrate that the contribution of the interface one is strongly higher with respect to the others. In any case, the sum of the single cracks opening is however directly related to the global drift (Figure 158). On the consequences of this, considering the common presence of overlapped reinforcement at the column base due to construction reasons, it is here assumed a single crack formation at the column ends. The approach is consistent with the evidence of the experimental tests about seismic behaviour of RC elements reinforced with plain bars (for more details see Section 2.2).
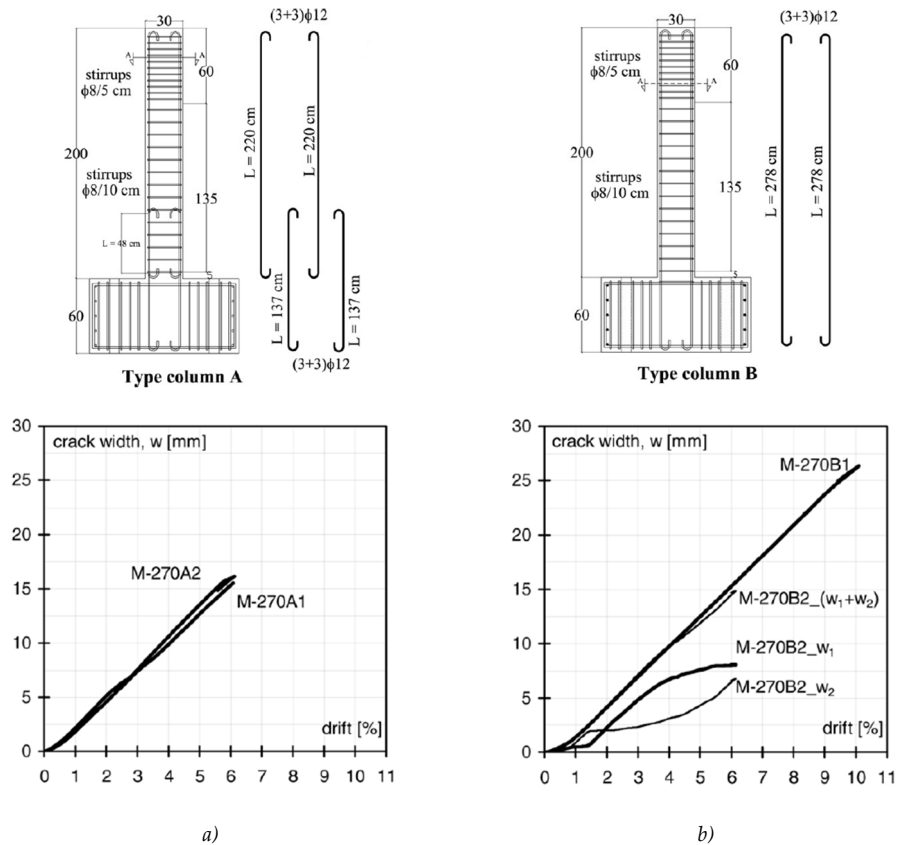
216

Figure 158: Influence of the column base crack width on the member drift definition: case of lap-splices presence a) and continuous b) longitudinal rebar on classic column solution (Verderame et al., 2008b).

Few experimental results are available in literature regarding the behaviour of beam reinforced with smooth bar. According to the author knowledge, the crack pattern shown by these members are briefly analysed on the bases of (Fernandes et al., 2011) and (Marefat et al., 2009) works. The former authors test a two-span continuous beam under the action of vertical point load in the midspans. The observations confirm the absence of a spread cracking in element reinforced with smooth bar; more in detail only a crack is observed at the central support whereas not more than two open below the load application point. A more detailed analysis is proposed by Marefat et al. (Marefat et al., 2009), where the crack pattern of beam reinforced both with deformed and plain rebar are drawn. The experimental results (Figure 159) show like several cracks form also in presence of smooth rebar. However, a strong difference in term of crack number and width is visible by the comparison with the result of the specimen with ribbed reinforcement. In spite of this, the authors (Marefat et al., 2009)

217

demonstrate that the beams deformation is mainly governed by the smooth rebar slip into the concrete; furthermore, the main role played by the near interface crack opening is confirmed. It is worth noting that the analysed beam specimens present continuous bar crossing the beam end, few cracks are so expected in presence of overlapping near the beam end regions, according to (Verderame et al., 2008b) suggestions. Similar conclusion can be treated also observing the cyclic response beam-column joints sub-assemblages. In this case, the cracks are lumped in the joint-member interface zone. No data are herein reported about, since it results an extension of the above expressed concepts, a deep discussion of the experimental observation is however reported in this work (Section 2.1).
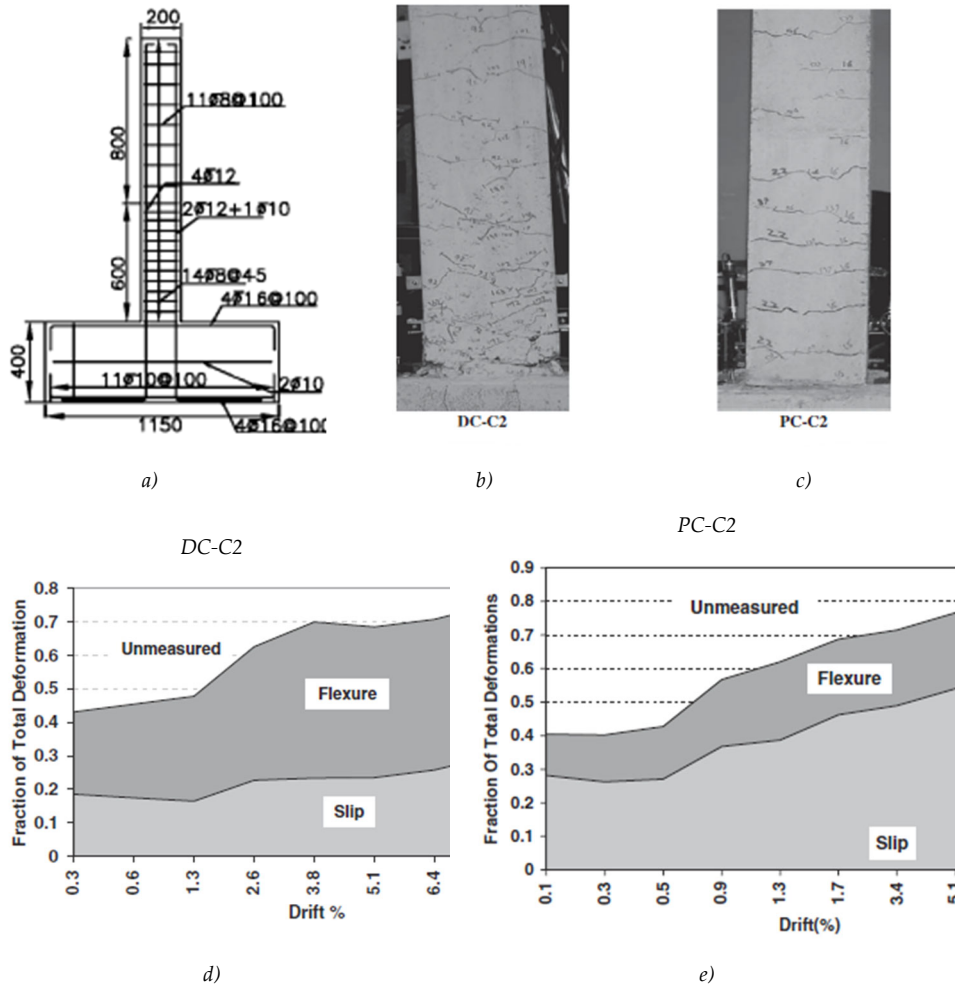

Figure 159: Experimental observed crack pattern for beam reinforced with deformed b) and smooth rebars c); global deformation contribution for the same specimens d) and e). (Marefat et al., 2009).

218

The above described crack pattern could be explained by the observation of the bending action profile along the member length and by the sudden change in stiffness and strength exhibited in the passage from the joint (or foundation) to the effective structural member (column or beam). High seismic bending gradient favourites the crack opening in the joint-element interface. On the other hand, the opposition of the combined gravity and seismic loads actions on a beam can characterize a sub-horizontal bending diagram (very low gradient) or, even, a maximum bending action point far from the interface zone (Figure 160). In the latter case, the assumption of a single crack formation at the member end could not be justified. Despite this, the author thinks the herein proposed model is however good in the GLD frame member deformation capacity assessment. Therefore, the crack width (thus the lumped hinge rotation) is calculated basing on a required anchorage length, which should be considered not dependent on the crack spreading and location.

The application on a single interface crack of the suggested stress-slip calculation can result useful in the definition of the total bar slip from a member end. However, it can not be considered representative of the single crack opening. A schematization of the concept is reported in Figure 160. The following assumption is taken:

$$w \simeq \sum w_i \simeq \sum s_i \simeq s \qquad (181)$$

where w is the total crack opening assumed to be lumped in the member end, w_i is the single crack opening, and s_i the expected slip from the $i-th$ crack concrete side in case of spread pattern; finally, s is the total slip calculated with the stress-slip analytical model herein presented.
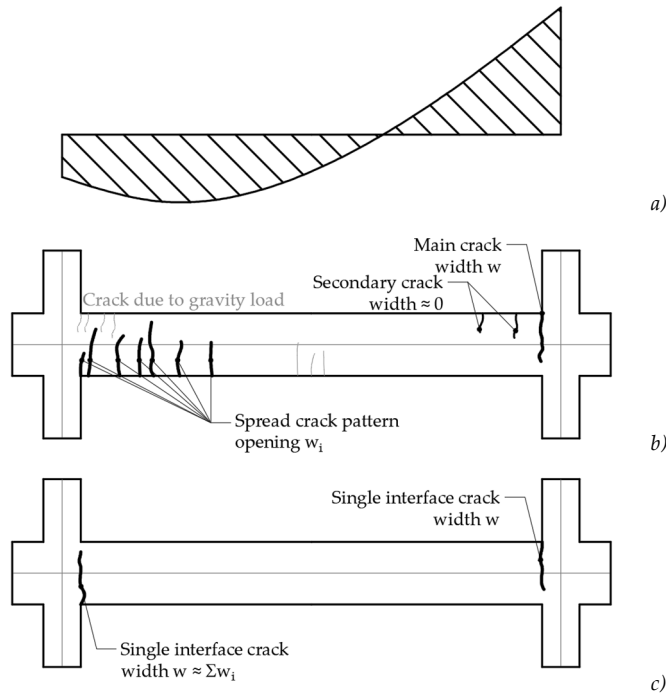
Figure 160: Difference in the crack pattern of two opposite ends of a continuous beam inner bay: bending profile a), expected crack pattern b) and assumed simplification c).

Modelling concept

The proposed approach is based on the modelling of the crack opening, accounting for non-linear reinforcement steel and concrete behaviour by lumping their effect at the crack location. A single crack is supposed to form at the column base interface or in the beam-column joint-member one. On the other hand, all the elements length is considered to remain uncracked and thus having an elastic behaviour. The crack location is shifted from and connected to the joint centreline by a a rigid beam element, in order to reproduce the real position of the crack interface and to guarantee the internal action transmission across the same joints. Schematic representation of the proposal in Figure 161.

The crack faces, owing to the adjoining elements (beam-joint or column-joint) are represented by a pair of transversal rigid elements, which reproduce the element size depth. The same sides are connected to each other by two sets of interface non-linear axial springs (Figure 161.b). The first simulates the bar stress-slip response along the rebar anchoring length; the second represents the concrete non-linear behaviour around the crack. The suggested modelling technique lumps all the members deformation capacities in a single dimensionless non-linear hinge; despite this, its

behaviour is influenced by steel strain spread along the rebar embedded length. Consequently, the non-linear springs employed for the steel and concrete modelling must be expressed in the form of i) force vs displacement or ii) stress vs displacement relationships.

It is noteworthy to observe that the model organization also allows the addition of a specific shear hinge at the member end (see Figure 161.a). Thus, the element brittle shear failure can be captured, as well as a possible sliding mechanism on the member-joint interface.

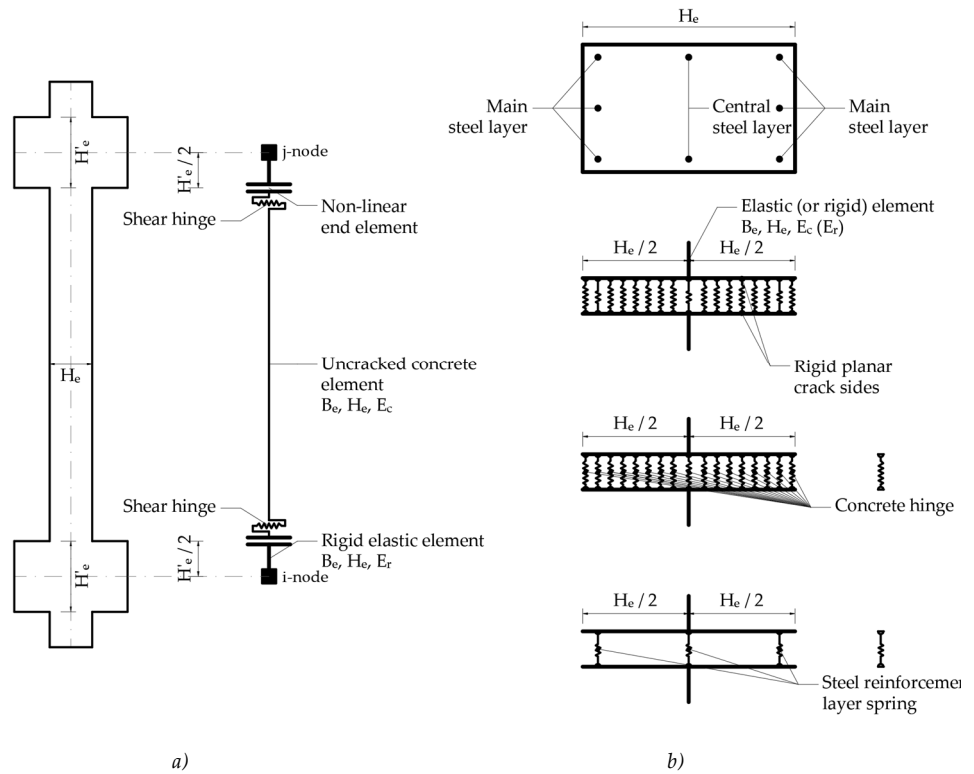*a)*   *b)*

Figure 161: Proposed lumped plasticity model for the GLD frame seismic response representation: Element structure a) and details on the non-linear crack representation b).
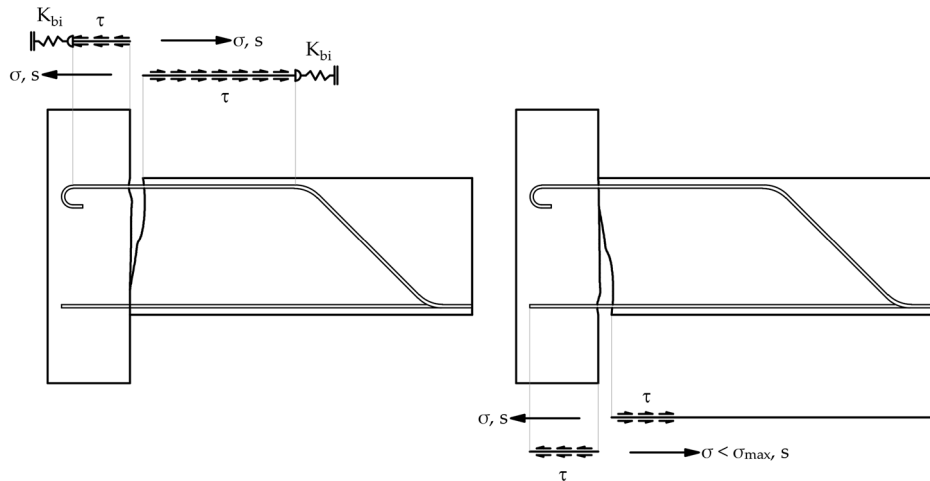
Figure 162: Schematization of a T-joint in presence of different anchorage solutions.

Reinforcement steel stress-slip definition on a single crack side

With reference to each single crack side, different configuration of bar anchorage can be identified. They differ for the embedded straight length, herein called L_b, and for the end type anchorage device. The rules previously defined can be employed for the bar slip calculation, paying attention to maximum axial stress capacity in presence of straight length anchorage (see an example for the lower beam reinforcement in Figure 162):

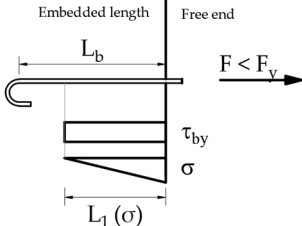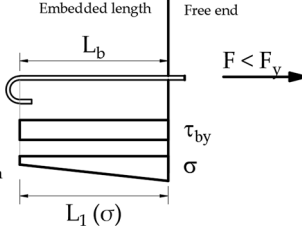$$\sigma_{max} = \frac{4\tau_b L_b}{d_b} \qquad (182)$$
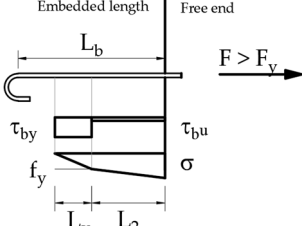
In the following Table 26, representative calculations for a hooked-end embedded bar slip are explicitly shown, with reference to each possible stress distribution. In presence of bent rebar, the approach is the same, since the end anchorage is however treated like an axial spring of known hysteretic behaviour $\sigma_b(s_b)$. As already mentioned, in absence of a specific stress-slip relationship representative of the bent bar pull-out, the hook-end hysteretic law can be used as a first approximation. Under the hypothesis of sufficient straight embedment, the length required to balance the yielding stress (Case A) and the overstrength (Case C) are respectively:

$$L_y = \frac{f_y d_b}{4\tau_{by}} \qquad (183)$$

$$L_u = \frac{(f_u - f_y)d_b}{4\tau_{bu}} \qquad (184)$$

When the minimum required embedded length results higher than the available anchoring straight length L_b, the following scenarios can be identified:

- case B: End device activation required to balance an elastic axial stress;
- case D: End device elastic activation in presence of a pull-out force higher than the yielding one;
- case E: Axial stress on all the straight length embedment higher than the yielding one.

A		$h_1 = h_y = \dfrac{f_y d_b}{4\tau_{by}} < L_b$
		$s_{el} = \dfrac{2\tau_{by}h_1{}^2}{E_s d_b}$
B		$h_1 = L_b < \dfrac{f_y d_b}{4\tau_{by}}$
		$\sigma_h = \sigma - \dfrac{\tau_{by}h_1}{d_b}$
		$s_{el} = \dfrac{2\tau_{by}h_1{}^2}{E_s d_b} + s_{b,el}$
C		$h_1 = h_y = \dfrac{f_y d_b}{4\tau_{by}} < L_b$
		$h_2 < h_u = \dfrac{(\sigma - f_y)d_b}{4\tau_{bu}} < L_b - h_1$
		$s_{el} = \dfrac{f_y h_1}{E_s} + 2\dfrac{t_{by}h_1^2}{E_s d_b}$
		$s_{pl} = 2\dfrac{t_{bu}h_2^2}{E_h d_b}$

D	Embedded length / Free end L_b $F > F_y$ τ_{by} / τ_{bu} σ_h / σ f_y L_1 / L_2	$h_1 = L_b - h_2$ $h_2 = \dfrac{(\sigma - f_y)d_b}{4\tau_{bu}} < L_b$ $\sigma_h = f_y - \dfrac{4\tau_{by}h_1}{d_b} < f_y$ $s_{el} = \dfrac{\sigma_h h_1}{E_s} + \dfrac{f_y h_2}{E_s} + 2\dfrac{t_{by}h_1^2}{E_s} + s_{b,el}$ $s_{pl} = 2\dfrac{t_{bu}h_2^2}{E_h d_b}$
E	Embedded length / Free end L_b $F > F_y$ τ_{bu} $\sigma_h > f_y$ / σ L_2	$h_1 = 0$ $h_2 = \dfrac{(\sigma - f_y)d_b}{4\tau_{bu}} > L_b$ $\sigma_h = \sigma - 4\dfrac{\tau_{bu}L_b}{d_b}$ $s_{el} = \dfrac{f_y L_b}{E_s} + s_{b,el}$ $s_{pl} = 2\dfrac{\tau_{bu}h_2^2}{E_h d_b} + s_{b,pl}$

Table 26: Application of the proposed stress-slip model to the different situation that characterize a general configuration of stress distribution in a smooth hook-end anchored rebar (Nomenclature previously defined).

Concrete non-linear behaviour around cracks

In the crack region, the concrete is assumed to react only in compression, therefore any resource in tension is neglected. The choice can be considered well acceptable for the column member ends, since the interfaces between the same and the floor beam (of base foundation) are characterized by construction cold joints. On the other hand, it slightly overestimates the deformation at low stress level on the joint-beam interface crack. Nevertheless, since i) the seismic excitation is characterized by cyclic loading, ii) the concrete quality of GLD buildings is poor, and iii) the structure may probably experience cracking at the beam end due to static loading, the approximation is considered adequate in the assessment of real structures.

A stress (or force)-deformation law must be defined for the concrete non-linear equivalent spring. To convert concrete strain in finite displacement, a useful choice consists in defining the spring stress-displacement stiffness as a function of the concrete modulus of elasticity. The modelling concept is directly related to the approach of Beam on Inelastic Foundation (BIF). Therefore, it is possible to refer to the studies suggestions on this topic (Dei Poli et al., 1992). The cited authors identify

a concrete stiffness for an equivalent EBEF (elastic) model with an initial value K_{c0} (adapted from Soroushian et al., 1987) that gradually decreases with the increase of the contact force. It's worth noting that the reference model is directed to the dowel mechanism representation, thus to a concrete highly local non-linear behaviour. This is non directly comparable with the situation of the concrete stress state on an RC crack; nevertheless, it is used as a reference for the establishment of the concrete spring stiffness order of magnitude (see the original formulations in the State of the Art). The following is assumed as a reference:

$$K_{cf} = \frac{E_c}{100} \qquad (185)$$

Sensitive analysis about the defined stiffness influence on the structural modelling is reported in Appendix B, in order to justify the simplified approach.

5.5   *Empirical based model components*

To adequately represent the structural behaviour of the herein considered RC frame, additional phenomena, other than the smooth bar slip, must be considered. In the following a brief description of the model used to represents the behaviour of an external T beam-column joint is presented. No emphasis is put on it since the specific behaviour is not analysed in the present work.

Substandard beam-column joints modelling

The seismic response of the GLD frame buildings is deeply influenced by the behaviour of beam-column joints. In most of the cases, these regions are characterized by the lack of transversal reinforcement; furthermore, they present a low shear strength due to the poor mechanical properties of the concrete. The most critical joints are the T-type ones, which present a side not confined by the presence of a converging beam and, consequently, they show a very low strength against diagonal cracking. At the same time, no more resource is guaranteed after the failure under diagonal tension; therefore, no further resistant mechanism can be activated. For these reasons, the modelling of the only exterior beam-column joints behaviour is herein treated.

Principle Stress Limitation Method (PSLM) is herein assumed as a reference to assess the beam-column joints shear strength (Metelli et al., 2015; O'Reilly and Sullivan, 2017; Pampanin et al., 2002; Priestley, 1997). The following limit p_t is assumed as a reference for the tensile principle stress causing the diagonal cracking (shear failure) of the joint panel ((Pampanin et al., 2002)):

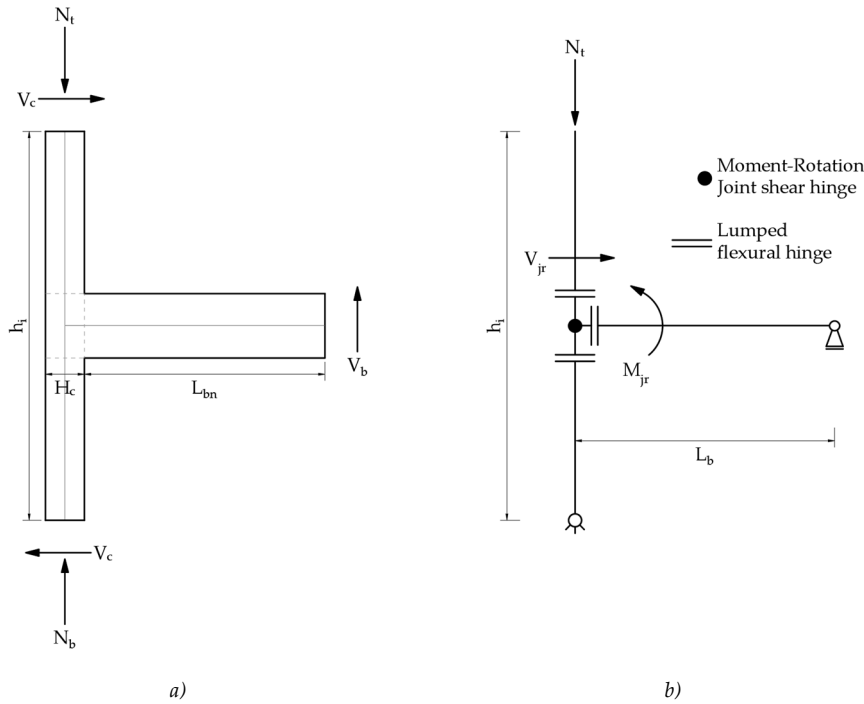$$p_t = 0.2\sqrt{(f_c)} \qquad (186)$$

225

Figure 163: Geometry configuration of a T-type beam-column joint a) and schematic representation of its numerical modelling b).

The maximum shear stress is then evaluated on the Mohr's circle and it is related to the joint panel shear strength V_{jr}. For modelling purpose, it is easier to introduce a Moment-Rotation hinge at the beam end, instead of a shear hinge, and the equivalent joint resistant moment is thus defined:

$$M_{jr} = V_{jr} \left(\frac{z_b h_i}{L_{bn} h_i - L_b z_b} \right) L_b \qquad (187)$$

where z_b is the internal lever arm of the beam cross section, h_i and L_b are respectively the interstorey height and the beam shear length, and $L_{bn} = L_b - 0.5 H_c$ is the net beam length (Figure 163).

The response envelope is defined according to the work of Pampanin et al. (Pampanin et al., 2003). The above calculated shear strength is reached with a single linear loading phase at a deformation level equal to 0.0002rad. After the joint cracking a constant shear strength is assumed, no degradation effects are so considered. Anyway, the shear panel damage is empirically identified, and it is associated to the reach of different reference strain levels, which are associated to four different Limit States (LS). Details are reported in Table 27 and in Figure 164. The hysteretic model is the Takeda one; it is defined by a symmetric behaviour and the cyclic degrading

effects are represented with a secant peak-oriented reloading. The herein reported modelling technique is not accurate in the assessment of the joint behaviour after the reach of the peak strength. On the other hand its effectiveness in catching the diagonal cracking has been proved (Metelli et al., 2015; O'Reilly and Sullivan, 2017; Pampanin et al., 2002). According to the aim of the present work, which does not want to well represent the post-peak response, the presented model is considered sufficient for the application. More refined techniques have been discussed in the literature survey.

Table 27: Joint shear panel strength and deformation associated with different Limit State (Pampanin et al., 2003).

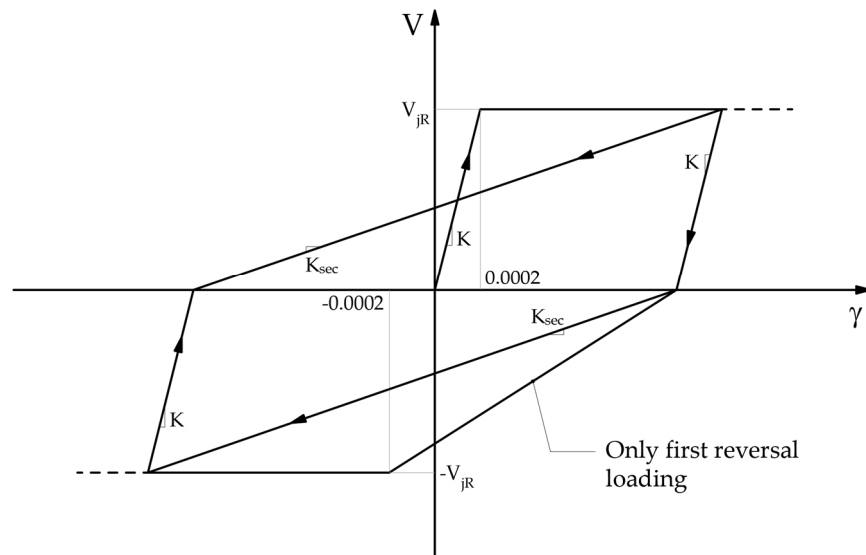| Limit State	PSLM	Shear deformation [rad]
Diagonal cracking	$0.2\sqrt{(f_c)}$	0.0002
Extensive damage	$0.2\sqrt{(f_c)}$	0.0050
Critical damage	$0.2\sqrt{(f_c)}$	0.0100
Incipient collapse	$0.2\sqrt{(f_c)}$	0.0150

Figure 164: Basic representation of the adopted hysteretic model for beam-column joint shear modelling.

5.6   Numerical tools and laws

In this section the analytical and conceptual proposal is translated in an effective numerical model. The main following information are related to the definition of the different non-linear hysteretic behaviours, which need some simplification respect to the previous defined theoretical approach. The numerical implementation is done in OpenSees environment (McKenna et al., 2000). Each element and material used in the model is thus described with reference to the library available for the software code.

With reference to the concept summarized in Figure 161, it follows the definition of the numerical representation of: i) elastic elements, ii) non-linear concrete and iii) non-linear steel stress-slip behaviour. Finally, the tool used for the external beam-column joint shear response representation is presented.

Only in-plane frame seismic response is considered. Coupled bending action due to transversal loading is herein not represented. The equivalent Beam on Inelastic Foundation (BIF) crack modelling allows to account for axial load effect on member behaviour step by step. On the other hand, possible shear failure (often critical in case of infilled frame) can be simply caught by the mean of a specific hinge or, indirectly, by a post-processing safety check. Elements internal actions, non-linear material hysteretic response, crack width, boundary reactions, and nodes displacement are registered for each analysis step. Therefore, each kind of verification can so be pursued, allowing a good control of the structural response.

Numerical elements

The elastic components of the model, that is the member length and the joint geometry simulation, are numerically defined with ElasticBeamColumnElement (OpenSees 1D planar beam):

ElasticBeamColumnElement $eleTag $iNode $jNode $A $E $Iz $ transTag

where $eleTag$ is an integer identification number for the specific element, $iNode$ and $jNode$ are the nodes linked by the same element (they correspond to its ends), $A = b_e H_e$ is the element cross section, $Iz = b_e H_e^3/12$ is the second moment of area, and E is the modulus of elasticity associated to the element. The last parameter is assumed to be E_c for the uncracked concrete elements and E_r for the rigid beam used for joint geometry simulation. For the first, the suggestion of Priestley et al. is taken as a reference (Priestley et al., 2007); the second is instead set three order of magnitude higher.

$$E_c = 5000\sqrt{f_c} \qquad (188)$$

$$E_r > 1000E_c \qquad\qquad (189)$$

Stress-displacement spring-based crack model is implemented thorough the fibre section tools:

section Fiber $secTag {
patch rect $matTag $numSubdivY $numSubdivZ $yl $zl $yj $zj
fiber $yLoc $zLoc $A $matTag
fiber $yLoc $zLoc $A $matTag
fiber $yLoc $zLoc $A $matTag
}

In which the concrete subgrade is represented with a $numSubdivY fibre number on the reference plane element dimension, and with a single discretization $numSubdivZ = 1 on the other principal direction. No distinction between core and cover material concrete is assumed since poor transversal reinforcement is typical employed in this kind of structures. Three different steel fibres are implemented, one for each section steel layer herein considered (two main layer and a central one). They are characterized by the total reinforcement area $A and by the reinforcement steel mechanical properties. If more than a diameter rebar type is present in the reference section, weighted mean values are considered. The section is assigned to a dimensionless element (end hinge) and so no strain integration on a finite length is possible; therefore, the non-linear materials associated to each fibre must be defined in term of stress versus displacement relationships. The choice results in a more useful and robust simulation of a BIF model. A step by step monitoring of each fibres stress-slip behaviour is pursued.

To assign the fibre section, the following zero-length element is employed. In each spring location point, two overlapped nodes must be defined (Figure 165).

element zeroLengthSection $eleTag $iNode $jNode $secTag

Only the axial (normal to the crack plane) behaviour of the equivalent spring is defined. To avoid transversal free displacements, a specific shear hinge should be introduced, otherwise the following instrument can be set:
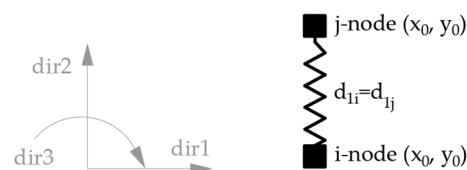
equalDOF $iNode $jNode $dof1

Figure 165: Numerical links for the element end nodes.

Concrete behaviour

Non-linear concrete hinges are characterized by elastic-plastic no tension behaviour. The parameters needed to define it are only two:

- concrete compressive strength;
- equivalent force-displacement stiffness.

The former may be defined in term of medium value, in order to represent the most probable deformation capacities of the elements. Furthermore, the concrete strength directly defines the bond strength capacity and thus it has a great influence on the bar slip assessment. Regarding the second parameter, the previous reported indication in Eq.(185) is followed; thus, a Winkler stiffness equal to two order of magnitude lower than the concrete elastic modulus is considered.

Regarding the cyclic behaviour, a model able to represent concrete damage in compression is chosen; no strength degradation is instead considered. A constant strength is imposed in the plastic field, whereas the reloading branch starts only when plastic deformation is completely recovered (Figure 166.b). More complex behaviour, accounting for non-linear loading and strength degradation, are herein not considered, with the aim to guarantee a simpler modelling technique. The choice is also consistent with the typical lack of information available in assessing an existing structure and with the typical target displacement of retrofitted structures, where interstorey drift demand is kept small to limit the damage to non-structural elements.

In OpenSees environment the Elastic Perfectly Plastic material is considered:

$uniaxialMaterial\ ElasticPPgap$ \$matTag\ \$E\ \$Fy\ \$gap\ damage

where the equivalent stiffness is $\$E = Ec/100$, the yield stress is the concrete compressive strength $\$Fy = f_c$ and no initial gap is set $\$gap = 0$.
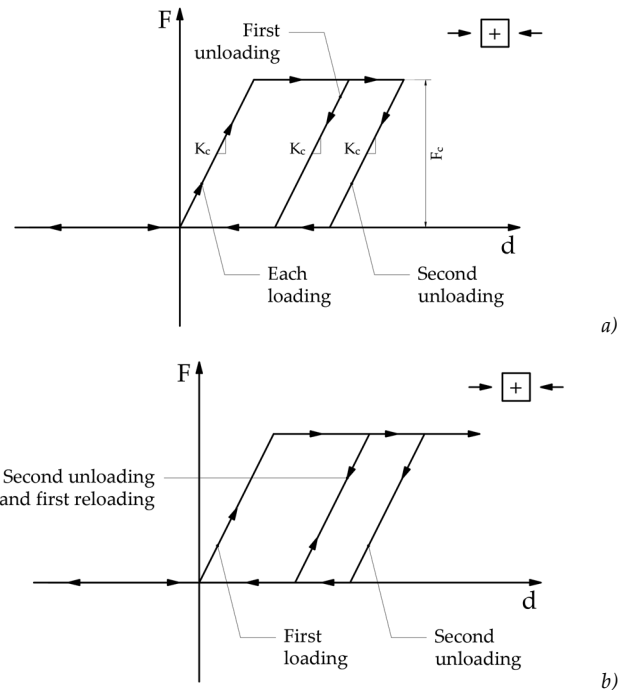
Figure 166: Considered hysteretic behaviour for the concrete cyclic response b) and comparison with a classical elastic-plastic no tension proposal a).

Smooth reinforcement behaviour

The strongly non-linear stress-slip behaviour of a smooth straight anchored rebar is numerically represented with a multilinear force-displacement relationship. This is associated to a hysteretic material. The envelope of the investigated response is simulated with a three-linear curve, identified by the followings:

- yielding;
- failure;
- anchoring device activation.

Beyond and below the yielding point the stress-slip behaviour is strongly modified, due to the sudden decay in the bond strength capacity and to the clear loss of stiffness shown in the plastic response. The representation of this phenomenon is thus essential. On the other hand, the definition of the failure point is a pure convention, since in the interesting deformation field no significance is attributed to it. A key choice results the representation of the anchoring device activation, which is strictly related to the bond capacities of the straight anchorage length. This reference can be associated to a bar stress lower or higher than the yielding one, as it is respectively

shown for the case C, D, and E in Table 26. By the application of the previous suggested stress-slip relationships (see Sections 5.2 and 5.3), each reference point of the multi-linear curve is then associated to a specific couple of stress and slip values. During the numerical model definition this work is done by specific MatLab functions, which are reported in Appendix A.

The chosen code reference material is the Hysteretic one. It presents a three-linear symmetric envelop, which is described by the stresses $s_{ip} = s_{in}$ and by the relative displacements $e_{ip} = e_{in}$:

uniaxialMaterial Hysteretic $matTag $s1p $e1p $s2p $e2p $ < $s3p $e3p $ >
$s1n $e1n $s2n $e2n $ < $s3n $e3n $ > $pinchX $pinchY $damage1 $damage2

Several other parameters must be defined to completely identify the material. Since they are related to the cyclic behaviour, they are discussed only after the following presentation of the reversal and repeated loading simulation. Examples for the most representative cases are reported in Figure 168. The elastic branch is better represented if the rebar end anchorage is activated below the yielding point (Case E). Indeed, the strong non-linear behaviour exhibited on the straight bar length is mainly related with lower stress levels.

The strategy schematized in Figure 167 is followed to account for the bar slip from both the element and the joint sides. Indeed, different boundary conditions characterize them. Since the model is based on a single crack lumped plasticity approach, each side stress-slip relationships are connected in series to each other. The element and joint end-anchorage devices are activated at different bar stress levels, due to their different distance from the crack side. Therefore, the complete stress-slip behaviour is defined by a more general backbone curve, which is identified by four different significant points. To avoid too complex numerical relationships and according to the OpenSees available models, a three-linear curve is however considered. For the purpose, the following material is defined:

uniaxialMaterial Series $matTag $matTag1 $matTag2

The above law allows to define a material which guarantee equal stress transfer between the linked relationships $matTag1$ and $matTag2$ and it exhibits a total displacement equal to the sum of the two.

a)   b)
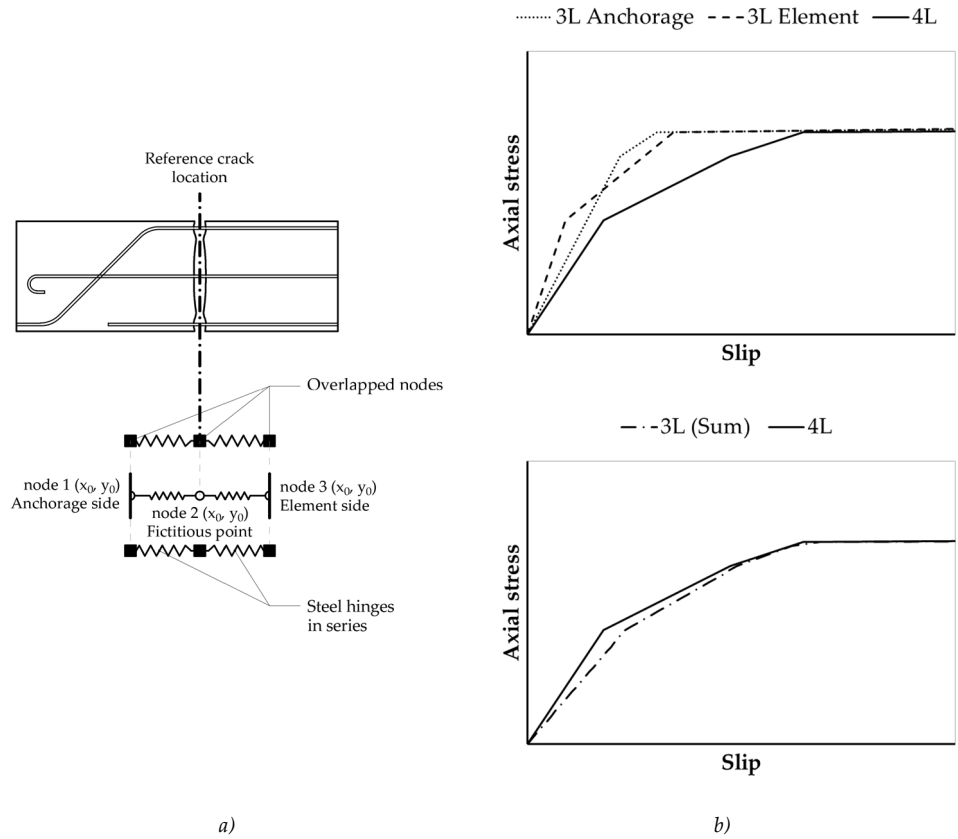
Figure 167: "In parallel coupled hinges strategy" to consider both the element and anchorage sides stress-slip behaviour a); comparison between the combination of two three-linear (3L) behaviour on the crack sides and the global one (4L) b).
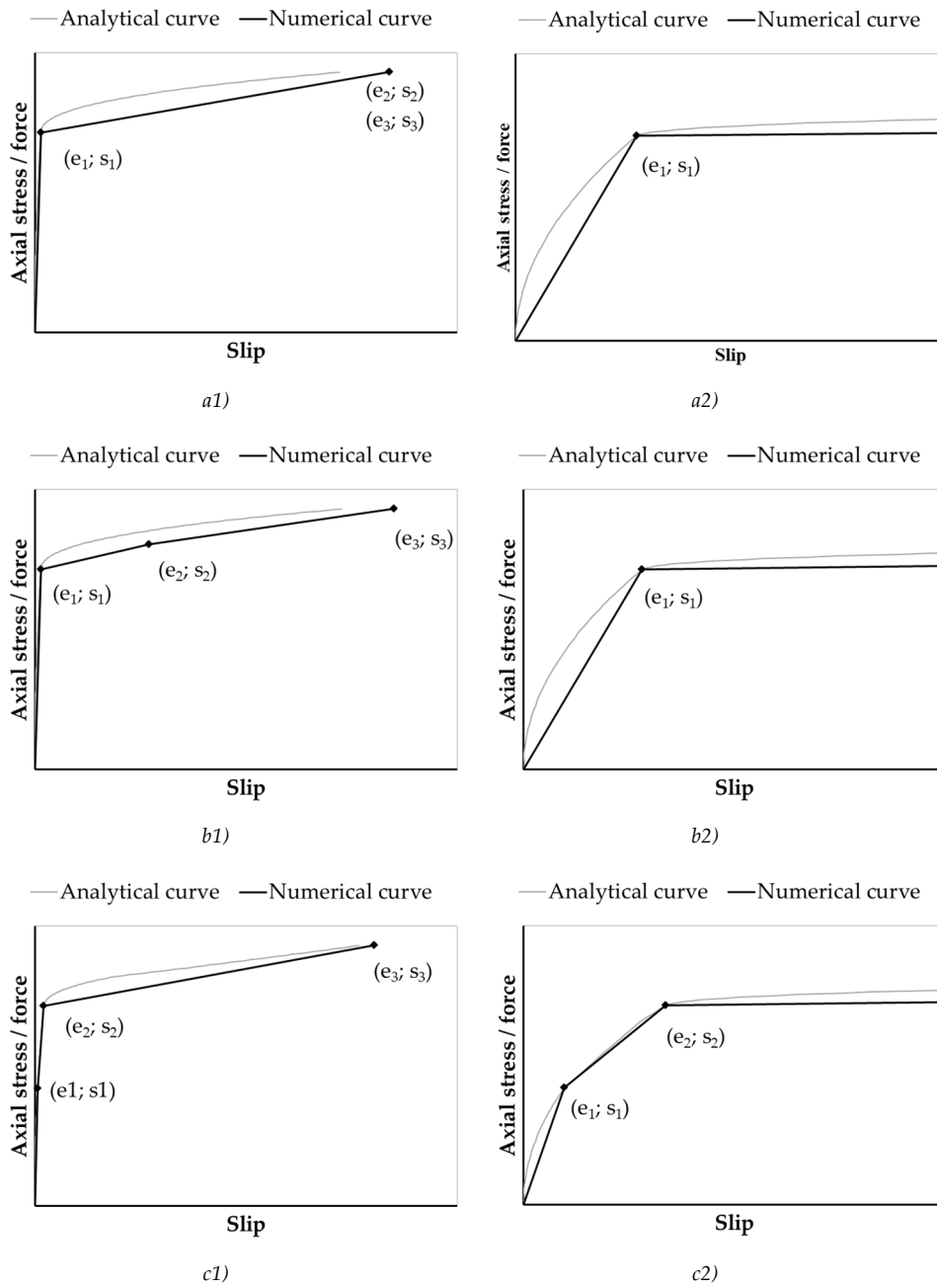
Figure 168: Analytical versus numerical stress-slip behaviour in presence of sufficient straight length to anchor the bar failure stress a) and in presence of hook activation in the plastic b) or elastic c) field. Complete curve up to rebar failure 1) and detail on the elastic branch 2).

The main numerical approximation is related to the representation of the stress-slip cyclic behaviour. The analytical interpretation of this response is based on the following three hypotheses:

- bar yielding cause bond strength reduction (Poisson effect);
- in the unloading phase all and only the elastic strain of the reinforcement steel is recovered;
- cyclic bond strength degradation occurs in reloading after the first loading application.

The herein presented proposal is based on a simplified model, which accounts respectively for: i) unloading and ii) reloading stiffness degradation. Graphical scheme of the choice in Figure 169, where the unloading stiffness is equal to:

$$K_{un} = K_l \mu^{-\beta} \qquad (190)$$

where K_l is the loading stiffness (define by the first branch of the envelope curve), μ is the actual displacement ductility, and β is a calibration coefficient. The latter is the only one which governs the cyclic response independently from the imposed displacement path. Strength and loading stiffness degradation are instead considered by a secant reloading behaviour to a fraction of the previous cycle maximum reached strength. In the OS hysteretic material definition (previously presented):

$pinchX = 1
$pinchX = 1
$damageX = $damageY = 0

The complete hysteretic material definition required the definition of the following:

- The coefficient β, governing the unloading stiffness;
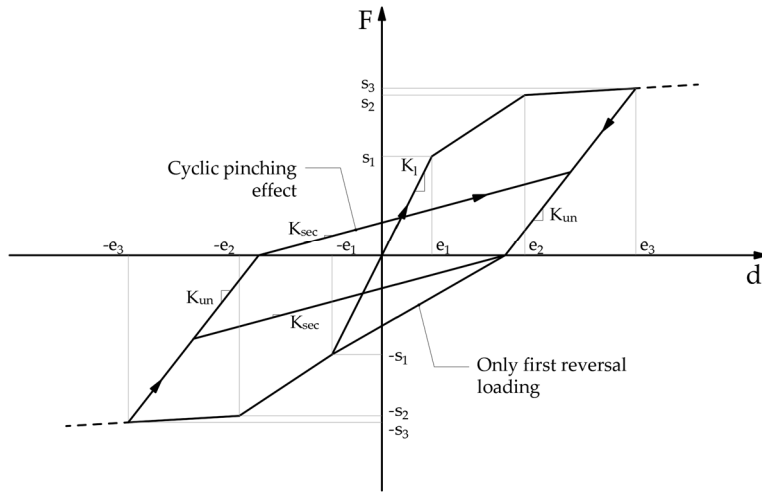- The strength reduction factor due to pinching effect R_f.

Figure 169: Schematization of the implemented hysteretic model for the reinforcement rebar stress-slip characterization: OpenSees (McKenna et al., 2000) Hysteretic material.

The determination of the coefficient β is based on the previous presented analytical concept, which provides to recover all the elastic deformation during the unloading phase. A direct analytical definition is not possible since the elastic part of the deformation changes during each cycle and since a different bond strength degradation characterizes the different cycles of the hysteretic response. A calibration on a reference drift target is thus suggested. Looking at the performance of an existing GLD building, it is possible to identify a deformation level at which a flexural Near Collapse Limit State is not expected to be reached. This value is set in term of drift and it is assumed equal to 1.50%. It (θ_t) can be considered equal to the base element interface rotation θ_b, consistently with the empirically observed rocking mechanism:

$$\theta_t \simeq \theta_b \qquad (191)$$

It follows the calculation of a specific reinforcement layer elongation $e_i(\theta_t)$, assuming a distance z_i from the element corner in compression:

$$e_i(\theta_t) = e_{i,el}(\theta_t) + e_{i,pl}(\theta_t) = \theta_b z_i \simeq \theta_t z_i \qquad (192)$$

After the axial stress related to the above calculated elongation is known, it is possible to analytical define its elastic $e_{i,el}(\theta_t)$ and the plastic $e_{i,pl}(\theta_t)$ components. Then, the unloading stiffness value related to the chosen performance level is defined:

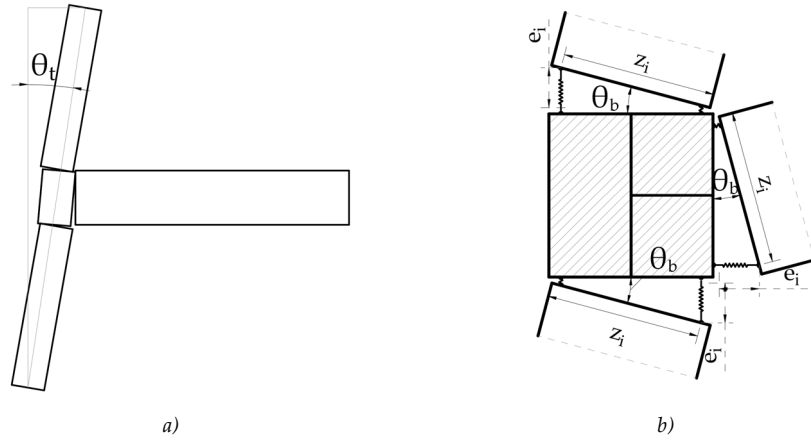$$K_{un}(\theta_t) = \frac{\sigma(\theta_t)}{s(\theta_t)} \qquad (193)$$

Figure 170: GLD frames external T-Joint under seismic excitation: global expected deformed shape a) and detailing of the interfaces crack opening b). No web (central) reinforcement is considered.

Note that the proposed approach calibrates the unloading stiffness based on the range of deformation explored by the RC element. It overestimates the unloading stiffness degradation in the deformation field higher than the set limit θ_t; on the other hand, it underestimates it at the lower amplitude cycles. Because of this, a higher energy dissipation capacity must be expected for the hysteretic response which main works at drift levels lower than the target one, and vice-versa. In any case, the herein presented target deformation level can be changed, according to the specific structural analysis. For static monotonic and/or cyclic analysis, the significant level of deformation is known; for Non-Linear Time-History Analysis (NLTHA) a trial value can be set and successive iterations can improve the analysis.

To avoid non-sense definition, the unloading stiffness moves in a range defined by the following maximum and minimum values (Figure 171):

$$K_{un,max} = K_1 \qquad (194)$$

$$K_{un,min} = K_{sec}(d_{max,i}) \qquad (195)$$

where K_1 is the slope of the three-linear first loading branch, $d_{max,i}$ is the maximum reached displacement at the considered $i - th$ cycle and $K_{sec}(d_{max,i})$ is the relative secant slope at $d_{max,i}$. It is worth noting that the value of K_1 is not related to the yielding secant stiffness, indeed, they are the same only if no hook activation characterizes the elastic response. From a numerical point of view, the following mathematical limit is set:

$$\beta_{max} \leq \frac{K_{el}}{K_{un}(\theta_t)} \mu(\theta_t) \tag{196}$$

where $\mu(\theta_t)$ is the ductility at the reference drift θ_t. It is a function of the slip value related to the first point e_1 of the adopted backbone curve (see Figure 169):

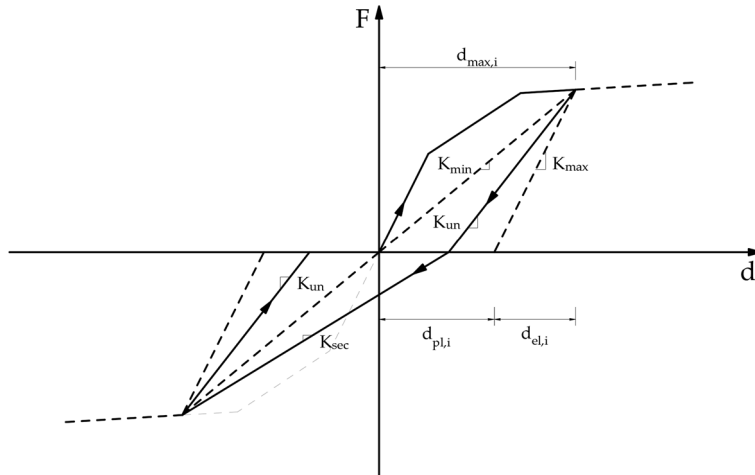$$\mu(\theta_t) = \frac{\theta_t z_i}{e_1} \tag{197}$$

Figure 171: Definition of the admitted unloading stiffness slopes with reference to maximum explored displacement $d_{max,i}$.

In Figure 172 the linearized cyclic stress-slip behaviour of a straight (group a) and of a hooked-end (group b) smooth rebar is presented. Both the elastic and the plastic fields are analysed, up to the yielding point and to a conventional target one. The graphs are relative to a 12mm plain rebar, with 480mm (40 diameters) straight length preceding the hook device. The slip excursion after the bar yielding is set according to the imposition of the above presented target drift ($\theta_t = 1.50\%$) on a 30cm square column. Axial stress is imposed, the relative slip value is calculated with the suggested analytical model, and a three-linear first loading branch is finally defined. A secant behaviour is instead assumed for the unloading and reloading successive paths. Load reversal and cyclic effects below the yielding point cause a slip increase proportional to the bond strength decay. This is herein assumed in consequence of what has been experimentally proved (Verderame et al., 2009a). No combined Poisson and bond degradation effects are considered, respectively due to the bar yielding and the cyclic loading degradation effects. Nevertheless, these combined effects should result only in a less hardening post-yielding response, thus not affecting so much the shown hysteresis. The application shows that the detrimental effect of the cyclic loading plays a very significant role only on the bar straight length

(case a); indeed, an increased deformation demand is noticed. On the other hand, its influence becomes negligible in presence of an end anchorage device (case b).

Therefore, the calibration of the pinching factor R_f should be based on the different anchorage solution. A lower reloading strength ratio R_f can be assumed on the element anchorage side since a straight bar presence is expected. On the contrary, a higher value can be defined for the joint (or foundation) side; indeed, the presence of a hook-end device is predicted. For the sake of simplicity, a unit value is assumed for the joint side and the ratio R_f between cyclic and peak bond strength is suggested for the element anchorage side evaluation:

$$R_f = \frac{0.05}{0.30} \simeq 0.17 \qquad (198)$$
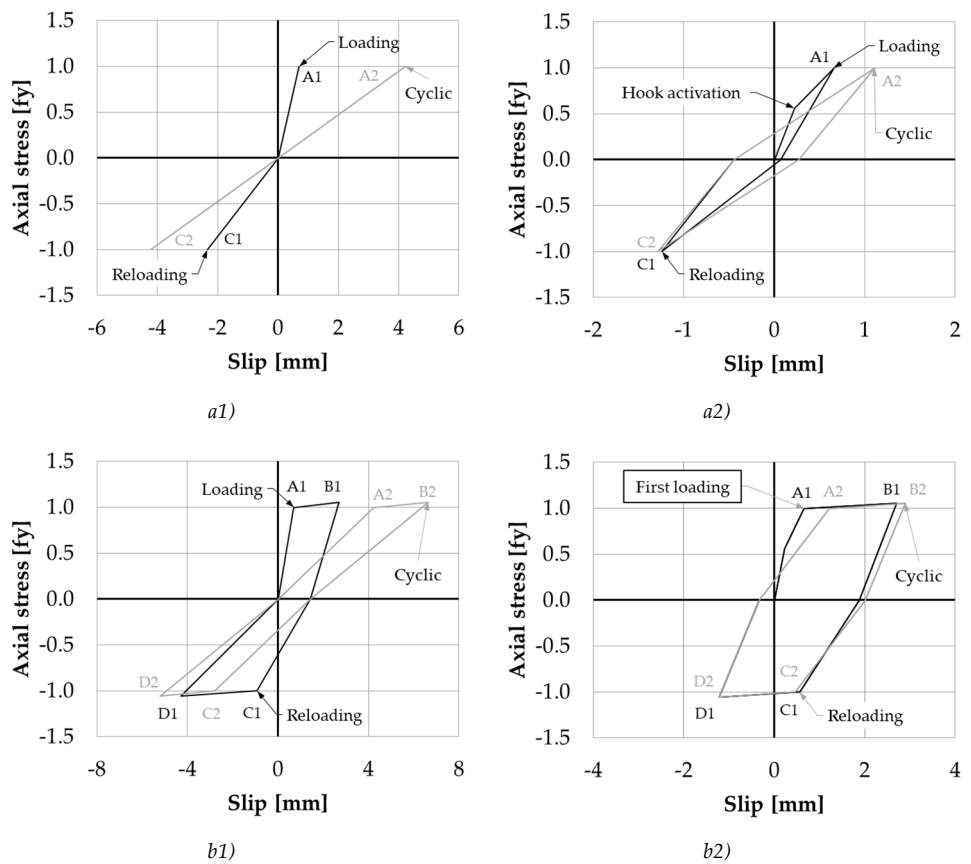
$$d_b = 12mm, \qquad f_y = 330MPa, \qquad f_u = 430MPa, \qquad Dl = 15\%, \qquad f_c = 15MPa$$

Figure 172: Analytical cyclic behaviour of straight 1) and hook-ended rebar 2) below a) and beyond b) yielding. Application on a reference case study.

239

Beam-column joint modelling

The numerical representation of the Moment-Rotation equivalent joint shear hinge is now treated. A zero-Length element with a single DOF material hysteresis is used.

element zeroLength $eleTag $iNode $jNode $-$ mat $matTag $-$ dir $dir3

The non-linear force-displacement relationship $matTag$ is described with the Hysteretic material already presented, with no pinching e no damage modelling. The translational DOF on $dir1$ and $dir2$ are blocked with equalDOF command.

In absence of joint shear panel strength degradation modelling, a post-processing check of the strain experienced by the shear equivalent hinge is necessary. Therefore, no large deformation can be accepted, to avoid the activation of brittle failure mechanisms. A fast check can be done by the imposition of the reference shear deformation suggested in the literature and reported in Table 27 (Pampanin et al., 2003).

6 SIMULATION OF STRUCTURAL MEMBER TESTS AND DISCUSSION

6.1 Introduction

In the following a series of experimental tests on different RC columns (Verderame et al., 2008b, 2008a), a T beam-column joint (Beschi et al., 2015) and a whole frame (Calvi et al., 2002b, 2001) are simulated through the application of the previously defined numerical model. The estimated overall force versus displacement behaviour, crack opening and members hysteresis are discussed and compared with the experimental evidences. A further comparison with a Code (CEN Eurocode 8, 2005) standardized approach, described in the following, is also suggested to show the difference in the response assessment of RC structures reinforced with plain rebars.

Definition of the Code based reference approach

The Eurocode suggests empirical formulation for the assessment of existing RC building seismic response (CEN Eurocode 8, 2005). Yielding and failure chord rotation are mathematically defined for a general RC element, depending on its structural significance against the seismic action (primary and secondary elements), and on the level of reinforcement detailing. The role of smooth rebars employment in the deformation capacity definition is also accounted for. On the other hand, no load-displacement behaviour shape is defined, neither for monotonic loading nor for the cyclic response; a simple and rational approach is thus presented in the following (with only reference to the monotonic behaviour).

For the comparison presented in the following, a lumped plasticity model is considered (Figure 173). It represents flexural and shear behaviour of the RC members with force versus displacement relationships (schematized in Figure 174). A bilinear elastic-perfectly plastic behaviour is assumed to represent the bending moment versus rotation relationship; an elastic-brittle behaviour is instead considered for the shear response. Only monotonic loading is considered.

The plastic hinge max strength is defined in the following way, respectively for the bending moment and for the shear action:

- sectional analysis on a defined element cross-section, considering the effective reinforcement layout and the role of the axial load;
- maximum strength between the Morsch resistant mechanism V_{Rd} and the shear capacity of a beam element without transversal reinforcement $V_{Rd,c}$.

Mean concrete compressive strength f_c and mean steel yielding stress f_y are considered in the section analysis and for the shear mechanism strength evaluation. Plane section hypothesis and no bar slip are assumed; concrete tension stiffening and steel hardening contributions are neglected. After the reach of the ultimate chord rotation capacity, and after the reach of the shear peak strength respectively, the resisted bending moment and the shear strength capacity assume a residual value equal to the 40% of the peak one.
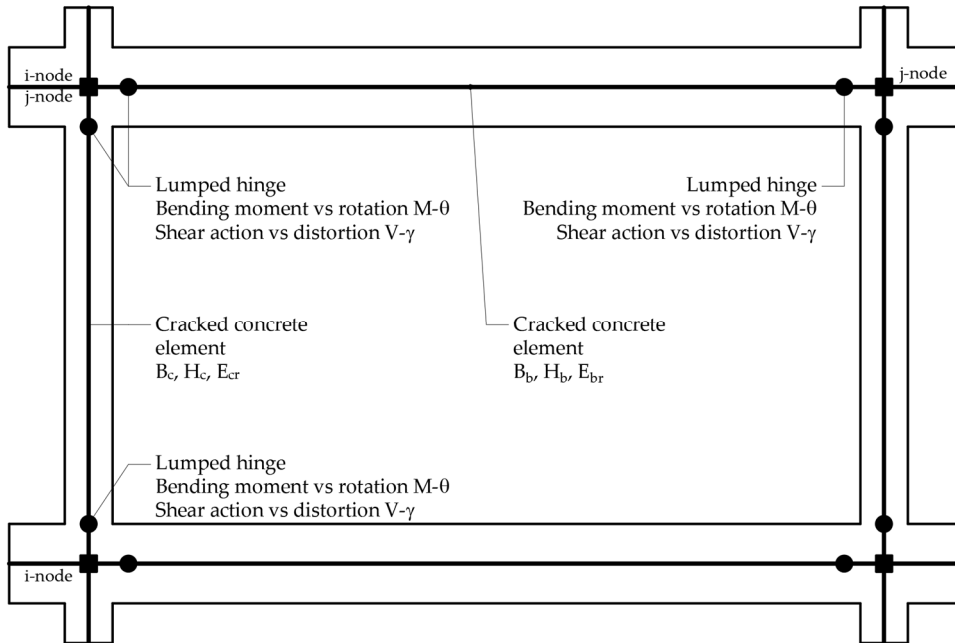

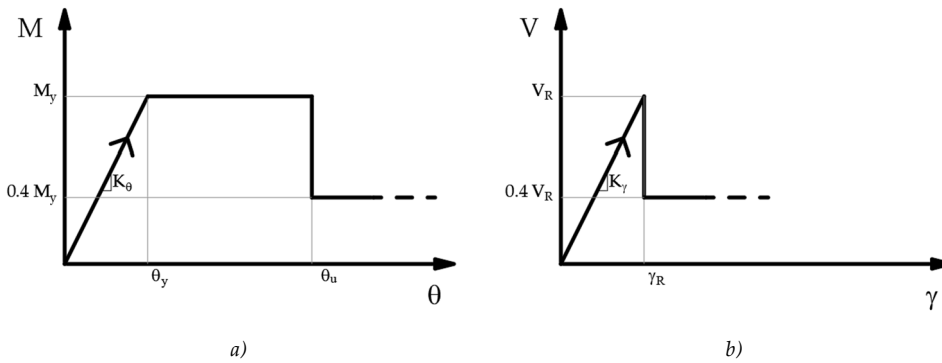Figure 173: Schematization of the reference lumped plasticity model approach.

Figure 174: Bending moment vs rotation a) and shear action vs deformation b) relationships implemented for the lumped plasticity Code based reference approach.

To define the elastic stiffness of the lumped hinge force-displacement behaviour, the flexural and the shear elastic stiffness are considered. A concrete modulus $E_c = 5000\sqrt{f_c}$ is assumed according to a specific literature suggestion (Priestley et al., 2007). To completely define the lumped hinge behaviour only the yielding θ_y and the ultimate θ_u chord rotations are missing. With reference to the Code (CEN Eurocode 8, 2005):

$$\theta_y = \phi_y \frac{L_V}{3} + 0.0014 \left(1 + 1.5 \frac{h}{L_V}\right) + \frac{\varepsilon_y}{d - d'} \frac{d_{b,l} f_y}{6\sqrt{f_c}} \tag{199}$$

$$\theta_u =$$

$$\frac{1}{\gamma_{el}} 0.016(0.3)^\nu \left[\frac{max(0.01; \, \omega')}{max(0.01; \, \omega)} f_c\right]^{0.225} \left(min\left(9; \frac{L_V}{h}\right)\right)^{0.35} 25^{\left(\alpha \rho_{sx} \frac{f_{yw}}{f_c}\right)} (1.25^{100\rho_d}) \tag{200}$$

with h depth of the cross section, d and d' lever arm of the tensile and compressive reinforcement layer respect to the compressive side edge, d_{bl} longitudinal rebar diameter and L_V shear span; ν is the normalized axial load, ω and ω' the mechanical longitudinal reinforcement ratio in tension and compression, f_c the concrete compressive strength, f_y and f_{yw} the longitudinal and confining steel yielding stress, ρ_{sx} and ρ_d are the ratio of the shear reinforcement and of the diagonal one respectively. The confinement efficiency factor α must be taken equal to zero, due to the use of stirrups with 90° hook end; $\gamma_{el} = 1.5$ for primary elements and $\gamma_{el} = 1.0$ for secondary ones.

Regarding the ultimate chord rotation capacity, the Code suggestion reduces it in presence of seismic lack of detailing and in presence of smooth rebar. In the following application, these reduction factors are not considered for two reasons: i) the main attention is put on the structural stiffness assessment and not on the ultimate deformation capacity; ii) the experimental evidence show effective capacities significantly higher respect to the Code (CEN Eurocode 8, 2005) indication; for more details see the state of the art in Section 2.2.

Beam-column joint shear failure is verified on the frame external T-connection. Since the Code suggestions for the existing structure (CEN Eurocode 8, 2009) refer to the new construction verification method, the simpler and more consistent Principle Stress Limitation Method is considered (Circolare applicativa NTC, 2019; Pampanin et al., 2002). The approach provides the following checks:

$$\sigma_{jt} = \left| \frac{N}{2A_j} - \sqrt{\left(\frac{N}{2A_j} \right)^2 + \left(\frac{V_j}{A_j} \right)^2} \right| \leq k_t \sqrt{f_c} \qquad (201)$$

$$\sigma_{jc} = \frac{N}{A_j} + \sqrt{\left(\frac{N}{2A_j} \right)^2 + \left(\frac{V_j}{A_j} \right)^2} \leq k_c f_c \qquad (202)$$

N and V_j are the axial and the shear load acting in the joint panel, where the latter is the sum of the upper column shear load and the force due to the bending action in the upper beam chords; A_j is the net joint cross section area. The first check is relative to the panel crack control, whereas the second one to its compressive failure. Referring to non-conforming beam-column joints, the governing mechanism is the first one, given the lack of stirrups in the joint. A coefficient $k_t = 0.2$ is used for the definition of the reference principle tensile concrete stress, according to empirical evidence (Pampanin et al., 2003). The choice is consistent with the reference strength assumed in the analytical model proposal, previously presented, and applied in the following.

6.2   Monotonic and Cyclic behaviour of column members

A wide experimental campaigns reported in the literature (Verderame et al., 2008b, 2008a) is considered for the evaluation of both the monotonic and the cyclic response of substandard RC columns reinforced with smooth bars. The member geometry and the reinforcement detailing well reflect the most common configurations that characterize the herein considered GLD frame buildings (Figure 175). The role of longitudinal reinforcement lap splice, axial load, and number of loading cycles are investigated. The first letter of the specimen label is referred to the loading protocol (M for monotonic and C for cyclic loadings), the number is the axial load magnitude (in kN), and the last letter refers to the overlapping presence (Figure 175). A total amount of 6 different specimen arrangements is identified and subjected to both monotonic and cyclic loading.
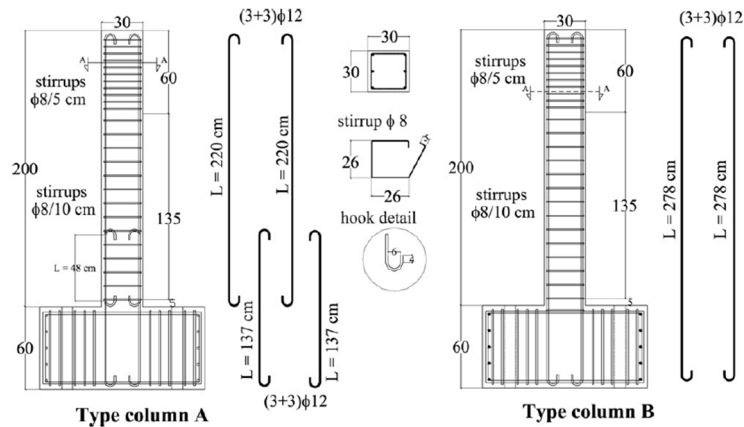
Figure 175: Reference samples (Verderame et al., 2009b, 2009a).

Reinforcement steel		Concrete	
Yielding stress	355Mpa	Mean strength	29.34MPa
Failure stress	470MPa	Nominal strength	25.00MPa
Ultimate elongation	20.0%		

Table 28: Data of the reference experimental campaign (Verderame et al., 2008b, 2008a).

Monotonic behaviour

The herein reported observation is stopped at a maximum level drift of 3.00%, over which significant strength degradation takes place due to different mechanisms, such as the concrete crashing, the cover spalling, and the longitudinal reinforcement buckling. The modelling proposal does not consider the cited effects since the high deformation field is not of interest.

Very good representation of stiffness and strength capacity can be noticed (Figure 176). An initial linear branch characterizes the structural response until the rocking mechanism is activated ($25 \div 30 kN$ for the samples M-270, and about $40 kN$ for the specimens M-540). A progressive crack opening at the column base is then reflected in a successive non-linear elastic field; finally, the reinforcement yielding characterizes the response up to the reference 3% drift level.

A comparison with the reference Code based approach is proposed is reported in Figure 177, accounting both the elastic stiffness and a reduced one (by a factor 0.5). It results interesting to observe that the standardized procedure results significantly stiffer respect to the presented modelling technique. Column plasticization is thus anticipated, and higher shear action occurs at lower deformation level. A common simplified approach suggests considering a reduced elastic stiffness, to account for concrete cracking influence on the structural deformation capacity. A reduction

245

factor equal to two is not enough to represent the column deformation at the yielding point; furthermore, a wrong representation of the initial stiffness in noticed. Details are available in Figure 177.

The influence of the bar slip contribution from the foundation crack side and from the element one is outlined in Figure 178. By the comparison it results that they play a similar role on the overall deformation capacity. On the other hand, a stiffness degradation is expected in the cyclic response of Type B specimen since the bond strength degradation arises during cyclic loading on the straight bar anchorage. This conclusion is based on the experimental evidence previously discussed. Crack opening monitoring is reported in Figure 179, where also a comparison with experimental readings is shown.
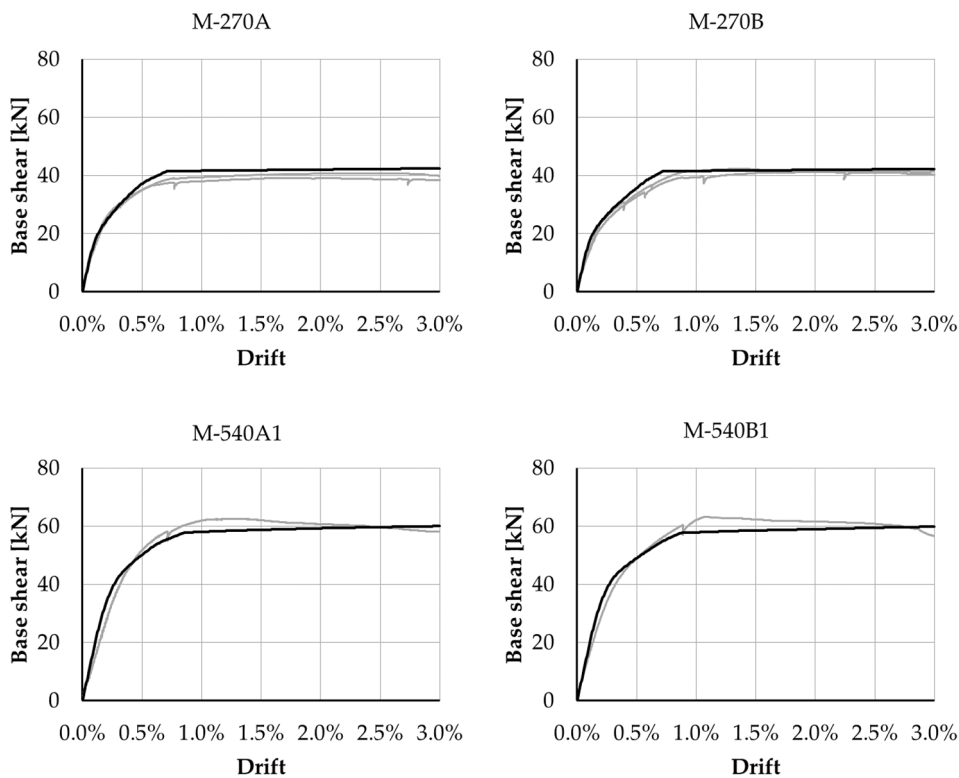

Figure 176: Comparison between experimental results on column monotonic behaviour (Verderame et al., 2008b) (thin grey line) and their prediction based on the proposed modelling technique(bolted black line).
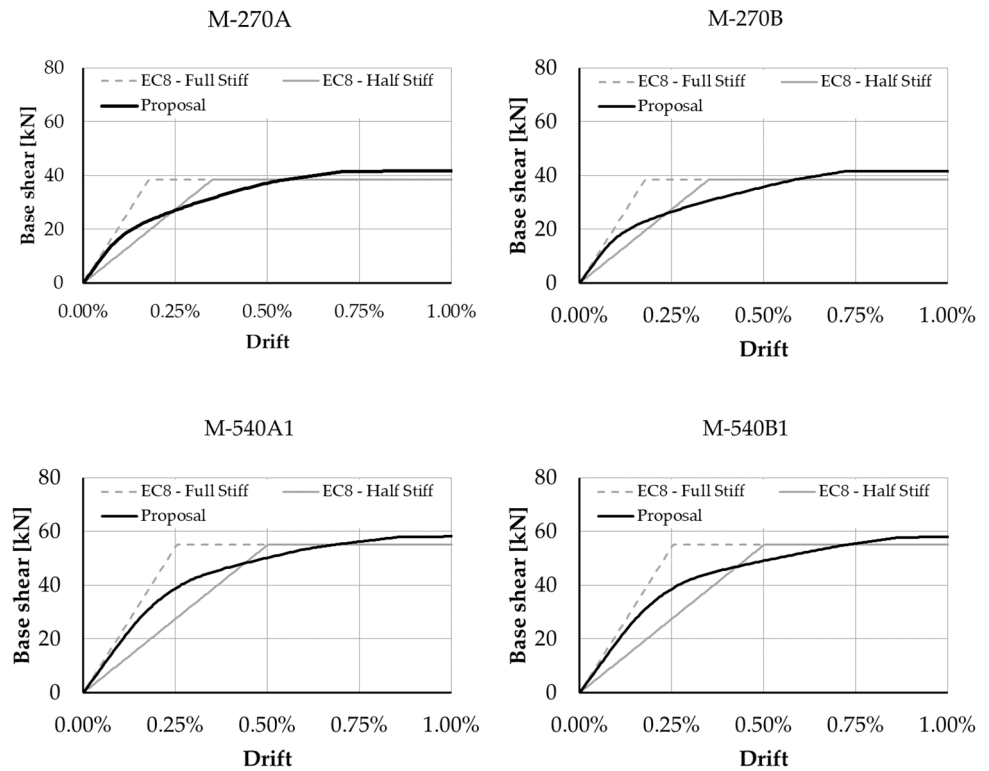
M-270A

M-270B

M-540A1

M-540B1

Figure 177: Comparison between Code based approach with full elastic stiffness (dotted grey line) and reduced stiffness (continuous line); modelling proposal in black curve.
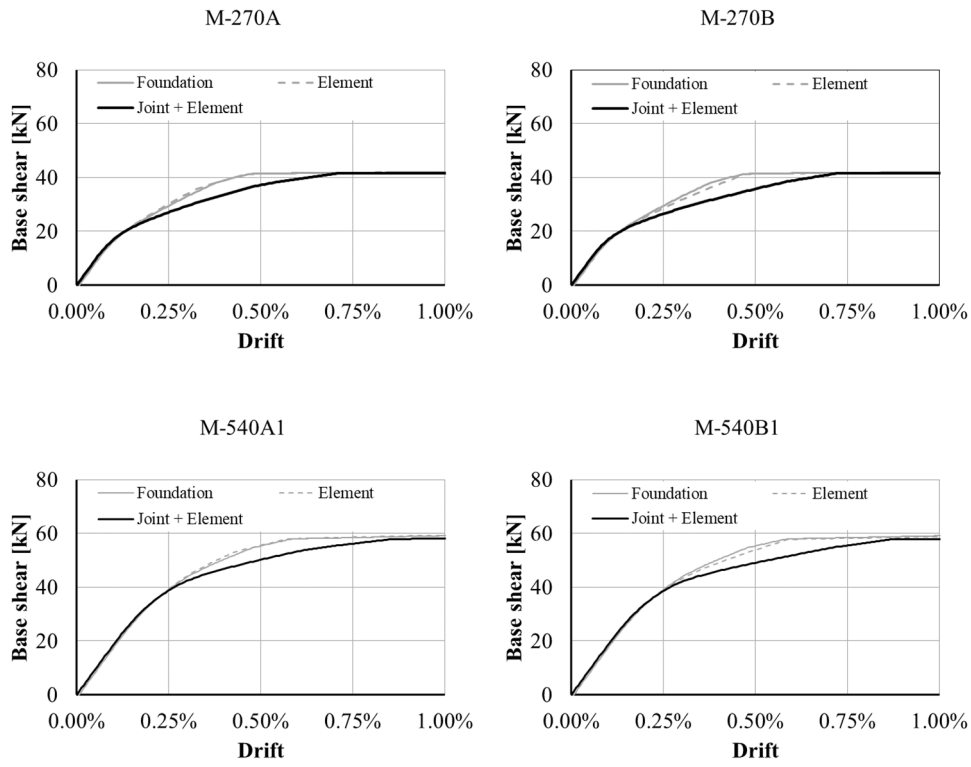
Figure 178: Bar slip contribution on foundation and element side to the global deformation.
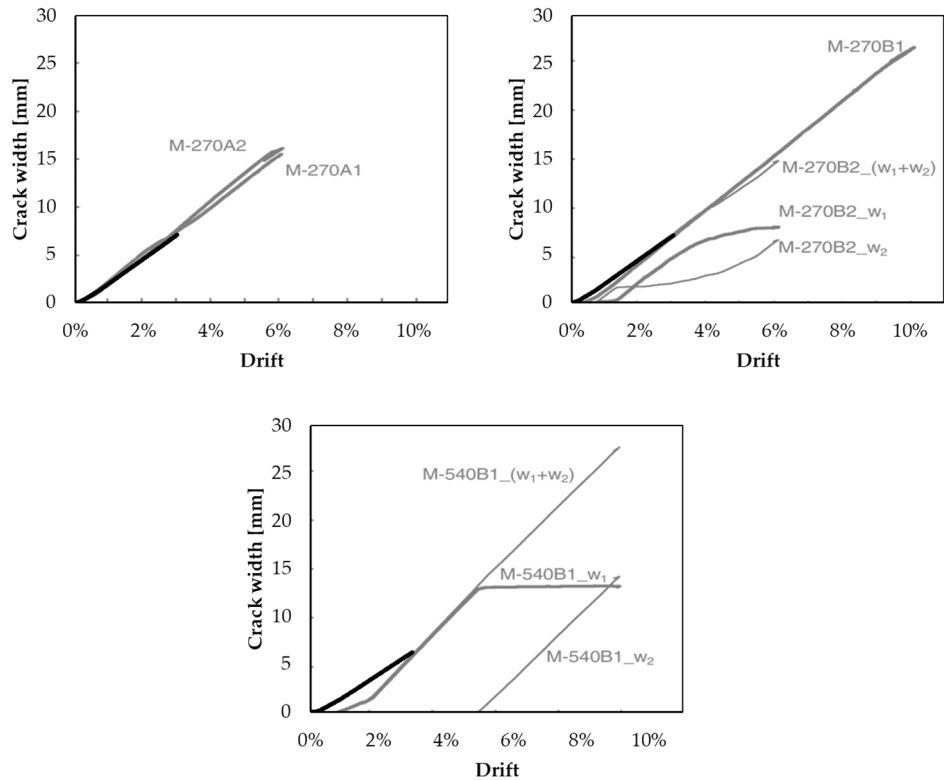
Figure 179: Comparison between column base crack width and global drift: experimental results (Verderame et al., 2008b) versus numerical prediction.

Cyclic behaviour

In analogy with the monotonic response and for the same range of drift, in the following the cyclic response of the previously analysed columns subjected to lateral load are presented. The loading behaviour is well captured for all the cases. On the other hand, the reloading and unloading stiffness exhibit a numerical overestimation of the pinching definition, especially at the lower axial load level and without rebars overlapping at the column base (C-270B1 sample). Load versus drift graphs are reported in Figure 180; a detail on the yielding deformation level is proposed in Figure 181. Column base crack opening versus global drift is also compared (Figure 182) The numerical estimation of the crack width represents the opening of the extreme concrete fibres used in the crack modelling (see the definition of the crack non-linear modelling in Chapter 5).
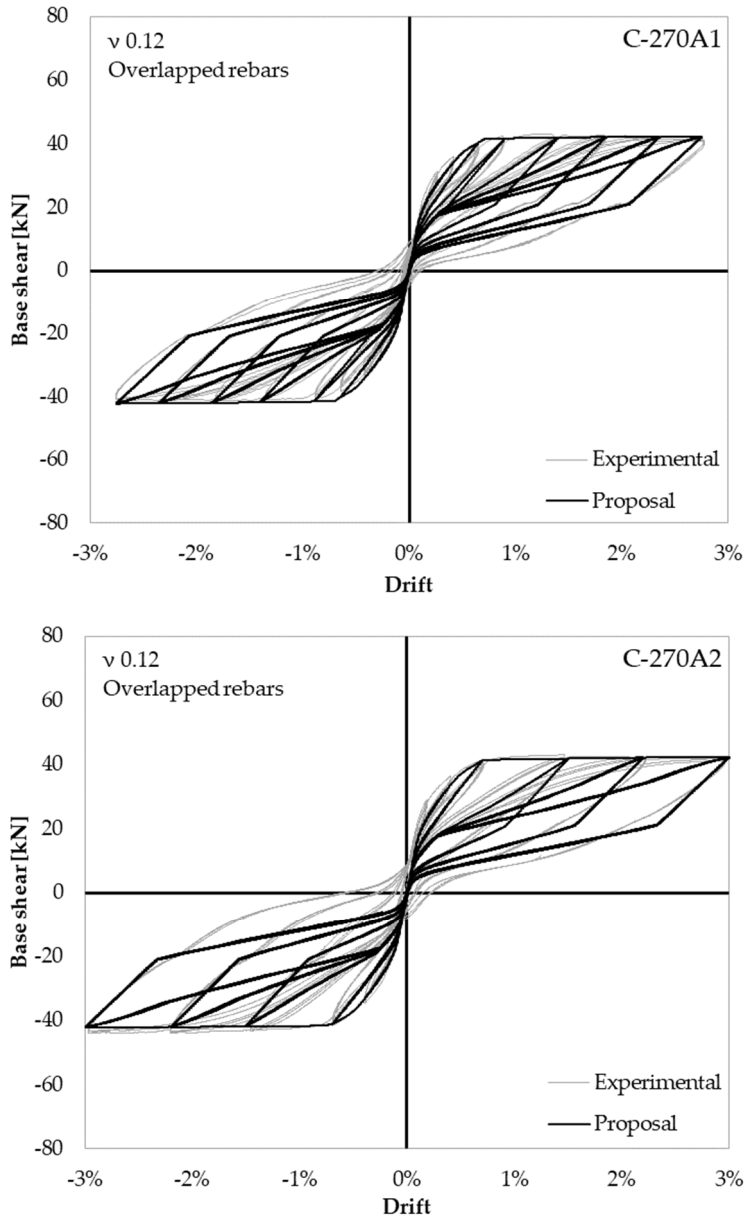
Figure 180 (Pt. 1 of 3)

Figure 180 (Pt. 2 of 3)
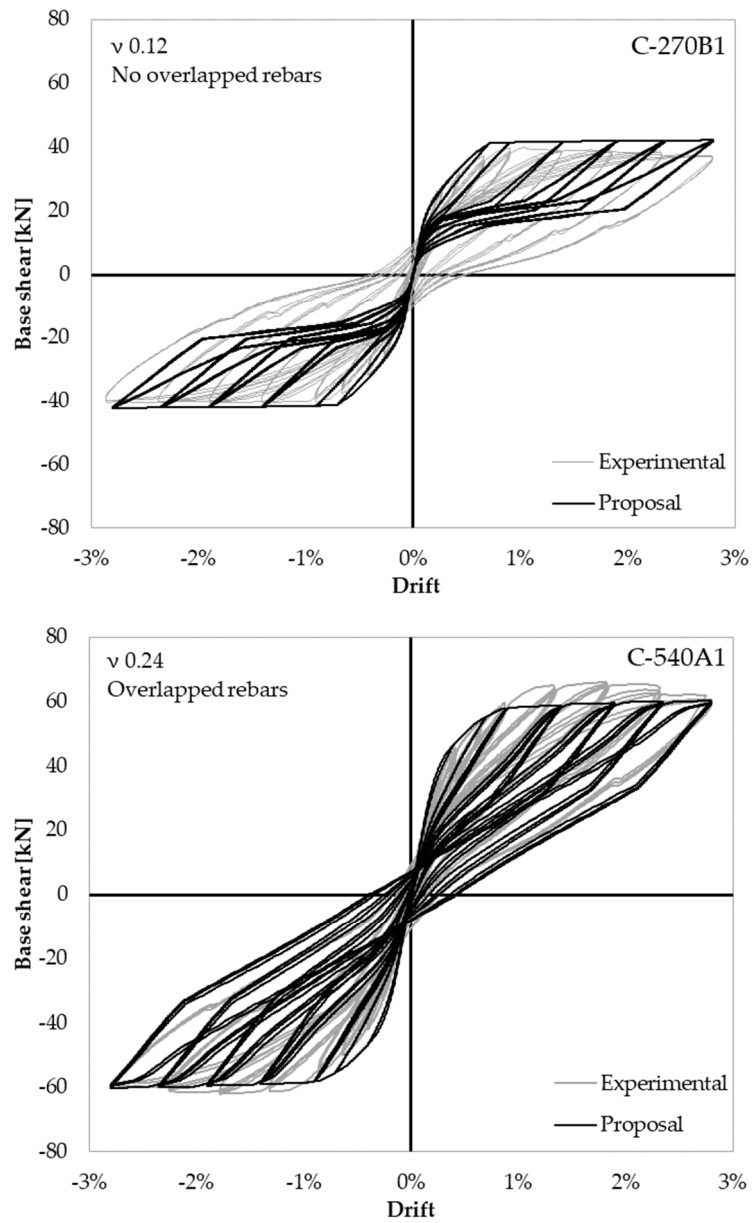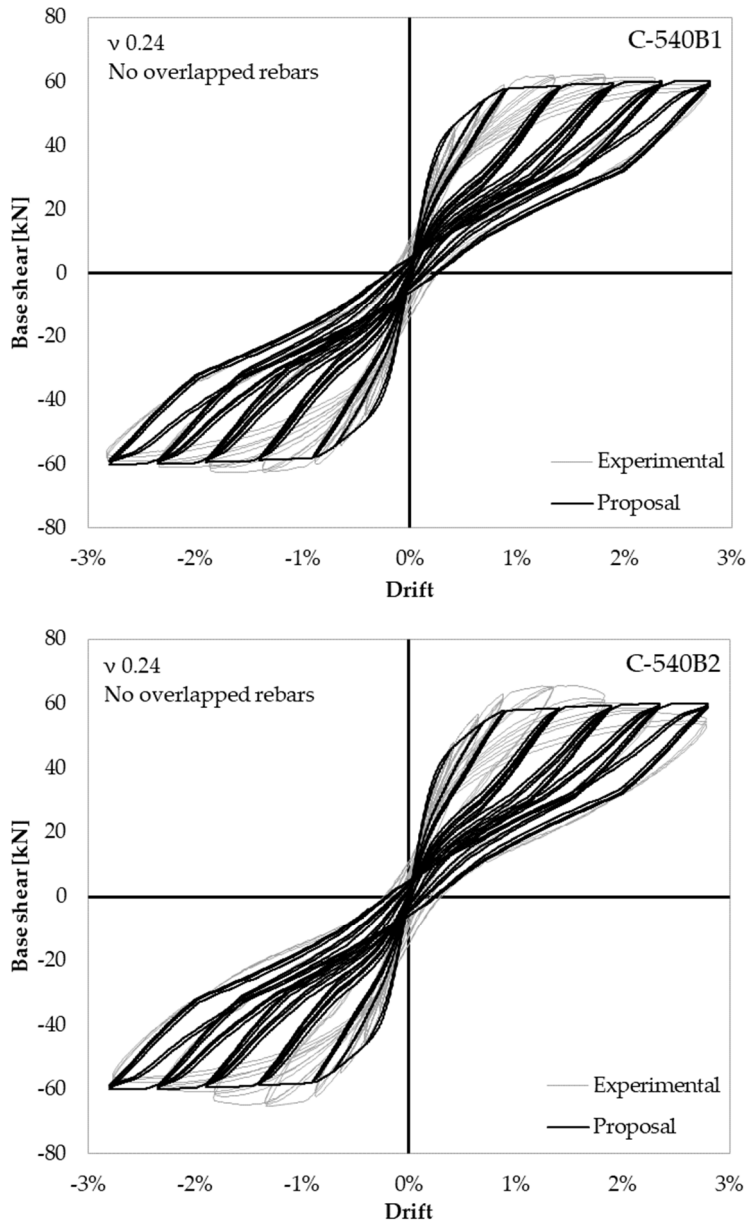
(Pt. 3 of 3)

Figure 180: Comparison between experimental results on column cyclic behaviour in term of force versus drift and numerical prediction.
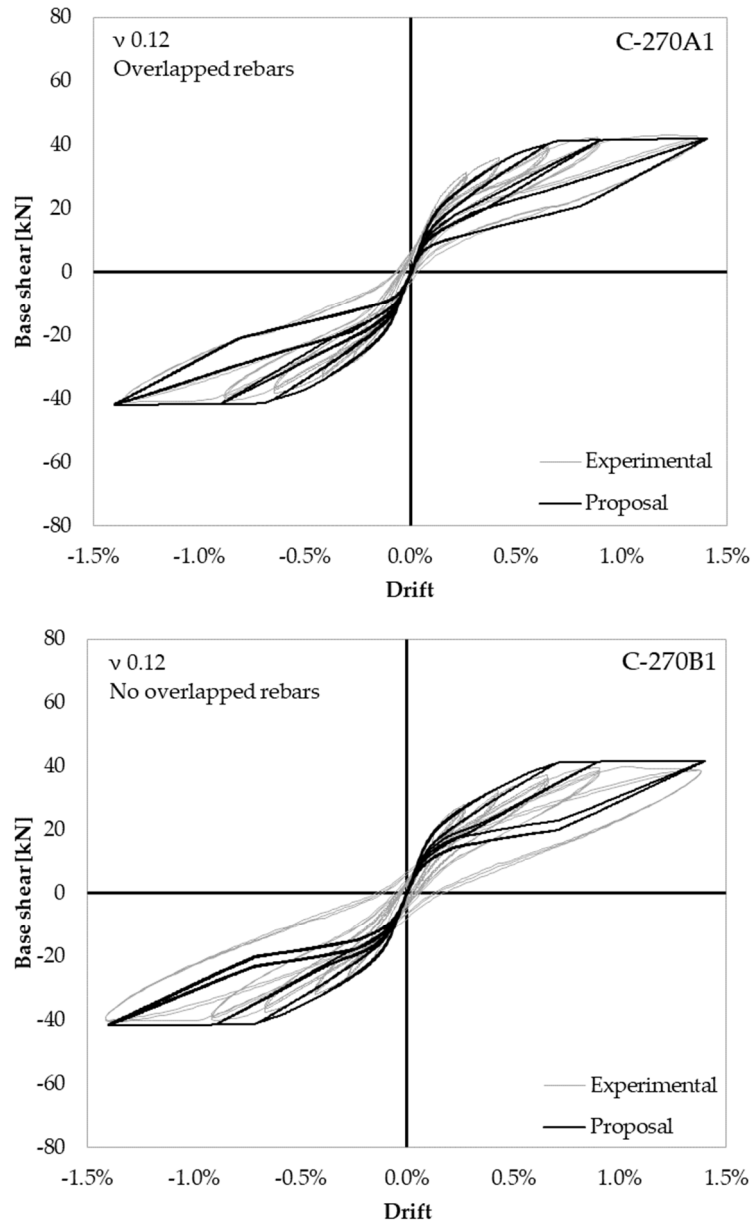
Figure 181 (Pt. 1 of 2)
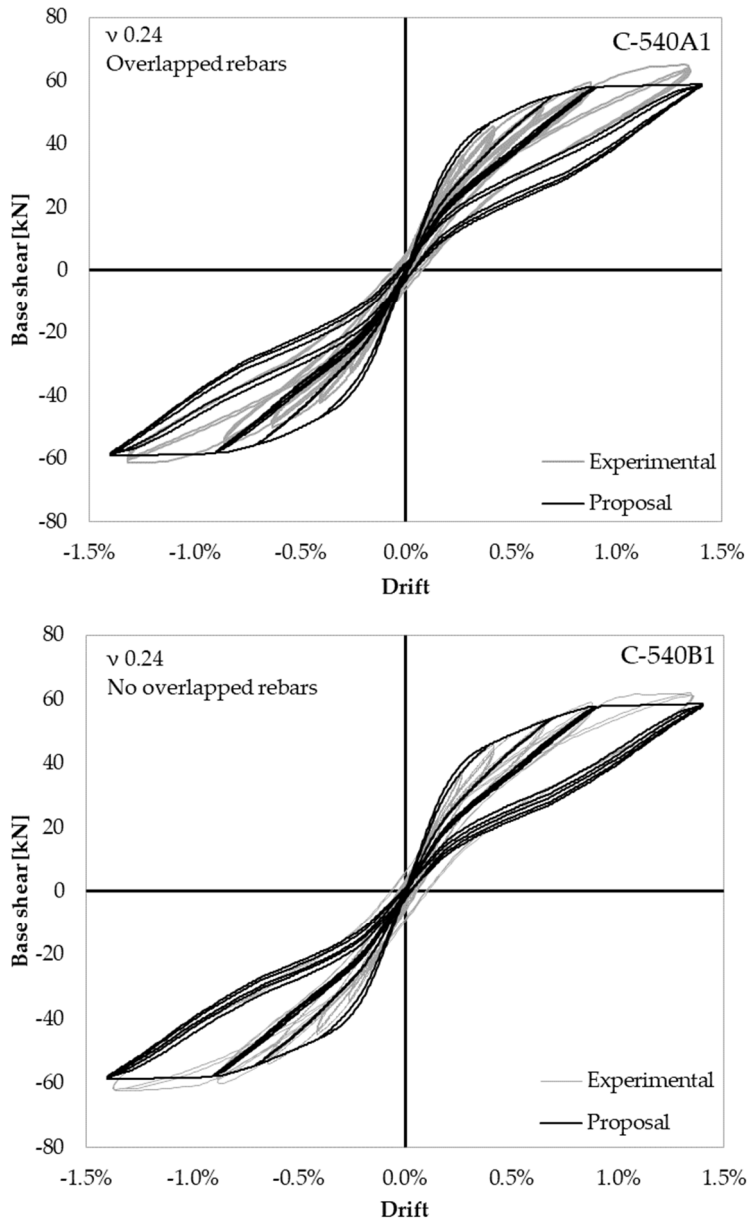
(Pt. 2 of 2)

Figure 181: Focus on the yielding deformation level. Only four different specimens are herein considered; experimental (Verderame et al., 2008a) curves in grey and numerical ones in black line.

The numerical modelling does not show a condition in which the column base crack is completely opened along the entire member cross section. However, the experimental results show un uplift during the reloading phase; its value increases with the explored deformation level and assumes a maximum value of $0.6mm$. It can be argued that the experimental evidence could be related to aspect not considered in the herein presented modelling technique.
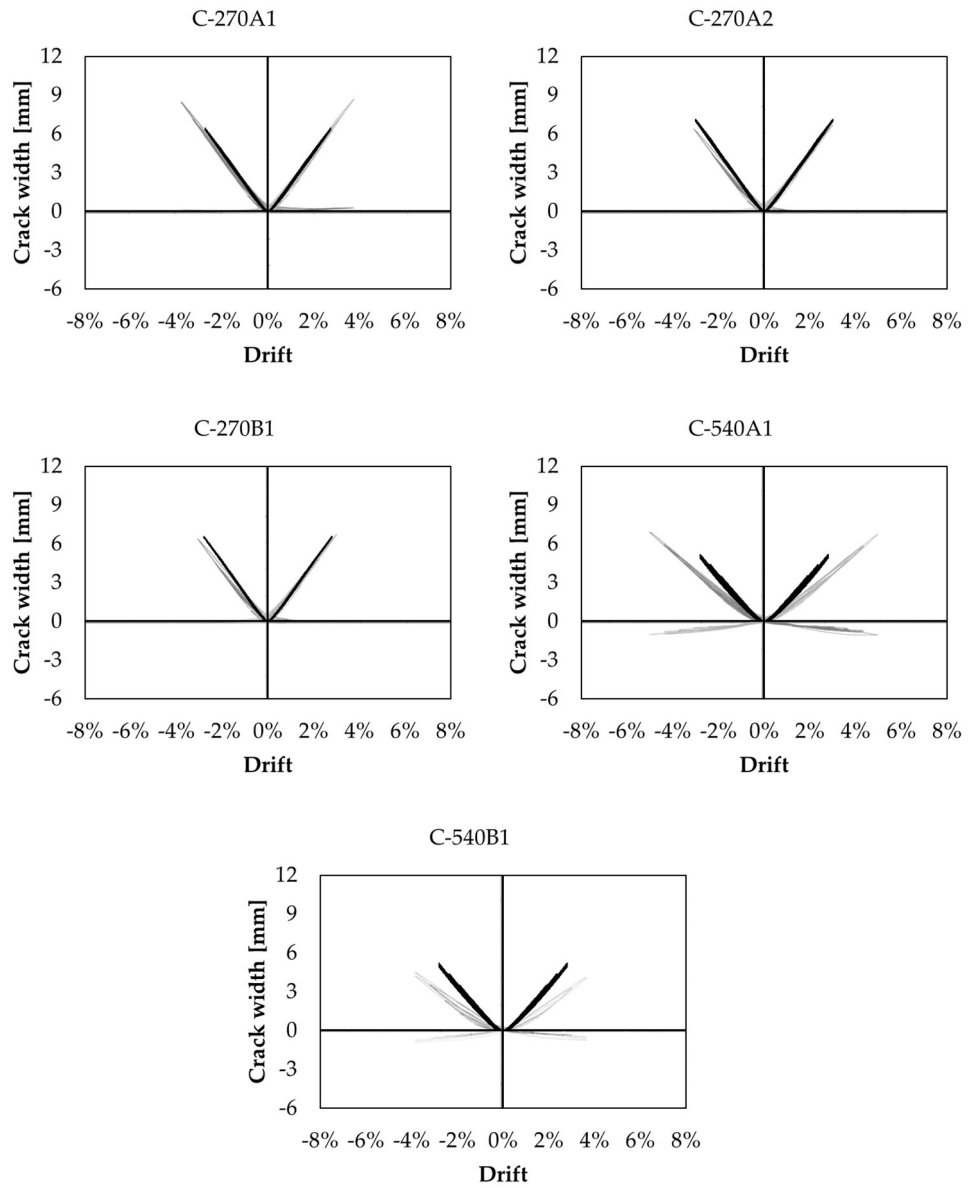
Figure 182: Column base crack width assessment in presence of cyclic loading.

255

6.3 Cyclic behaviour of external beam-column joints

Figure 183: Specimen geometry and reinforcement configuration a) and mechanical material properties b) of the considered joint subassemblies (Beschi et al., 2015).

An experimental test on a beam-column T-joint is now considered (Beschi et al., 2015). Its geometry and the reinforcement arrangement is reported in Figure 183. The experimental response shows beam flexural yielding in a loading direction and a joint panel shear failure in the other, as a result of the asymmetric configuration of the reinforcement. The reference sample, with the aim of simulating a corner connection, is also characterized by a transversal secondary beam, which is not considered in the modelling.

Experimental response simulation

All the experimental loading history is simulated, allowing the investigation of the model performance at different level of drift. The global hysteresis (Figure 184) is well captured in term of predicted stiffness, strength, and energy dissipation. With specific reference to the response exhibited at the low drift levels, which is the field of main interest, it is very clear as the assessed loading and reloading stiffness are very well represented, whereas worse prediction is noticed for the unloading stiffness branch.

Observing the single elements stress-strain (displacement) relationships (Figure 185), it is possible to notice like both the semi-columns do not affect the structural response; indeed, they behave in the elastic field. Rocking mechanism seems to be activated but the overall system deformation is mainly related to the beam crack opening. The latter is numerically estimated as the opening of the concrete fibres used in the crack modelling at the beam extrados (or intrados). On the other hand, the shear deformation demand on the joint panel exceed acceptable values, therefore the predicted response cannot be considered representative for the highest drift level imposition (only in the negative direction). Empirically, this is confirmed by the strength degradation that occurs after the reach of a drift $\theta = 1.50\%$, which is assumed as a reference for the Near Collapse (NC) Limit State, according to Table 27.
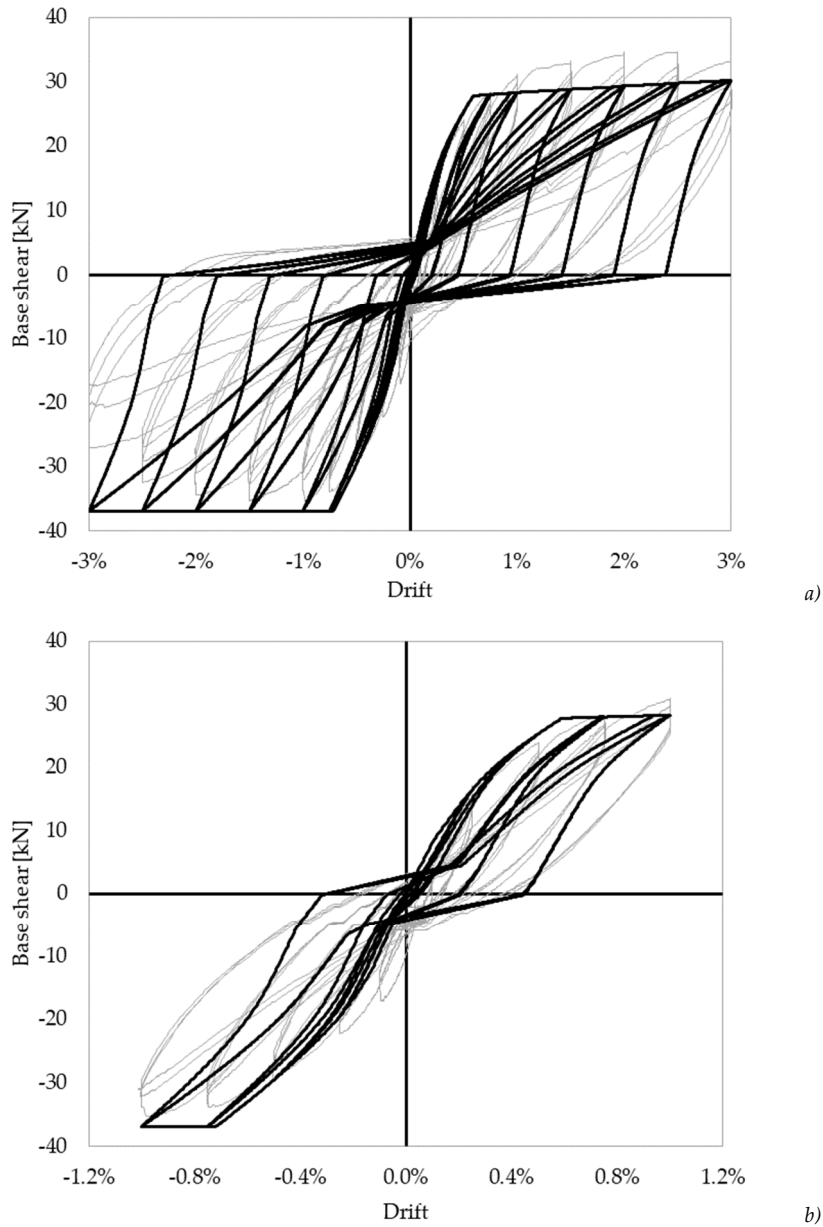
257

Figure 184: Global hysteresis of the analysed beam-column T-joint a) and detail on the low drift level response b).
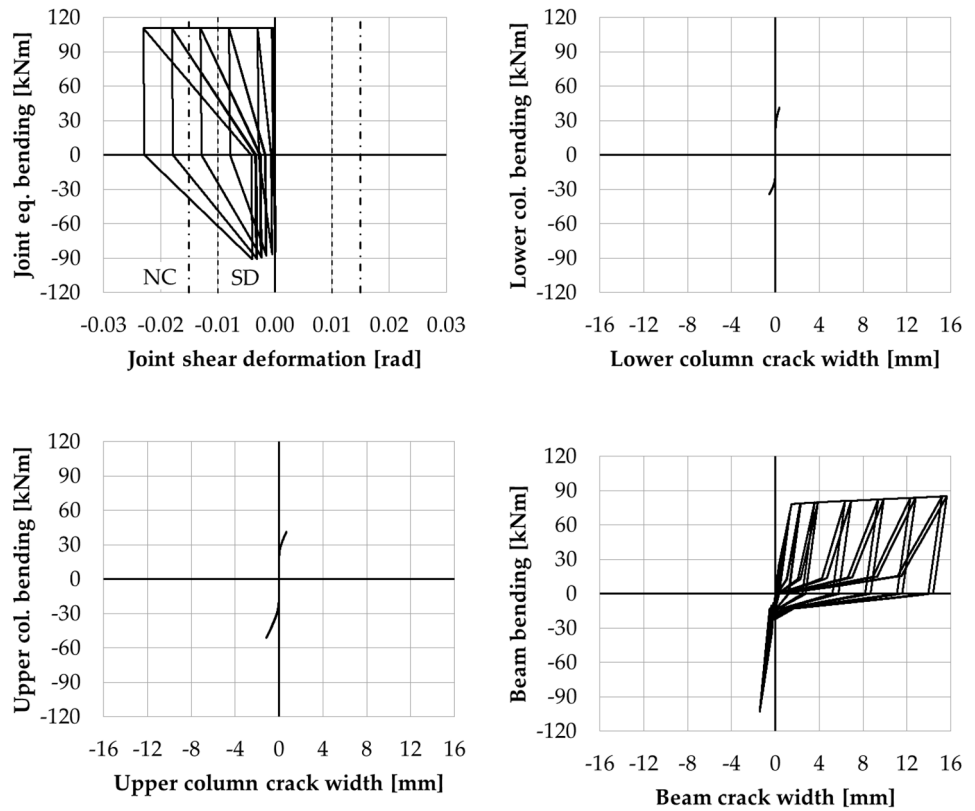
Figure 185: Hysteretic response for the members part of the considered joint sub-assemblies.

Comparison with Code based prediction model

In the following, the envelope of the joint experimental response is presented up to a drift level equal to 1.00%, so basically within the elastic field and just above the yielding of the rebars in test specimens. Both the positive and the negative direction response are analysed since they are controlled by different mechanisms activation. On the other hand, higher drift levels are not considered; indeed, they are out of the interesting range of deformation, and the proposed model is not able to catch strength degradation due to joint panel progressive damage. A comparison with the reference Code (CEN Eurocode 8, 2005) based approach is also presented, in order to discuss the ability of the different models in representing the beam-column joint behaviour at the low imposed drift level, in other words below the yielding point. Both the elastic stiffness and a reduced one (by a factor 0.5) are considered in the standardized approach.

The proposed model assesses a higher deformation capacity, with reference to the beam yielding in the positive direction and to the joint shear cracking in the negative one (Figure 186). Respect to what has been previously observed for the column monotonic response, a greater variance is also noticed in the stiffness definition. This conclusion is probably related to the role played by each element converging in the joint; indeed, both the semi-columns (after the rocking mechanism activation) and the beam are interested by a crack opening. The deformation capacity of the joint sub-assembly is up to four times higher with respect to the one assessed with the other analysis methods (Figure 186). A higher stiffness causes the arise of the shear cracking in the joint panel at lower drift level; more in detail, the stiffer elastic response based on the Code reference approach must be considered not acceptable in the drift range $\theta \geq 0.20\%$. Indeed, the cracking of the shear panel should define a limit for the strength capacity, cause to the lack of transverse reinforcement in the joint region. Despite this, the analysed approach shows an increase of strength.
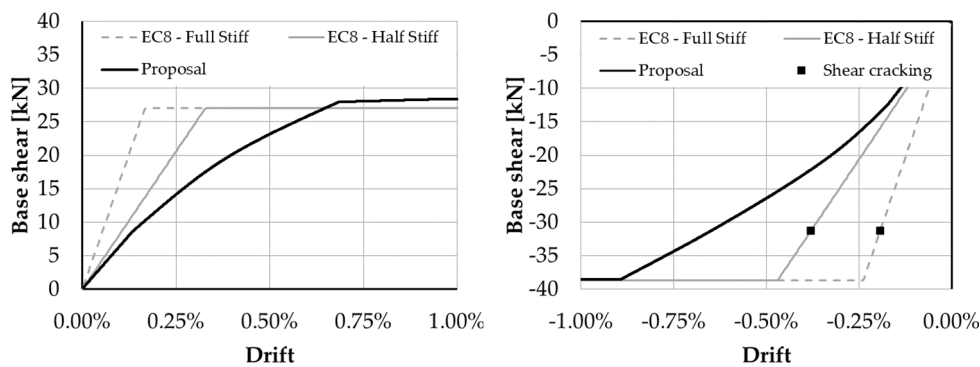

Figure 186: Comparison between modelling proposal and Code based approach for the tested beam-column subassembly (Beschi et al., 2015); a monotonic loading up to 1.00% drift level is considered for each direction.

6.4   Monotonic and cyclic behaviour of 2D planar frame

The previous analysed applications show like the modelling of plain rebar slip allows a good prediction of: i) elastic stiffness, ii) yielding strength and iii) hysteretic behaviour of non-conforming RC elements with plain rebars. A deep influence of the same phenomena is also seen analysing the response of a whole frame. In this case, the behaviour results strongly affected by the internal action re-distribution and, consequently, the definition of a specific activation history of the collapse mechanism is of particular interest.

In the following, the simulation of the experimental test on a 3-bays-3storeys frame under cyclic excitation is performed. The reference sample is represented in Figure 187 (Calvi et al., 2002b, 2001).

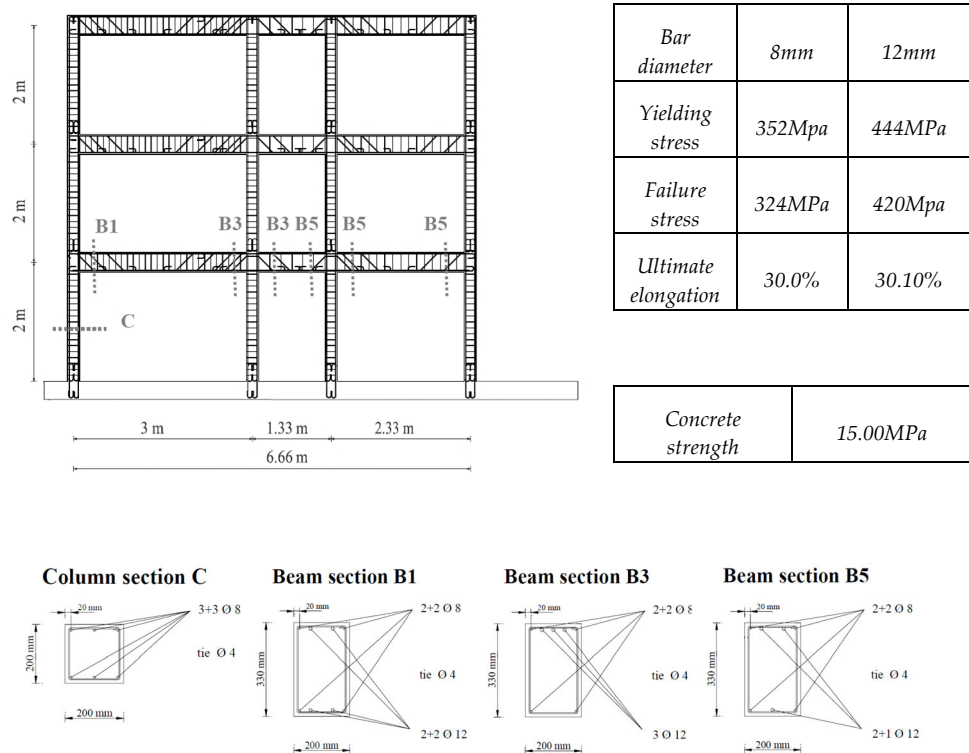| Bar diameter	8mm	12mm
Yielding stress	352Mpa	444MPa
Failure stress	324MPa	420Mpa
Ultimate elongation	30.0%	30.10%

Concrete strength	15.00MPa

Figure 187: 2D planar frame experimentally investigated (Calvi et al., 2002b, 2001) and numerically simulated.

Simulation of the experimental results

The authors show like the frame response is mainly governed by the poor performance of the external T-Joints; their shear cracking, however, allows the internal action re-distribution on the adjacent members prior to the strength decay due to joint panel extensive damage. The peculiar behaviour avoids the activation of a classic soft storey mechanism, as it is clearly understood by the observation of the deformed shape (Figure 188.b). Beam elements behave elastically, whereas the column presents a crack pattern characterized by the formation of a main crack at the joint-member interface region. This experimental evidence is consistent with the conceptual base of the herein presented modelling technique. The adopted equivalent joint modelling technique also allows to capture the joint shear cracking, but it is not able in predict the shear strength decay due its extensive damage. Because of this, a limit to the model representativeness must be set.

In Figure 189 the progressive activation of the flexural and shear mechanisms is shown. A comparison with the experimentally observed crack pattern is instead reported in Figure 190. the shear cracking on four beam-column joint panels precedes the yielding of the column; no plasticization occurs in the beam elements.

The numerical proposal well predicts the system hysteretic response (Figure 191); more details about it are reported in Appendix C.

a)   *b)*
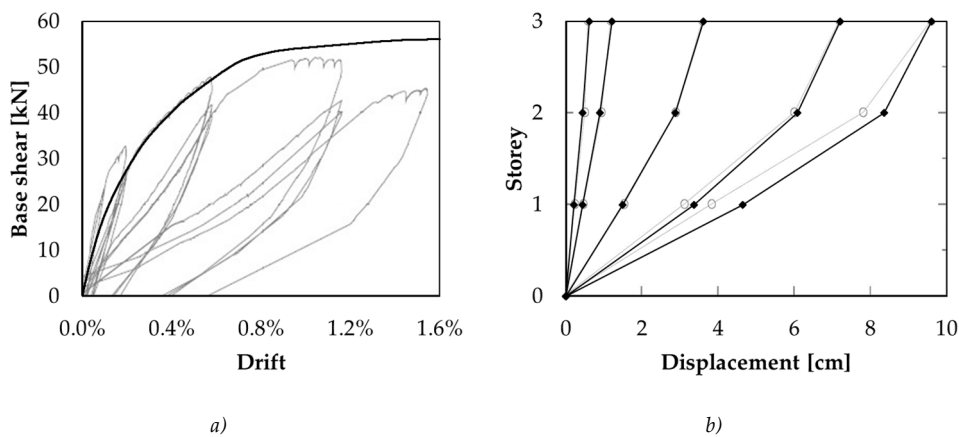
Figure 188: Numerical envelope of the experimental frame behaviour a) and comparison of the real and numerical predicted displacement profile b).
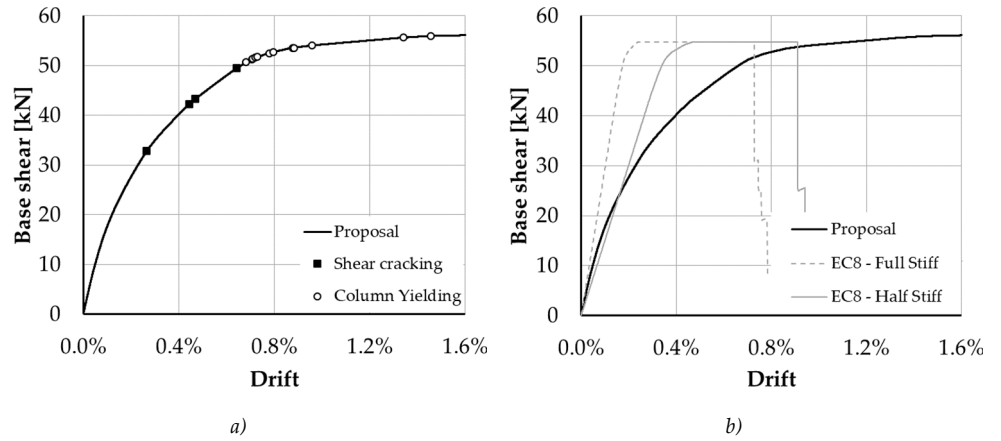
a)   *b)*

Figure 189: Frame mechanisms activation history a) and comparison with Code reference approach b).
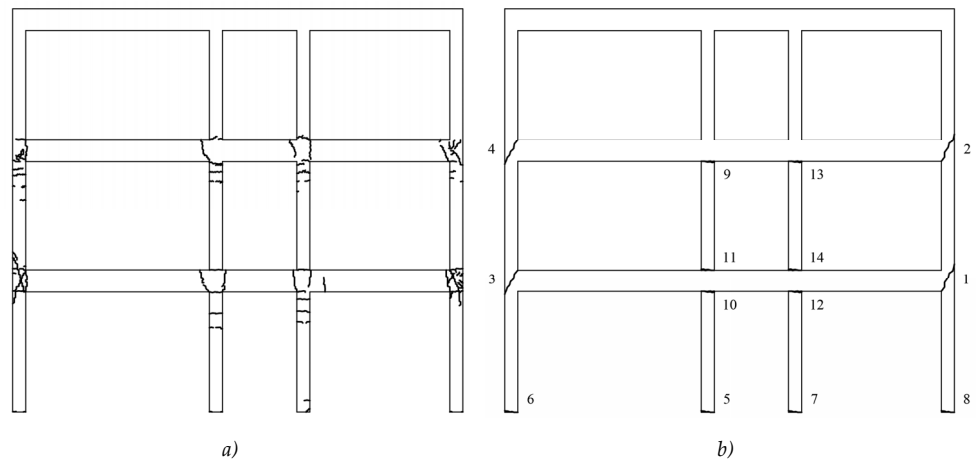

a)   *b)*

Figure 190: Comparison between the experimentally observed crack pattern (Calvi et al., 2002b, 2001) a), and the numerical hinge activation history b).
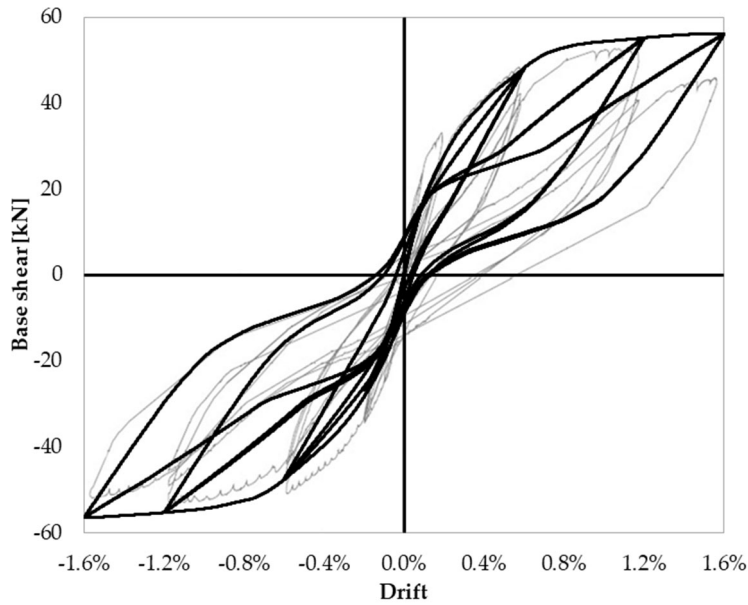
263

Figure 191: Cyclic response of a 3-bays-3-storeys substandard RC frame: experimental (light grey) vs numerical prediction (black line).

Identification of the structural collapse

The maximum interstorey drift demand amounts to 2.30%, in presence of a global drift equal to 1.60%. The peak value is registered at the first interstorey (Figure 188.b) and it is lower than the typical capacity of the column members discussed in the previous Chapter 2. Flexural failure is thus not considered relevant in the frame collapse assessment.

In the following, a focus on the frame monotonic behaviour up to a global drift $\theta = 1.35\%$ is reported. At this imposed deformation level, in the first-floor right edge beam-column joint, the following distortion is reached:

$$\gamma_j \geq 0.015 rad \tag{203}$$

Therefore an Incipient Collapse Limit State can be considered reached (Pampanin et al., 2003). Analogously, it is possible to identify the reach of a Significant Damage Limit State at a global drift magnitude of 1.00% ($\gamma_j = 0.010$). It is worth observing that the experimental response shows a strength decay at a deformation level consistent with the identified Limit States (Figure 188.a). More details about the hinge hysteresis at the reach of the identified Limit States in Appendix C.

7 CONCLUSIONS

The seismic behaviour of existing Gravity Load Designed (GLD) buildings is herein discussed. Specific attention is put on the Reinforced Concrete frame structures built from World War II to the 70's. This type of structure is characterized by a high seismic vulnerability, due to lack in seismic detailing (they were designed according to obsolete Codes). The use of plain reinforcement was common in the reference period. Poor bond capacities of smooth reinforcement significantly affect the seismic response of GLD buildings. With respect to the modern structures reinforced with deformed rebars, the smooth bar slip from both the element and the joint embedded lengths is the cause of lower elastic stiffness. Furthermore, despite the lack in seismic detailing, high deformation capacity is however observed in the frame members. They can reach a drift level higher than 3.00% without significant loss of their resistance. On the other hand, a great vulnerability is due to external T-type beam-column joints, whose panel shear failure is the cause of significant damage and of consequent loss of strength. Nevertheless, a minimum interstorey drift demand of 1.00% is accepted without exhibiting strength decay. It is noteworthy to observe that the above described deformation capacities can be reached only in bare frames. Indeed, the presence of infills often causes the premature brittle failure of RC members due to infill-frame interaction at lower drift levels. Engineered solutions for the infill-frame interaction mitigation were found to be effective in limiting the masonry wall strength and to ensure high deformation capacities. The same can be applied on existing masonry infills.

Due to their very low resistance against seismic action, GLD frames often require strengthening interventions. The introduction of external additional seismic resistant elements (walls or bracings), coupled to the existing structure, is a widespread solution. Indeed, it allows to limit the invasiveness of the interventions and to ensure high strength capacity. Strong and stiff exoskeleton or shear walls can be introduced to limit the deformation demand on the existing frame structures. On the other hand, a detailed design of the strengthening elements can be pursued only if the existing structure capacity is well known, in particular its deformation capacity up to the triggering of local failures.

A model to represent the flexural behaviour of GLD frames is herein presented; it allows to consider the smooth reinforcement slip that develops from both the element and the joint sides, simulating the real structural stiffness and its deformation capacity.

A further focus regards the dowel mechanism behaviour of rebars in the presence of coupled axial and shear action. The aim is to understand the effective strength offered by the sliding resistant mechanism in the presence of cross crack, where the transmission of shear and bending actions is required. The application is useful for

the shear safety check of existing RC members in the load reversal phase (presence of cross cracks). The results of the analysis can be also useful for the control of non-axially loaded RC shear walls, which can be introduced in a retrofitting design of the herein analysed structures.

A first experimental investigation on anchorage performance of straight and shaped smooth rebars is presented. A further test campaign on the dowel behaviour of both smooth and deformed bars is then proposed. Analytical models are defined to represent the experimental evidence; such models are then implemented for the structural modelling of whole GLD RC frames. A comprehensive numerical modelling is finally suggested. It allows to accurately represent the flexural behaviour of the herein studied structures, requiring no empirical calibration. External T-Joint shear behaviour is also considered, with reference to methods available in the literature.

7.1   Experimental evidence

Cyclic tests on anchored smooth rebars

Straight, hook-ended, and 45° bent embedded rebars were tested by the imposition of a cyclic head slip; therefore, both tension and compressive rebar axial stress were investigated.

The anchorage performance of the straight rebars varied as a function of the total embedded length. Cyclic degradation of stiffness and strength was not observed prior to the mobilization of the bond stress on the entire bar length; in other words, prior to bar end slip. At the triggering of the bar tail section movement, a strength decay was noticed. After this, a lower anchorage strength was observed, due to the degradation of the bond performance. The first reloading capacity (at higher slip demand) was higher than the cyclic strength, whose decay with respect to the bond peak bond capacity was represented by a factor slightly lower than 6. The assessed bond strength capacities were consistent with the values available in the literature, despite the latter referred only to short length anchorage. The bar yielding did not seem to affect the bond strength, with respect to the analysed deformation demand (head slip lower than $6mm$). Hook and 45° bent shape were found to be effective in anchoring the bar yielding without exhibiting strength degradation, up to a head slip demand of about $30mm$. The bar hardening was also balanced. The compressive loads caused bar buckling in the presence of a slip demand higher than $15mm$. The cyclic response of the different anchors did not show strength degradation and the unloading stiffness did not significantly vary. The reloading stiffness was secant to the previous reach maximum displacement point; however a reduced stiffness was observed during the reloading in compression.

266

Dowel behaviour in the presence of axial load

The dowel mechanism offered by a reinforcement bar crossing a crack was found to be strongly dependent on the axial stress applied on the same rebar. By increasing the axial load acting in the dowel, the yielding shear load of the mechanism decreased. The influence of the axial stress on the mechanism was non-linear; it increased whit axial stress increasing. After the mechanism yielding, a hardening behaviour was ensured in presence of a tensile load, due to the kinking effect. The hardening branch slope was proportional to the axial load magnitude. Anyway, at a fixed sliding demand, the dowel mechanism strength was always reduced by the applied axial load. An analytical based model is developed to represent the experimental observed force-sliding behaviour, in terms of both stiffness and strength capacities in the elastic and plastic field.

7.2 *Effectiveness of the proposed modelling technique*

Different analytical models are herein defined to represent the stress-slip behaviour of both a straight and a hooked anchorage of plain rebars. The former is based on the definition of an equivalent bond stress profile, which balances the applied axial stress on a certain straight length. It also accounts for the cyclic degradation of the bond strength. The latter considers the force applied on the hooked head balanced by friction stress on the same device length. These friction forces are due to: i) micro-interlocking on the hook bar length, ii) concrete pressure which balances the applied load on the hook inner surface, and iii) the action of the concrete bearing stress due to bar straightening caused by its pull-out. Modified Takeda hysteretic rules are then adopted to simulate the cyclic behaviour of the anchored plain rebars. Their calibration is also analytically based.

A single crack opening at the element-joint interface is assumed to represent the cyclic behaviour of RC substandard members; the base is the experimentally observed rocking behaviour over interfaces of the elements. The contact on the crack sides is simulated by a Beam on Elastic Foundation (BEF) model reference, but the employed springs are characterized by an only-compression elastic-plastic behaviour; an incremental damage is also considered through a slip model implementation. Each bar layer crossing the crack is represented by means of a uniaxial element defined by a stress-slip relationship. The latter is based on the analytical based model herein presented, considering both the bar anchorage length in the element and in the joint (or foundation) side.

The effectiveness of the modelling proposal is validated by comparison through the simulation of several experimental tests. Monotonic and cyclic response of single members, beam-column joints, and a whole frame is investigated. The role of different axial loads, element geometries and reinforcement detailing are considered.

267

The numerical results show a good match between the experimental evidence and the predictive behaviour, both in terms of the strength and stiffness assessment. Furthermore, the simulation of the cyclic behaviour shows the ability of the proposal to represent the pinching effect due to the smooth reinforcement slip.

A comparison with the structural response predicted with Code approaches is also presented. The difference in terms of assessed stiffness is wide. In detail, the Code based approach underestimates the deformation capacity of the RC substandard elements in their elastic response. The result is very significant for the retrofitting of a GLD frame. If strengthening elements are coupled to the existing structure, their stiffness governs the overall structural behaviour, and the deformation demand on the whole building. The imposed displacement on the retrofitted structure defines the internal actions in the existing RC elements. The distributions of the actions is controlled by the existing structural stiffness. Higher stiffness is related to higher forces on column and beam elements, and vice versa. The beam-column element shear force is also controlled by the same stiffness parameters. The definition of the real stiffness of RC elements reinforced with smooth rebar is thus of interest, and the herein proposed model could be a valid way to assess it. It is worthy to remember that the proposal is phenomenologically based, so not requiring empirical or numerical calibration, therefore, it can be considered reliable for the analysis of a general structural configuration, at least for the range of structural types and geometry analysed in the research.

7.3   Recommendations for the future works

Experimental tests

The empirical evidence herein presented about the anchorage performance of smooth rebar are referred to a low number of tested specimens. Further investigation on the monotonic and cyclic behaviour of straight embedded lengths can help to define the effective bond stress acting on the rebar length. Their distribution along the same can also be defined. More pull-out tests on bent rebar must be performed to further investigate the mechanism governing the response of this type of anchorage. The relative data are also useful for the definition of a stress-slip analytical model for bent rebars.

Definition of a design procedure for the sliding verification of RC elements

A practical design procedure can be defined to express the dowel contribution in the sliding verification of an RC element subjected to cyclic loading. Based on the experimental data herein discussed, a strength dominion could be defined to facilitate the sliding verification. The role of the coupled axial and shear load on the resistant dowel mechanism should be explicit.

Structural assessment

The herein suggested proposal about the numerical modelling is useful for a pushover-based assessment technique or to simulate the static cyclic behaviour of RC structures. Sensitive analyses on reference cases of study can be performed to outline how the typical GLD structural configurations control the design of the strengthening elements added in a retrofitting intervention. Specific attention should be put on the stiffness required for the new elements to guarantee the structural safety and the post-earthquake damage mitigation, limiting the intervention invasiveness and its costs. Implementing the model in an environment capable of representing the dynamic response of the structures, Non-Linear-Time-History-Analysis (NLTHA) can be performed. In this way a detailed study of the structural performance could be done. Fragility functions can help in translating the dynamic structural response in the estimation of the economic loss related to the building vulnerability.

Finally, abacus can be defined to support a preliminary design of strengthening interventions, only with reference to the main structural parameters governing the seismic response. Data about the existing GLD building height and mass can be directly related to the exoskeleton or external shear wall stiffness required to guarantee a specific structural performance.

REFERENCES

ABRAMS, D.P., ANGEL, R., UZARSKI, J., 1996. Out-of-Plane Strength of Unreinforced Masonry Infill Panels. Earthquake Spectra 12, 825–844. https://doi.org/10.1193/1.1585912

ACI COMMITTEE 318, 1999. ACI 318-99. Building Code Requirements for Structural Concrete. American Concrete Institute.

AL-CHAAR, G., ISSA, M., SWEENEY, S., 2002. Behavior of Masonry-Infilled Nonductile Reinforced Concrete Frames. J. Struct. Eng. 128, 1055–1063. https://doi.org/10.1061/(ASCE)0733-9445(2002)128:8(1055)

AL-CHAAR, G., LAMB, G.E., ABRAMS, D.P., 2003. Effect of Openings on Structural Performance of Unreinforced Masonry Infilled Frames 13.

ANIL, Ö., ALTIN, S., 2007. An experimental Study on Reinforced Concrete Partially Infilled Frames. Engineering Structures 29, 449–460. https://doi.org/10.1016/j.engstruct.2006.05.011

ARANI, K.K., MAREFAT, M.S., AMROLLAHI-BIUCKY, A., KHANMOHAMMADI, M., 2010. Experimental Seismic Evaluation of Old Concrete Columns Reinforced by Plain Bars. Struct. Design Tall Spec. Build. 22, 267–290. https://doi.org/10.1002/tal.686

ARANI, K.K., MAREFAT, M.S., DI LUDOVICO, M., PROTA, A., MANFREDI, G., 2013. Hysteretic Cyclic Response of Concrete Columns reinforced with Smooth Bars. Bull Earthquake Eng 11, 2033–2053. https://doi.org/10.1007/s10518-013-9469-9

ASCE, 2007a. ASCE SEI/41: Seismic Rehabilitation of existing buildings.

ASCE, 2007b. ASCE SEI/41: Seismic Rehabilitation of existing buildings - Supplement 1.

ASTERIS, P.G., ANTONIOU, S.T., SOPHIANOPOULOS, D.S., CHRYSOSTOMOU, C.Z., 2011. Mathematical Macromodeling of Infilled Frames: State of the Art. J. Struct. Eng. 137, 1508–1517. https://doi.org/10.1061/(ASCE)ST.1943-541X.0000384

ASTERIS, P.G., CAVALERI, L., DI TRAPANI, F., TSARIS, A.K., 2017. Numerical Modelling of Out-of-Plane Response of Infilled Frames: State of the Art and Future Challenges for the Equivalent Strut Macromodels. Engineering Structures 132, 110–122. https://doi.org/10.1016/j.engstruct.2016.10.012

BERTOLDI, S.H., DECANINI, L.D., GAVARINI, C., 1993. Infilled frame subjected to earthquake action, a simplified model: numerical and experimental comparison (in Italian). Presented at the ANIDIS.

BESCHI, C., RIVA, P., METELLI, G., MEDA, A., 2015. HPFRC Jacketing of Non Seismically Detailed RC Corner Joints. Journal of Earthquake Engineering 19, 25–47. https://doi.org/10.1080/13632469.2014.948646

271

BIOLZI, L., GIURIANI, E., 1990. *Bearing Capacity of a Bar Under Transversal Loads. Materials and Structures 23, 449–456. https://doi.org/10.1007/BF02472028*

BOLIS, VALENTINO, PADERNO, A., METELLI, G., PRETI, M., 2019. *The Masonry Infill "Downgrade" in the Seismic Strengthening of Existing Reinforced Concrete Buildings. Presented at the ANIDIS - L'Ingegneria Sismica in Itali. Ascoli Piceno (AP), p. 7.*

BOLIS, V., PADERNO, A., PRETI, M., 2020. *Experimental Assessment of an Innovative Isolation Technique for the Seismic Downgrade of Existing Masonry Infills. Presented at the IB2MaC 2020, p. 8.*

BOLIS, V., PADERNO, A., PRETI, M., 2019. *Infill With Sliding Panels in Presence of a Full-Height Opening: Experimental In-Plane Response. Engineering Structures 197, 109368. https://doi.org/10.1016/j.engstruct.2019.109368*

BOLIS, V., STAVRIDIS, A., PRETI, M., 2017. *Numerical Investigation of the In-Plane Performance of Masonry-Infilled RC Frames with Sliding Subpanels. J. Struct. Eng. 143, 04016168. https://doi.org/10.1061/(ASCE)ST.1943-541X.0001651*

BRAGA, F., DE CARLO, G., GIGLIOTTI, R., LATERZA, M., 2001. *Bond Modelling in Beam-Column RC Joints in Presence of Smooth Reinforcement. Presented at the Anidis, Matera.*

BRAGA, F., GIGLIOTTI, R., LATERZA, M., 2009. *R/C Existing Structures with Smooth Reinforcing Bars: Experimental Behaviour of Beam-Column Joints Subject to Cyclic Lateral Loads. TOBCTJ 3, 52–67. https://doi.org/10.2174/1874836800903010052*

BRAGA, F., GIGLIOTTI, R., LATERZA, M., D'AMATO, M., KUNNATH, S., 2012. *Modified Steel Bar Model Incorporating Bond-Slip for Seismic Assessment of Concrete Structures. J. Struct. Eng. 138, 1342–1350. https://doi.org/10.1061/(ASCE)ST.1943-541X.0000587*

BRENNA, A., DEI POLI, S., DI PRISCO, M., 1990. *Dowel Action: Some Experimental and Theoretical Results Regarding Special Concretes (in Italian). Studi e Ricerche.*

BUONOPANE, S.G., WHITE, R.N., 1999. *Pseudodynamic Testing of Masonry Infilled Reinforced Concrete Frame. Journal of Structural Engineering 125, 578–589. https://doi.org/10.1061/(ASCE)0733-9445(1999)125:6(578)*

CAIRNS, J., PLIZZARI, G., METELLI, G., 2012. *Proceeding of 4th International Symposium: Bond in concrete 2012: Bond, Anchorages, Detailing. General Aspects of Bonds -Vol.1.*

CALVI, G.M., BOLOGNINI, D., 2001. *Seismic Response of Reinforced Concrete Frames Infilled With Weakly Reinforced Masonry Panels. Journal of Earthquake Engineering 5, 153–185. https://doi.org/10.1080/13632460109350390*

272

CALVI, G.M., BOLOGNINI, D., 1999. *Seismic Response of RC Frames Infilled With Weakly Reinforced Hollow Masonry Panels 182.*

CALVI, G.M., MAGENES, G., PAMPANIN, S., 2002a. *Relevance of Beam-Column Joint Damage and Collapse in RC Frame Assessment. Journal of Earthquake Engineering 6, 75–100. https://doi.org/10.1080/13632460209350433*

CALVI, G.M., MAGENES, G., PAMPANIN, S., 2002b. *Experimental Test on a Three Storey RC Frame Designed for Gravity Only. Proceedings of 12th European Conference on Earthquake Engineering 8.*

CALVI, G.M., MAGENES, G., PAMPANIN, S., 2001. *Studio Sperimentale sulla Risposta Sismica di Edifici a Telaio in Cemento Armato Progettati per Soli Carichi da Gravità 12.*

CARDONE, D., PERRONE, G., 2017. *Damage and Loss Assessment of Pre-70 RC Frame Buildings with FEMA P-58. Journal of Earthquake Engineering 21, 23–61. https://doi.org/10.1080/13632469.2016.1149893*

CAVALERI, L., DI TRAPANI, F., 2015. *Prediction of the Additional Shear Action on Frame Members Due to Infills. Bull Earthquake Eng 13, 1425–1454. https://doi.org/10.1007/s10518-014-9668-z*

CEN EUROCODE 2, 2004. *EN 1992-1-1:2004 Eurocode 2: Design of Concrete Structures : Part 1-1: General Rules and Rules for Buildings.*

CEN EUROCODE 8, 2009. *EN 1998-3:2004 Eurocode 8 (Corrigenda): Design of Structures for Earthquake Resistance - Part 3: Assessment and retrofitting of buildings.*

CEN EUROCODE 8, 2005. *EN 1998-1:2004 Eurocode 8: Design of Structures for Earthquake Resistance - Part 3: Assessment and retrofitting of buildings.*

CIRCOLARE APPLICATIVA NTC, 2019. Circolare 21 Gennaio 2019 n.7 C.S.LL.PP. (in italian).

COSENZA, E., MANFREDI, G., VERDERAME, G.M., 2002. *Seismic Assessment of Gravity Load Designed RC Frames: Critical Issues in Structural Modelling. Journal of Earthquake Engineering 6, 101–122. https://doi.org/10.1080/13632460209350434*

CRISAFULLI, F.J., CARR, A.J., PARK, R., 2000. *Analytical Modelling of Infilled Frame Structrures - A General Review. Bulletin of the New Zealand Society for Earthquake Engineering 33.*

DE RISI, M.T., DEL GAUDIO, C., RICCI, P., VERDERAME, G.M., 2019. *Numerical Modelling of Infilled RC Frames: The Detection of Column Failue Due to Local Shear Interaction. Presented at the Compdyn.*

DECANINI, L.D., DE SORTIS, A., GORETTI, A., LIBERATORE, L., MOLLAIOLI, F., BAZZURRO, P., 2004a. *Performance of Reinforced Concrete Buildings during the 2002*

Molise, Italy, Earthquake. Earthquake Spectra 20, 221–255. https://doi.org/10.1193/1.1765107

DECANINI, L.D., SARAGONI, R., MOLLAIOLI, F., *Mura, A., 2004b. Seismic Performance of Masonry Infilled R/C Frames 15.*

DEI POLI, S., DI PRISCO, M., GAMBAROVA, P.G., *1992. Shear Response, Deformations, and Subgrade Stiffness of a Dowel Bar Embedded in Concrete. ACI Structural Journal 89.*

DEL GAUDIO, C., DE MARTINO, G., DI LUDOVICO, M., MANFREDI, G., PROTA, A., RICCI, P., VERDERAME, G.M., *2017. Empirical Fragility Curves From Damage Data on RC Buildings After the 2009 L'Aquila Earthquake. Bull Earthquake Eng 15, 1425–1450. https://doi.org/10.1007/s10518-016-0026-1*

DI DOMENICO, M., RICCI, P., VERDERAME, G.M., *2020. Experimental Assessment of the Influence of Boundary Conditions on the Out-of-Plane Response of Unreinforced Masonry Infill Walls. Journal of Earthquake Engineering 24, 881–919. https://doi.org/10.1080/13632469.2018.1453411*

DI LUDOVICO, M., VERDERAME, G.M., PROTA, A., MANFREDI, G., COSENZA, E., *2014. Cyclic Behavior of Nonconforming Full-Scale RC Columns. J. Struct. Eng. 140, 04013107. https://doi.org/10.1061/(ASCE)ST.1943-541X.0000891*

DI LUDOVICO, M., VERDERAME, G.M., PROTA, A., MANFREDI, G., COSENZA, E., *2013. Experimental Behavior of Nonconforming RC Columns with Plain Bars under Constant Axial Load and Biaxial Bending. J. Struct. Eng. 139, 897–914. https://doi.org/10.1061/(ASCE)ST.1943-541X.0000703*

DI TRAPANI, F., MACALUSO, G., CAVALERI, L., PAPIA, M., *2015. Masonry Infills and RC Frames Interaction: Literature Overview and State of the Art of Macromodeling Approach. European Journal of Environmental and Civil Engineering 19, 1059–1095. https://doi.org/10.1080/19648189.2014.996671*

DULACSKA, H., *1972. Dowel Action of Reinforcement Crossing Cracks in Concrete. ACI Journal 69.*

EL-ARISS, B., *2007. Behavior of Beams with Dowel Action. Engineering Structures 29, 899–903. https://doi.org/10.1016/j.engstruct.2006.07.008*

EL-DAKHAKHNI, W.W., ELGAALY, M., HAMID, A.A., *2003. Three-Strut Model for Concrete Masonry-Infilled Steel Frames. J. Struct. Eng. 129, 177–185. https://doi.org/10.1061/(ASCE)0733-9445(2003)129:2(177)*

ELIGEHAUSEN, R., POPOV, E.P., BERTERO, V.V., *1983. Local Bond Stress-Slip Relationships of Deformed Bars Under Generalized Excitations 180.*

274

EN 197-1, 2007. EN 197-1:2000/A3, Cement - Part 1: Composition, Specifications and Conformity Criteria for Common Cements.

EN 12350-2, 2009. EN 12350-2 Testing Fresh Concrete - Part 2: Slump Test.

FABBROCINO, G., VERDERAME, G.M., MANFREDI, G., 2005. Experimental behaviour of anchored smooth rebars in old type reinforced concrete buildings. Engineering Structures 27, 1575–1585. https://doi.org/10.1016/j.engstruct.2005.05.002

FABBROCINO, G., VERDERAME, G.M., MANFREDI, G., COSENZA, E., 2004. Structural Models of Critical Regions in Old-Type RC Frames With Smooth Rebars. Engineering Structures 26, 2137–2148. https://doi.org/10.1016/j.engstruct.2004.07.018

FELDMAN, L., BARTLETT, M., 2007. Bond Stresses Along Plain Steel Reinforcing Bars in Pullout Specimens. ACI Structural Journal 104, 685–692.

FELDMAN, L., BARTLETT, M., 2005. Bond Strength Variability in Pullout Specimens with Plain Reinforcement. ACI Structural Journal.

FEMA 273, 1997. NEHRP Guidelines for the Seismic Rehabilitation of Buildings.

FEMA E-74, 2015. Reducing the RIsk of Nonstructural Earthquake Damage - A Practical Guide, Fourth Edition.

FERNANDES, C., MELO, J., VARUM, H., COSTA, A., 2011. Cyclic Behavior of a Two-Span RC Beam Built with Plain Reinforcing Bars. Per. Pol. Civil Eng. 55, 21. https://doi.org/10.3311/pp.ci.2011-1.03

FILIPPOU, F.C., POPOV, E.P., BERTERO, V.V., 1983. Effects of Bond Deterioration on Hysteretic Behavior of Reinforced Concrete Joints.

FIORATO, A.E., SOZEN, M.A., GAMBLE, W.L., 1970. An Investigation of the Interaction of Reinforced Concrete Frames With Masonry Filler Walls.

FLANAGAN, R.D., BENNETT, R.M., 1999. In-Plane Behavior of Structural Clay Tile Infilled Frames. Journal of Structural Engineering 125, 590–599. https://doi.org/10.1061/(ASCE)0733-9445(1999)125:6(590)

FURTADO, A., RODRIGUES, H., ARÊDE, A., VARUM, H., 2016. Experimental Evaluation of Out-of-Plane Capacity of Masonry Infill Walls. Engineering Structures 111, 48–63. https://doi.org/10.1016/j.engstruct.2015.12.013

GAMBAROVA, P., PLIZZARI, G., BALAZS, G., 2000. Bond mechanics including pull-out and splitting failures. In fib Bulletin 10: Bond of Reinforcement in Concrete. (pp. 1–98).

GELFI, P., GIURIANI, E., 1987. Theoretical Constitutive Law for Dowel Connections (in Italian). Studi e Ricerche 9.

GHOSH, A.K., AMDE, A.M., 2002. Finite Element Analysis of Infilled Frames. J. Struct. Eng. 128, 881–889. https://doi.org/10.1061/(ASCE)0733-9445(2002)128:7(881)

GIURIANI, E., 2012. Strengthening of historical buildings (in Italian). UTET.

GODA, K., KIYOTA, T., POKHREL, R.M., CHIARO, G., KATAGIRI, T., SHARMA, K., WILKINSON, S., 2015. The 2015 Gorkha Nepal Earthquake: Insights from Earthquake Damage Survey. Front. Built Environ. 1. https://doi.org/10.3389/fbuil.2015.00008

HAK, S., MORANDI, P., MAGENES, G., SULLIVAN, T.J., 2012. Damage Control for Clay Masonry Infills in the Design of RC Frame Structures. Journal of Earthquake Engineering 16, 1–35. https://doi.org/10.1080/13632469.2012.670575

HASELTON, C.B., LIEL, A.B., LANGE, S.T., DEIERLEIN, G.G., 2008. Beam-Column Element Model Calibrated for Predicting Flexural Response Leading to Global Collapse of RC Frame Buildings.

HASHEMI, A., MOSALAM, K.M., 2006. Shake-Table Experiment on Reinforced Concrete Structure Containing Masonry Infill Wall. Earthquake Engng Struct. Dyn. 35, 1827–1852. https://doi.org/10.1002/eqe.612

HE, X.G., KWAN, A.K.H., 2001. Modeling Dowel Action of Reinforcement Bars for Finite Element Analysis of Concrete Structures. Computers and Structures 10.

HOFBECK, J.A., IBRAHIM, I.O., MATTOCK, A.H., 1969. HShear Transfer in Reinfroced Concrete. ACI Journal 66.

HWANG, S.-J., LEE, H.-J., 2002. Strength Prediction for Discontinuity Regions by Softened Strut-and-Tie Model. Journal of Structural Engineering 128, 1519–1526. https://doi.org/10.1061/(ASCE)0733-9445(2002)128:12(1519)

HWANG, S.-J., LEE, H.-J., 2000. Analytical Model for Predicting Shear Strengths of Interior Reinforced Concrete Beam-Column Joints for Seismic Resistance. ACI Structural Journal 47, 35–44.

HWANG, S.-J., LEE, H.-J., 1999. Analytical Model for Predicting Shear Strengths of Exterior Reinforced Concrete Beam-Column Joints for Seismic Resistance. SJ 96. https://doi.org/10.14359/739

ILKI, A., DEMIR, C., BEDIRHANOGLU, I., KUMBASAR, N., 2009. *Seismic Retrofit of Brittle and Low Strength RC Columns Using Fiber Reinforced Polymer and Cementitious Composites. Advances in Structural Engineering 12, 325–347.* https://doi.org/10.1260/136943309788708356

ISTAT, 2011. *Censimento della Popolazione e delle Abitazioni.*

KAKALETSIS, D., KARAYANNIS, C., 2007. *Experimental Investigation of Infilled RC Frames with Eccentric Openings. Structural Engineering and Mechanics 26, 231–250.* https://doi.org/10.12989/SEM.2007.26.3.231

KAPPOS, A.J., 2000. *Seismic Design and Performance Assessment of Masonry Infilled RC Frames, in: Proc., 12th World Conf. on Earthquake Engineering, International Association of Earthquake Engineering (IAEE), Tokyo.*

KOSE, M.M., 2009. *Parameters Affecting the Fundamental Period of RC Buildings with Infill Walls. Engineering Structures 31, 93–102.* https://doi.org/10.1016/j.engstruct.2008.07.017

LATERZA, M., D'AMATO, M., GIGLIOTTI, R., 2017. *Modeling of Gravity-Designed RC Sub-Assemblages Subjected to Lateral Loads. Engineering Structures 130, 242–260.* https://doi.org/10.1016/j.engstruct.2016.10.044

LIAUW, T.C., KWAN, K.H., 1983. *Plastic Theory of Non-integral Infilled Frames. Proc. Inst. Civ. Eng. 379–396.*

LOWES, L.N., ALTOONTASH, A., 2003. *Modeling Reinforced-Concrete Beam-Column Joints Subjected to Cyclic Loading. Journal of Structural Engineering 129, 1686–1697.* https://doi.org/10.1061/(ASCE)0733-9445(2003)129:12(1686)

MAEKAWA, K., QURESHI, J., 1997. *Stress Transfer Across Interfaces in RC Due to Aggregate Interlock and Dowel Action 14.*

MAEKAWA, K., QURESHI, J., 1996a. *Embedded Bar Behavior in Concrete Under Axial Pullout and Tansverse Displacement 13.*

MAEKAWA, K., QURESHI, J., 1996b. *Computational Model for Reinforcing Bar Embedded in Concrete Under Combined Axial Pullout and Transverse Displacement 13.*

MAGONETTE, G., NEGRO, P., MOLINA, J., MOLA, E., 2004. *Full-Scale Psd Testing of a Torsionally Unbalanced Three-Storey Non-Seismic RC Frame. Proceeding of 13th World Conference on Earthquake Engineering 16.*

MAINSTONE, R.J., WEEKS, G.A., 1970. *The Influence of a Bounding Frame on the Racking Stiffnesses and Strengths of Brick Walls 7.*

MANFREDI, G., PECCE, M., 1998. *A refined RC Beam Element Including Bond-Slip Relationship for the Analysis of Continuous Beams. Computers and Structures 10.*

MAREFAT, M.S., HASSANZADEH SHIRAZI, S.M., ROSTAMSHIRAZI, R., KHANMOHAMMADI, M., 2009. Cyclic Response of Concrete Beams Reinforced by Plain Bars. Journal of Earthquake Engineering 13, 463–481. https://doi.org/10.1080/13632460902837769

*Gli aggiornamenti automatici delle citazioni sono disabilitati. Per vedere la bibliografia clicca "Ricarica" nel tab di Zotero.**MASI, A., SANTARSIERO, G., NIGRO, D.**, 2013. Cyclic Tests on External RC Beam-Column Joints: Role of Seismic Design Level and Axial Load Value on the Ultimate Capacity. Journal of Earthquake Engineering 17, 110–136. https://doi.org/10.1080/13632469.2012.707345*

MCKENNA, F., FENVES, G., FILIPPOU, F.C., 2000. Open System for Earthquake Engineering Simulation (OpenSees).

MEHARBI, A.B., SHING, P.B., 2003. Seismic Analysis of Masonry-Infilled Reinforced Concrete Frames 14.

MEHRABI, A.B., BENSON SHING, P., SCHULLER, M.P., NOLAND, J.L., 1996. Experimental Evaluation of Masonry-Infilled RC Frames. Journal of Structural Engineering 122, 228–237. https://doi.org/10.1061/(ASCE)0733-9445(1996)122:3(228)

MELO, J., FERNANDES, C., VARUM, H., RODRIGUES, H., COSTA, A., ARÊDE, A., 2011. Numerical Modelling of the Cyclic Behaviour of RC Elements Built with Plain Reinforcing Bars. Engineering Structures 33, 273–286. https://doi.org/10.1016/j.engstruct.2010.11.005

MELO, J., VARUM, H., ROSSETTO, T., 2015. Experimental Cyclic Behaviour of RC Columns with Plain Bars and Proposal for Eurocode 8 Formula Improvement. Engineering Structures 88, 22–36. https://doi.org/10.1016/j.engstruct.2015.01.033

MERGOS, P.E., KAPPOS, A.J., 2012. A Gradual Spread Inelasticity Model for R/C Beam–Columns, Accounting for Flexure, Shear and Anchorage Slip. Engineering Structures 44, 94–106. https://doi.org/10.1016/j.engstruct.2012.05.035

MERGOS, P.E., KAPPOS, A.J., 2008. A Distributed Shear and Flexural Flexibility Model with Shear-Flexure Interaction for RC Members Subjected to Seismic Loading. Earthquake Engng Struct. Dyn. 37, 1349–1370. https://doi.org/10.1002/eqe.812

METELLI, G., MESSALI, F., BESCHI, C., RIVA, P., 2015. A Model for Beam–Column Corner Joints of Existing RC Frame Subjected to Cyclic Loading. Engineering Structures 89, 79–92. https://doi.org/10.1016/j.engstruct.2015.01.038

MODEL CODE, 2010. Model Code for Concrete Structures 2010 fib – International Federation for Structural Concrete).

MODEL CODE, 1990. CEB-FIP Model Code 1990. Design Code-Comite Euro-International du Beton.

278

MOHYEDDIN, A., GOLDSWORTHY, H.M., GAD, E.F., 2013. *FE Modelling of RC Frames with Masonry Infill Panels under In-Plane and Out-of-Plane Loading. Engineering Structures 51, 73–87. https://doi.org/10.1016/j.engstruct.2013.01.012*

MONTI, G., SPACONE, E., 2000. *Reinforced Concrete Fiber Beam Element with Bond-Slip. J. Struct. Eng. 126, 654–661. https://doi.org/10.1061/(ASCE)0733-9445(2000)126:6(654)*

MORADI, A.R., SOLTANI, M., TASNIMI, A.A., 2012. *A Simplified Constitutive Model for Dowel Action across RC Cracks. ACT 10, 264–277. https://doi.org/10.3151/jact.10.264*

NORME TECNICHE PER LE COSTRUZIONI, 2018. *Decreto Ministeriale 17 Gennaio 2018 - Norme Tecniche per le Costruzioni (in Italian). Ministero delle Infrastrutture (in italian).*

NZS 3101, 1995. *NZS 3101 - Design of concrete structures. Associations of New Zealand.*

O'REILLY, G.J., SULLIVAN, T.J., 2017. *Modeling Techniques for the Seismic Assessment of the Existing Italian RC Frame Structures. Journal of Earthquake Engineering 23, 1262–1296. https://doi.org/10.1080/13632469.2017.1360224*

PAMPANIN, S., CALVI, G.M., MORATTI, M., 2002. *Seismic Behaviour of RC Beam-Column Joints Designed for Gravity Loads 11.*

PAMPANIN, S., MAGENES, G., CARR, A., 2003. *Modelling of Shear Hinge Mechanism in Poorly Detailed RC Beam-Column Joints. Concrete Structures in Seismic Regions, Athens, Greece.*

PAOLACCI, F., GIANNINI, R., 2012. *An Experimental and Numerical Investigation on the Cyclic Response of a Portal Frame Pier Belonging to an Old Reinforced Concrete Viaduct. Earthquake Engng Struct. Dyn. 41, 1109–1127. https://doi.org/10.1002/eqe.1175*

PAULAY, T., PRIESTLEY, M.J.N., 1992. *Seismic Design Of Reinforced Concrete And Masonry Buildings.*

PETRANGELI, M., PINTO, P.E., CIAMPI, V., 1999. *Fiber Element for Cyclic Bending and Shear of RC Structures. I: Theory. Journal of Engineering Mechanics 125, 994–1001. https://doi.org/10.1061/(ASCE)0733-9399(1999)125:9(994)*

POLESE, M., DI LUDOVICO, M., MARCOLINI, M., PROTA, A., MANFREDI, G., 2015. *Assessing Reparability: Simple Tools for Estimation of Costs and Performance Loss of Earthquake Damaged Reinforced Concrete Buildings. Earthquake Engng Struct. Dyn. 44, 1539–1557. https://doi.org/10.1002/eqe.2534*

POLYAKOV, S.V., 1960. *On the Interaction Between Masonry Filler Walls and ENclosing Frame when Loading in the Plane of the Wall. EERI.*

POPOV, E.P., 1984. *Bond and Anchorage of Reinfrocing Bars Under Cyclic Loading.*

PRAKASH, V., POWELL, G.H., CAMPBELL, S., *1993. DRAIN-2DX Base Programm Description and User Guide-Version 1.10.*

PRETI, M., BETTINI, N., PLIZZARI, G., *2012. Infill Walls with Sliding Joints to Limit Infill-Frame Seismic Interaction: Large-Scale Experimental Test. Journal of Earthquake Engineering 16, 125–141. https://doi.org/10.1080/13632469.2011.579815*

PRETI, M., BOLIS, V., *2017. Masonry Infill Construction and Retrofit Technique for the Infill-Frame Interaction Mitigation: Test Results. Engineering Structures 12.*

PRETI, M., MIGLIORATI, L., GIURIANI, E., *2014. Experimental Testing of Engineered Masonry Infill Walls for Post-Earthquake Structural Damage Control. Bull Earthquake Eng 23.*

PRIESTLEY, M.J.N., *1997. Displacement-Based Seismic Assessment of Reinforced Concrete Buildings. Journal of Earthquake Engineering 1, 157–192.*

PRIESTLEY, M.J.N., *Calvi, G.M., Kowalsky, M.J., 2007. Displacement Based Seismic Design of Structures, IUSS Press. ed.*

PRIESTLEY, M.J.N., VERMA, R., XIAO, Y., *1994. Seismic Shear Strength of Reinforced Concrete Columns. Journal of Structural Engineering 120, 2310–2329. https://doi.org/10.1061/(ASCE)0733-9445(1994)120:8(2310)*

RASMUSSEN, B.H., *1963. The Carrying Capacity of Transversely Loaded Bolts and Dowels Embedded in Concrete. Bygningsstatiske Meddelser 34.*

RD 2229, *1939. Regio Decreto n.2229 del 19 Novembre 1939 (in italian).*

RICCI, P., DI DOMENICO, M., VERDERAME, G.M., *2018. Empirical-Based Out-of-Plane URM Infill Wall Model Accounting for the Interaction with In-Plane Demand. Earthquake Engng Struct Dyn 47, 802–827. https://doi.org/10.1002/eqe.2992*

RICCI, P., VERDERAME, G.M., MANFREDI, G., *2013. ASCE/SEI 41 Provisions on Deformation Capacity of Older-Type Reinforced Concrete Columns with Plain Bars. J. Struct. Eng. 139, 04013014. https://doi.org/10.1061/(ASCE)ST.1943-541X.0000701*

RUSSO, G., PAULETTA, M., 2012. *Seismic Behavior of Exterior Beam-Column Connections with Plain Bars and Effects of Upgrade. SJ 109. https://doi.org/10.14359/51683633*

SANEINEJAD, A., HOBBS, B., *1995. Inelastic Design of Infilled Frames. Journal of Structural Engineering 121, 634–650. https://doi.org/10.1061/(ASCE)0733-9445(1995)121:4(634)*

SANTARELLA, L., *1956. Il Cemento Armato - La Tecnicha e la Statica (in Italian). Hoepli.*

SASSUN, K., SULLIVAN, T.J., MORANDI, P., CARDONE, D., 2016. *Characterising the In-Plane Seismic Performance of Infill Masonry. BNZSEE 49, 98–115. https://doi.org/10.5459/bnzsee.49.1.98-115*

SHARMA, A., ELIGEHAUSEN, R., REDDY, G.R., 2011. *A New Model to Simulate Joint Shear Behavior of Poorly Detailed Beam–Column Connections in RC Structures Under Seismic Loads, Part I: Exterior joints. Engineering Structures 33, 1034–1051. https://doi.org/10.1016/j.engstruct.2010.12.026*

SHIMA, H., CHOU, L., OKAMURA, H., 1987. *Micro and Macro Model for Bond Behaviour in Reinforced Concrete. Journal of the Faculty of Engineering, University of Tokio 39.*

SOLTANI, M., MAEKAWA, K., 2008. *Path-Dependent Mechanical Model for Deformed Reinforcing Bars at RC Interface Under Coupled Cyclic Shear and Pullout Tension. Engineering Structures 30, 1079–1091. https://doi.org/10.1016/j.engstruct.2007.06.013*

SOROUSHIAN, P., OBASEKI, K., ROJAS, M.C., 1987. *Bearing Strength and Stiffness of Concrete Under Reinforcing Bars. ACI Materials Journal 8.*

SOROUSHIAN, P., OBASEKI, K., ROJAS, M.C., JONGSUNG, S., 1986. *Analysis of Dowel Bars Acting Against Concrete Core. ACI Journal 83.*

SPACONE, E., FILIPPOU, F.C., TAUCER, F.F., 1996. *Fibre Beam–Column Model for Non-Linear Analysis of RC Frames: Part I: Formulation. LINEAR ANALYSIS 15.*

STAFFORD-SMITH, B., 1967. *The Composite Behaviour of Infilled Frames, in: Tall Buildings. pp. 465–480. https://doi.org/10.1016/B978-0-08-011692-1.50026-2*

STAFFORD-SMITH, B., 1962. *Lateral Stiffness of Infilled Frames. J. Struct. Div. ASCE 183–199.*

STAVRIDIS, A., KOUTROMANOS, I., SHING, P.B., 2012. *Shake-Table Tests of a Three-Story Reinforced Concrete Frame With Masonry Infill Walls. Earthquake Engng Struct. Dyn. 41, 1089–1108. https://doi.org/10.1002/eqe.1174*

SURENDRAN, S., 2012. *Masonry Infill RC Frames with Openings: Review of In-plane Lateral Load Behaviour and Modeling Approaches. TOBCTJ 6, 126–154. https://doi.org/10.2174/1874836801206010126*

TIMOSHENKO, S., LESSELS, J.M., 1925. *Applied Elasticity. Westinghouse Technical Night School Press.*

UNI EN 206, 2016. *UNI EN 206:2016 Concrete - Specification, Performance, Production and Conformity Criteria.*

UNI EN 10025-2, 2005. *UNI EN 10025-2:2005 Prodotti lamianti a Caldo di Acciai per Impieghi Strutturali - Parte2: Condizioni Tecniche (in Italian).*

UNI EN 10080, 2005. UNI EN 10080 Steel for the Reinforcement of Concrete - Weldable Reinforcing Steel.

UNI EN 12390-3, 2003. UNI EN 12390-3 Testing Hardened Concrete - Compressive Strength of Test Specimens.

UNI EN 12390-13, 2013. UNI EN 12390-13 Testing Hardened Concrete - Determination of Secant Modulus of Elasticity in Compression.

VECCHIO, F.J., COLLINS, M.P., 1986. The Modified Compression Field Theory for Reinforced Concrete Elements Subjected to Shear.

VERDERAME, G.M., DE CARLO, G., RICCI, P., FABBROCINO, G., 2009a. Cyclic Bond Behaviour of Plain Bars. Part II: Analytical Investigation. Construction and Building Materials 23, 3512–3522. https://doi.org/10.1016/j.conbuildmat.2009.07.001

VERDERAME, G.M., FABBROCINO, G., MANFREDI, G., 2008a. Seismic Response of RC Columns with Smooth Reinforcement. Part I: Monotonic Tests. Engineering Structures 30, 2277–2288. https://doi.org/10.1016/j.engstruct.2008.01.025

VERDERAME, G.M., FABBROCINO, G., MANFREDI, G., 2008b. Seismic Response of RC Columns with Smooth Reinforcement. Part II: Cyclic Tests. Engineering Structures 30, 2289–2300. https://doi.org/10.1016/j.engstruct.2008.01.024

VERDERAME, G.M., IERVOLINO, I., RICCI, P., 2009c. Report on the Damages on Buildings Following the Seismic Event of 6th of April 2009 Time 1.32 (UTC) – L'Aquila M=5.8 17.

VERDERAME, G.M., RICCI, P., CARLO, G.D., MANFREDI, G., 2009b. Cyclic Bond Behaviour of Plain Bars. Part I: Experimental Investigation. Construction and Building Materials 23, 3499–3511. https://doi.org/10.1016/j.conbuildmat.2009.07.002

VERDERAME, G.M., RICCI, P., ESPOSITO, M., SANSIVIERO, F.C., 2001. Mechanical Properties of Reinforcement Used for RC Constructions from 1950 to 1980 (in Italian). 10th national conference "L'Ingegneria Sismica in Italia" 8.

VERDERAME, G.M., RICCI, P., MANFREDI, G., COSENZA, E., 2010. Ultimate Chord Rotation of RC Columns With Smooth Bars: Some Considerations About EC8 Prescriptions. Bull Earthquake Eng 8, 1351–1373. https://doi.org/10.1007/s10518-010-9190-x

VINTZĒLEOU, E.N., TASSIOS, T.P., 1987. Behavior of Dowels Under Cyclic Deformations. ACI Structural Journal 84.

VINTZĒLEOU, E.N., TASSIOS, T.P., 1986. Mathematical Models for Dowel Action Under Monotonic and Cyclic Conditions. Magazine of Concrete Research 38, 13–22. https://doi.org/10.1680/macr.1986.38.134.13

WALRAVEN, J.C., REINHARDT, H.W., *1981. Theory and Experiment on the Mechanical Behaviour of Cracks in Plain and Reinforced Concrete Subjected to Shear Loading. HERON Journal 26.*

WOOD, R.H., *1978. Plasticity, Composite Action and Collapse Design of Unreinforced Shear Wall Panels in Frames. Proc. Inst. Civ. Eng. Part 2, 381–411.*

XU, L., HAI, T.K., KING, L.C., *2014. Bond Stress-Slip Prediction under Pullout and Dowel Action in Reinforced Concrete Joints. ACI Structural Journal 111. https://doi.org/10.14359/51686816*

YALCIN, C., KAYA, O., SINANGIL, M., *2008. Seismic Retrofitting of R/C Columns Having Plain Rebars Using CFRP Sheets for Improved Strength and Ductility. Construction and Building Materials 22, 295–307. https://doi.org/10.1016/j.conbuildmat.2006.08.017*

ZARNIC, R., GOSTI, S., CREWE, A.J., TAYLOR, C.A., *2001. Shaking Table Tests of 1:4 Reduced-Scale Models of Masonry Infilled Reinforced Concrete Frame Buildings. Earthquake Engng. Struct. Dyn. 30, 819–834. https://doi.org/10.1002/eqe.39*

ZIMOS, D.K., MERGOS, P.E., KAPPOS, A.J., *2018. Modelling of R/C Members Accounting for Shear Failure Localisation: Hysteretic Shear Model. Earthquake Engng Struct Dyn 47, 1722–1741. https://doi.org/10.1002/eqe.3037*

283

APPENDIX A.   NUMERICAL TOOLS FOR THE STRESS-SLIP RELATIONSHIP DEFINITION

For the numerical implementation of the stress-slip relationships herein described, a reference hysteretic behaviour must be defined. OpenSees (McKenna et al., 2000) Hysteretic material is considered; the definition of both its skeleton curve and its cyclic behaviour is herein treated. A three-linear envelope characterizes the material behaviour, on the other hand, a secant unloading stiffness is considered. The reference is to the analytical model, previously discussed (Section 5.2 for the monotonic behaviour, and Section 5.3 for the cyclic one). In the following, the definition of the numerical laws used for the representation of the smooth bar behaviour is presented, on the bases of what is discussed in the previous Section 5.6.

A.1.   *Approach to the calculation*

Only a crack side anchorage behaviour is herein treated, with reference to a straight bar or a hook-ended one. Different behaviours are identified, depending on the bond performance and on the straight embedded length (Figure 192):

- ▪ Case A: bar yielding stress balanced on the straight length;
- ▪ Case B: bar yielding stress balanced with hook activation;
- ▪ Case C: bar failure stress balanced on the straight length;
- ▪ Case D: bar failure stress balanced with elastic hook;
- ▪ Case E: bar failure stress balanced with hook stress beyond the yielding point.

To define the envelope of the reference backbone curve, three reference points must be defined. Their significance is summarized in the map of Figure 193.
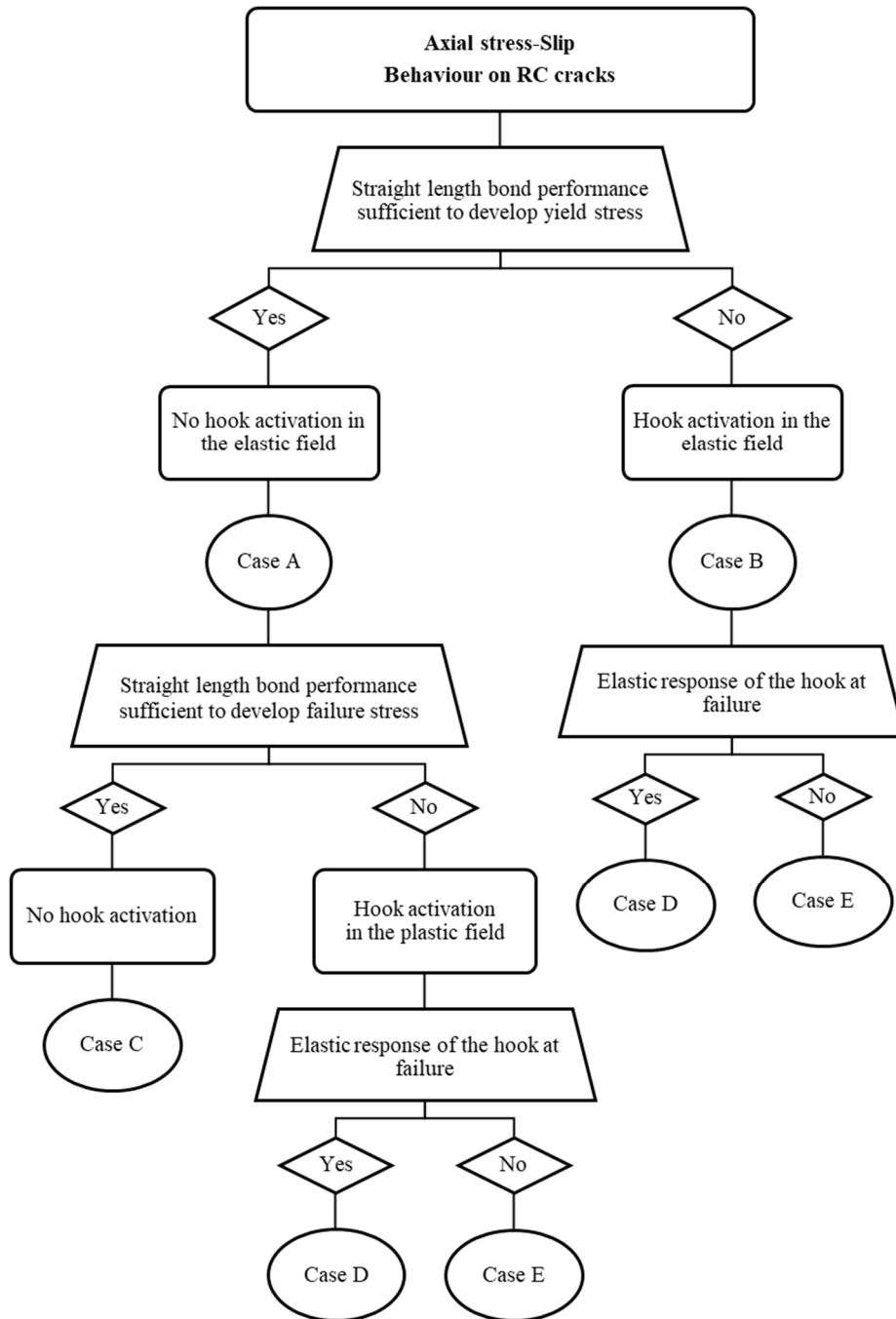
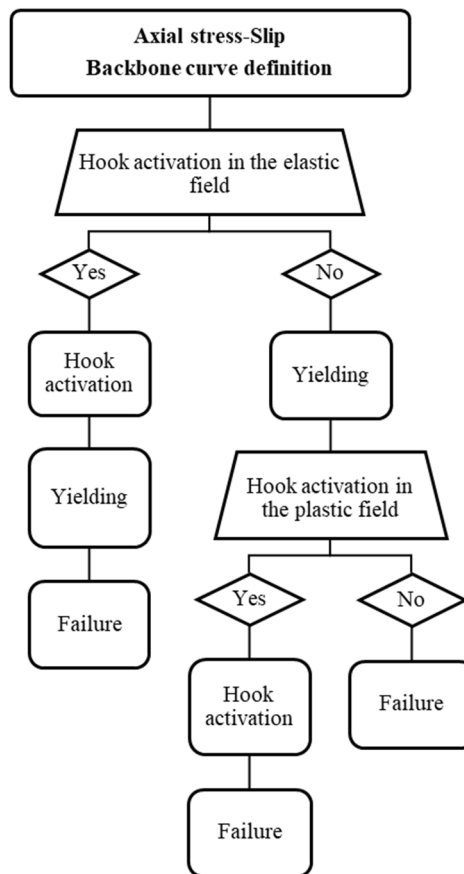*Figure 192: Smooth rebar anchorage scenarios.*

Figure 193: Reference points for the numerical definition of the three-linear backbone curve used in the representation of a smooth rebar anchorage in presence (or not) of a hook-end device.

A.2.   *Matlab functions*

The mathematical formulation of the stress-slip couples identifying the three reference points above mentioned is herein presented. Firstly, the definition of the hook device stress-slip behaviour is proposed. In a second moment, the general definition of the reference three-linear stress-slip behaviour is treated.

Hook stress-slip behaviour

```
function [stress, slip_el, slip_pl, slip] = AH (db_1, db_2, nb_1, nb_2, fy_1, fy_2, fu_1, fu_2, fc)

% ----------
% HYPOTHESIS

% Steel modulus
Es=200000;
Eh=Es/100;

% Concrete bearing strength
fcc=5*fc;

% Concrete steel friction
mu=0.40;

% Bond capacities
tb_p=0.3*sqrt(fc);
tb_c=0.05*sqrt(fc);
tb_u=tb_c;
tb_f=mu*fcc;

% Reference geometry
Di=5; % Moltiplication factor for hook arch length inner diameter
Le=3; % Moltiplication factor for hook straight end length


% ----------------
% DATA ELABORATION

% Service parameters
pi=acos(-1);

% Reinforcement amount
As1=nb_1*pi/4*db_1^2;
As2=nb_2*pi/4*db_2^2;
As=As1+As2;

% Reinforcement medium mechanical parameters
db=(db_1*nb_1+db_2*nb_2)/(nb_1+nb_2);
fy=(As1*fy_1+As2*fy_2)/(As);
fy=round(fy);
fu=(As1*fu_1+As2*fu_2)/(As);
fu=round(fu);

% Empty vector for hook stress-slip backbone behaviour
stress=linspace(1,fu,fu);
stress=stress';
slip_el=zeros(fu,1);
```

```
slip_pl=zeros(fu,1);
sigmaB=zeros(fu,1);
sigmaC=zeros(fu,1);
sigmaD=zeros(fu,1);
sigmaE=zeros(fu,1);
sigma_ch=zeros(fu,1);


% ----------------------------
% PHASE 1 (Head plasticization)

% Reference dowel length
Leff0=db*sqrt(2*fy/(3*fcc));

% Initial plastic slip
Ds=0;

% Progressive stress calculation
for sigmaH=1:fu
   % Stress calculation in the hook head
   lamh=sigmaH/fy;
   if lamh<=1
      Leffh=Leff0*sqrt((1-lamh^2));
   else
      Leffh=0;
   end
   LAH_pl=min(Leff0, max(0,sigmaH-fy)*pi*db/(4*tb_f));
   LAH_el=min(Leff0-LAH_pl, min(sigmaH,fy)*pi*db/(4*tb_f));
   sigmaH_corr=sigmaH-4*tb_f*(LAH_el+LAH_pl)/(pi*db);
   % Slip calculation on AH length
   sAH_el=min(sigmaH_corr,fy)*LAH_el/Es+2*tb_f*LAH_el^2/(Es*pi*db);
   sAH_pl=max(sigmaH_corr-fy,0)*LAH_pl/Eh+2*tb_f*LAH_pl^2/(Eh*pi*db);
   % Slip calculation on HB length
   LHB_pl=min(Leff0, max(0,sigmaH_corr-fy)*pi*db/(4*(tb_f+pi*tb_u)));
   LHB_el=min(Leff0-LHB_pl, min(sigmaH_corr,fy)*pi*db/(4*(tb_f+pi*tb_p)));
   sigmaBi=sigmaH_corr-4*(tb_f+pi*tb_p)*LHB_el/(pi*db)-4*(tb_f+pi*tb_u)*LHB_pl/(pi*db);
   sHB_el=min(sigmaBi,fy)*LHB_el/Es+2*tb_f*LHB_el^2/(Es*pi*db)+2*tb_p*LHB_el^2/(Es*db);
   sHB_pl=max(sigmaBi-
fy,0)*LHB_pl/Eh+2*tb_f*LHB_pl^2/(Eh*pi*db)+2*tb_u*LHB_pl^2/(Eh*db);
   % Plastic slip addiction
   DLeff=Leff0-Leffh;
   Ds=Ds+2*DLeff/Eh;
   % Concrete stress on the arch length
   sigma_chi=sigmaH_corr*pi*db^2/4/(Di*db^2);
   % Matrix allocation
   slip_el(sigmaH)=sAH_el+sHB_el;
   slip_pl(sigmaH)=sAH_pl+sHB_pl+Ds;
   sigmaB(sigmaH)=sigmaBi;
   sigma_ch(sigmaH)=sigma_chi;
end
```

```
% ---------------------------------
% PHASE 2 (Friction on arch length)

% Reference length
LBDmax=pi*(Di+1)/2*db-2*Leff0;

% Progressive stress calculation
for sigmaH=1:fu
    % Contact friction stress
    tb_fc=sigma_ch(sigmaH)*mu;
    % Slip calculation on BD length
    LBD_pl=min(LBDmax, max(0,sigmaB(sigmaH)-fy)*pi*db/(4*(tb_fc+pi*tb_u)));
    LBD_el=min(LBDmax-LBD_pl, min(sigmaB(sigmaH),fy)*pi*db/(4*(tb_fc+pi*tb_p)));
    sigmaDi=sigmaB(sigmaH)-4*(tb_fc+pi*tb_p)*LBD_el/(pi*db)-4*(tb_fc+pi*tb_u)*LBD_pl/(pi*db);
    sBD_el=min(sigmaDi,fy)*LBD_el/Es+2*tb_fc*LBD_el^2/(Es*pi*db)+2*tb_p*LBD_el^2/(Es*db);
    sBD_pl=max(sigmaDi-
fy,0)*LBD_pl/Eh+2*tb_fc*LBD_pl^2/(Eh*pi*db)+2*tb_u*LBD_pl^2/(Eh*db);
    % Matrix allocation
    slip_el(sigmaH)=slip_el(sigmaH)+sBD_el;
    slip_pl(sigmaH)=slip_pl(sigmaH)+sBD_pl;
    sigmaD(sigmaH)=sigmaDi;
end


% ---------------------------------------
% PHASE 3 (Arch length end plasticization)

% Initial plastic slip
Ds=0;

% Progressive stress calculation
for sigmaH=1:fu
    % Stress calculation on hook arch length end
    LDT_pl=min(Leff0, max(0,sigmaD(sigmaH)-fy)*pi*db/(4*(tb_f+pi*tb_u)));
    LDT_el=min(Leff0-LDT_pl, min(sigmaD(sigmaH),fy)*pi*db/(4*(tb_f+pi*tb_p)));
    sigmaT=sigmaD(sigmaH)-4*(tb_f+pi*tb_p)*LDT_el/(pi*db)-4*(tb_f+pi*tb_u)*LDT_pl/(pi*db);
    lamt=sigmaT/fy;
    if lamt<=1
        Lefft=Leff0*sqrt((1-lamt^2));
    else
        Lefft=0;
    end
    % Slip calculation on DT length
    sDT_el=min(sigmaT,fy)*LDT_el/Es+2*tb_f*LDT_el^2/(Es*pi*db)+2*tb_p*LDT_el^2/(Es*db);
    sDT_pl=max(sigmaT-fy,0)*LDT_pl/Eh+2*tb_f*LDT_pl^2/(Eh*pi*db)+2*tb_u*LDT_pl^2/(Eh*db);
    % Slip calculation on TC length
    LTC_pl=min(Leff0, max(0,sigmaT-fy)*pi*db/(4*(tb_f+pi*tb_u)));
    LTC_el=min(Leff0-LTC_pl, min(sigmaT,fy)*pi*db/(4*(tb_f+pi*tb_p)));
    sigmaCi=sigmaT-4*(tb_f+pi*tb_p)*LTC_el/(pi*db)-4*(tb_f+pi*tb_u)*LTC_pl/(pi*db);
    sTC_el=min(sigmaBi,fy)*LTC_el/Es+2*tb_f*LTC_el^2/(Es*pi*db)+2*tb_p*LTC_el^2/(Es*db);
```

```
  sTC_pl=max(sigmaBi-fy,0)*LTC_pl/Eh+2*tb_f*LTC_pl^2/(Eh*pi*db)+2*tb_u*LTC_pl^2/(Eh*db);
  % Plastic slip addiction
  DLeff=Leff0-Lefft;
  Ds=Ds+2*DLeff/Eh;
  % Matrix allocation
  slip_el(sigmaH)=slip_el(sigmaH)+sDT_el+sTC_el;
  slip_pl(sigmaH)=slip_pl(sigmaH)+sDT_pl+sTC_pl+Ds;
  sigmaC(sigmaH)=sigmaCi;
end


% ---------------------------
% PHASE 4 (Hook end friction)

% Max available resistant length
LCEmax=Le*db-Leff0;

for sigmaH=1:fu
  % Anchorage length calculation
  LCE_pl=min(LCEmax, max(0,sigmaC(sigmaH)-fy)*db/(4*tb_u));
  LCE_el=min(LCEmax-LCE_pl, min(sigmaC(sigmaH),fy)*db/(4*tb_p));
  % End stress calculation
  sigmaE(sigmaH)=sigmaC(sigmaH)-4*tb_p*LCE_el/db-4*tb_u*LCE_pl/db;
  if sigmaE>1
     Check=0;
  else
     Check=1;
  end
  % Slip calculation on TC length
  sCE_el=min(sigmaE(sigmaH),fy)*LCE_el/Es+2*tb_p*LCE_el^2/(Es*db);
  sCE_pl=max(sigmaE(sigmaH)-fy,0)*LCE_pl/Eh+2*tb_u*LCE_pl^2/(Eh*db);
  % Matrix allocation
  slip_el(sigmaH)=slip_el(sigmaH)+sCE_el;
  slip_pl(sigmaH)=slip_pl(sigmaH)+sCE_pl;
end


% ------------
% FUNCTION END

if Check==0
  % Hook fail, introduction of anchorage slippage
  sCE_s=10*(sCE_el+sCE_pl);
else
  sCE_s=0;
end

% Total slip
slip=slip_el+slip_pl+sCE_s;

end
```

291

Anchored smooth rebar stress-slip behaviour

```
function [F1, F2, F3, s1, s2, s3, beta] = BSSC (thetat, Hc, cs, db_1, db_2, nb_1, nb_2, fc, fy_1, fy_2,
fu_1, fu_2, Lb_1, Lb_2)

% ----------
% HYPOTHESIS

% Steel modulus
Es=200000;
Eh=Es/100;



% ----------------
% DATA ELABORATION

% Reinforcement amount
As1=nb_1*pi/4*db_1^2;
As2=nb_2*pi/4*db_2^2;
As=As1+As2;

% Reinforcement medium mechanical parameters
db=(db_1*nb_1+db_2*nb_2)/(nb_1+nb_2);
fy=(As1*fy_1+As2*fy_2)/(As);
fu=(As1*fu_1+As2*fu_2)/(As);
Lb=(As1*Lb_1+As2*Lb_2)/(As);

% Bond in Concrete at loading (p), cyclic (c) and failure
% conditions
tb_p=0.30*sqrt(fc);
tb_c=0.05*sqrt(fc);
tb_u=tb_c;



% -------------------------------
% PECULIAR PARAMETERS DEFINITION

% Hook stiffness (Analytical behaviour)
[stress, slip_el, slip_pl, slip] = AH (db_1, db_2, nb_1, nb_2, fy_1, fy_2, fu_1, fu_2, fc);
stressH=stress;
slipH_el=slip_el;
slipH_pl=slip_pl;
slipH=slip;

% Straight length required to balance yielding (y) and overstrength (u) at loading (p), cyclic (c)
and failure
% conditions
hy_p=fy*db/(4*tb_p);
hu_p=(fu-fy)*db/(4*tb_u);
```

```
% -----------------------
% TARGET POINT DEFINITION

% Slip at the target deformation point
st=thetat*(Hc-cs);


% -------------------
% BACKBONE DEFINITION

% First loading (l) backbone definition
if Lb>(hy_p+hu_p)
    % Case A + Case C
    % Length involved in bar equilibrium
    hy_l=hy_p;
    hu_l=hu_p;
    % Yielding slip
    sy_l_el=2*tb_p*hy_l^2/(Es*db);
    sy_l_pl=0;
    sy_l=sy_l_el+sy_l_pl;
    % Failure slip
    su_l_el=fy*hu_l/Es+2*tb_p*hy_l^2/(Es*db);
    su_l_pl=2*tb_u*hu_l^2/(Eh*db);
    su_l=su_l_el+su_l_pl;
    % Conventional hook stress definition
    fh_l=fu*(1-1.0e-3);
    % Slip at conventional hook activation
    sh_l=su_l*(1-1.0e-3);
    % Target point force
    if st<sy_l
        ftt=1;
        stt=ftt^2*db/(8*tb_p*Es);
        Di=st;
        Dii=abs(st-stt);
        while Dii<Di
            ftt=ftt+1;
            stt=ftt^2*db/(8*tb_p*Es);
            Di=Dii;
            Dii=abs(st-stt);
        end
        ft_l=ftt-1;
    else
        ftt=fy;
        stt=ftt^2*db/(8*tb_p*Es);
        Di=st;
        Dii=abs(st-stt);
        while Dii<Di
            ftt=ftt+1;
            hut=(ftt-fy)*db/(4*tb_u);
            stt=fy^2*db/(8*tb_p*Es)+fy*hut/Es+2*tb_u*hut^2/(Eh*db);
```

293

```
        Di=Dii;
        Dii=abs(st-stt);
      end
    ft_l=ftt-1;
  end
  % Target point slip
  hu_t_l=(ft_l-fy)*db/(4*tb_u);
  hy_t_l=min(Lb-hu_t_l,hy_p);
  if st<sy_l
    st_l_el=2*tb_p*hy_t_l^2/(Es*db);
  else
    st_l_el=fy*(hu_t_l)/Es+2*tb_p*hy_p^2/(Es*db);
  end
  % Incremental slip points
  s_l=[sy_l, su_l, sh_l];
  s_l=sort(s_l);
  s1=s_l(1);
  s2=s_l(2);
  s3=s_l(3);
  % Incremental force points
  f_l=[fy, fu, fh_l];
  f_l=sort(f_l);
  F1=f_l(1);
  F2=f_l(2);
  F3=f_l(3);
  % Reference parameters for stiffness calibration
  Kref=F1/(fy*s1);
  Kun_l=ft_l/(fy*st_l_el);
  mu=st/s1;
else
  if Lb>hy_p && Lb>hu_p
    % Case A + Case D
    % Length involved in bar equilibrium
    hu_l=hu_p;
    hy_l=Lb-hu_l;
    % Yielding slip
    sy_l_el=2*tb_p*hy_p^2/(Es*db);
    sy_l_pl=0;
    sy_l=sy_l_el+sy_l_pl;
    % Hook stress level
    fh_l=fy+4*tb_u*(Lb-hy_p)/db;
    fhu_l=fy-4*tb_u*hy_l/db;
    % Slip at hook activation
    sh_l=fy*(Lb-hy_p)/Es+2*tb_u*(Lb-hy_p)^2/(Eh*db)+2*tb_p*hy_p^2/(Es*db);
    % Failure slip
    shu_l=slipH(find(stressH==round(fhu_l),1));
    su_l_el=fy*hu_l/Es+fhu_l*hy_l/Es+2*tb_p*hy_l^2/(Es*db)+shu_l;
    su_l_pl=2*tb_u*hu_l^2/(Eh*db);
    su_l=su_l_el+su_l_pl;
    % Target point
    if st<sy_l
```

294

```
        ftt=1;
        stt=ftt^2*db/(8*tb_p*Es);
        Di=st;
        Dii=abs(st-stt);
        while Dii<Di
            ftt=ftt+1;
            stt=ftt^2*db/(8*tb_p*Es);
            Di=Dii;
            Dii=abs(st-stt);
        end
        ft_l=ftt-1;
    else
        ftt=fy;
        stt=sy_l;
        Di=st;
        Dii=abs(st-stt);
        while Dii<Di
            ftt=ftt+1;
            hut=(ftt-fy)*db/(4*tb_u);
            hyt=Lb-hut;
            if ftt<fh_l
                stt=fy^2*db/(8*tb_p*Es)+fy*hut/Es+2*tb_u*hut^2/(Eh*db);
            else
                fht=fy-4*tb_p*hyt/db;
                sht=slipH(find(stressH==round(fht),1));
                stt=fy*hut/Es+2*tb_u*hut^2/(Eh*db)+fht*hyt/Es+2*tb_p*hyt^2/(Es*db)+sht;
            end
            Di=Dii;
            Dii=abs(st-stt);
        end
        ft_l=ftt-1;
    end
    % Target point slip
    if st<sy_l
        st_l_el=ft_l^2*db/(8*tb_p*Es);
    else
        % Length involved
        hu_t_l=(ft_l-fy)*db/(4*tb_u);
        hy_t_l=min(Lb-hu_t_l,hy_p);
        % Hook stress level
        fht_l=fy-4*tb_p*hy_t_l/db;
        sht_el=slipH_el(find(stressH==round(fht_l),1));
        % Slip
        st_l_el=fy*hu_t_l/Es+fht_l*hy_t_l/Es+2*tb_p*hy_t_l^2/(Es*db)+sht_el;
    end
    % Incremental slip points
    s_l=[sy_l, su_l, sh_l];
    s_l=sort(s_l);
    s1=s_l(1);
    s2=s_l(2);
    s3=s_l(3);
```

```
% Incremental force points
f_l=[fy, fu, fh_l];
f_l=sort(f_l);
F1=f_l(1);
F2=f_l(2);
F3=f_l(3);
% Reference parameters for stiffness calibration
Kref=F1/(fy*s1);
Kun_l=ft_l/(fy*st_l_el);
mu=st/s1;
else
  if Lb>hy_p && Lb<hu_p
    % Case A + Case E
    % Length involved in bar equilibrium
    hu_l=Lb;
    hy_l=Lb-hy_p;
    % Yielding slip
    sy_l_el=2*tb_p*hy_p^2/(Es*db);
    sy_l_pl=0;
    sy_l=sy_l_el+sy_l_pl;
    % Hook stress level
    fh_l=fy+4*tb_u*hy_l/db;
    fhy_l=fy+4*tb_u*Lb/db;
    fhu_l=fu-4*tb_u*hu_l/db;
    % Slip at hook activation
    sh_l=fy*hy_l/Es+2*tb_u*hy_l^2/(Eh*db)+2*tb_p*hy_p^2/(Es*db);
    % Failure slip
    shu_l_el=slipH_el(find(stressH==round(fhu_l),1));
    shu_l_pl=slipH_pl(find(stressH==round(fhu_l),1));
    su_l_el=fy*hu_l/Es+shu_l_el;
    su_l_pl=2*tb_u*hu_l^2/(Eh*db)+(fhu_l-fy)*hu_l/Eh+shu_l_pl;
    su_l=su_l_el+su_l_pl;
    % Target point force
    if st<sy_l
    ftt=1;
    stt=ftt^2*db/(8*tb_p*Es);
    Di=st;
    Dii=abs(st-stt);
      while Dii<Di
        ftt=ftt+1;
        stt=ftt^2*db/(8*tb_p*Es);
        Di=Dii;
        Dii=abs(st-stt);
      end
    ft_l=ftt-1;
    else
      ftt=fy;
      stt=sy_l;
      Di=st;
      Dii=abs(st-stt);
      while Dii<Di
```

```
        ftt=ftt+1;
         hut=(ftt-fy)*db/(4*tb_u);
         hyt=Lb-hut;
        if ftt<fh_l
           stt=fy^2*db/(8*tb_p*Es)+fy*hut/Es+2*tb_u*hut^2/(Eh*db);
        else
           if ftt<fhy_l
              fht=fy-4*tb_p*hyt/db;
              sht=slipH(find(stressH==round(fht),1));
              stt=fy*hut/Es+2*tb_u*hut^2/(Eh*db)+fht*hyt/Es+2*tb_p*hyt^2/(Es*db)+sht;
           else
              hut=Lb;
              fht=fu-4*tb_p*hut/db;
              sht=slipH(find(stressH==round(fht),1));
              stt=(fht-fy)*hut/Eh+2*tb_u*hut^2/(Eh*db)+fy*hut/Es+sht;
           end
        end
        Di=Dii;
        Dii=abs(st-stt);
    end
ft_l=ftt-1;
hu_t_l=min((ft_l-fy)*db/(4*tb_u),Lb);
end
% Target point slip
if st<sy_l
    st_l_el=ft_l^2*db/(8*tb_p*Es);
else
    if hu_t_l<Lb
        % Length involved
        hy_t_l=min(Lb-hu_t_l,hy_p);
        % Hook stress level
        fht_l=fy-4*tb_p*hy_t_l/db;
        sht_el=slipH_el(find(stressH==round(fht_l),1));
        % Slip
        st_l_el=fy*hu_t_l/Es+fht_l*hy_t_l/Es+2*tb_p*hy_t_l^2/(Es*db)+sht_el;
    else
        % Length correction
        ht_l=Lb;
        % Hook stress level
        fht_l=ft_l-4*tb_u*ht_l/db;
        sht_el=slipH_el(find(stressH==round(fht),1));
        % Slip
        st_l_el=fy*ht_l/Es+(fht_l-fy)*ht_l/Es+sht_el;
    end
end
% Incremental slip points
s_l=[sy_l, su_l, sh_l];
s_l=sort(s_l);
s1=s_l(1);
s2=s_l(2);
s3=s_l(3);
```

```
            % Incremental force points
            f_l=[fy, fu, fh_l];
            f_l=sort(f_l);
            F1=f_l(1);
            F2=f_l(2);
            F3=f_l(3);
            % Reference parameters for stiffness calibration
            Kref=F1/(fy*s1);
            Kun_l=ft_l/(fy*st_l_el);
            mu=st/s1;
        else
            if Lb<hy_p && Lb>hu_p
            % Case B + Case D
            % Length involved in bar equilibrium
            hu_l=Lb;
            hy_l=Lb-hu_l;
            % Hook stress level
            fh_l=4*tb_p*hy_l/db;
            fhy_l=fy-4*tb_p*hy_p/db;
            % Slip at hook activation
            sh_l=2*tb_p*hy_p^2/(Es*db);
            % Yielding slip
            shy_l=slipH(find(stressH==round(fhy_l),1));
            sy_l_el=2*tb_p*Lb^2/(Es*db)+fhy_l*Lb/Es+shy_l;
            sy_l_pl=0;
            sy_l=sy_l_el+sy_l_pl;
            % Hook stress level
            fhu_l=fy-4*tb_p*hy_l/db;
            % Failure slip
            shu_l=slipH(find(stressH==round(fhu_l),1));
            su_l_el=fy*hu_l/Es+fhu_l*hy_l/Es+2*tb_p*hy_l^2/(Es*db)+shu_l;
            su_l_pl=2*tb_u*hu_l^2/(Eh*db);
            su_l=su_l_el+su_l_pl;
            % Target point
            if st<sy_l
                ftt=1;
                stt=ftt^2*d_b/(8*tb_p*Es);
                Di=st;
                Dii=abs(st-stt);
                while Dii<Di
                    ftt=ftt+1;
                    stt=ftt^2*d_b/(8*tb_p*Es);
                    Di=Dii;
                    Dii=abs(st-stt);
                end
                ft_l=ftt-1;
            else
                ftt=fy;
                stt=sy_l;
                Di=st;
                Dii=abs(st-stt);
```

```
            while Dii<Di
                ftt=ftt+1;
                hut=(ftt-fy)*db/(4*tb_u);
                hyt=Lb-hut;
                if ftt<fh_l
                    stt=fy^2*db/(8*tb_p*Es)+fy*hut/Es+2*tb_u*hut^2/(Eh*db);
                else
                    fht=fy-4*tb_p*hyt/db;
                    sht=slipH(find(stressH==round(fht),1));
                    stt=fy*hut/Es+2*tb_u*hut^2/(Eh*db)+fht*hyt/Es+2*tb_p*hyt^2/(Es*db)+sht;
                end
                Di=Dii;
                Dii=abs(st-stt);
            end
            ft_l=ftt-1;
    end
    % Target point slip
    if st<sy_l
        st_l_el=ft_l^2*db/(8*tb_p*Es);
    else
        % Length involved
        hu_t_l=(ft_l-fy)*db/(4*tb_u);
        hy_t_l=min(Lb-hu_t_l,hy_p);
        % Hook stress level
        fht_l=fy-4*tb_p*hy_t_l/db;
        sht_el=slipH_el(find(stressH==round(fht),1));
        % Slip
        st_l_el=fy*hu_t_l/Es+fht_l*hy_t_l/Es+2*tb_p*hy_t_l^2/(Es*db)+sht_el;
    end
    % Incremental slip points
    s_l=[sy_l, su_l, sh_l];
    s_l=sort(s_l);
    s1=s_l(1);
    s2=s_l(2);
    s3=s_l(3);
    % Incremental force points
    f_l=[fy, fu, fh_l];
    f_l=sort(f_l);
    F1=f_l(1);
    F2=f_l(2);
    F3=f_l(3);
    % Reference parameters for stiffness calibration
    Kref=F1/(fy*s1);
    Kun_l=ft_l/(fy*st_l_el);
    mu=st/s1;
    else
        if Lb<hy_p && Lb<hu_p
        % Case B + Case E
        % Length involved in bar equilibrium
        hu_l=Lb;
        % Hook stress level
```

```
fh_l=4*tb_p*Lb/db;
fhy_l=fy-4*tb_p*Lb/db;
% Slip at hook activation
sh_l=2*tb_p*hu_l^2/(Es*db);
% Yielding slip
shy_l=slipH(find(stressH==round(fhy_l),1));
sy_l_el=2*tb_p*Lb^2/(Es*db)+fhy_l*Lb/Es+shy_l;
sy_l_pl=0;
sy_l=sy_l_el+sy_l_pl;
% Hook stress level
fhu_l=fu-4*tb_u*hu_l/db;
% Failure slip
shu_l_el=slipH_el(find(stressH==round(fhu_l),1));
shu_l_pl=slipH_pl(find(stressH==round(fhu_l),1));
su_l_el=fy*hu_l/Es+shu_l_el;
su_l_pl=2*tb_u*hu_l^2/(Eh*db)+(fhu_l-fy)*hu_l/Eh+shu_l_pl;
su_l=su_l_el+su_l_pl;
% Target point force
if st<sy_l
    ftt=1;
    stt=ftt^2*db/(8*tb_p*Es);
    Di=st;
    Dii=abs(st-stt);
    while Dii<Di
        ftt=ftt+1;
        stt=ftt^2*db/(8*tb_p*Es);
        Di=Dii;
        Dii=abs(st-stt);
    end
    ft_l=ftt-1;
else
    ftt=fy;
    stt=sy_l;
    Di=st;
    Dii=abs(st-stt);
    while Dii<Di
        ftt=ftt+1;
        hut=min((ftt-fy)*db/(4*tb_u),Lb);
        hyt=min(Lb-hut,hy_p);
        if ftt<fh_l
            stt=fy^2*db/(8*tb_p*Es)+fy*hut/Es+2*tb_u*hut^2/(Eh*db);
        else
            fht=ftt-4*tb_u*hut/db-4*tb_p*hyt/db;
            sht=slipH(find(stressH==round(fht),1));
            stt=fht*hyt/Es+2*tb_p*hyt^2/(Es*db)+2*tb_u*hut^2/(Eh*db)+fy*hut/Es+sht;
        end
        Di=Dii;
        Dii=abs(st-stt);
    end
    ft_l=ftt-1;
    hu_t_l=min((ft_l-fy)*db/(4*tb_u),Lb);
```

```
            end
            % Target point slip
            if st<sy_l
                st_l_el=ft_l^2*db/(8*tb_p*Es);
            else
                if hu_t_l<Lb
                    % Length involved
                    hy_t_l=Lb-hu_t_l;
                    % Hook stress level
                    fht_l=fy-4*tb_p*hy_t_l/db;
                    sht_el=slipH_el(find(stressH==round(fht),1));
                    % Slip
                    st_l_el=fy*hu_t_l/Es+fht_l*hy_t_l/Es+2*tb_p*hy_t_l^2/(Es*db)+sht_el;
                else
                    % Length correction
                    ht_l=Lb;
                    % Hook stress level
                    fht_l=ft_l-4*tb_u*ht_l/db;
                    % Slip
                    sht_el=slipH_el(find(stressH==round(fht_l),1));
                    st_l_el=fy*ht_l/Es+sht_el;
                end
            end
            % Incremental slip points
            s_l=[sy_l, su_l, sh_l];
            s_l=sort(s_l);
            s1=s_l(1);
            s2=s_l(2);
            s3=s_l(3);
            % Incremental force points
            f_l=[fy, fu, fh_l];
            f_l=sort(f_l);
            F1=f_l(1);
            F2=f_l(2);
            F3=f_l(3);
            % Reference parameters for stiffness calibration
            Kref=F1/(fy*s1);
            Kun_l=ft_l/(fy*st_l_el);
            mu=st/s1;
            end
        end
    end
end


% ----------------------------
% CYCLIC BEHAVIOUR DEFINITION

% Unloading stiffness calibration
K=Kun_l;
```

```
Kr=K/Kref;
beta=-log(Kr)/log(mu);
beta_max=-log(ft_l/(st*fy*Kref))/log(mu);
beta=min(beta, beta_max);

end
```

APPENDIX B.   SENSITIVITY ANALYSES

B.1.   Role of the concrete subgrade stiffness

With reference to the crack modelling suggested in the previous Chapter 5, a discussion about the concrete subgrade stiffness is herein proposed. The contact between the crack sides is represented with a series of only-compression elastic-plastic springs, which properties can be summarized in the followings (see Figure 166):

- yielding strength defined by the concrete mean cylindrical compressive strength;
- elastic stiffness K_c defined according to Eq.(204);
- no strength degradation;
- no unloading and reloading stiffness degradation;
- reloading only after the recovery of the previously exhibited plastic deformation (slip model).

Considered the concrete modulus of elasticity E_c and a coefficient $\beta > 0$; the equivalent spring elastic stiffness is defined by the following:

$$K_c = \frac{E_c}{\beta} \qquad (204)$$

In the following, a sensitive analysis is pursued with the aim of analyse the role of the elastic concrete stiffness on the definition of a column monotonic response. A monotonic loading up to the member yielding is imposed. Experimental tested samples are considered for the evaluation (Verderame et al., 2008b).

OpenSees (McKenna et al., 2000) ElasticPPGap material (with damage consideration) is used for the numerical modelling of the concrete equivalent springs.

To outline the prediction sensitivity to the investigated parameter, the followings are herein considered:

- Very High concrete Stiffness (VHS) $\beta = 10$;
- High concrete Stiffness (HS) $\beta = 50$;
- Normal concrete Stiffness (NS) $\beta = 100$;
- Low concrete Stiffness (LS) $\beta = 200$;
- Very Low concrete Stiffness (VLS) $\beta = 1000$.

Remember that the effectiveness of the modelling proposal has been already demonstrated in the previous Chapter 6, considering a coefficient $\beta = 100$ (here called NS condition).

The numerical analyses are stopped at a drift level $\theta = 1.00\%$. Indeed, only the elastic field of the response is of interest. A qualitative comparison is shown by the plot of

the assessed load-displacement curves in the graphs from Figure 194 to Figure 197. A quantitative evaluation is instead reported in terms of difference between the predicted drift at a reference horizontal force (base shear). Rocking mechanism activation $(\theta_r; V_r)$ and column yielding $(\theta_y; V_y)$ are considered as reference points. The drift data are not reported for the case of Very Low Stiffness (VLS), due to its lack in representativeness (see the comparison with the experimental results). Note that the tested specimens were six, whereas the herein reported data are relative to four different samples; two couples of the original ones had indeed the same properties (M-270A1 and M-270A2; M-270B1 and M-270B2).

It can be concluded that a variation by a factor 2 of the considered concrete subgrades stiffness does not significantly affect the prediction results. A maximum difference lower than 5.00% is evaluated at the yielding point (Table 30), on the other hand a higher variance (up to the 30%) is assessed near to the rocking activation point (Table 29).

Specimen	V_r [kN]	θ_r (VHS) [%]		θ_r (HS) [%]		θ_r (NS) [%]		θ_r (LS) [%]	
M-270A1 (A2)	20	0.096	-29%	0.115	-14%	0.134	±0%	0.166	+24%
M-270B1 (B2)	20	0.102	-24%	0.115	-14%	0.134	±0%	0.166	+24%
M-540A1	40	0.197	-26%	0.236	-12%	0.268	±0%	0.325	+21%
M-540B1	40	0.197	-28%	0.236	-14%	0.274	±0%	0.331	+21%

Table 29: Comparison between the predicted drift at the reference yielding load.

Specimen	V_y [kN]	θ_y (VHS) [%]		θ_y (HS) [%]		θ_y (NS) [%]		θ_y (LS) [%]	
M-270A1 (A2)	40	0.618	-4%	0.624	-3%	0.643	±0%	0.675	+5%
M-270B1 (B2)	40	0.643	-3%	0.650	-2%	0.662	±0%	0.694	+5%
M-540A1	57	0.777	-4%	0.796	-2%	0.809	±0%	0.841	+4%
M-540B1	57	0.803	-4%	0.822	-1%	0.834	±0%	0.866	+4%

Table 30: Comparison between the predicted drift at the reference yielding load.
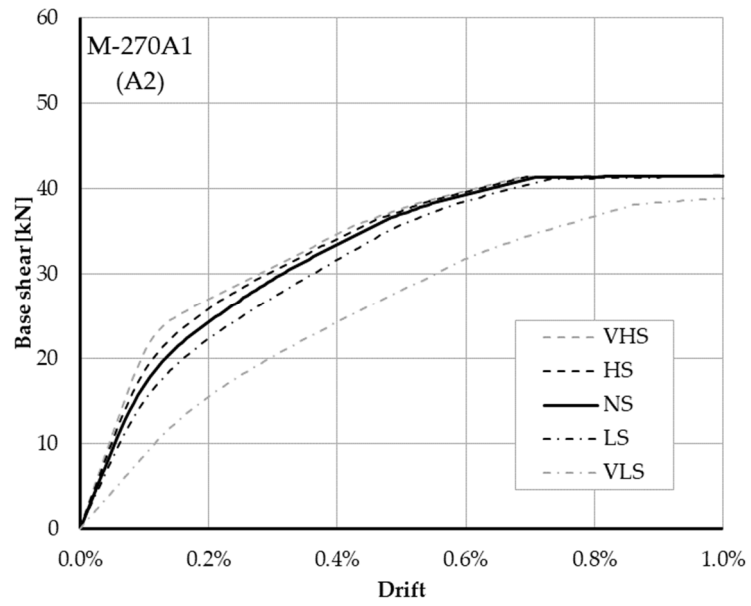
Figure 194: Analysis on the specimen M-270A1 (A2).
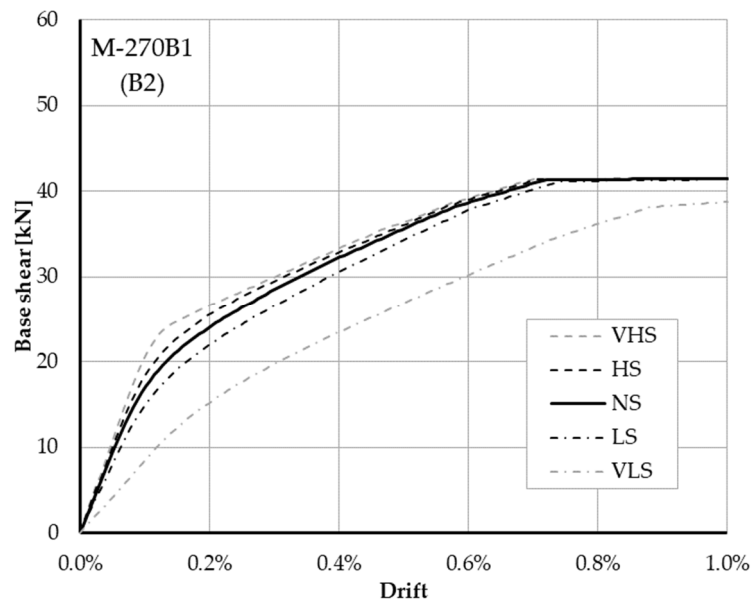
Figure 195: Analysis on the specimen M-270B1 (B2).
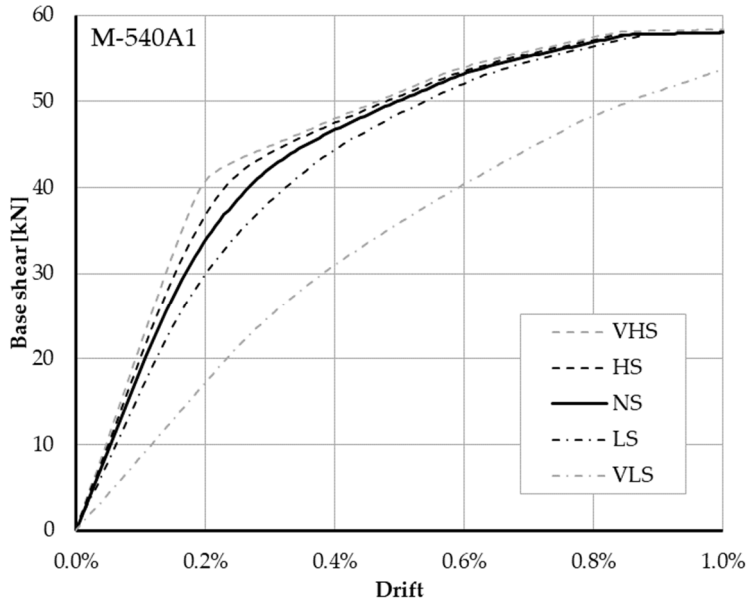
Figure 196: Analysis on the specimen M-540A1.
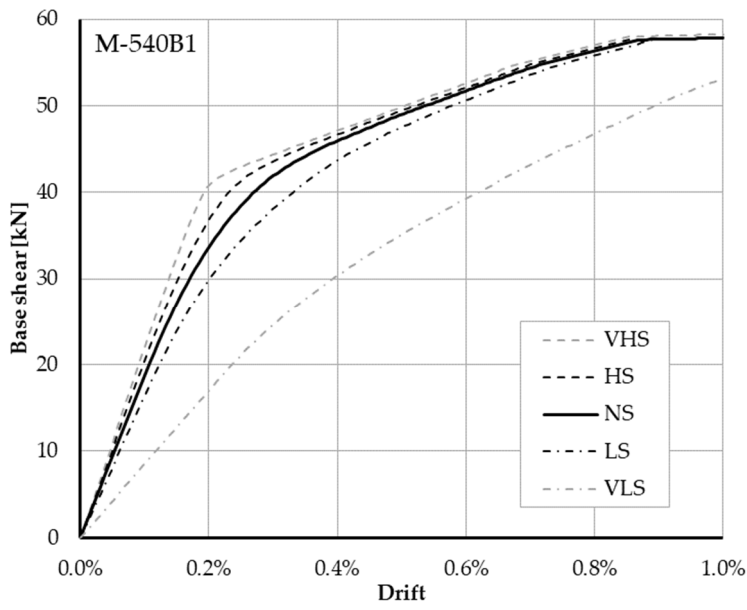
Figure 197: Analysis on the specimen M-540B1.

APPENDIX C.   VALIDATION OF THE PROPOSED MODEL

Further experimental test simulations on columns (Di Ludovico et al., 2014; Melo et al., 2015) and beam-column joints (Braga et al., 2009; Pampanin et al., 2002) are herein presented. The predicted cyclic behaviour, in term of acting shear force versus drift $(V_b - \theta)$, is plotted on the reference paper curves. Furthermore, details about the predicted local behaviour are then reported about a T-joint subassembly (Braga et al., 2009) and a 2D planar frame (Calvi et al., 2002b, 2001). The detailed results are reported with the format of the routine defined in Matlab environment to facilitate the model input and output data elaboration.

C.1.   General considerations

A discussion about the model ability in predicting column and beam-column joint force-displacement behaviour is presented, with reference to different deformation demands. As already mentioned in Chapter 5, the proposed model is not able in representing strength decay due to flexural damage at the column ends, joint panel shear damage, and reinforcement buckling. As visible in the following comparisons, the herein proposed model can be considered representative of the column behaviour up to a drift demand equal to about 0.03. Indeed, after this deformation level, the influence of the not considered mechanisms begin significant. Regarding the beam-column joint response, a good prediction can be observed for drift levels lower than 1.00%-1.50%; indeed, in presence of shear failure, the experimentally observed strength degradation cannot be simulated.

Deformation demands higher than the limits above defined can be considered not consistent with the expected performance of a GLD frame building. In reinforced structures, the global deformation is typically controlled by additive stiffening and strengthening systems; these must limit the drift demand in an acceptable range, in which the response of the existing elements results stable and does not suffer significant strength decay.

According to the aim of this work, the modelling technique is considered adequate in representing RC members seismic behaviour up to a drift level consistent with the expected demand on a retrofitted frame structure.

Reference specimens

The analysed specimens are defined in the reference literature works (Di Ludovico et al., 2014; Melo et al., 2015). A summary of their characteristics is reported in Table 31, whereas a schematization of the same is visible in Figure 198 and Figure 199. Different element slenderness, axial load ratio, and reinforcement ratio are considered; the presence or not of the overlapping at the element base is also investigated. Only columns reinforced with smooth rebar are treated.

Sample	Cross-section [cm]	Axial load ratio	Longitudinal rebars	Overlapping
S300P_c	30x30	0.20	3+2+3 Φ8	NO
R300P_c	50x30	0.10	5+2+5 Φ12	NO
R500P_c	30x50	0.10	3+2+2+2+3 Φ12	NO
CPA-1	30x30	0.18	3+3 Φ12	NO
CPA-3	30x30	0.18	3+3 Φ12	NO
CPB	30x30	0.18	3+3 Φ12	YES
CPC	30x30	0.18	4+4 Φ12	NO
CPD	30x40	0.18	3+2+3 Φ12	YES
CPE	30x50	0.18	4+2+4 Φ12	NO

Table 31: Main characteristics of the investigated reference samples (Di Ludovico et al., 2014; Melo et al., 2015).

Main results

The influence of column cross section geometry in presence of continuous reinforcement is investigated in the first three simulated tests (Di Ludovico et al., 2014). A good representation of the force-displacement response is noticed in presence of a square cross section (S300P-c sample); lower energy dissipation in instead assessed in presence of a rectangular section (R-300P-c and R500P-c). The last simulation on R500P-c sample (Di Ludovico et al., 2014) neglects the peak exhibited strength, which is about the 15% higher with respect to the assessed one.
Overlapping presence and influence of reinforcement ratio are analysed with reference to the other considered experimental campaign (Melo et al., 2015). A 30-diameter overlapping length (CPB and CPD) seems to be not adequate in guarantee the same strength observed in presence of continuous reinforcement (CPA-1 and CPA-3), despite hook device presence at the bar ends. With higher reinforcement ratio and continuous rebars (CPC) a lower energy dissipation capacity is represented, but only at the higher drift demands.
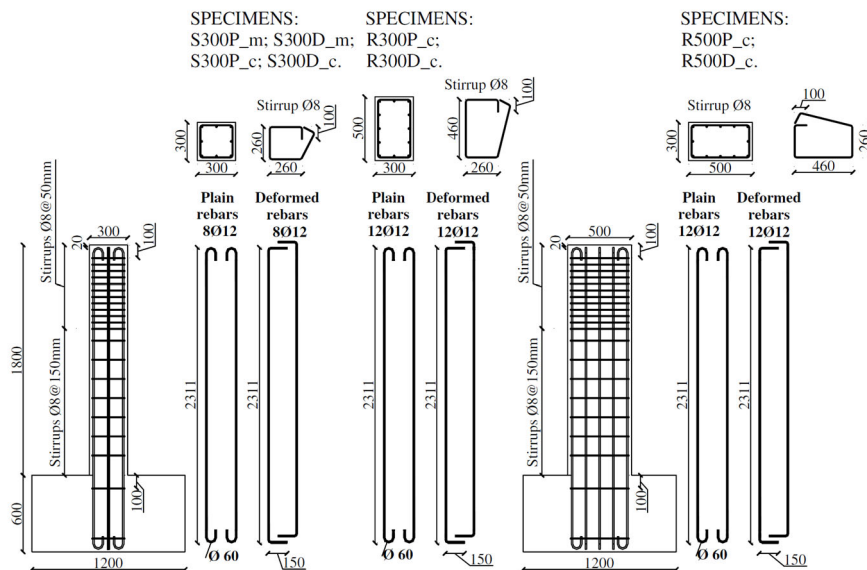
Figure 198: Reference specimens (Pt. a) (Di Ludovico et al., 2014).
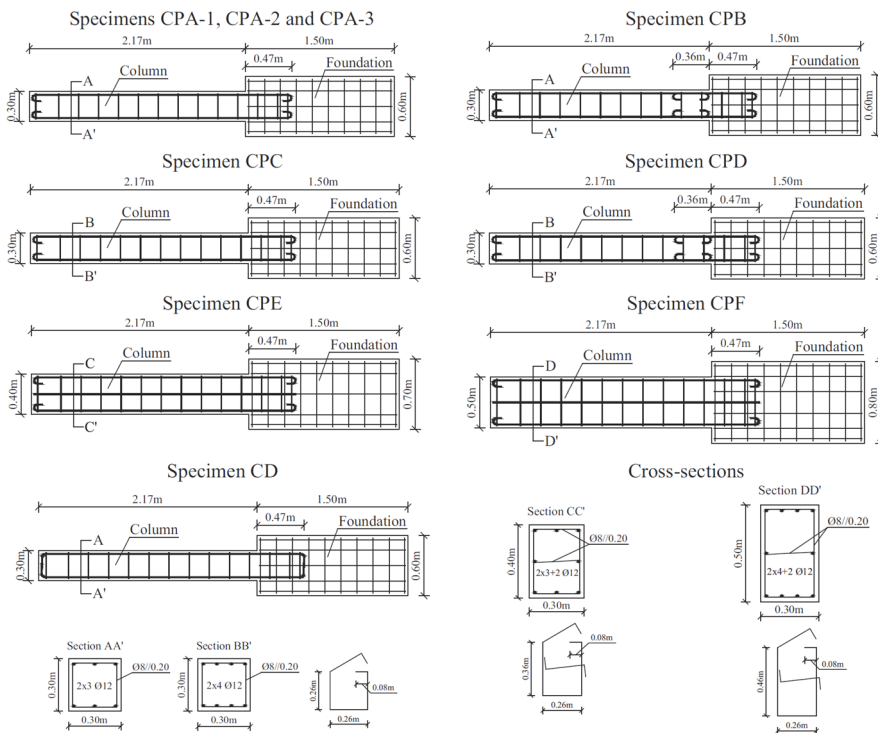
Figure 199: Reference specimens (Pt. b) (Melo et al., 2015).

Cyclic behaviour comparison

Figure 200 (Pt. 1 of 2)

310
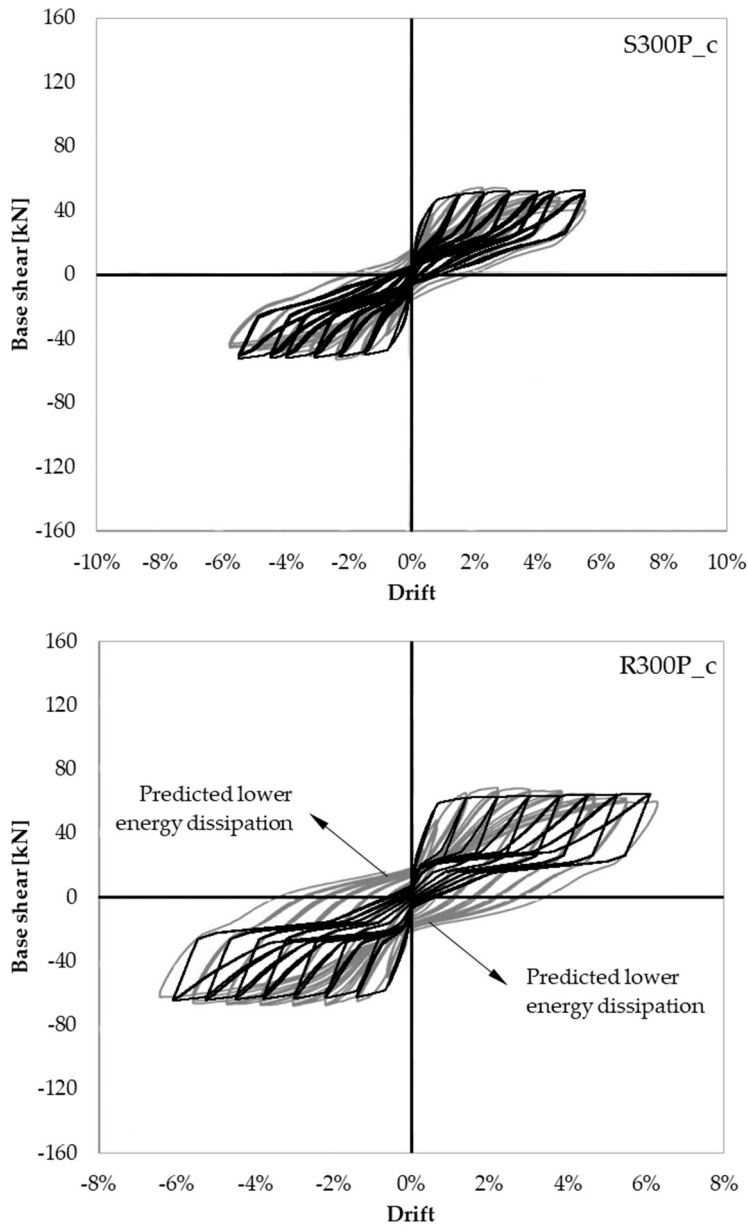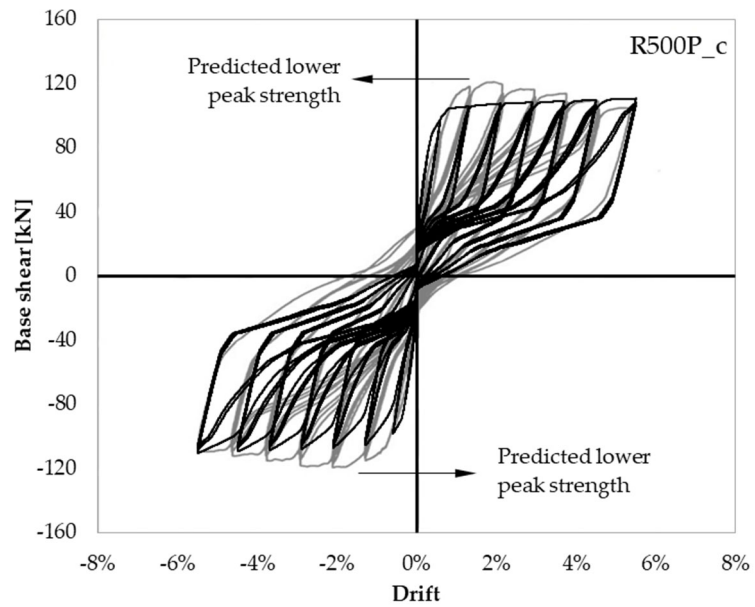
(Part 2 of 2)

Figure 200: Prediction of substandard column behaviour in presence of different cross section geometries (Di Ludovico et al., 2014); grey line for the experimental test and black one for the modelling prediction.
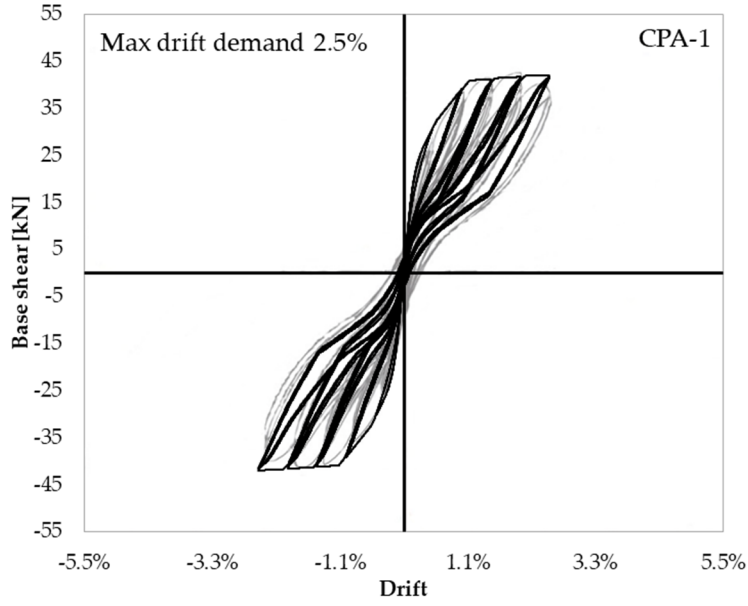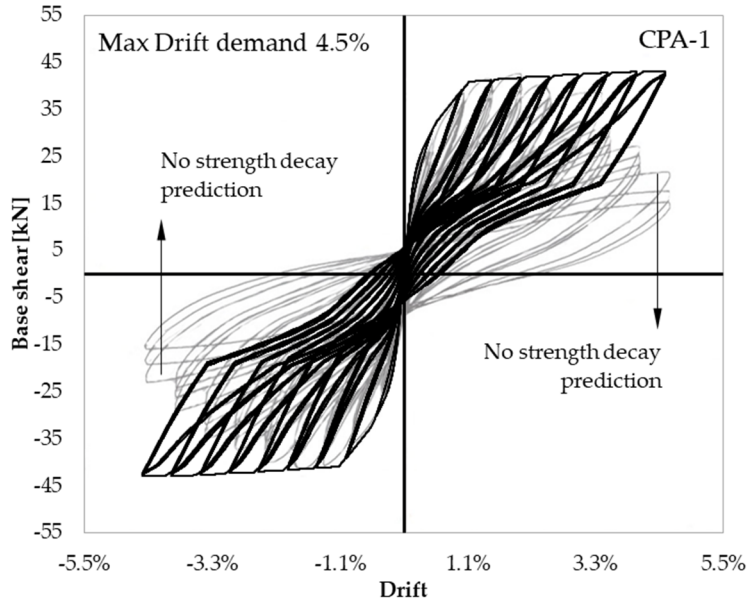
Figure 201 (Pt. 1 of 5)

Figure 201 (Pt. 2 of 5)

Max drift demand 5.0%

CPB (Overlapping)

Significant higher strength prediction

No strength decay prediction

No strength decay prediction

Signficant higher strength prediction

Max drift demand 3.0%

CPB (Overlapping)

Significant higher strength prediction

Possibility of strength reduction due to insufficient overlapping length
The model does not represent it

Signficant higher strength prediction

Figure 201 (Pt. 3 of 5)

Figure 201 (Pt. 4 of 5)
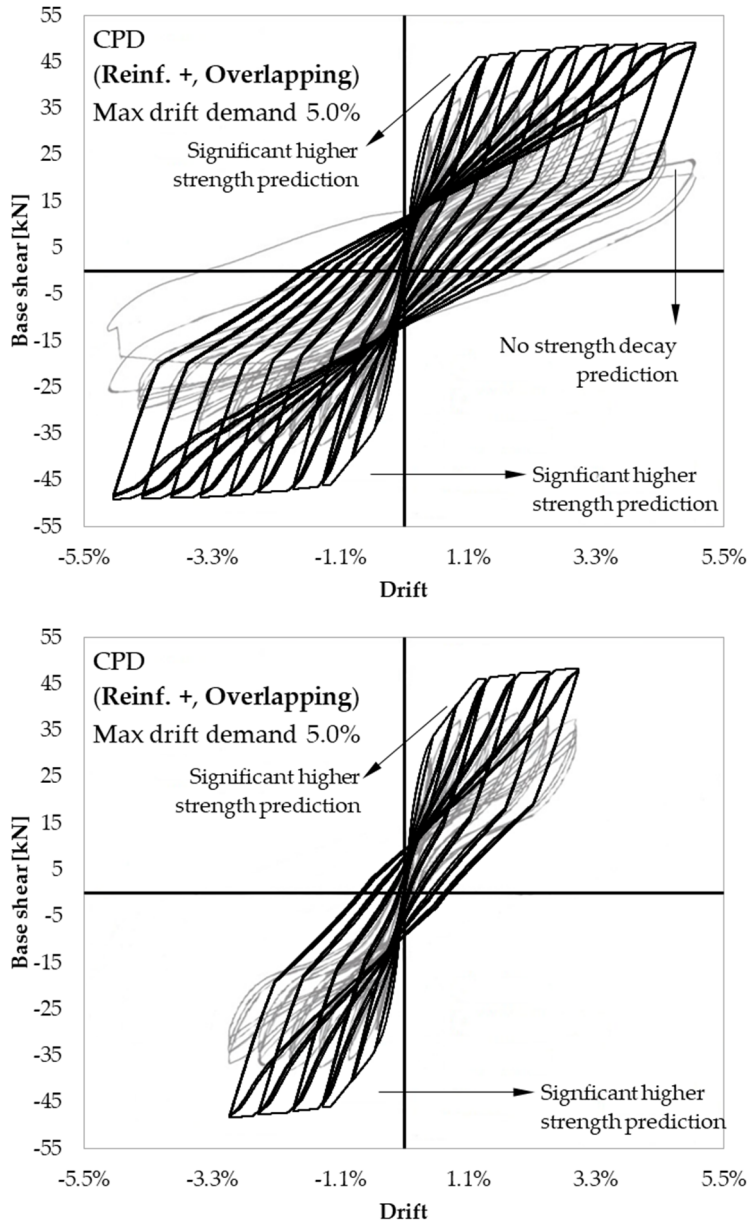
(Pt. 5 of 5)

Figure 201: Comparison between cyclic behaviour of different configurations of substandard column members (Melo et al., 2015) and the relative predicted cyclic force-displacement response.

C.2. *Non detailed beam-column joints*

Reference specimens

Applications on a T-beam-column subassembly is herein treated. The reference specimens is reported in Figure 202 (Braga et al., 2009), with indications about the mechanical properties of the employed materials. Details about the reinforcement arrangement are presented in Table 32. The beam longitudinal reinforcement is bent out of the support region; nevertheless, this detail is not considered in the herein presented modelling.

The T-type connection analysed in the following suffers a hybrid failure characterized by the panel shear cracking and beam longitudinal reinforcement yielding. Since the proposed model does not account for shear strength degradation, the simulation of the complete experimental response is not representative. Therefore, the cyclic analysis are stopped (in a second moment) at the triggering of the joint panel collapse, as it is described by the reference model (Pampanin et al., 2003). To identify the global deformation associated with the reach of the Near Collapse (NC) limit state, monotonic analyses are performed.

Element	Cross-section [cm]	Axial load ratio	Longitudinal rebars	Overlapping
Column	20 x 20	0.17	3 + 3 Φ8	YES
Beam (Intrados)	20 x 33	0.00	2 Φ8 + 1(2) Φ12	NO
Beam (Extrados)	20 x 33	0.00	2 Φ8 + 2 Φ12	NO

Table 32: Beam and column main properties for the reference T-joint.

T-Joint

Concrete compressive Strength	17.5 MPa
8mm rebar yielding stress	350MPa
12mm rebar yielding stress	325MPa
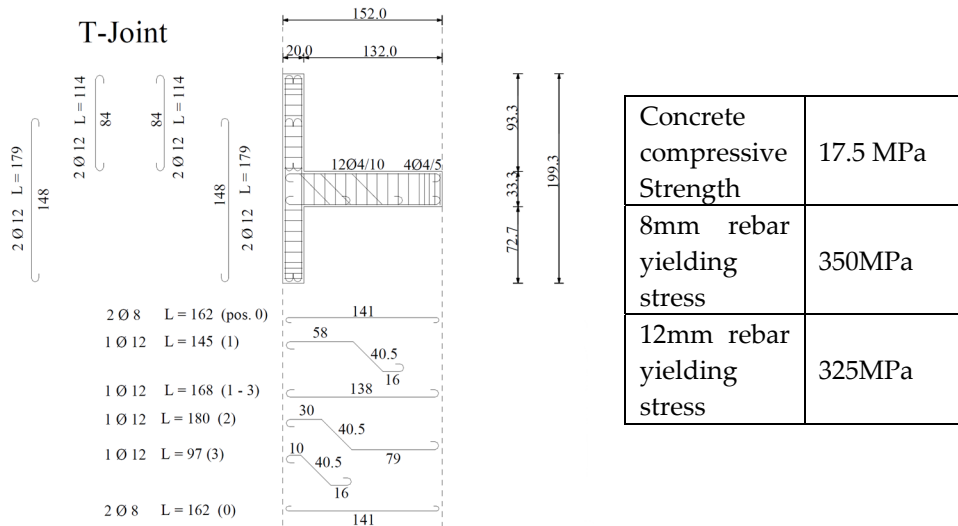
Figure 202: Reference T-Joint specimens in presence or not of bent longitudinal reinforcement.

Full Experimental response

For positive drift imposition (first quarter in graph of Figure 203) the elastic stiffness is well predicted by the numerical model, whereas the peak strength is slightly underestimated. However, the joint resistance at the higher drift level is consistent with the assessed one. For negative loading (third quarter), the assessed stiffness is overestimated, whereas the peak of strength is well predicted. The test showed degradation of strength in negative displacement imposition, due to a shear failure of the joint panel. In the following an insight through the shear and the flexural behaviour of the subassembly elements is analysed more in detail.
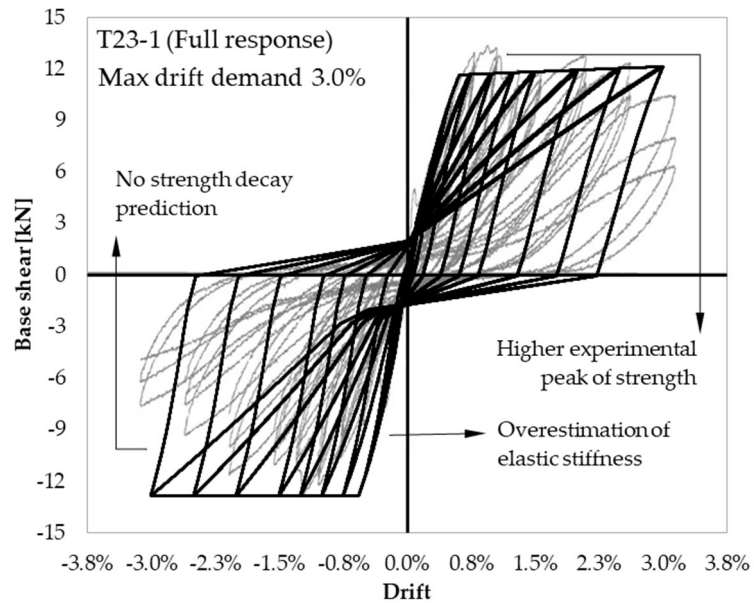
Figure 203: Simulation of full T-joint cyclic response (Braga et al., 2009).

Monotonic behaviour up to joint panel shear fail

The simulation of the monotonic behaviour of the sample T23-1 (Braga et al., 2009) shows a flexural failure for positive drift imposition and a joint shear failure in the opposite direction. It is clear observing the behaviour of the joint panel equivalent hinge (Figure 205), which shows a joint elastic response in the former case and the reach of a NC Limit State in the latter. Despite this, the lateral strength of the reference joint is comparable in both the direction; a hybrid mechanism can so be justified since the flexural and the shear mechanisms are characterized by a very similar strength.

a)   *b)*
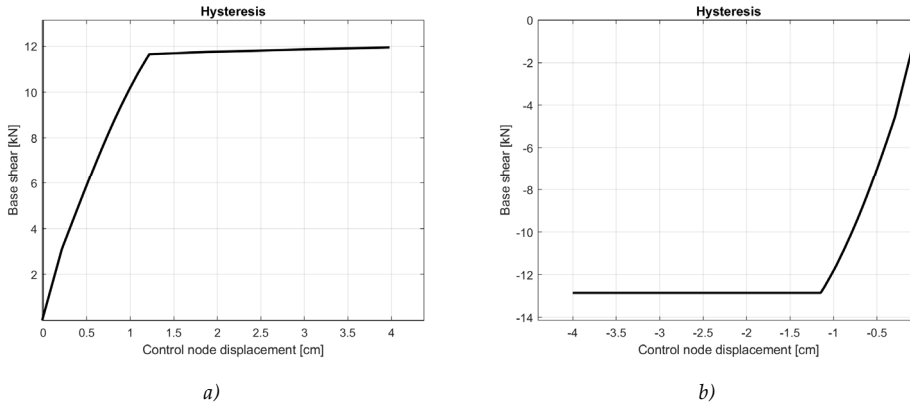
Figure 204: Joint monotonic response in positive a) and negative loading direction b). (Matlab output).

a)   *b)*
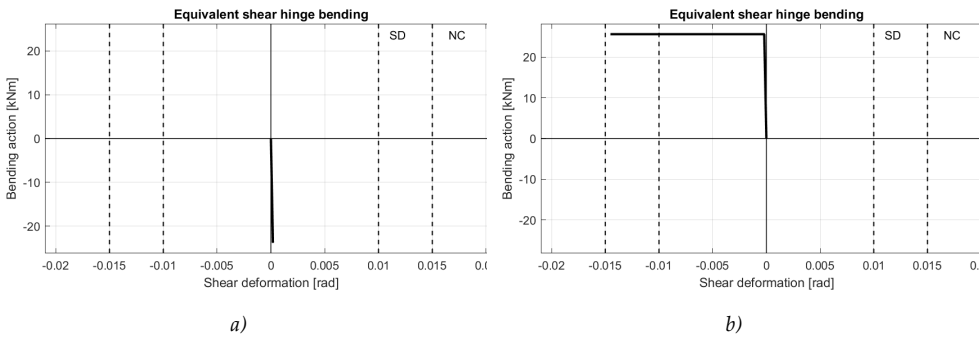
Figure 205: Joint shear deformation demand at a drift imposition equal to $\theta = 2.00\%$ in positive a) and negative direction b) (Matlab output).

Cyclic behaviour simulation up to shear failure

It follows, in Figure 206, the representation of the predicted cyclic behaviour up to the reach of the above defined shear strength (global drift equal to 0.02). A focus on the cycles at which the shear panel cracking took place is also presented in Figure 207.
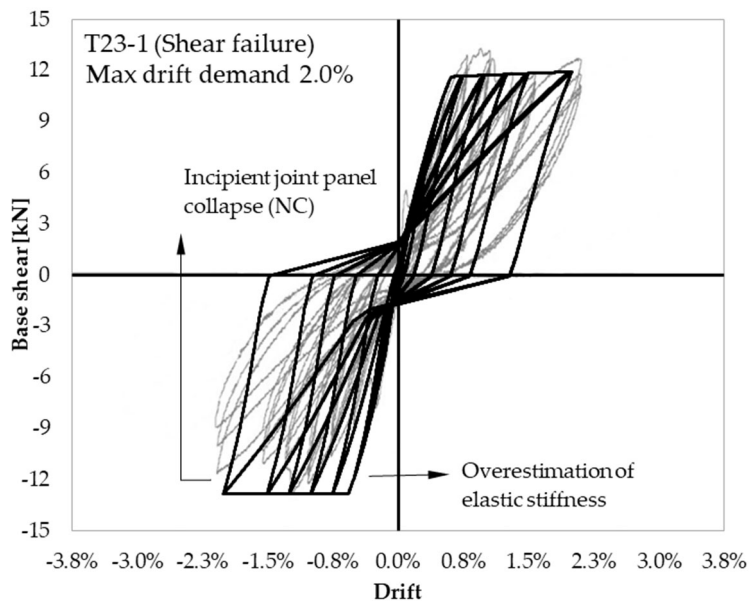
Figure 206: Focus on the difference between the experimental observed and the predicted response of the analysed joint.
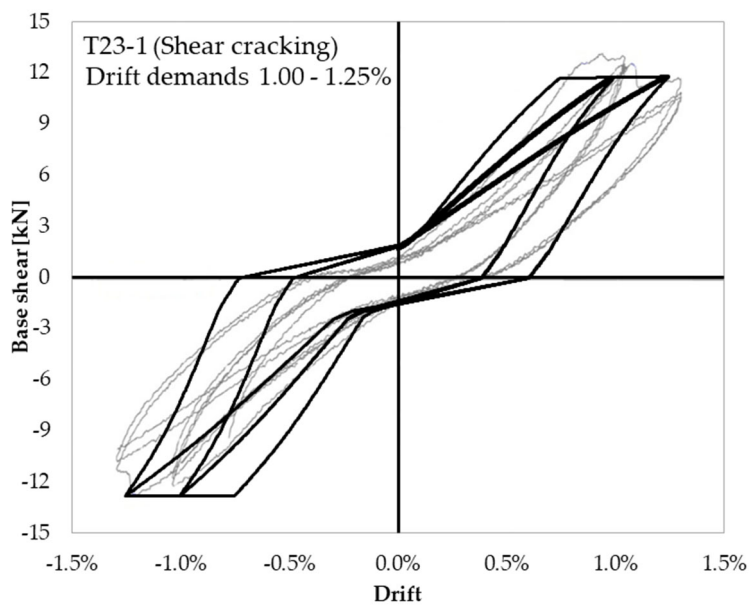
Figure 207: Focus on the cycles at which the T23-1 specimen showed the shear panel cracking.

In the following, the hysteresis of each member converging in the joint is analysed, with reference to the crack at the member-joint interface. Both the steel stress-slip and the concrete stress-displacement relationships are presented (from Figure 208 to Figure 210). The maximum imposed deformation is equal to θ = 2.00%, the model can so be retained adequate in representing the experimental observed behaviour; indeed, the analysis is stopped at the reach of the shear NC limit state. The column elements behave in the elastic field; indeed, they do not show the steel yielding or the concrete plasticization. The beam reaches its yielding in the positive loading direction. On the other hand, as already described, the equivalent shear panel moment-rotation hinge shows the fail in the opposite loading direction (Figure 211).
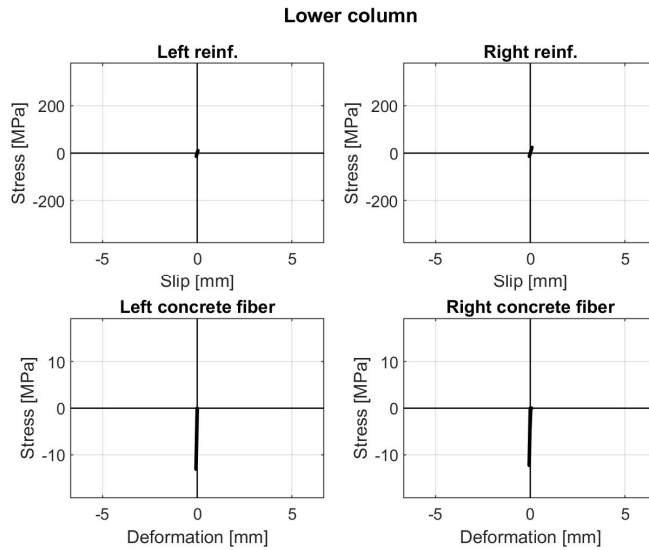
Figure 208: Lower column end hinge hysteresis (Matlab output).
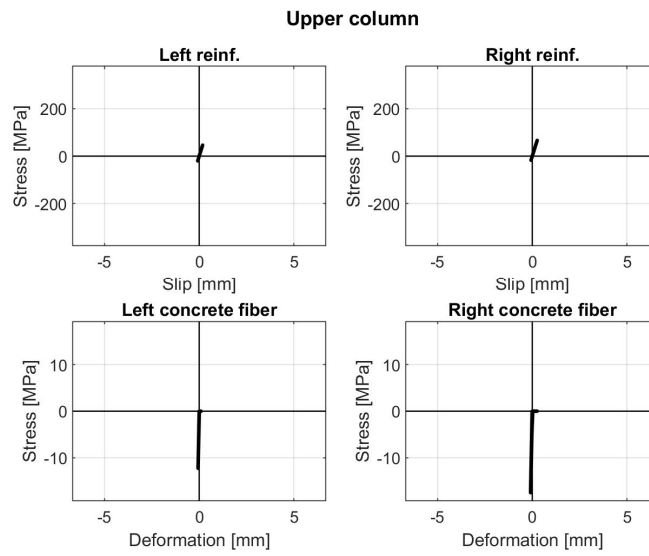
Figure 209: Upper column end hinge hysteresis (Matlab output).
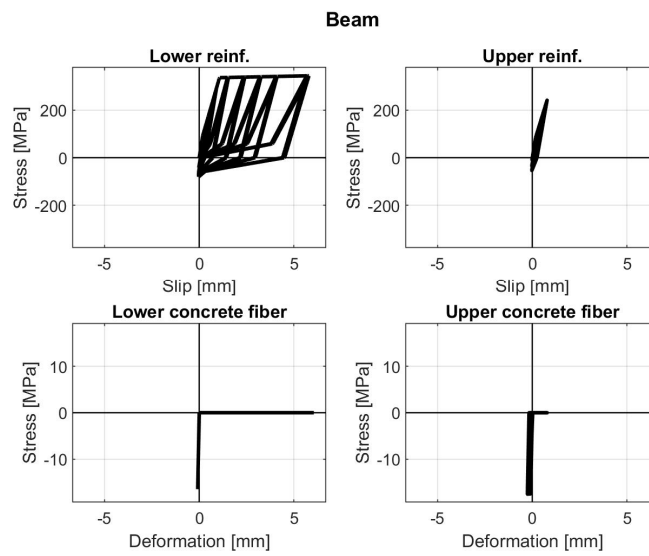
Figure 210: Beam end hinge hysteresis (Matlab output).
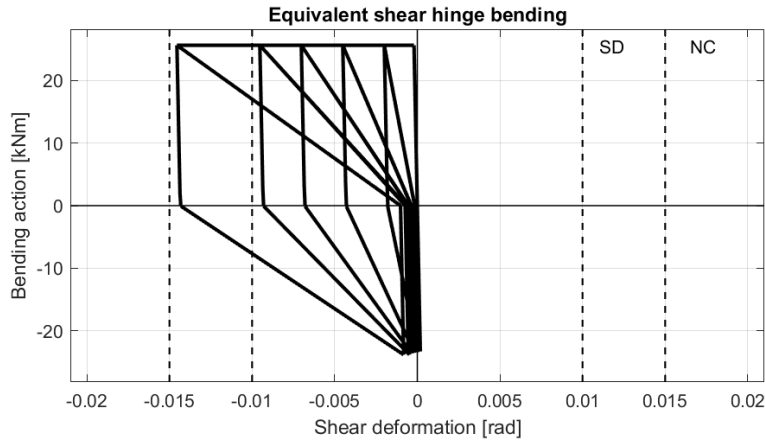
Figure 211: Equivalent joint shear panel hinge hysteresis (Matlab output).

C.3.   Non detailed 2D planar frame

In the present section, details about the prediction of both the monotonic and the cyclic response of a whole substandard frame (Calvi et al., 2002b, 2001) are presented. A first focus analyses the hysteretic behaviour of RC members and external T-joint in presence of the maximum drift experimentally imposed. In a second moment, a monotonic analysis is performed up to the drift level at which the first joint reaches its failure (see Chapter 6); a detailed representation of the elements and beam-column joints behaviour is also presented.

Reference specimen

The representation of the frame geometry, members cross-section dimensions, reinforcement arrangement, and material mechanical properties is reported in the previous Figure 187. For more details see the reference literature (Calvi et al., 2002b, 2001).
In Figure 212, the element nomenclature is schematized to interpretate the following graphs.
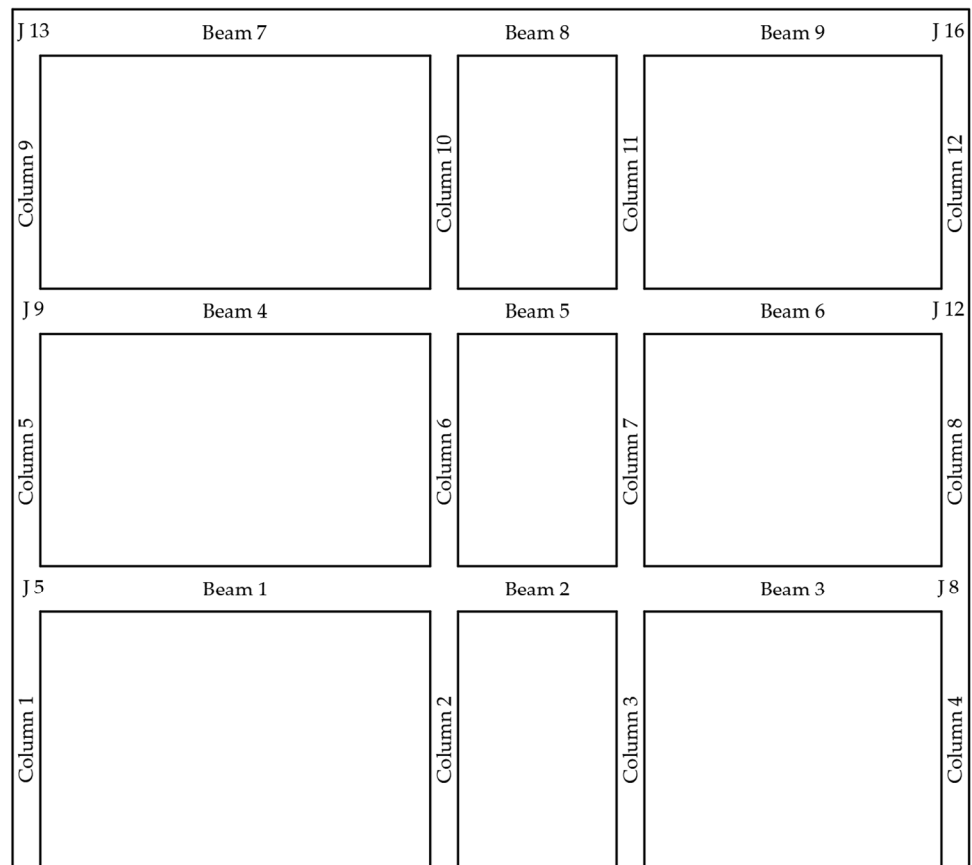
Figure 212: Numbering of the frame elements in the numerical model.

Cyclic response details

The experimental displacement pattern is imposed to the top of the frame. The member bending moment versus crack width behaviour is herein reported (Figure 213 and Figure 214). The crack width is assumed equal to the outer concrete fibre elongation; in other words, to the max distance between the interface crack sides (see Chapter 5 for the non-linear modelling of the end crack).
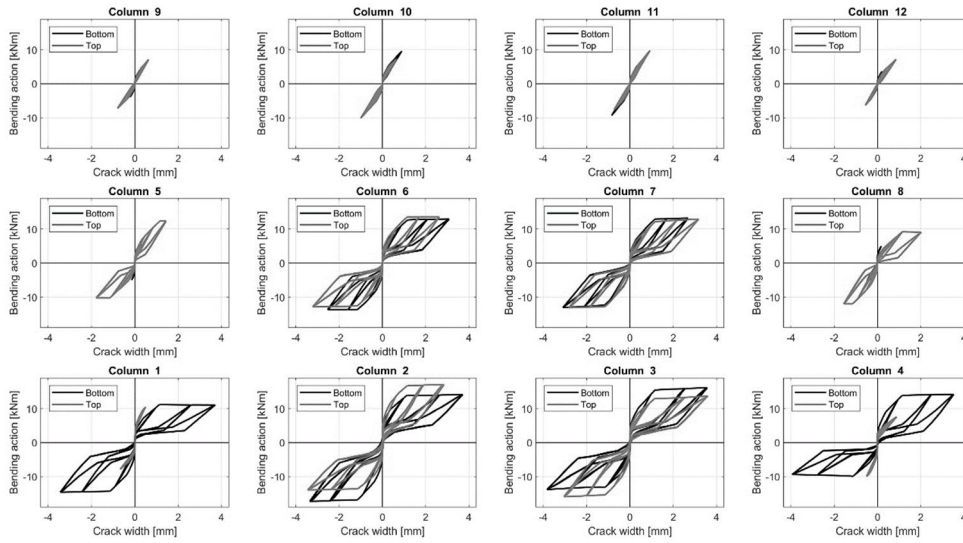
Figure 213: Frame column hysteresis in term of bending moment versus end crack width (Matlab output).
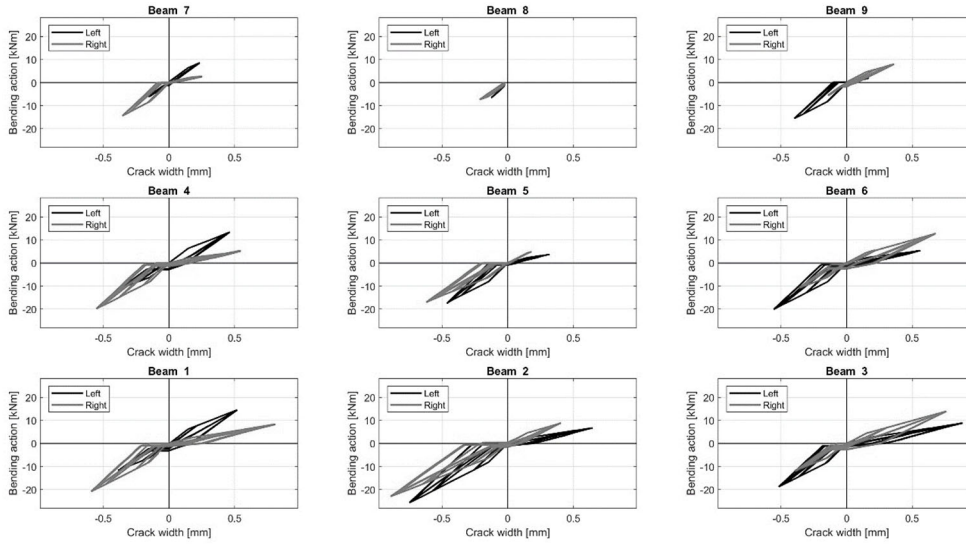
Figure 214: Frame beam hysteresis in term of bending moment versus end crack width (Matlab Output).
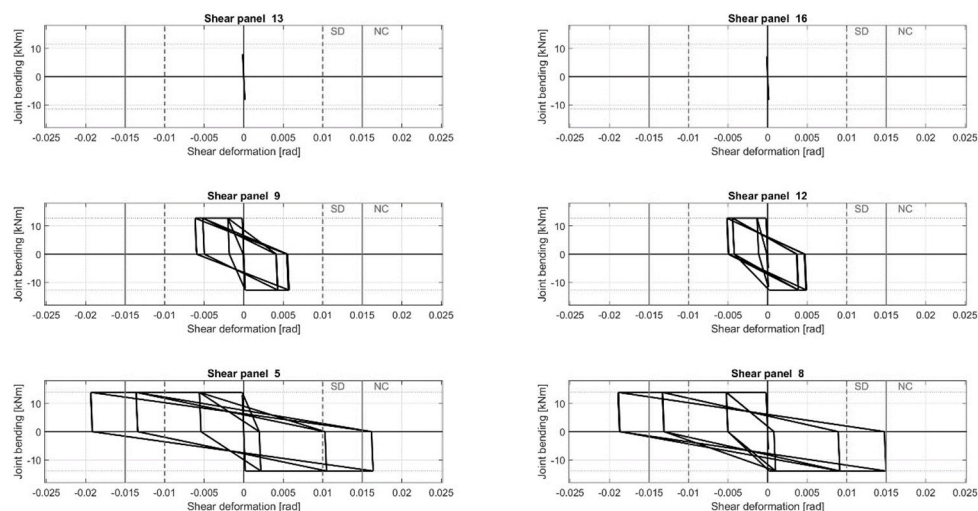
Figure 215: Joint panel behaviour in terms of equivalent bending moment versus equivalent rotation (Matlab output).

Monotonic behaviour up to a joint shear failure

A monotonic analysis up to a drift level equal to $\theta = 1.35\%$ is performed, to identify the reach of a Near Collapse Limit State in a beam-column external T-joint. A summary of the structural response is reported in Figure 216 in term of i) global hysteresis, ii) interstorey shear, iii) deformed shape, and iv) interstorey drift demand. Beam and column hysteretic behaviour, in term of bending moment versus crack width, is shown in the following graphs of Figure 217 and Figure 218. The crack width is estimated as above mentioned. The moment-rotation behaviour of the equivalent shear panel hinge, adopted to model the external T-joint, is visible in Figure 219. The reach of the NC Limit State in the outer right joint at the first floor is clearly visible. Its shear distortion is equal to the limit imposed for the reference Limit State to non-detailed T-beam-column joints reinforced with smooth rebars (Pampanin et al., 2003).

$$\gamma_j = 0.015 rad \qquad (205)$$

Finally, the hinge activation history is represented in Figure 220.
The frame response at the reach of a Significant damage is summarized in Figure 221. As already mentioned, the highest deformation demand is on the right outer T-joint at the first floor (Figure 222); it is equal to the reference SD maximum admissible shear distortion in a non-detailed T-type joint (Pampanin et al., 2003).

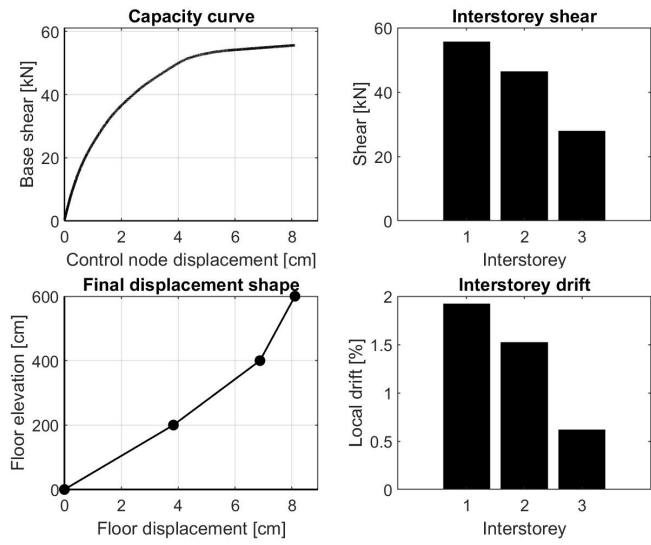$$\gamma_j = 0.010 rad \qquad (206)$$

327

Figure 216: Summary of the frame monotonic response up to a global drift level $\theta = 1.35\%$
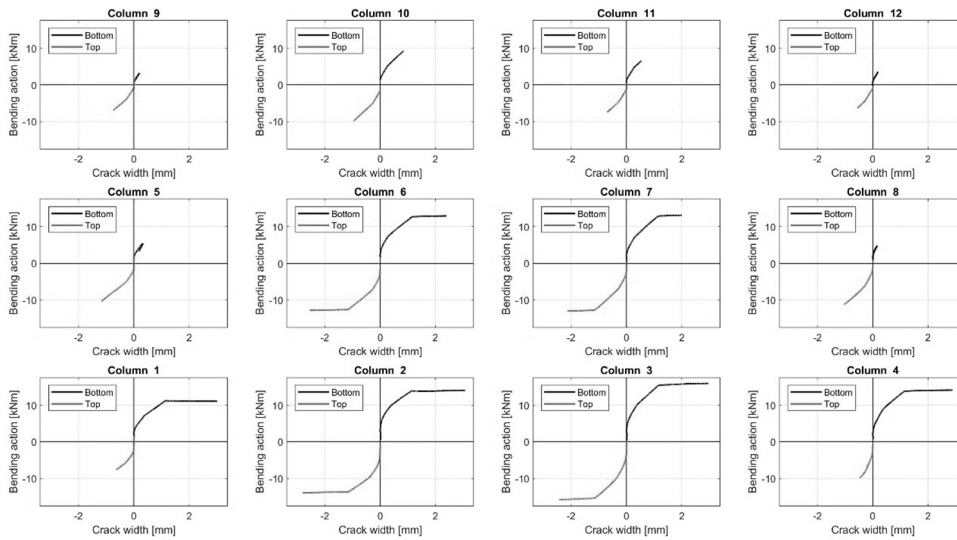*(Matlab output).*

*Figure 217: Column bending versus crack width relationships in the frame monotonic
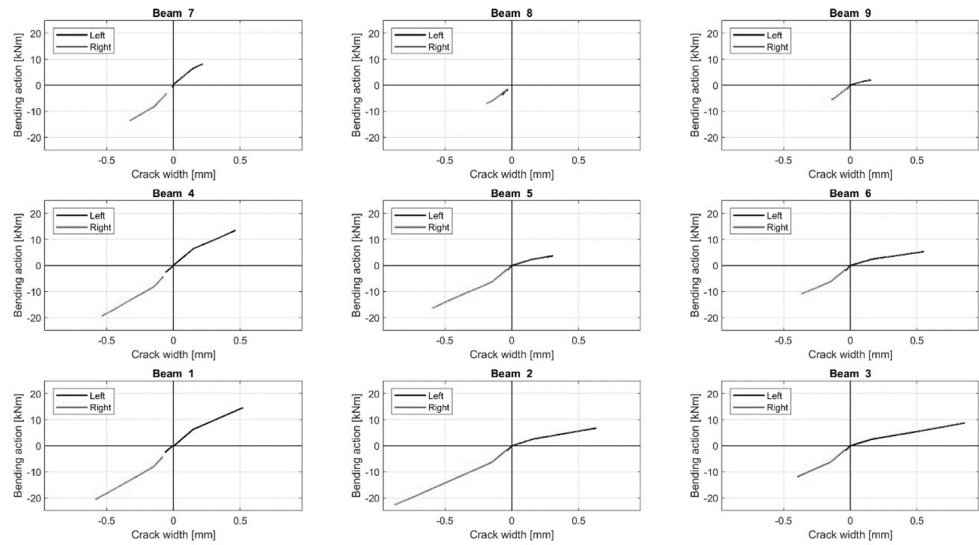response (Matlab output).*

Figure 218: Beam bending versus crack width relationships in the frame monotonic response (Matlab output).
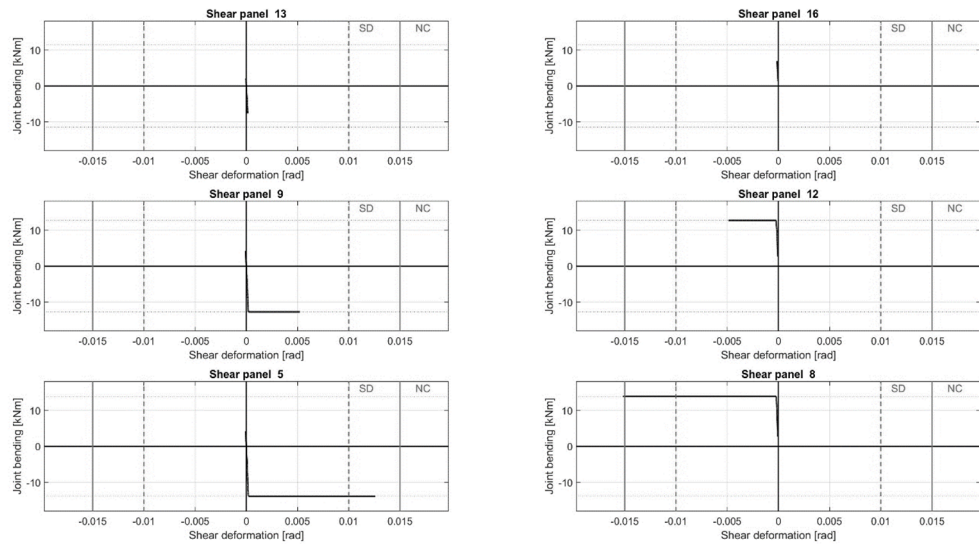

Figure 219: Equivalent moment-rotation behaviour for the modelling of the external T-type joints in presence of a deformation demand which cause the reach of Near Collapse Limit State ($\theta = 1.35\%$) (Matlab output).
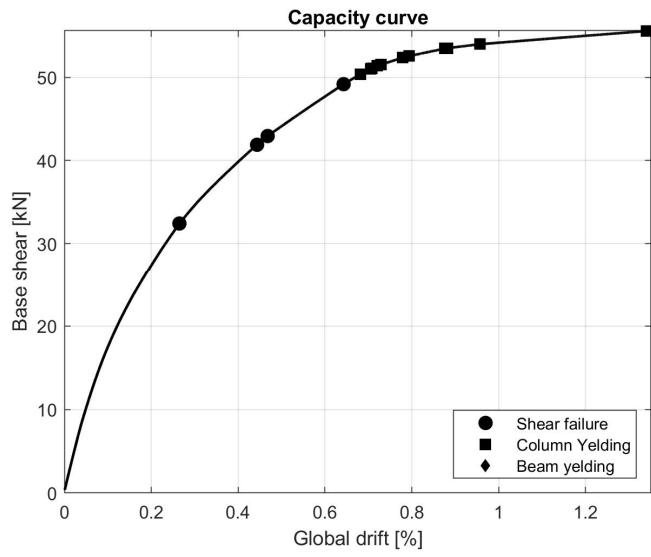
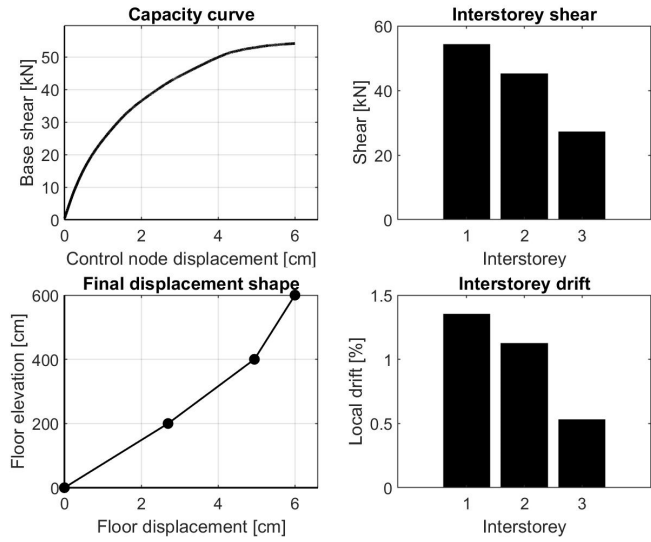*Figure 220: Hinge activation history prior to the reach of a NC limit state (Matlab output).*

Figure 221: Summary of the frame response at the reach of the SD Limit State ($\theta = 1.00\%$) (Matlab output).
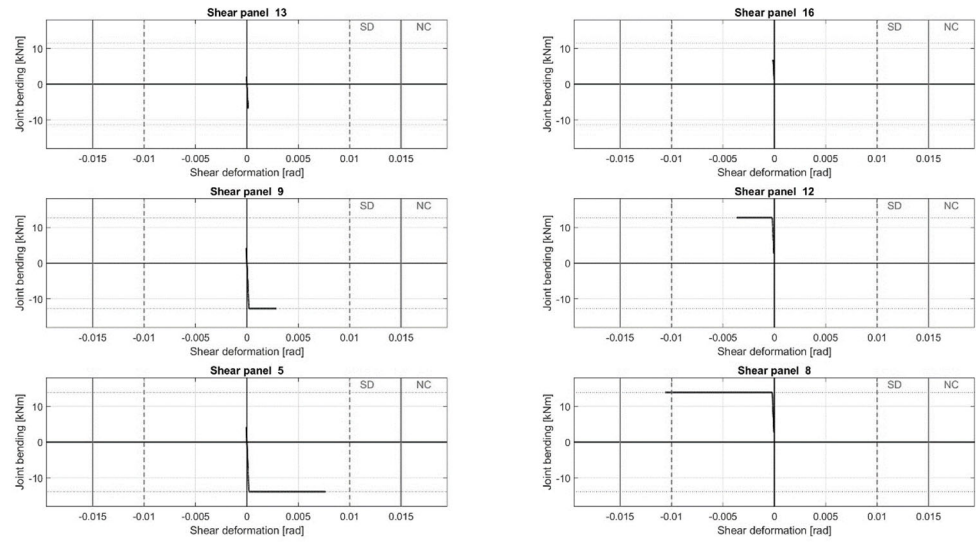
Figure 222: Equivalent joint shear panel behaviour in term of moment versus rotation relationship; reach of an SD Limit State (Matlab output).